ABSTRACT

Title of dissertation: ALL-SKY SEARCH FOR NEUTRINOS CORRELATED WITH GAMMA-RAY BURSTS IN EXTENDED TIME WINDOWS USING EIGHT YEARS OF ICECUBE DATA

Elizabeth Friedman
Doctor of Philosophy, 2021

Dissertation directed by: Professor Kara Hoffman
Department of Physics

GRBs have long been considered as potential sources of hadronic acceleration of ultra-high energy cosmic rays and, more recently, as potential sources of the diffuse neutrino flux measured by IceCube. This thesis presents a search for neutrinos correlated with 2,091 gamma-ray bursts (GRBs) in prompt and extended time windows using data from the IceCube Neutrino Observatory ranging from May 2011 to October 2018. Ten time windows, ranging from 10 seconds to -1/+14 days around the time of the GRB's gamma-ray emission, were searched for coincident neutrino emission and a p-value was assigned based on the most significant time window. The results for all 2,091 GRBs were divided by region of the sky and observed gamma-ray emission time, and were evaluated with a Binomial test, which was found to be consistent with background. The 23 most significant GRBs were examined in more detail and they were also found to be consistent with background. Limits were set assuming two flux models: equal neutrino flux at Earth for every

GRB and standard candle neutrino emission. The equal flux at Earth model led to similar constraints as previous IceCube prompt GRB studies, namely that GRBs are responsible for, at most, a few percent of the diffuse flux. The results of the standard candle analysis, however, indicate GRBs may be contributing up to 11% of the diffuse neutrino flux up to 1,000 second timescales, which leaves the door open to GRBs as neutrino sources and hadronic accelerators of at least some of the ultra-high energy cosmic rays.

All-Sky Search for Neutrinos Correlated with Gamma-Ray Bursts in Extended Time Windows Using Eight Years of IceCube data

By

Elizabeth Friedman

Dissertation submitted to the Faculty of the Graduate School of the
University of Maryland, College Park in partial fulfillment
of the requirements for the degree of
Doctor of Philosophy
2021

Advisory Committee:
Dr. Kara Hoffman, Chair/Advisor
Dr. Gregory Sullivan
Dr. Erik Blaufuss
Dr. Regina Caputo
Dr. Suvi Gezari

Acknowledgments

It is an impossible task to thank everyone who has helped me reach the point of completing this thesis. I am fortunate to have so many mentors, friends, and family supporting me through this entire process. Thank you all.

Thank you to all my teachers. Ms. Soulis, thank you for developing my interest in chemistry. I am honestly not sure if I would have taken a college science class if you had not been my teacher. Thank you to Lindley Winslow and Rene Ong for telling me to go to graduate school and for meaning it. Thank you to Fred Sinder for supporting my interest in physics, including flying across the country for my college graduation. Thank you to Dana Dlott for my first research job and to Brian Mason and Bill Hartkopf (Hail Friedonia!) for my first astronomy project. Thank you all for your guidance and encouragement.

I would like to acknowledge the University of Maryland and the National Science Foundation for their financial support of my graduate studies and research. Thank you to UMD for admitting me and taking a chance that I would be a successful graduate student. Thank you to NSF for selecting me as a GRFP Fellow. That acknowledgement of my potential early on in my career gave me confidence during the more difficult portions of graduate school.

Working on IceCube and ARA in graduate school has been incredible. I would like to thank my advisor, Kara Hoffman, for inviting me to join the Maryland IceCube group all those years ago. I have felt welcomed into the particle astrophysics group since my first visit as a prospective student, and your support over the years

has been so helpful. You were absolutely right that working on both ARA and IceCube would lead to a balanced PhD and I would learn hardware and analysis skills. Thank you for sending me to the South Pole (twice!) and for giving me room to develop skills beyond physics.

Thank you to Greg Sullivan, my co-advisor, for always asking the tough questions, and to Erik Blaufuss for putting those questions in practical perspective. You both taught me so much over the years. A special thank you to Don La Dieu for all the coding help, and to Alex Olivas for being my collaboration meeting exploring buddy. Walking through Tokyo was a highlight of graduate school. Thank you to Mike Richman, John Felde, and Ryan Maunu for getting me started on GRBs. In particular, thanks Mike for still helping me out as I wrote this dissertation! To all my fellow graduate students, past and present, thank you for making PSC 2238 so much fun. Josh Wood, thanks for teaching me how to solder my very first week at UMD. John Evans and Kwok Lung Fan, thanks for saving me from being the only graduate student in the group. That was a lonely year. Michael Larson, thank you for teaching me everything about IceCube, likelihoods, python, and all the bits and pieces that go into an analysis. I would still be struggling to start my analysis if you had not come to Maryland. Elim Thompson, thank you for everything. I am so glad we got to go to Pole together. Thank you to Naomi Russo and Yu Zhang for the endless administrative support for the collaboration meetings and conference travel. The whole Maryland particle astrophysics group is truly special.

To the Askaryan Radio Array and IceCube collaborations, thank you for the adventures, travel, and fun times. From collaboration meetings to the South Pole,

I cannot imagine a more exciting graduate school experience. I am grateful for the leadership opportunities and the trust to take on bigger projects. In particular, thank you to Chad Finley and Imre Bartos for reviewing my analysis and holding it to collaboration standards.

Graduate school would have been impossible without my friends and support system at Maryland beyond IceCube. Thank you to Jack Touart for teaching me about electronics, woodworking, cars, boats, and photography. Thank you to Steve Rolston for the opportunity to TA the Physics of Climate Change class. I learned so much in that class and I am grateful for the experience. A very special thank you to my first year study group and housemates at Cool Spring and Radcliffe. You all made grad school so much fun, even during the pandemic.

To my family, I do not have enough words to thank you for supporting me. Becki, Will, Torbin, Kyria, and Keefan - you are the best in-laws I could ever imagine. I need a Dunkin' Donuts napkin as I write this. To my nieces and nephew, Konstance, Katriel, and Kieran, thank you for being so much fun. The daily pictures and videos are fantastic, and graduate school got a lot easier once you three were around. Mom, Dad, Ben, and Becky - thank you for everything. Thank you for listening to practice talks and catching typos in this dissertation. I realize it is not easy for lawyers to listen to graduate level physics so thank you for politely smiling and nodding as much as you do.

Finally, thank you to Tristin. For everything.

Table of Contents

List of Tables

List of Figures

Chapter 1: Introduction

The IceCube Neutrino Observatory was "first light" for high energy neutrino astronomy, ushering in the age of multi-messenger astronomy. Correlating neutrinos with gamma-ray emission from high-energy sources would offer smoking-gun evidence of hadronic acceleration of ultra-high energy cosmic rays (UHECRs), as well as answer the century-old question about the origin of those cosmic rays. The source of the diffuse neutrino flux - neutrinos observed across the entire sky detected by IceCube in 2013 - is also a mystery that could be (at least partially) solved by a neutrino-gamma-ray source correlation.

Gamma-ray bursts (GRBs) are a potential source of UHECRs and neutrinos. They meet the energy and magnetic field requirements (see Figure 2.2) to produce the highest energy cosmic rays, but recent experimental searches have yet to find direct evidence of a connection between GRBs and high energy neutrinos. These studies have set tight limits on prompt neutrino emission, but the limits on extended time windows are far less strict. In addition to prompt, this analysis considers time windows well beyond the burst duration, continuing out to +/-1 day and -1/+14 days around the GRB.

This thesis examines 2,091 GRBs from 2011-2018, often separating them by

northern and southern sky, as well as short ($\leq$2s) and long (>2s) duration GRBs. An unbinned log likelihood was used to study ten time windows centered on the time of the GRB. The most significant time window is selected to represent the GRB in a Binomial test. The method to calculate the p-value for each GRB is designed to be relatively short (approximately 20 minutes of computation time per GRB) in an effort to run this analysis as a real-time follow-up to GRB alerts.

This thesis is organized as follows. An introduction to cosmic rays and GRBs is given in Chapter 2. Chapter 3 covers neutrinos and generic models for neutrino production from GRBs. The IceCube detector and accompanying hardware is outline in Chapter 4, and the neutrino candidate selection is described in Chapter 5. Chapter 6 discusses the unbinned log likelihood method and frequentist statistics. Chapter 7 explains the details of the analysis and Chapter 8 provides the results and limits, including summary tables for the 23 most significant GRBs and plots for the single most significant GRB from each sub-population. Chapter 9 discusses possible future research and paths forward for neutrino-GRB studies. Appendix A includes result plots for all of the most significant GRBs in this analysis. Full GRB tables are available as a supplemental PDF, but are not included directly in this thesis.

Chapter 2: Cosmic Rays and Gamma-Ray Bursts

Any discussion of astrophysical neutrino sources must include a word about cosmic rays. Earth's atmosphere is constantly being bombarded with charged particles, known as cosmic rays, with energies extending to greater than 10^{20} eV. The origin of the most energetic of these particles is still a mystery. The connection between gamma rays, cosmic rays, and neutrinos is a fundamental question in particle astrophysics. The composition of cosmic rays is not completely understood, but protons are known to make up a sizable portion of the cosmic ray spectrum. Therefore, a powerful accelerator must exist to propel those protons (or heavier ions) to energies above 10^{18} eV. Gamma-ray bursts meet the energy requirements for this acceleration. If gamma-ray bursts were accelerating protons to these high energies, then neutrinos would most probably be produced as well. Detection of neutrinos from any astrophysical source, including those correlated with gamma-ray bursts, would indicate a source of hadronic acceleration and hence cosmic rays.

2.1 Cosmic Rays

Although cosmic rays below $\sim$1 PeV can be measured directly by satellites, those interacting in the Earth's atmosphere cascade down in a shower of hadrons

and leptons. Ground-based experiments measure the resulting particles from these showers and estimate the energy of the original cosmic ray. These approaches can determine the energy of the cosmic ray, but they provide limited information about the location of the source. The direction of the original particle is reconstructed; however, charged particles will bend in magnetic fields, which makes them poor candidates for directional reconstruction. On the other hand, neutrinos are neutral and rarely interacting, which means, like photons, they are suitable for source identification. Neutrinos play an important role in multi-messenger astronomy, because they could provide information on hadronic acceleration pinpointed to an astrophysical source location.

2.1.1 First Detection of Cosmic Rays

Before cosmic rays were discovered, people believed radiation only came from the Earth. In the early 1900s, scientists began to realize there was more radiation at high altitude than expected. In 1910, Theodore Wulf found inconsistently high levels of ionization at the top of the Eiffel Tower compared to the bottom [1]. From 1911-1913, Victor Hess began mounting instruments in a hot air balloon to demonstrate that there was more ionization miles above the Earth than on the ground [1]. The most famous of Hess's flights took place during a partial solar eclipse in 1912, and he showed no decrease in the ionization levels, which proved that these cosmic rays were coming from a source other than the Sun. Robert Millikan named this radiation "cosmic rays" in 1925 [1], and nearly 100 years later their origin is still not fully

understood.

2.1.2 Current Cosmic Ray Research

Cosmic rays are still being studied in modern times. Satellites can observe lower energy cosmic rays up to roughly 1 PeV, while ground-based experiments are needed for higher energies. Auger [2], Telescope Array (TA) [3], and HiRes [4] are among the experiments able to probe the highest energy cosmic rays with energies around 10^{18}-10^{20} eV. The composition of these highest energy cosmic rays is disputed, with recent measurements indicating a mix of protons, helium, and heavier ions [5].

Identifying the astrophysical sources accelerating these cosmic rays is a complicated task. One step is to determine what objects have enough power to accelerate particles to these high energies. For cosmic rays below 1 PeV (indicated as the "knee" in Figure 2.1), for example, supernova remnants (SNRs) meet the energy requirements and are widely believed to be the source of these GeV to TeV cosmic rays [6] [7]. An argument can also be made based on acceleration mechanisms. In 1949, Enrico Fermi proposed a method to accelerate particles through interaction with "wandering magnetic fields" [8]. This method was proposed for magnetic fields in interstellar space, and was later shown to apply to shock fronts as well [9]. This mechanism, known as first order Fermi acceleration, produces a distribution of proton energies following a power law spectrum, which matches observations of cosmic rays [10]. When specifically applied to supernova remnants, it is clear that

Fermi acceleration is a viable mechanism to accelerate cosmic rays to the observed energies [6]. Electrons would also be accelerated, producing gamma rays from synchrotron radiation followed by inverse-Compton scattering. Fermi acceleration is discussed in more detail in 3.1.2.

Figure 2.1 shows the features of the isotropic cosmic ray spectrum, including the knee around 10^{15} eV, and the "ankle" around 10^{18} eV. The vast range of cosmic ray energies indicates a variety of progenitors for these particles. As previously discussed, supernova remnants are generally accepted as the progenitor of cosmic rays below the knee, following a $\frac{dN}{dE} \approx E^{-2.7}$ power law [11]. From the knee to the ankle, a $\frac{dN}{dE} \approx E^{-3}$ behavior is observed. The origin of these sources is largely unknown, but is believed to be a combination of galactic and extragalactic [9]. The energy where the sources transition from galactic is disputed, and it is possible that other galactic sources, such as young massive star clusters, become relevant around PeV energies [12].

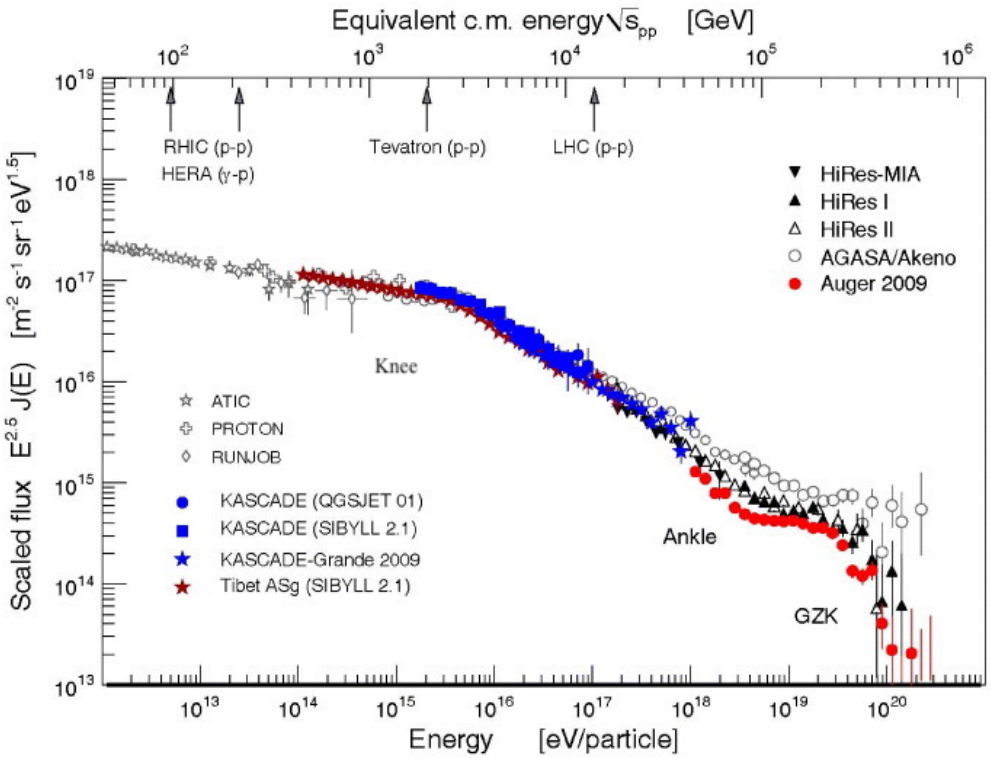

Figure 2.1: The cosmic ray spectrum showing the "knee" at 10^{15} eV and the "ankle" at $10^{18.6}$ eV [13].

Figure 2.2, known as a Hillas plot, is a helpful way to visualize potential sources of cosmic rays [14]. The maximum energy a particle can attain via Fermi acceleration (3.1.2) depends on the size of the accelerator and the strength of the magnetic fields. The three reference lines indicate a size and magnetic field strength required to accelerate iron to 100 EeV (green line), or protons to 100 EeV (dotted red line) and 1 ZeV (solid red line). Supernova remnants are not able to accelerate particles to the highest measured energies, which is consistent with their categorization as accelerators up to the knee. SNRs are relatively large, but their magnetic fields are not strong enough to confine particles long enough to accelerate them to very high energies. For more energetic cosmic rays, the likely sources appear to be compact

objects with large magnetic fields or extended objects [15].

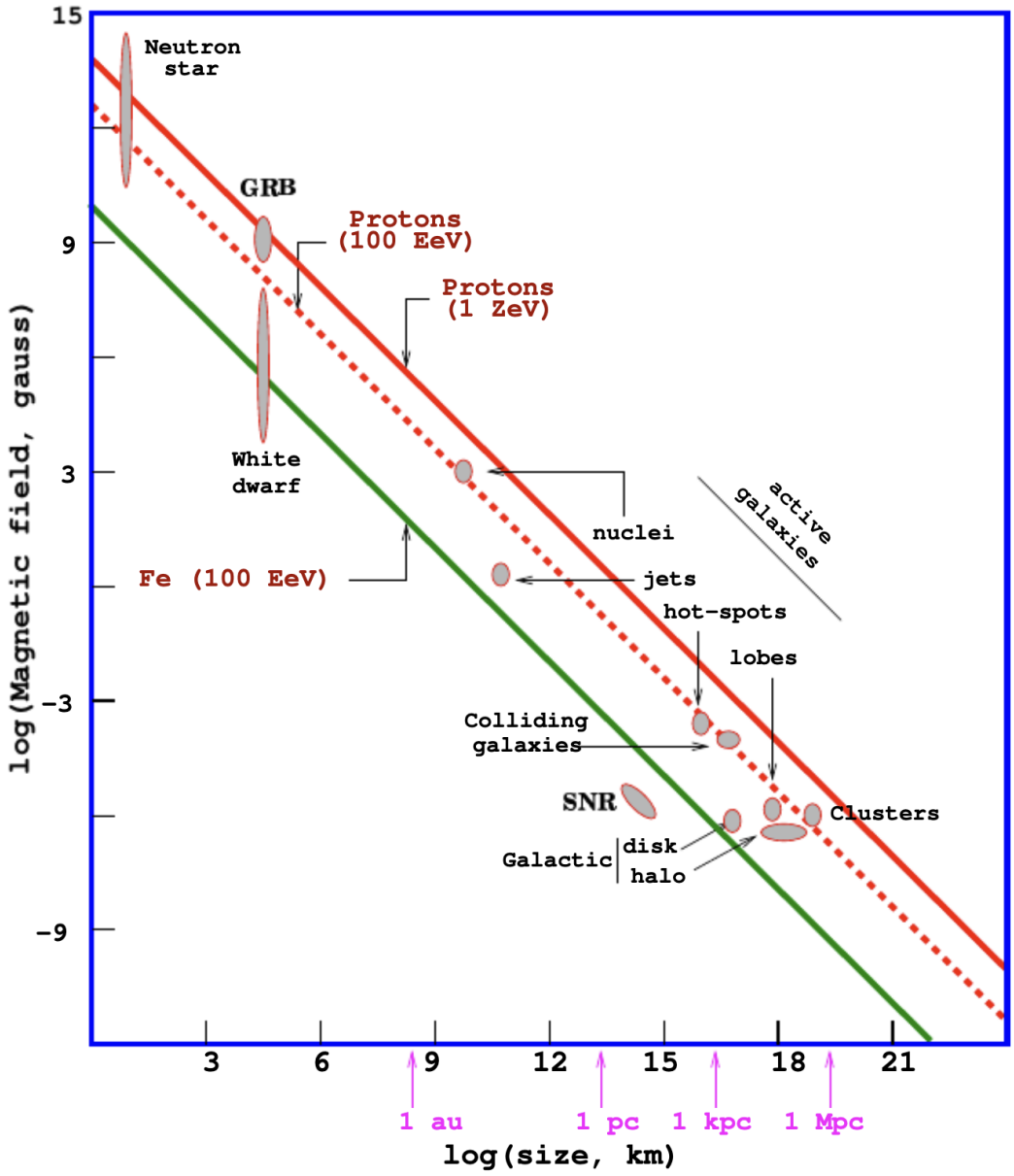

Figure 2.2: A Hillas plot showing potential accelerators of cosmic rays. GRBs are one of the few sources with a combination of size and magnetic field strength to accelerate protons above 1 ZeV, making them an ideal candidate for UHECR acceleration. The size of the GRB refers to the radius of the stellar envelope, which is roughly the size of the magnetic fields [16]. Figure from [15], modified from [14].

Above the ankle, the energy spectrum returns to $\frac{dN}{dE} \approx E^{-2.7}$ [17]. Sources producing cosmic rays with energies above $10^{18.6}$ eV are commonly believed to be

extragalactic, because the magnetic field of the galaxy cannot contain them [18]. It is difficult to comment on anything above 10^{20} eV, because there are very low statistics in this energy region due to a cutoff above $10^{19.5}$ eV called the Greisen-Zatsepin-Kuzmin (GZK) cutoff. This cutoff comes from the high energy protons interacting with photons from the cosmic microwave background via the Delta-resonance [18], [19]. A possible result of the Delta-resonance is a neutral pion and proton. After this interaction, the proton energy is below the GZK cutoff. It is worth noting that cosmic rays close to the GZK cutoff may be less influenced by magnetic fields (if they are protons), and would be better at providing directional information if they originate in relatively nearby sources [20]. Unfortunately, the low statistics make this a limited source of information.

It is ultimately the cosmic rays above approximately 10^{18} eV that are relevant to the work in this thesis. By energy and acceleration arguments, these ultra-high energy cosmic rays must be produced by some of the most energetic and cataclysmic events in the universe. Gamma-Ray Bursts (GRBs) meet the energy requirements and are thought to include shock waves that could accelerate protons enough to produce the highest energy cosmic rays.

2.1.3 Cosmic Rays as Sources of Background

When a cosmic ray enters the atmosphere, it can interact with a nucleus and create pions. These pions then decay into showers of photons, neutrinos, electrons and muons that are measured by various ground experiments (see 2.1.2). The

particle showers caused by cosmic ray interactions in the atmosphere are shown in Figure 2.3. Some research in IceCube is devoted to studying these cosmic ray air showers, but the analysis presented in this thesis is focused on neutrinos produced outside Earth's atmosphere. Those neutrinos, called "astrophysical neutrinos" are hypothesized to be the byproduct of hadronic acceleration in extremely energetic sources [21]. The neutrinos created in a cosmic-ray air shower are called "atmospheric neutrinos" throughout this thesis. Atmospheric neutrinos are a 4π irreducible source of background that is carefully measured and modeled in simulation.

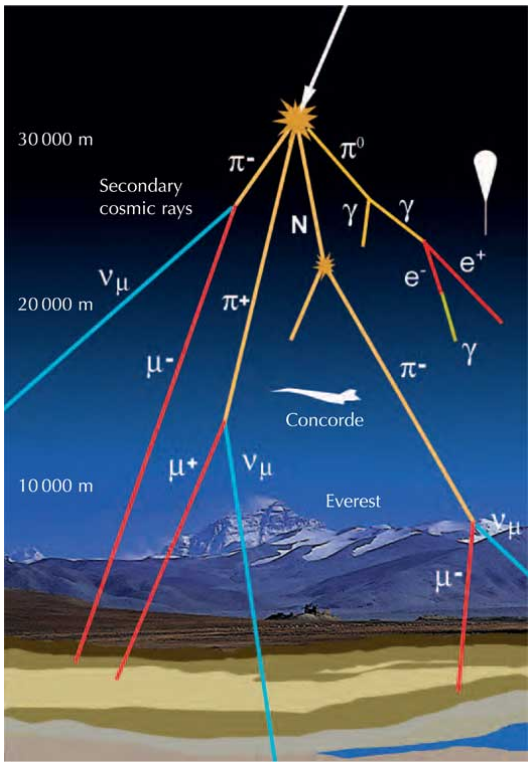

Figure 2.3: A cartoon illustration of a cosmic-ray air shower. A proton interacts in the atmosphere, producing photons, neutrinos, electrons, and muons. Figure from [22].

The muons created by the π^+ interaction are the other major source of background in this analysis. These muons are shielded by the Earth for the northern sky, but

the southern sky and horizon see large numbers of atmospheric muons enter the detector. For every atmospheric neutrino, there are roughly 10^6 muons entering the detector. These muons can be difficult to distinguish from a muon created by a neutrino interacting within the detector. Separating cosmic-ray muons and muons resulting from a neutrino interaction, and further separating the astrophysical and atmospheric neutrinos, is the focus of Chapter 5.

2.2 Gamma-Ray Bursts

Gamma-ray bursts are enormously bright and energetic transient astrophysical objects. The photon energy corresponding to the peak spectral flux, E_{peak}, can be used to estimate the total isotropic radiated energy, E_{iso}, as shown in Figure 2.4. This estimated isotropic energy spans many orders of magnitude, from $\sim 10^{50}$ to $\sim 10^{54}$ ergs [23].

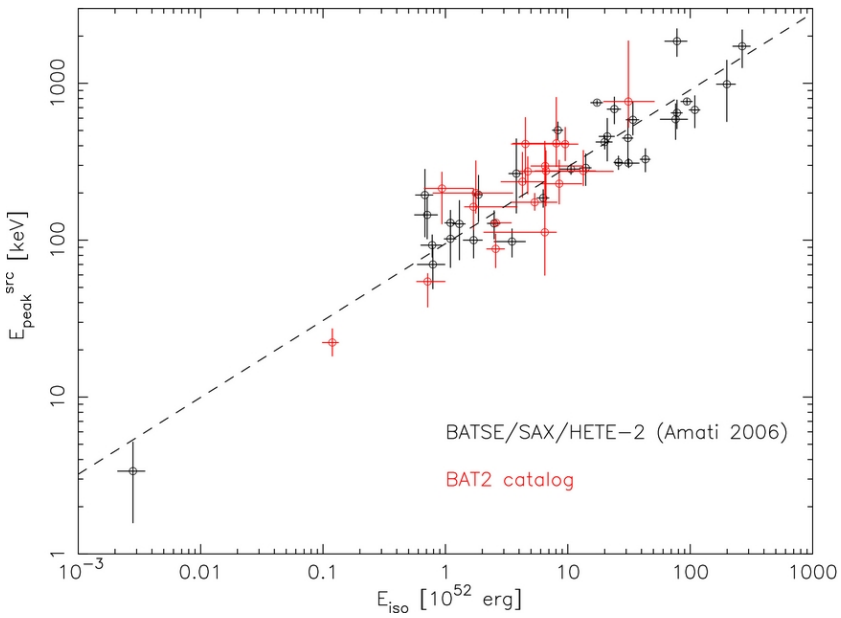

Figure 2.4: The estimated total isotropic radiated energy versus the peak spectral energy of BATSE and Swift GRBs. The typical total energy of these GRBs ranges from 10^{50} to 10^{54} ergs. Figure from [24].

GRB duration varies by many orders of magnitude as well. They have been measured lasting from milliseconds to hundreds of seconds, where those lasting less than two seconds are named "short" GRBs and the ones lasting longer than two seconds are "long" GRBs (see Figure 2.5). Short GRBs are believed to be associated with compact binary mergers, which is supported by LIGO's recent detection of a gravitational wave that overlapped in time and space with a short GRB detected by the Fermi Gamma-Ray Telescope [25] [26]. Long GRBs are thought to result from collapsars, a type of core collapse supernova [27].

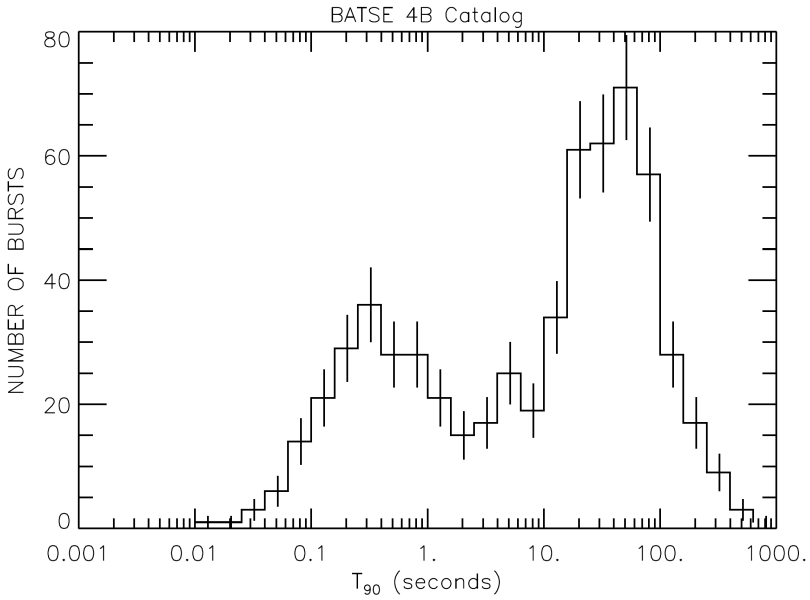

Figure 2.5: The clear separation of GRBs into two distinct classes as measured by BATSE. Short GRBs have measured gamma-ray emission for less than two seconds, while long GRBs last longer than two seconds (though typically less than 1,000 seconds). Figure from [28].

2.2.1 History of Gamma-Ray Burst Detection

Gamma-ray bursts were first detected in 1967 when the Vela satellites [29] detected a gamma-ray signal that was unfamiliar. These satellites were launched by the United States to enforce the Nuclear Test-Ban Treaty from 1963, which banned testing nuclear weapons in the upper atmosphere and space [30]. The satellites were positioned to monitor gamma rays emitted in such tests, but the short bursts of gamma rays observed did not match any known nuclear weapon signatures and did not seem to originate on the Earth or Sun [29]. In 1971, the IMP-6 satellite was launched by Russia to further study the mysterious bursts of gamma rays [31]. In 1973, IMP-6 confirmed the Vela detections and noted that "the observed gamma-ray bursts represent[ed] an entirely novel form of cosmic energy release" [31].

Nearly twenty years passed before there was consensus in the scientific community regarding the origin of gamma-ray bursts. GRBs were first thought to come from neutron stars in the galactic disk. The Compton Gamma-ray Observatory, which included the Burst Transient Source Experiment (BATSE), launched in 1991 and observed that GRBs were isotropically distributed [32]. The uniform distribution meant the sources could not be limited to the galactic disk, and therefore provided strong evidence for extragalactic sources. GRBs are still actively researched to this day, because their energy production mechanisms are poorly understood. A few of the currently favored models are discussed below. While the details may be unknown for now, any process that emits the energy of a GRB in hadronic cosmic rays must also produce neutrinos. Measuring neutrinos - or a lack thereof - helps reveal details of the central engine, the surrounding matter, and acceleration mechanisms of the gamma-ray burst.

2.2.2 Current Gamma-Ray Burst Models

The Fireball model is a broad name for several specific models of the GRB's central engine and acceleration mechanism that predict neutrinos coincident with gamma-ray emission. The Fireball involves a highly relativistic jetted outflow of matter, containing relativistic shells made up of a plasma of electrons, photons, and protons. These shells collide and produce shocks, which leads to conditions to accelerate protons via Fermi acceleration (see 3.1.2). Electrons are also accelerated by these shock fronts, leading to synchrotron radiation and inverse-Compton scattering

to produce the observed gamma rays [33]. The sub-class of Fireball model that include these shocks inside the plasma is known as the "internal shock" model. Recent IceCube analyses set tight constraints on prompt neutrino emission from the internal shock model [34].

Two other sub-classes of the Fireball model were constrained in [34]: "photosphere" and "ICMART" [35]. These models both feature shock acceleration of charged particles farther from the GRB's central engine than the internal shock model. The dissipative photosphere model results in gamma-ray emission in a region with larger optical depth, which predicts increased neutrino production but overall lower energies compared to the internal shock model. The Internal Collision-induced MAgnetic Reconnection and Turbulence (ICMART) model predicts a highly magnetized outflow that suppresses photon emission until a large radius. When the internal shocks can finally disrupt the ordered magnetic fields, a runaway magnetic dissipataion process is predicted, resulting in reconnection and gamma-ray emission at the largest radius of the three models. ICMART predicts the lowest neutrino flux of the three and therefore has the weakest constraints in [34].

There is increasing interest in models that predict neutrinos as precursors [36] [37] or afterglows [38], because the lack of tight constraints could keep GRBs as candidates for hadronic acceleration of UHECRs and still be consistent with the non-detection of neutrinos correlated with prompt gamma rays. The analysis presented in this thesis was designed to be generic due to large variation in predicted neutrino fluxes from GRBs. The theoretical predictions that motivate an expectation for neutrinos correlated with gamma rays will be discussed in Chapter 3.

2.3 Modern Gamma-Ray Burst Detectors

Today, satellites are used to detect gamma-ray bursts. The Neil Gehrels Swift Observatory (commonly known as "Swift") [39] and Fermi satellite are responsible for nearly 90% of the world's GRB detections [17]. The Swift observatory has three instruments working together to observe GRBs, including gamma-ray measurements as well as follow-ups in X-ray, ultraviolet, and optical wavelengths. The three components of Swift are the Burst Alert Telescope (BAT) [40], the X-ray Telescope (XRT) [41], and the UV/Optical Telescope (UVOT) [42]. Swift observes roughly 100 bursts per year [43] and sends alerts to the Gamma-ray Coordinates Network (GCN) for further study (see 2.3.1).

Swift BAT is able to measure GRBs with excellent precision due to its coded aperture mask [44]. Swift scans the sky with a 1.4 steradian field of view and determines the location of a GRB within 1-4 arcminutes. The satellite can then slew to the gamma-ray direction within one minute of observation, which allows the X-ray and UV/optical follow-ups to pinpoint the direction of the GRB. The X-ray followup can resolve the position to arcseconds, and UV/optical followup can improve the position uncertainty to sub-arcseconds. This resolution exceeds that of IceCube, which has a lower bound single event angular uncertainty of 0.2 degrees.

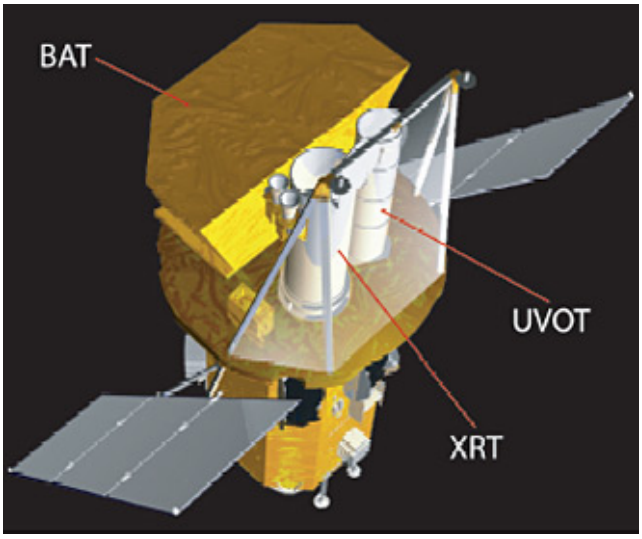

Figure 2.6: The Swift satellite with its three telescopes [45]

The Fermi Gamma-ray Space Telescope is another satellite studying high energy astrophysics. Fermi has two instruments: the Large Area Telescope (LAT) and the Gamma-ray Burst Monitor (GBM). Fermi-LAT's field of view is more than one-fifth of the sky, and can cover the entire sky every three hours [46]. Fermi-GBM observes the full unocculted sky, which means it detects many GRBs, but it has poor angular resolution. The angular resolution of Fermi-GBM is addressed in more detail in 2.3.3.

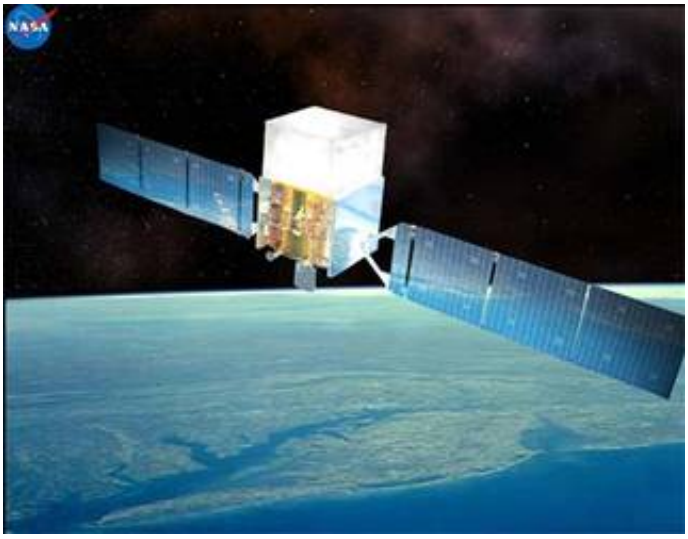

Figure 2.7: The Fermi satellite [47]

Other satellites contribute to GCN notices as well. The International Gamma-Ray Astrophysics Laboratory (INTEGRAL) [48], Konus-Wind [49], the Monitoring All-sky X-ray Image (MAXI) [50], AGILE [51] [52], the Suzaku satellite's Wide-band All-sky Monitor (WAM) [53] [54], and Third Interplanetary Network (IPN) [55] are all currently searching for GRBs.

2.3.1 Gamma-ray Coordinates Network (GCN)

When GRBs are detected by any of these satellites, an alert is sent to the NASA Gamma-ray burst Coordinates Network (GCN) [56]. GCN alerts are part of the larger Transient Astronomy Network (TAN). This gives the scientific community a chance to perform follow-up measurements with other satellites or ground-based detectors.

The three types of GCN alerts are notices, circulars, and reports. Notices provide the coordinates of the GRB (or other transients) as quickly as possible.

These are machine-readable alerts intended to offer the fastest follow-up. Circulars are the human-readable emails sent out after the notice. The circular may include updated timing, localization, or other measurements as well as calls to coordinate with specific observatories. Reports are issued considerably later than both notices and circulars. Reports contain write-ups of the observation, full analyses, and any relevant corrections.

IceCube's Realtime Neutrino Alert Stream [57] and Fast Response Analysis [58] [59] regularly send notices and circulars to the community accompanying IceCube's neutrino alerts and follow-up analyses. Although the analysis described in this thesis is not conducted in real-time, a version of the analysis could join the Fast Response framework as a neutrino follow-up to GRBs.

2.3.2 GRBweb

Many experiments announce their detections, from gamma rays to gravitational waves and beyond, via the GCN system. These alerts are an excellent resource for rapid follow-up and immediate communication. For long-term studies, however, it is necessary to gather the relevant alerts into a single database. GRBweb is a catalog of gamma-ray bursts that collects information from all the satellites discussed in 2.3 [60] [61]. This is a publicly available SQL database that is easily sorted and downloaded using Python. A summary table with all GRB properties is also available to view in a web browser and download as a text file. GRBweb is automatically updated weekly and is hosted by the IceCube Collaboration [62].

Satellite	Number of GRBs	Percent of Catalog
Fermi-GBM	1236	59.1%
Swift	621	29.7%
IPN	146	7.0%
Fermi-LAT	79	3.8%
Other	9	0.4%

Table 2.1: The breakdown of gamma-ray bursts detected in this analysis by satellite. Multiple satellites can contribute information for a single GRB. This table gives a sense of satellite contribution by measuring the position of the GRB. The satellite with the lowest uncertainty in source position is selected. Here, "Other" refers to optical follow-ups sent via GCN circular (5 GRBs detected), Swift-XRT (2 GRBs detected), MAXI Det (1 GRB detected), and INTEGRAL (1 GRB detected) [62].

The goal of this analysis is to perform a model-independent search on as many GRBs as possible. The only information required to include a GRB in this search was a start and stop time of measured gamma rays, and a location of the GRB. The fluence and redshift were not considered when selecting GRBs for this analysis. The GRBs in this analysis (see 7.2) have a measured $T_{90,start}$, which is the time when the burst has reached 5% of the maximum gamma-ray fluence, and a T_{90}, which is the time between the 5% and 95% fluence levels [60]. The T_{90} is used to determine if the GRB is categorized as a long GRB ($T_{90} > 2$ seconds) or a short GRB ($T_{90} \leq 2$ seconds). A T_{100} is also required for every GRB, and is different from the T_{90} because it is defined as the time between the earliest measured gamma-ray and latest measured gamma-ray, even if those results come from different satellites. The T_{100} is calculated by subtracting the earliest gamma-ray trigger time from the latest end of the T_{90} intervals [62].

GRB names throughout this thesis follow the standard format from GRBweb, which is a six-digit date followed by a letter indicating its order in the day. For

example, GRBs 130408A and 130408B both occurred on April 8, 2013, but the "A" GRB happened earlier in the day than the "B" GRB. The times are based on UTC time to determine the end of a calendar day.

2.3.3 Fermi Gamma-Ray Burst Monitor Position Uncertainty

Understanding the uncertainty in the position of the GRB is a core part of this analysis. Many satellites can resolve the position of a GRB to less than a degree, but the position uncertainty for the Fermi Gamma-Ray Burst Moniter (GBM) can be very large and requires special attention. The method of handling this large position uncertainties is described in detail in section 7.4. The motivation for careful handling of the GBM position is the large *spread* in uncertainty. Figure 2.8 shows the variation in position uncertainty, with many GRBs at 20°-40°, and some even above a 60° position uncertainty. Previous IceCube analyses have attempted to estimate this large uncertainty as a weighted sum of Gaussian distributions with $\sigma_1 = 2.6°$ and $\sigma_2 = 10.4°$, with weights of 0.72 and 0.28, respectively [17]. This led to an under-estimation of the true GBM errors, as illustrated in yellow in Figure 2.9.

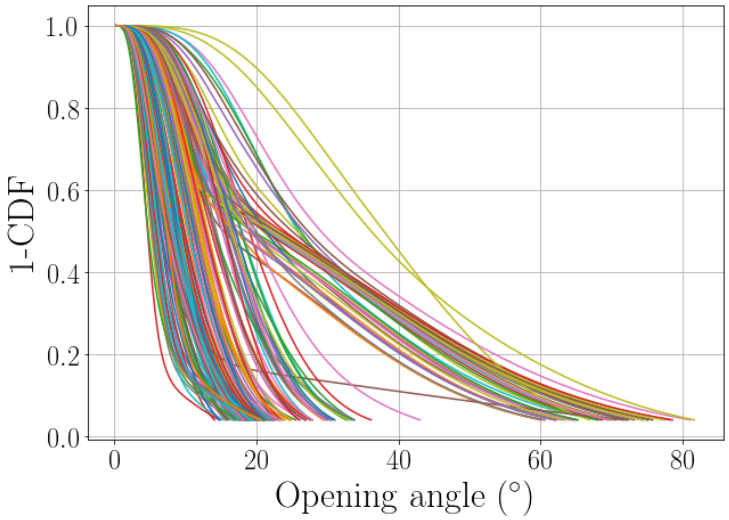

Figure 2.8: The large spread in position uncertainty for GRBs detected with the Fermi-GBM satellite. Each line repesents an individual GRB and the errors range from 20 to 80 degrees. A single position uncertainty does not correctly describe GBM bursts. Figure by P. Coppin based on [63].

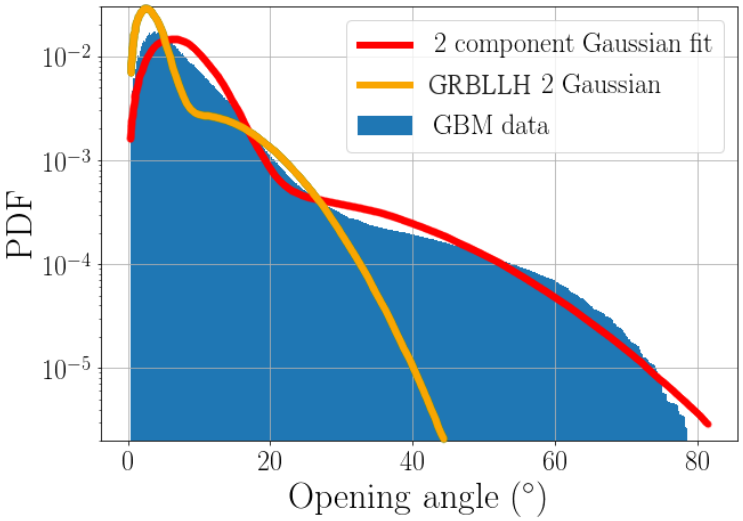

Figure 2.9: The large spread in position uncertainty for GRBs detected with the Fermi-GBM satellite is shown as a probability density function in blue. The yellow line indicates the sum of Gaussian distributions used by older software, known internally in the IceCube Collaboration as "GRBLLH," to approximate the GBM source position uncertainties. The red line indicates an attempt to approximate this PDF. Figure by P. Coppin [64].

Fortunately, the Fermi-GBM team has begun releasing healpix probability

maps that give far more detailed position uncertainty information. An example of a GBM probability skymap is shown in Figure 2.10. These are full-sky HEALPix maps with a resolution of 0.46° per pixel, and are produced quickly enough to be included in GCN circulars [63].

A large part of this analysis is built around implementing these skymaps in the likelihood calculations (discussed in detail in Chapter 6). To maintain a consistent analysis framework, the well-localized GRBs are also converted into probability skymaps and treated the same as GBM bursts. The well-localized skymaps place all the probability in a handful of equally weighted pixels, allowing any fits to scan one degree around the right ascension and declination reported on GRBweb.

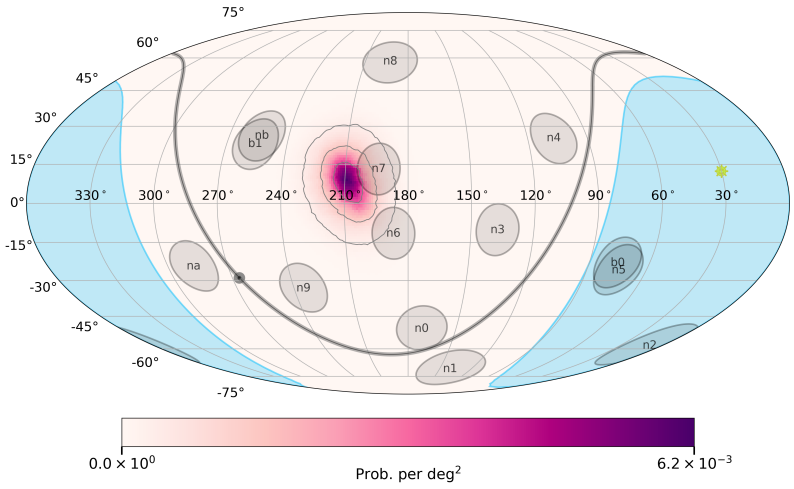

Figure 2.10: This figure shows an example skymap produced by the Fermi-GBM team to understand GRB position uncertainty in far more detail than previous estimates [65] [66]. These maps assign a probability (purple) to each pixel on the sky with a resolution of 0.46° per pixel. The grey circles around the burst indicate 1, 2, and 3 sigma contours. The light grey circles everywhere else on the skymap represent the detector pointings for all 14 GBM detectors at the time of the trigger. [63] [67]

Chapter 3: Neutrinos

3.1 Neutrinos as Cosmic Messengers

Neutrinos can provide information about the highest energy processes in the universe. Above a few TeV, photons are energetic enough to pair produce with infrared and Cosmic Microwave Background (CMB) photons long before they reach Earth [18]. Therefore, the distant universe is opaque in photons at the highest energies. Similarly, protons above roughly 5×10^{19} eV will interact with CMB photons while traveling to our detectors (see discussion in 2.1.2). Figure 3.1 illustrates the distances and energies where photons and protons are no longer observed due to pair production and photohadronic interactions. Neutrinos, however, interact so rarely that they are still able to reach us over long distances, even at extremely high energies.

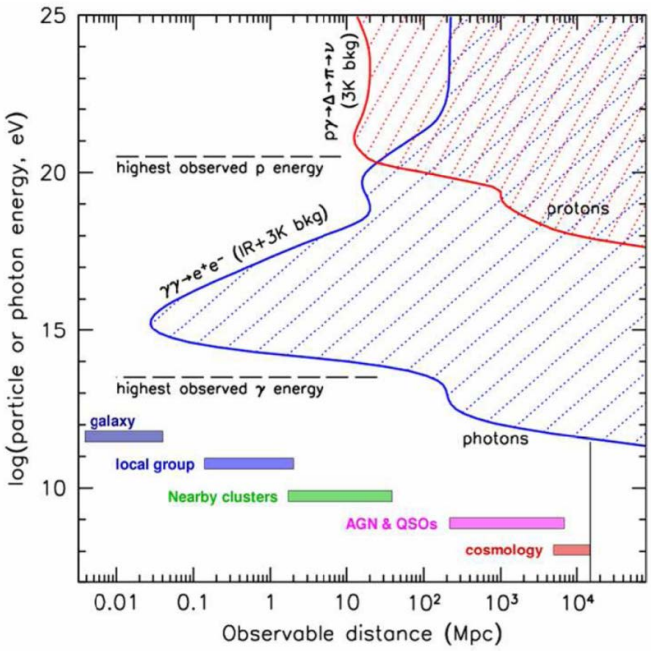

Figure 3.1: The distance photons and protons can travel versus their energy. The colorful bars along the bottom of the plot indicate distance scales of astrophysical objects, but are not referencing an energy range. The universe is opaque to both photons and protons in the highest energy regimes. Only neutrinos offer a glimpse of the highest energy events in the universe. Figure from [68].

Another advantage of studying neutrinos is their ability to point to their source location. Cosmic rays provide a lot of detail about energetic processes in the universe; yet, it is extremely difficult to determine the origin of these particles due to deflection from magnetic fields. Neutrinos have no charge, which means they travel unhindered through magnetic fields. A primary goal of the IceCube Neutrino Observatory is to use this directional information about neutrinos to determine their sources. Determining the sources of neutrinos would further our understanding of the highest energy processes in the universe.

3.1.1 What Neutrinos Tell Us About Cosmic Rays

The atmospheric neutrino spectrum is related to the cosmic-ray spectrum. IceCube's measurements have shown an atmospheric neutrino spectrum of $E^{-3.7}$ [69]. There is a hypothesized second component, called "prompt," to the atmospheric neutrino spectrum at higher energies with $E^{-2.7}$, which is shown in Figure 3.2. The fact that the cosmic-ray spectrum also has a spectral index of 2.7 is not a coincidence; the proposed prompt spectrum has the same shape because the neutrinos are the result of charmed particle decays in cosmic-ray showers. Charmed particles decay so fast that they rarely have time to interact (hence the term "prompt"), which means their spectrum is similar to the primary cosmic-ray spectrum [9]. The conventional atmospheric flux, however, results from decays and interactions of pions and kaons into muons and muon neutrinos.[1] Therefore, the neutrino spectrum is shifted in energy from the original cosmic rays [9].

[1]It is possible for pions to decay into electrons and electron neutrinos, but this is less common due to the small mass of the electron.

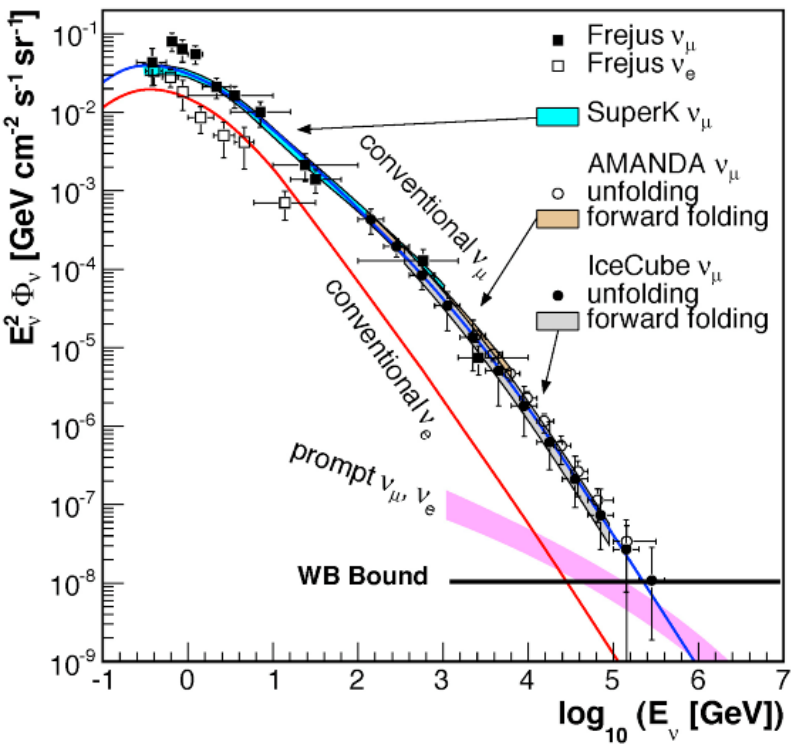

Figure 3.2: The conventional atmospheric spectrum is softer than the prompt or Waxman-Bahcall spectrum (labeled "WB bound"). The prompt spectrum is a predicted component of the atmospheric neutrino production. The WB bound results from a model of the GRB central engine that allows protons to escape freely.

The predicted neutrino spectrum of astrophysical sources is an entirely different matter. In 2013, IceCube detected an excess of neutrinos at high energies that did not fit with the measured atmospheric spectrum [70]. Figure 3.3 shows this excess. This astrophysical flux was initially discovered using High Energy Starting Events (HESE). The HESE event selection is so strict that the initial two-year dataset only contained 28 neutrino candidate events [71]. The events in this selection are extremely likely to be neutrinos, as opposed to atmospheric muons, because they are required to begin inside the detector volume. Because they only interact through the weak force, neutrinos are only indirectly detected from the nuclear

recoil and the charged leptons resulting from their capture on a nucleus. Therefore, a charged lepton track appearing to "start" in the detector is a unique signature of a neutrino interaction. The events are required to deposit a large amount of energy in the detector (equivalent to at least 30 TeV) and, to guard against atmospheric muons slipping into the instrumented volume undetected, only a small fraction of the earliest photons can be measured near the detector boundary [72]. These requirements ensure the neutrino candidate is able to produce a bright track beginning in the detector. There is an additional anti-coincidence muon veto to ensure atmospheric neutrinos are removed from the Southern Hemisphere, because atmospheric neutrinos are often accompanied by muons produced in the same cosmic-ray shower [72]. This is unavailable for the northern hemisphere, because the Earth shields these muons from reaching the detector. The current best fit spectral index for these astrophysical neutrinos is $2.87^{+0.20}_{-0.19}$ for the 1σ confidence level [73].

The HESE sample was essential for discovering the astrophysical all-flavor neutrino flux, but the harsh cuts resulted in a low number of events and made fitting the spectral index of the astrophysical neutrino flux difficult. A complementary analysis that allowed through-going muons and starting events (focused on muon neutrino candidates) was conducted to confirm the astrophysical flux [74]. The most recent version of this dataset, known internally in IceCube as the "diffuse" sample, contains roughly 650,000 neutrino candidate events [75]. The diffuse dataset maintains a high neutrino purity (99.7%) and reduces background atmospheric muons by limiting events to the Northern Hemisphere [74], [75]. Although dominated by atmospheric neutrinos, analysis of the diffuse dataset demonstrates an excess of

high-energy events that is inconsistent with the atmospheric neutrino spectrum and muon backgrounds. Figure 3.4 shows the fit for the spectral index using the diffuse sample, which is $\gamma_{astro} = 2.28$ [75].

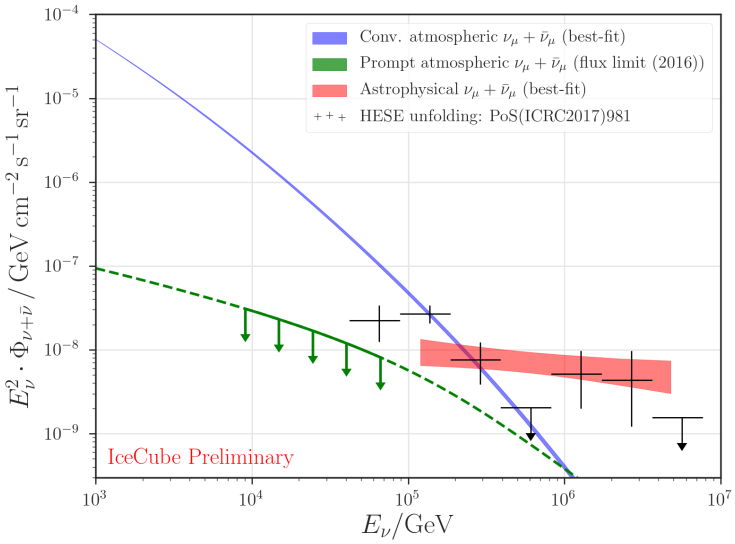

Figure 3.3: This figure shows the prompt (green) and conventional (purple) atmopsheric neutrino spectra, along with a statistically significant excess of high energy events (black) that are not explained by these atmospheric spectra. These events, known as High Energy Starting Events (HESE), led to the discovery of an atmospheric neutrino flux. The red is the best fit of the high-energy excess from the diffuse dataset, which focuses on through-going muons and muon neutrino candidates, rather than a fit to the all-flavor HESE events (black). Figure from [74].

This astrophysical neutrino flux is still a mystery. Recently, IceCube has found evidence of the blazar TXS+0506 and the Seyfert II galaxy NGC 1068 as potential neutrino sources [76] [77] [78]. Transient source candidates, including tidal disruption events, have been identified as well [79]. However, even the most generous estimates for these sources are insufficient to explain the entire diffuse neutrino flux. Previous studies of gamma-ray bursts with IceCube indicate GRBs are only contributing a maximum of a few percent to the diffuse flux [34]. See 3.2.2

for more details on the quasi-diffuse flux limits from this analysis.

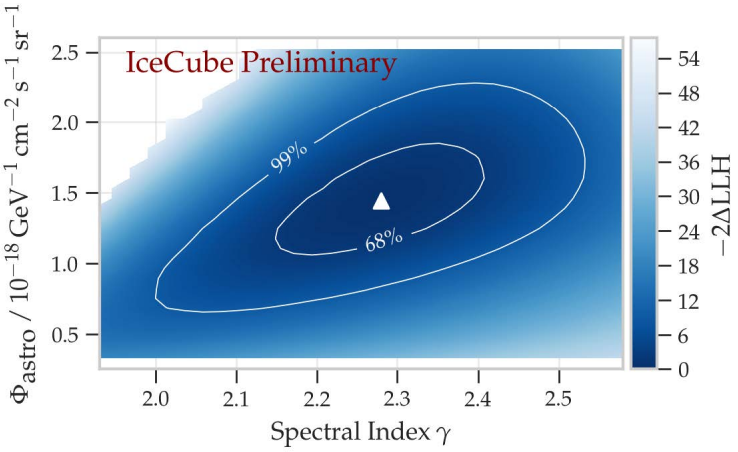

Figure 3.4: This figure shows the best fit astrophysical normalization and spectral index using nearly 10 years of diffuse data. The best fit spectral index was $\gamma_{astro} = 2.28$. Figure from [75].

3.1.2 First Order Fermi Acceleration

First-order Fermi acceleration theoretically leads to an E^{-2} spectrum of cosmic rays, which is close to what is observed. The neutrinos are expected to maintain a similar energy spectrum. The following derivation of Fermi acceleration is from [9]. The original paper by Enrico Fermi [8] considers a cloud of plasma - rather than a shock front - which is now known as second-order Fermi acceleration. Fermi acceleration requires moving magnetized plasma to transfer non-thermal energy to individual charged particles. This transfer of energy happens in a collisionless way, meaning there is no interaction between particles that would lead to energy loss.

We begin by considering a test particle that increases energy through "encounters" with the magnetized plasma. If $\Delta E = \xi E$ for each encounter, then after n encounters the partcle has E_n energy:

$$E_n = E_0 (1 + \xi)^n \tag{3.1}$$

where E_0 is the initial particle energy as it enters the accerator. This equation can be manipulated to isolate n, which would give the number of encounters needed to reach some energy threshold, E. Taking the log of both sides and applying $\ln(\mathrm{x^n}) = \mathrm{n}\ln(\mathrm{x})$ leads to the following for n:

$$n = \frac{ln\left(\frac{E}{E_0}\right)}{ln\,(1 + \xi)} \tag{3.2}$$

An important value to consider is P_{esc}, which is the probability per encounter that the particle will escape the acceleration region. If the particle escapes too early, then it will not reach the high energies needed to explain the UHECRs or diffuse neutrino flux. The probability of remaining in the acceleration region after n encounters is $(1 - P_{esc})^n$. The number of particles accelerated to this threshold energy, E, before escaping the acceleration region is found by summing all the encounters with $m \geq n$:

$$N(\geq E) \propto \sum_{m=n}^{\infty} (1 - P_{esc})^m = \frac{(1 - P_{esc})^n}{P_{esc}} \tag{3.3}$$

which is the beginning of the equation we are after. Substituting 3.2 into 3.3 (and remembering that $x^{lny} = y^{lnx}$), N becomes:

$$N(> E) \propto \frac{1}{P_{esc}} \left(\frac{E}{E_0}\right)^{-\gamma} \tag{3.4}$$

$$\gamma = \frac{ln\left(\frac{1}{1-P_{esc}}\right)}{ln\,(1+\xi)} \approx \frac{P_{esc}}{\xi} \tag{3.5}$$

Now we have a way to determine the spectral index, γ, resulting from Fermi acceleration. Because $\Delta E = \xi E$, it is helpful to find an expression in terms of the particle's energy and direction compared to the magnetized plasma. In the rest frame of the moving gas, the variables will be primed. The cosmic ray particle has total energy E_1', given by:

$$E_1' = \Gamma E_1\,(1 - \beta\cos\theta_1) \tag{3.6}$$

Here, $\Gamma = \frac{1}{\sqrt{1-\beta^2}}$ and $\beta = \frac{V}{c}$. The V contained in Γ and β refers to the "downstream" velocity of the shocked gas (see Figure 3.5). If the plane shock front, with velocity $-\hat{u_1}$, moves toward an "upstream" particle, which has initial velocity $\hat{u_2}$, then the total velocity of a (now downstream) shocked particle has $\hat{V} = -\hat{u_1} + \hat{u_2}$.

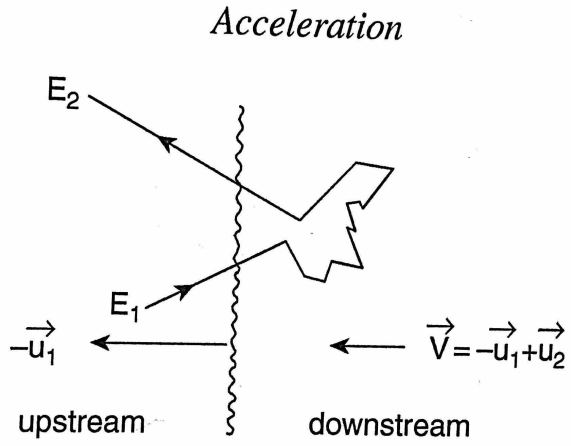

Figure 3.5: This figure shows the directions of the intial upstream particle, moving with $+\hat{u_2}$ velocity, and the plane shock front, moving with $-\hat{u_1}$. The velocity of a downstream particle is then $\hat{V} = -\hat{u_1} + \hat{u_2}$. Figure from [9].

The ΔE we want represents a particle that has been accelerated to the point just before it can escape. The energy of the particle in the moving plasma frame at this point is $E_2' = E_1'$. Transforming this back to the lab frame gives the energy of the particle after its encounter with the plasma:

$$E_2 = \Gamma E_2' \left(1 - \beta \cos\theta_2'\right) \tag{3.7}$$

and now equation 3.6 can plug into 3.7 to give an expression for ξ:

$$\xi = \frac{\Delta E}{E_1} = \frac{1 - \beta\cos\theta_1 + \beta\cos\theta_2' - \beta^2\cos\theta_1\cos\theta_2'}{1 - \beta^2} - 1 \tag{3.8}$$

For the rest of the derivation, [9] goes through both first-order (plane shock front) and second-order (plasma cloud) accereration. The main difference is how to take the angular averages of 3.8. A gas cloud would be integrated over all directions,

while the plane shock is the normalized projection of an isotropic flux onto a plane. This section will only cover first-order acceleration.

The normalized average of a continuous random variable x, with a probability density function $f(x)$, is given by:

$$< x >= \frac{\int_{-\infty}^{\infty} x f(x) dx}{\int_{-\infty}^{\infty} f(x) dx} \tag{3.9}$$

With this in mind, the angular average for $\cos\theta_2'$ and $\cos\theta_1$ depend on the following conditions:

$$\frac{dn}{d\cos\theta_2'} = 2\cos\theta_2' \quad , \quad 0 \leq \cos\theta_2' \leq 1 \tag{3.10}$$

In this case, the f(x) from 3.9 is $\frac{dn}{d\cos\theta_2'}$. This leads to the following angular average:

$$\begin{aligned} < \cos\theta_2' > &= \frac{\int_0^1 2\cos^2\theta_2' \; d\cos\theta_2'}{\int_0^1 2\cos\theta_2' \; d\cos\theta_2'} \\ &= \frac{\left[\frac{2\cos^3\theta_2'}{3}\right]_0^1}{[\cos^2\theta_2']_0^1} \\ < \cos\theta_2' > &= \frac{2}{3} \end{aligned} \tag{3.11}$$

The same can be done for $< \cos\theta_1 >$, where the distribution is the projection of an isotropic flux onto a plane with $-1 \leq \cos\theta_1 \leq 0$. This time, we have:

$$\frac{dn}{d\cos\theta_1} = \frac{c - V\cos\theta_1}{2c} \quad , \qquad -1 \leq \cos\theta_1 \leq 0 \tag{3.12}$$

Following the same procedure as 3.11, we find:

$$< \cos\theta_1 >= -\frac{2}{3} \tag{3.13}$$

Finally, we can take the angular average of 3.8, plugging in the averages for $\cos\theta_2'$ and $\cos\theta_1$:

$$\begin{aligned} \xi = \frac{\Delta E}{E_1} &= \frac{1 - \beta\left(-\frac{2}{3}\right) + \beta\left(\frac{2}{3}\right) - \beta^2\left(-\frac{2}{3}\right)\left(\frac{2}{3}\right)}{1-\beta^2} - 1 \\ &= \frac{1 + \frac{4}{3}\beta + \frac{4}{9}\beta^2}{1-\beta^2} - 1 \\ &\approx \frac{4}{3}\beta = \frac{4}{3}\frac{u_1 - u_2}{c} \end{aligned} \tag{3.14}$$

where $\beta = \frac{V}{c}$ refers to the relative velocity of the plasma flow, rather than an individual cosmic ray. The geometry of the infinite plane shock ($\cos\theta_2'$ is always positive and $\cos\theta_1$ is always negative) guarantees an encounter between a cosmic ray and the shock front will result in a gain in energy for the particle. In a gas cloud, however, the particle can lose or gain energy depending on the angles. This is why the shock wave is first-order and the gas cloud is second-order Fermi acceleration.

Now that we have an expression for ξ, the only missing component for determining

the spectral index, γ, is an expression for the escape probability, P_{esc}. The rate of encounters is given by the projection of an istropic cosmic ray flux onto the plane shock front. Here, the number density of cosmic rays being accelerated is given by ρ_{CR}.

$$\int_0^1 d\cos\theta \int_0^{2\pi} d\phi \frac{c\rho_{CR}}{4\pi}\cos\theta = \frac{c\rho_{CR}}{4} \tag{3.15}$$

The rate of convection downstream (away from the shock front) is $\rho_{CR} \times u_2$. Put together, this becomes:

$$P_{esc} = \frac{\rho_{CR}u_2}{c\rho_{CR}/4} = \frac{4u_2}{c} \tag{3.16}$$

Plugging 3.14 and 3.16 into 3.5, we find:

$$\gamma = \frac{P_{esc}}{\xi} = \frac{\frac{4u_2}{c}}{\frac{4}{3}\beta} = \frac{3u_2}{\underbrace{v}_{-u_2+u_1}} = \frac{3}{\frac{u_1}{u_2}-1} \tag{3.17}$$

After considering the specifics of diffusion, including the sound speed in the gas, the Mach number of the flow, the continuity of mass flow across the shock, and the monoatomic gas ratio of specific heats, the final approximation becomes:

$$\gamma \approx 1 + \frac{4}{M^2} \tag{3.18}$$

where M is the Mach number of the flow: $M = \frac{u_1}{c_1}$. For a strong shock, $M >> 1$, which leads to $\gamma = 1$. The final step is to realize 3.4 refers to the number of particles, but the value we refer to is the flux. Therefore:

$$N \propto \left(\frac{E}{E_0}\right)^{-1} \implies \frac{dN}{dE} \propto \left(\frac{E}{E_0}\right)^{-2} \tag{3.19}$$

3.1.3 Hadronic Acceleration of Cosmic Rays

The analysis presented in this thesis uses an E^{-2} spectrum for simulated signal neutrinos because this is predicted by Fermi shock acceleration [68]. There are many efforts to correlate the gamma-ray spectrum to that of cosmic rays and neutrinos. The neutrino, photon, and cosmic ray spectra are shown together in Figure 3.6.

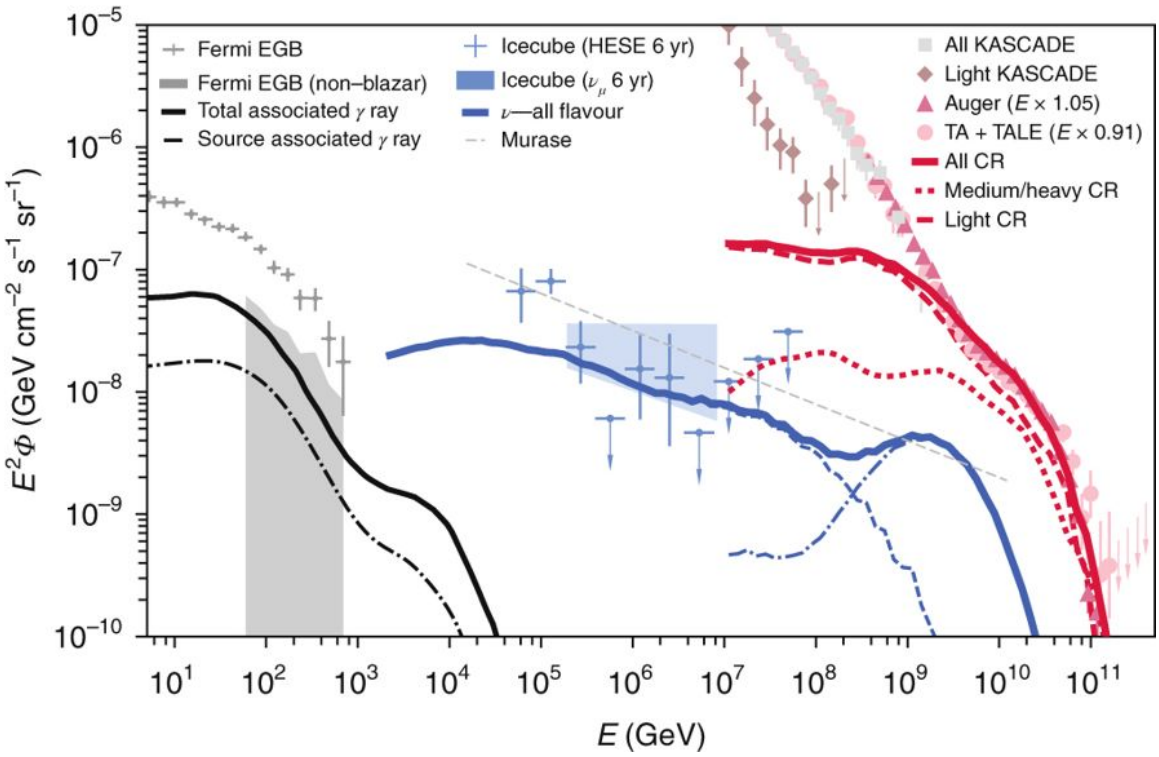

Figure 3.6: The neutrino, cosmic ray, and photon spectra observed on Earth and its orbiting satellites. This figure highlights the intrigue of multimessenger astronomy: the diffuse fit to high-energy neutrinos, cosmic rays above the ankle, and Fermi-detected gamma rays all have roughly the same energy flux. Many experiments around the world are working to connect these three messengers. Figure from [80].

As discussed in 2.1.2, neutrinos correlated with GRBs (or other high-energy

astrophysical phenomena) would be evidence of hadronic acceleration of the high-energy cosmic rays. The prediction of neutrinos follows from assumptions about the environment of the source. An environment that can create both gamma rays and extremely high-energy protons should have an acceleration region with large amounts of protons and electrons confined within magnetic fields [68]. Accelerated electrons would lose energy via synchrotron radiation, and the protons in this same region could then interact with the radiated photons to produce the observed neutrinos and gamma rays measured on Earth [68]. Some of the protons are believed to be shock accelerated up to 10^{15} eV, and these protons could interact with 1 MeV photons to produce 10^{14} eV neutrinos [81]. Finally, the UHECR protons could be created (with energies up to 10^{20} eV) through Fermi acceleration.

The Delta resonance, shown in equations 3.20-3.23, is the most favored photo-hadronic interaction that produces pions, which are necessary for high energy gamma rays and neutrinos:

$$p + \gamma \rightarrow \Delta^{+} \rightarrow \begin{cases} \pi^{0} + p \\ \pi^{+} + n \end{cases} \tag{3.20}$$

The Δ^{+} in equation 3.20 is an unstable, higher mass excitation of a proton. The decay of neutral pions produces the gamma rays measured by the satellites described in section 2.2:

$$\pi^{0} \rightarrow 2\gamma \tag{3.21}$$

These gamma rays can also result from synchrotron self-Compton emission, which occurs when synchrotron radiation from accelerated electrons transfers energy through inverse-Compton scattering. The neutrinos measured in IceCube result from the decay of the charged pion and subsequent muon:

$$\pi^+ \rightarrow \mu^+ + \nu_\mu \tag{3.22}$$

$$\mu^+ \rightarrow e^+ + \nu_e + \overline{\nu}_\mu \tag{3.23}$$

Equations (3.21), (3.22), and (3.23) show how the acceleration of charged particles such as protons can lead to the photons seen with gamma-ray satellites and the neutrino signal measured in IceCube. It is also possible to produce the pions that decay into neutrinos and gamma rays from interactions between protons and matter (e.g., proton-proton). Proton-proton interactions are more likely than proton-photon ($p - \gamma$) interactions if there is a higher density of gas than radiation [82] [83]. A GRB is considered more likely support $p - \gamma$ interactions due to the higher radiation density.

3.2 Predictions of Neutrinos from Gamma-Ray Bursts

Previous analyses on IceCube data have led to strong constraints on models predicting neutrinos coincident with GRBs [34] [84] [85] [86] [87] [88]. The analysis presented in this thesis expands on previous work by searching many time windows

beyond the prompt, which is the time during measured gamma-ray activity. The goal is a model-independent search capable of correlating neutrinos with GRBs up to -1/+14 days of the gamma-ray detection. The most recent IceCube stacking analyses suggest the prompt gamma-ray emission time of GRBs contribute to less than 1% of the observed astrophysical neutrino flux [34].

The results of this analysis, presented in Chapter 8, focus on the most significant GRBs and the Binomial test of four sub-populations. The aggregate result of searching 2,091 GRBs for neutrinos in different time windows can provide generic limits and demonstrate consistency with previous work. This thesis does not present limits on sub-classes of the Fireball model (see 2.2.2), but instead focuses on general GRB population limits, a generic double broken power law model of neutrino emission, and the contribution of GRBs to the quasi-diffuse neutrino flux measured by IceCube. The wide time windows and generic approach in this analysis are meant to complement model-dependent studies of neutrino emission from GRBs.

3.2.1 Generic Double Broken Power Law

One could approach the question of neutrino production from the view of cosmic rays or from gamma rays. Eli Waxman and John Bahcall chose cosmic rays, and wrote a seminal paper [81] predicting the neutrino flux assuming all cosmic rays with energies above 10^{19} eV were created by GRBs. This model assumes protons can escape from the GRB's central engine freely, which leads to a hard spectrum. The Waxman-Bahcall model predicts the maximum number of expected neutrinos (in a

proton escape model) because of the assumption that GRBs are 100% responsible for UHECRs [68].

Following the procedure in [33], a neutrino flux can be calculated for a break energy of $\varepsilon_b = 10^6$ GeV. The neutrino break energy, ε_b, is the energy where the broken power law spectrum (Equation 3.24) first changes spectral index. A double broken power law is used to model neutrino emission because the gamma-ray spectrum fits well with a double broken power law. Another parameter to consider for this model is the GRB variability time scale, $t_\nu = 10^{-3}$ s for short GRBs and $t_\nu = 10^{-2}$ s for long GRBs, which is chosen based on variation in GRB lightcurves and indicates fluctuations in the source environment. The bulk Lorentz factor, $\Gamma = 300$, and the gamma-ray isotropic luminosity is $L_\gamma^{iso} = 10^{51}$ ergs/s are also used in this calculation. The proton injection spectrum is expected to follow $\frac{dN_p}{dE_p} \propto E_p^{-2}$ and roughly 20% of the proton energy is converted to the pions. This leads to a per-flavor flux normalization of $\varepsilon_b \Phi_0 \approx 2.2 \times 10^{-9}$GeV cm^{-2}s^{-1}sr^{-1} [33] [17].

A similar calculation is done in [89], where the neutrino production is assumed allowing free neutron escape. This is another model-specific value that is determined using two basic assumptions: the protons are accelerated to high energies faster than the lifetime of the fireball, and the energy that is gained by these protons is not lost to synchrotron radiation or pion production [89]. These assumptions, using the same inputs from the Waxman-Bahcall model, lead to $\varepsilon_b \Phi_0 \approx 6 \times 10^{-9}$GeV cm^{-2}s^{-1}sr^{-1}

The Waxman-Bahcall and Ahlers et. al. models are both based on a generic double broken power law for neutrino flux:

$$\Phi_\nu(E_\nu) = \Phi_0 \times \begin{cases} \varepsilon_b^{-1} E_\nu^{-1}, & E_\nu \leq \varepsilon_b \\ E_\nu^{-2}, & \varepsilon_b < E_\nu \leq 10\varepsilon_b \\ E_\nu^{-4}(10\varepsilon_b)^2, & 10\varepsilon_b < E_\nu \end{cases} \tag{3.24}$$

where ε_b is the neutrino break energy and Φ_0 is the quasi-diffuse normalization of the flux. Figure 3.7 shows that the Waxman-Bahcall model of proton escape and Ahlers et. al. model of neutron escape are both excluded at over a 90% confidence level in the previous GRB study [34].

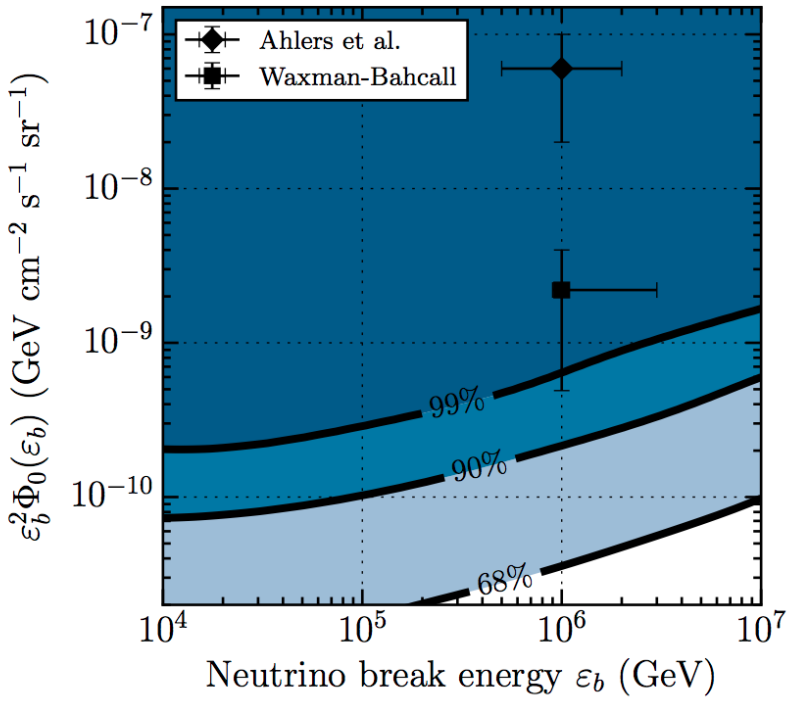

Figure 3.7: Constraints on a generic double broken power law neutrino spectrum. The parameters are the first break energy, ε_b, and the quasi-diffuse flux normalization, Φ_0. The two points indicate predicted neutrino fluxes motivated by cosmic ray flux measurements,. The error bars indicate the uncertainty in those cosmic ray flux values, as well as variation in the bulk Lorentz factor, time variability of the GRB, and the break energy. Figure from [34].

Both the Waxman-Bahcall and Ahlers et al. values were strongly ruled out by previous IceCube studies of the prompt phase of GRBs. Figure 3.7 shows the limits from a generic double broken power law. This plot was made by injecting flux for a variety of break energies and producing a stacked test statistic. The stacked test statistic is described in 6.4.1 and follows the standard procedure of comparing injected signal to the median of the background-only test statistic distribution. Chapter 8 shows similar limits based on the analysis from this thesis, with the 90% limit shown for each sub-population of GRBs in the prompt.

3.2.2 Quasi-Diffuse Flux

One goal of IceCube analyses is to understand how the result relates to the diffuse astrophysical neutrino flux. Answering this question can be difficult, especially in the world of GRBs. The simple method is to compare the unblinded stacked test statistic (described in 6.4.1) to test statistic distributions with injected flux. If the injected flux produces test statistics that are larger than the unblinded test statistic, say, 90% of the time, then that flux value can be ruled out at 90% confidence. That injected flux - the 90% flux limit - can be converted to a quasi-diffuse flux by:

$$F_{Diffuse} = \frac{Time - Integrated\ Flux}{GRB} \times \frac{667\ GRBs}{4\pi \cdot yr} \times \frac{1\ yr}{3.15 \times 10^7 s} \tag{3.25}$$

where 667 GRBs per year all-sky has been the historic density value used in IceCube GRB searches [90] [34]. There are two subtle details about this conversion from a

stacked flux limit to a quasi-diffuse limit. The first comes from the time-integrated flux per GRB. This value comes from injecting a given flux equally over all the GRBs, which treats every second in the observer frame as equally likely to detect neutrinos. This assumes all GRBs are producing an equal neutrino flux at Earth. This method also does not consider the redshift of a GRB; however, only a handful of GRBs have redshift measured, and there is quite a bit of observer bias involved (see 8.3.3 for further explanation).

The second detail to consider for equation 3.25 is the density of 667 GRBs per year all-sky. This may be a reasonable value to test, but it is perhaps more appropriate to consider a range of densities. Figure 3.8 shows the limits for previous IceCube GRB analyses, and the dashed lines show the limits on GRB contributions to the diffuse flux. The total diffuse flux measured by IceCube is 9×10^{-9} GeV cm^{-2} s^{-1} sr^{-1} [91] [92]. The dashed lines in Figure 3.8 indicate GRBs are responsible for, at most, a few percent of the diffuse flux under the assumptions of 667 GRBs per year all-sky and equal flux at Earth.

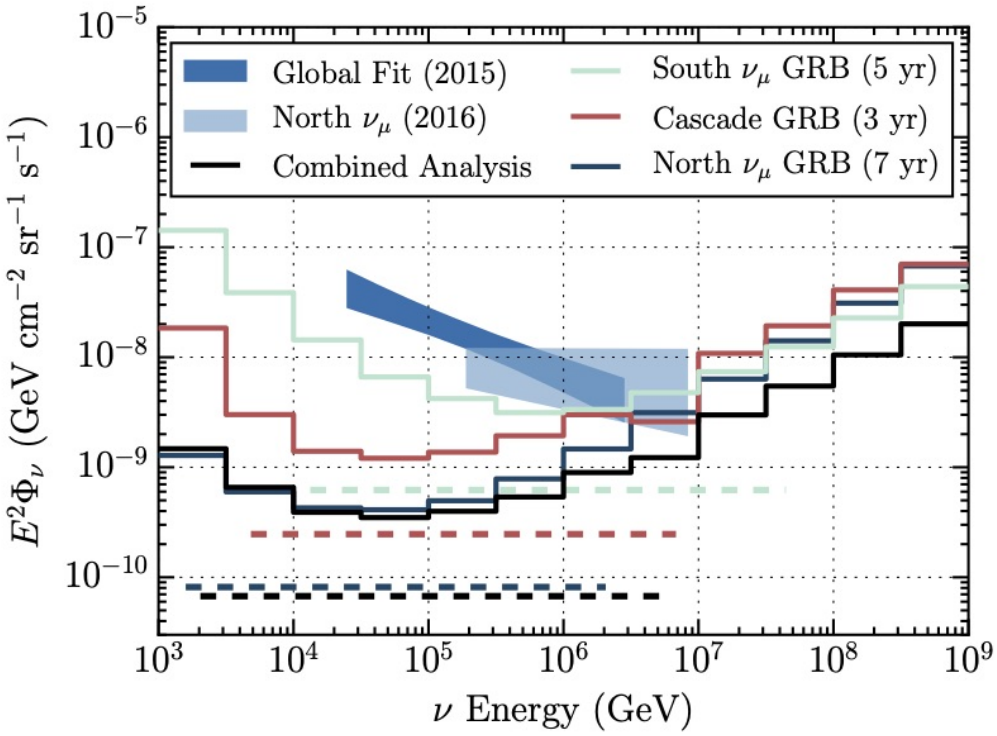

Figure 3.8: This plot shows the differential sensitivity for recent IceCube GRB analyses. A differential sensitivity is a sensitity per neutrino energy bin. The dashed lines show the limits on the quasi-diffuse neutrino flux for each of the GRB analyses. Figure from [34].

Chapter 8 shows the limits from the analysis presented in this thesis on the diffuse flux by sub-population and time window. A limit is also placed on GRB densities assuming different contributions to the diffuse flux under this "equal flux at Earth" model.

3.2.3 GRB Density

The following section draws heavily from the star-formation history paper by Madau and Dickinson [93].

Another way to consider the GRB contribution to the diffuse flux is to assume a

source model and stellar evolution. A stellar evolution model describes the formation and evolutionary phases of stars across redshifts, which leads to an estimate of the number of sources for a given redshift. The stellar evolution model used in this thesis gives the following relationship between density and redshift:

$$\rho(z) = 0.015 \ \frac{(1+z)^{2.7}}{1+\left(\frac{1+z}{2.9}\right)^{5.6}} \ M_{\odot} \ yr^{-1} \ Mpc^{-3} \tag{3.26}$$

where ρ is the source density and z is the redshift.

Modeling the source density is important for predicting neutrino flux, because GRBs are difficult to study due to their transient nature. In particular, identifying a redshift can be difficult if the GRB does not have a detectable afterglow. The larger the redshift, the less likely the satellites are to detect the GRB at all, let alone to determine that redshift. A choice of stellar evolution model and source luminosity estimates the total number of sources, creating a more complete picture of GRBs than simply those that are successfully detected. This allows more realistic constraints to be placed in the event of a non-detection of neutrinos correlated with GRBs, because those that are not measured in gamma rays may still be producing measurable neutrinos.

The modeling for the star-formation density is primarily based on recent galaxy surveys with star-formation rates measured in far-UV and far-IR. In most galaxies, the short-lived massive stars (the progenitors of core-collapse supernovae) are the dominant source of UV emission. Therefore, UV emission can be used as tracers and provide a direct measurement of the instantaneous star-formation rate density for a

given stellar initial mass function and dust content. Unfortunately, too much dust can be a significant limiting factor for measurements in UV. Interstellar dust absorbs UV light and re-radiates it as IR, which means dusty starburst galaxies observed in far-IR emission can also trace the star-formation rate. Starburst galaxies refer to galaxies with particularly high star-formation rates. Equation 3.26 was the best-fitting function to data points from far-UV and IR measurements, shown in Figure 3.9.

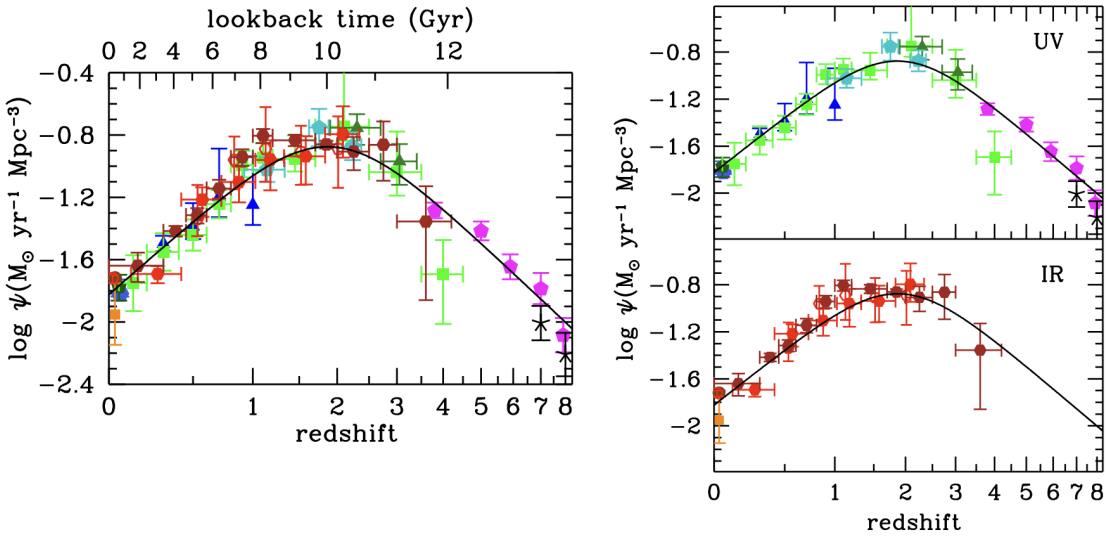

Figure 3.9: This plot shows far-UV and IR measurements converted to instantaneous star-formation rate densities. The solid curve shows the best-fit star-formation rate density (Equation 3.26). Figure from [93].

Madau and Dickinson express some uncertainty that this model correctly describes GRBs because they may require special conditions that are difficult to model. This may mean the star-formation density (Equation 3.26) is incomplete in the context of GRBs, and the results presented in Chapter 8 may require additional study. It is always difficult to discuss GRBs as a single group, because the redshifts,

lightcurves, and progenitors are so varied. The analysis in this thesis considers all 2,091 GRBs together for limits on GRB density and total energy (see 8.3.3). It is perhaps more correct to isolate the long GRBs in a future study. All discussions related to simulating population densities in this thesis make the assumption that we can combine GRBs according to this star-formation density model.

Chapter 4: Detecting Neutrinos with IceCube

Neutrinos were first proposed by Wolfgang Pauli to explain the missing energy in the products of beta decay [94]. We now know neutrinos are very light, neutral elementary particles that only interact via the weak force. When neutrinos do interact, they can produce charged leptons (see Figure 4.2). If enough energy is transferred in the neutrino interaction, the resulting leptons can travel faster than light in the ice, which emits a directional cone of blue light called Cherenkov radiation. Measuring Cherenkov radiation in the ice is the primary goal of the IceCube detector.

4.1 The IceCube Neutrino Detector

IceCube is a cubic-kilometer-scale neutrino detector located at the South Pole. The Antarctic ice is instrumented with 5,160 digital optical modules (DOMs) [95]. These DOMs include photomultiplier tubes optimized to detect blue light from Cherenkov radiation. Holes are drilled deep in the ice, allowing DOMs to be deployed at a depth of 1,450 to 2,450 meters (see figure 4.1) where the ice is optically clear.

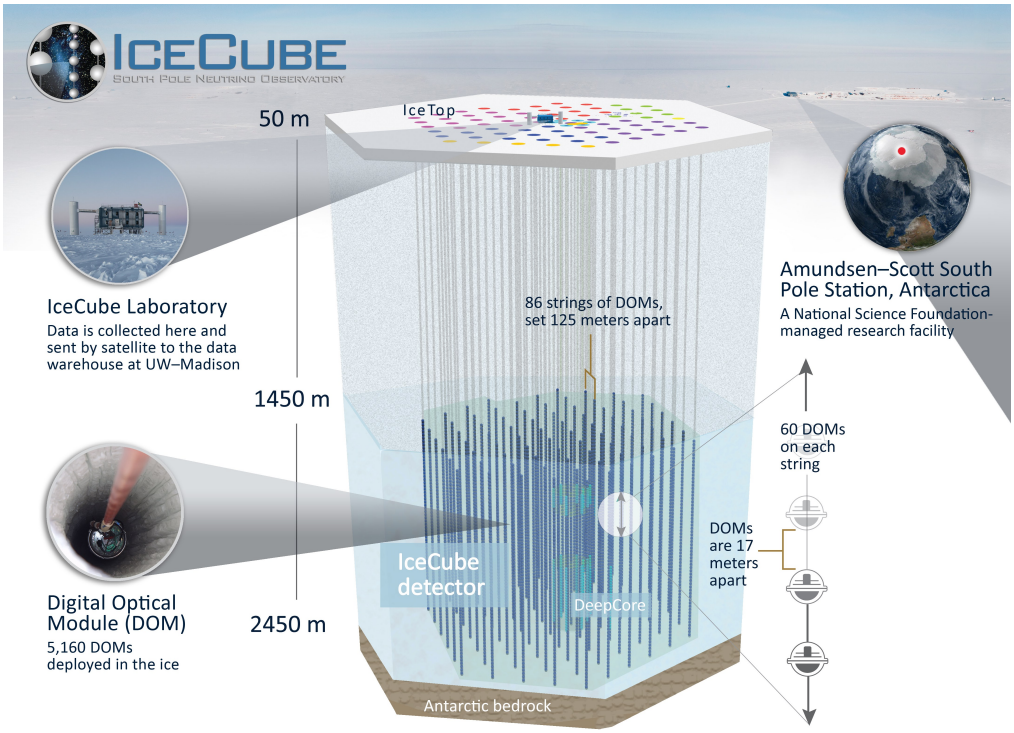

Figure 4.1: The IceCube neutrino detector located in ice at the South Pole. Figure from [96].

IceCube consists of 86 strings deployed on a hexagonal grid with 125 meters between each string. A string refers to a cable that includes 60 DOMs with 17 meter vertical DOM spacing and the associated power and readout electronics. Eight of these strings are spaced closer together and are called "DeepCore." These have 70 meter horizontal spacing and seven meter vertical spacing. DeepCore is used for lower energy measurements such as neutrino oscillations. Most of the IceCube strings are paired with two surface tanks. Each tank is filled with water and contains two DOMs. These tanks are called "IceTop" and form an array near the surface above the detector [97]. Dedicated analyses are performed with IceTop, including study of the cosmic ray spectrum.

The IceCube Laboratory (ICL) sits at the surface in the approximate center of the hexagonal grid. The ICL is the communication and power hub for the entire detector, including IceTop and all components frozen kilometers in the ice.

4.2 Neutrino Interactions in Ice

Neutrinos must be detected indirectly because they are neutral and only interact via the weak force. The most common interaction is an exchange of a W-boson with a quark from a proton or neutron of the hydrogen or oxygen atoms in the ice. If the resulting lepton has enough energy, then it will travel faster than light in its medium and produce Cherenkov radiation (see section 4.2.1), which is able to be detected by the IceCube DOMs.

There are three neutrino interactions that are relevant to this analysis in IceCube. The first is the "charged current" (CC) interaction, which gets its name from the exchange of the charged W-boson. This involves a neutrino or anti-neutrino interacting with a down or up quark, respectively, in the nuclei of the ice. This results in the charged lepton counterpart to the neutrino and changes the quark from down to up (or up to down).

The charged current interaction can occur for electron neutrinos (ν_e), muon neutrinos (ν_μ), or tau neutrinos (ν_τ). For a CC ν_e interaction, the resulting electron (or positron) produces a shower of electrons, positrons, and photons very close to the interaction vertex. An electron does not travel far before depositing its energy, which results in a roughly spherical photon emission shape, commonly called a cascade.

There is an additional hadronic shower that results from the nucleus recoiling and interacting with surrounding matter. The cascade and the hadronic shower fall on top of each other and are not easily distinguishable.

A CC ν_μ interaction results in a muon, which, if energetic enough, is able to travel more than a kilometer through the ice before decaying. The muon deposits its energy (and therefore light) along this long route, and the result is called a track. A minimum ionizing muon deposits roughly 1 GeV every 5 meters, which would mean the muon needs at least 200 GeV to produce a 1 kilometer track [98]. These interactions also result in a hadronic shower at the beginning of the track (see Figure 4.6). Tracks from muon neutrino interactions are the desired events for this analysis, because the long lever arm allows for better angular reconstruction.

CC ν_τ interactions are difficult to detect. Taus decay very close to the initial interaction hadronic cascade, making them difficult to distinguish from other interaction channels. The ideal signature of a high-energy tau interaction is the "double bang," which would occur if the decay vertex and initial interaction vertex could be distinguished. Only two candidates for tau neutrino events have been observed in IceCube [99] [100].

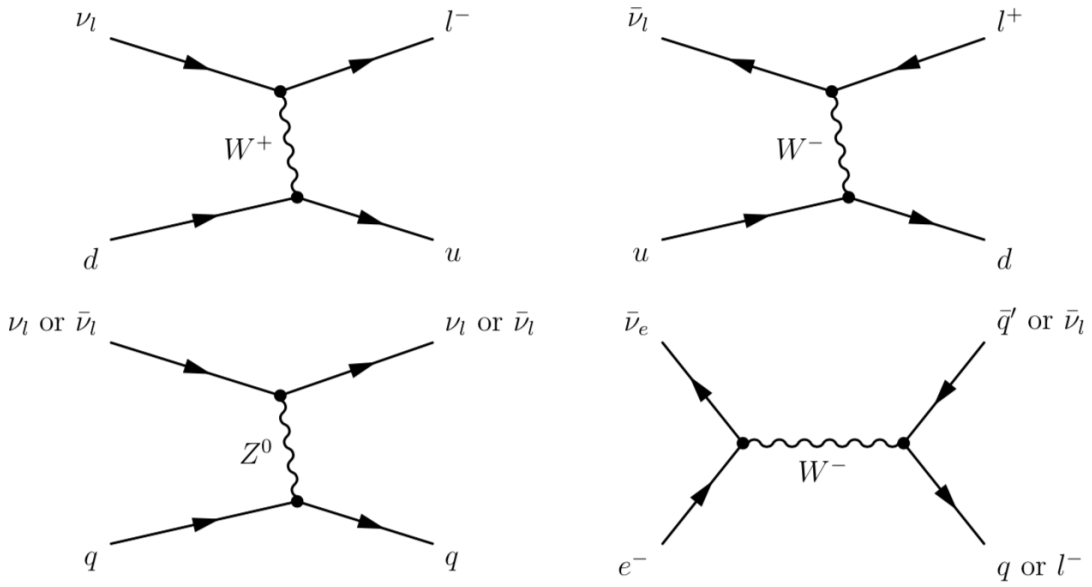

Figure 4.2: The Feynman diagrams for charged current (top two), neutral current (bottom left), and Glashow resonance (bottom right). Figure from [17].

Another possible interaction is the neutral current (NC) interaction, which occurs when a neutrino scatters off a quark and exchanges a Z-boson. Energy is transferred to the quark via the neutral Z boson, which leads to a hadronic shower very similar to the charged current. No charged lepton is emitted, meaning the hadronic shower is the only detected signal. A hadronic shower is produced in any neutrino interaction in ice, and therefore IceCube cannot distinguish between the neutral current and charged current (e^-, τ) cascades. All interaction channels are included in simulations.

The final interaction, the Glashow resonance, occurs when an electron-antineutrino interacts with an electron instead of a quark [101]. This interaction peaks for antineutrinos with an energy of 6.3 PeV. A W^- boson carries out the interaction and produces a pair of quarks or an anti-neutrino-lepton pair. This is theoretically

possible for all flavors of neutrino; however, electrons are the only target lepton available in the ice. Only one candidate event, which had a reconstructed energy of 6.05±0.72 PeV, has been measured by IceCube [100] [102]. The cross-sections of CC, NC, and Glashow resonance are shown in Figure 4.3.

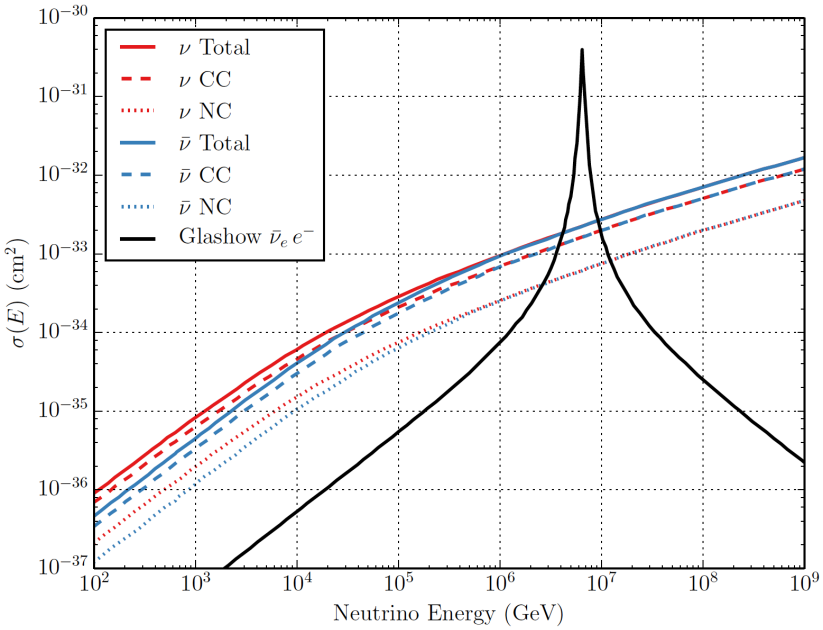

Figure 4.3: This figure shows the interaction cross sections for neutrinos and anti-neutrinos in deep inelastic scattering. The Glashow resonance (black) is clear at 6.3 PeV, though only one candidate event has been detected by IceCube. Figure from [17], adapted from [103] and [104].

4.2.1 Cherenkov Radiation

Relativisitc charged particles are capable of moving faster than the speed of light in ice (i.e., $\beta > \frac{1}{n}$). When this happens, light is emitted and propagated in a direction that forms an angle θ with the particle:

$$\cos\theta = \frac{1}{\beta n} \tag{4.1}$$

This is known as Cherenkov radiation [105] and results from the relativistic charged particle disturbing the medium's electromagnetic field. Equation 4.1 indicates the Cherenkov angle, which produces blue-UV wavelength light for high energy particles at $\theta \approx 41°$ and an index of refraction of $n_{ice} = 1.32$ [106]. The IceCube DOMs are designed to be sensitive to photons in this blue-UV range to detect Cherenkov photons as efficiently as possible.

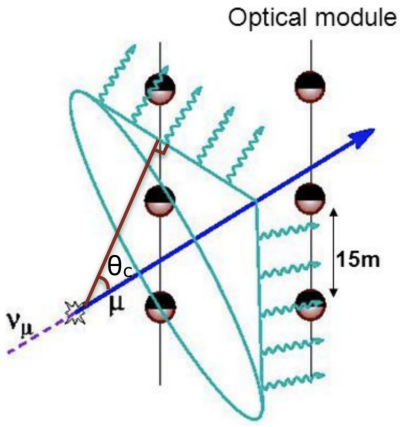

Figure 4.4: An illustration of a Cherenkov cone of radiation. Figure from [107].

4.2.2 Muon Propagation

Muons are central to this analysis, because tracks have the best angular reconstruction and are ideal for neutrino astronomy. High energy muons can travel for several kilometers before decaying, which means only a fraction of the muon energy may end up in the ∼1 km IceCube detector. Understanding those muon tracks, particularly how much energy is deposited by each type of energy loss, is important for reconstructing the particle's energy and direction accurately, and allows muons to be detected even if they are produced outside the detector volume.

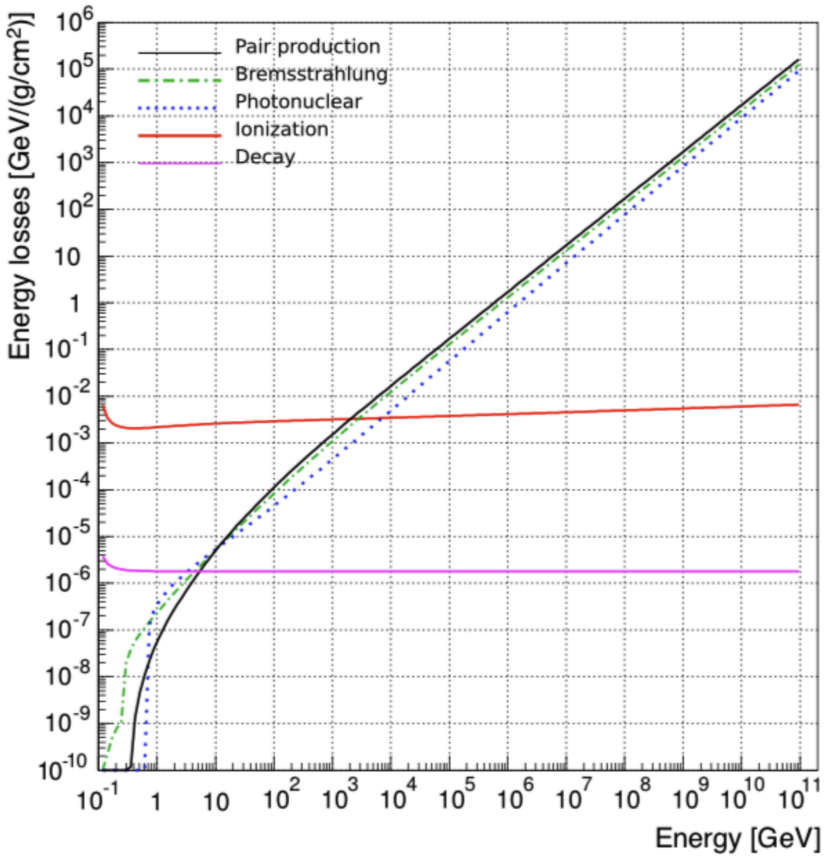

Figure 4.5: This figure shows the energy losses due to muon propagation through the ice. At lower energies, light is produced as the medium is ionized by the passing muon. Muons can also produce secondary radiation through pair production, photonuclear interactions, and bremsstrahlung radiation. These interactions can occur at random and are categorized as "stochastic" energy losses. These stochastic losses dominate at high energies and are important to include in simulation. Figure from [107] (adapted from [108]).

The muon that results from the interactions described in 4.2 loses energy continously as it travels through the dense ice. At low energies (below roughly 300 GeV), the ionization of the medium dominates the energy losses. The muon effectively rips electrons off nearby nuclei and those electrons undergo Cherenkov radiation. At higher energies, stochastic losses such as pair production, bremsstrahlung, and phtononuclear interactions take over as dominant mechanisms for energy loss

(see Figure 4.5). The average rate of energy loss for muons is given by:

$$\frac{dE}{dx} = -a - bE \tag{4.2}$$

where a and b can be approximated as constants referring to the energy loss from ionization and stochastic losses, respectively [109]. The ionization loss parameter can be found using the Bethe-Bloch formula, which describes the stopping power due to ionization. This leads to $a \approx 0.26$ GeV per meter-of-water-equivalent (mwe) and $b \approx 3.6 \times 10^{-4}$ mwe^{-1} [17].

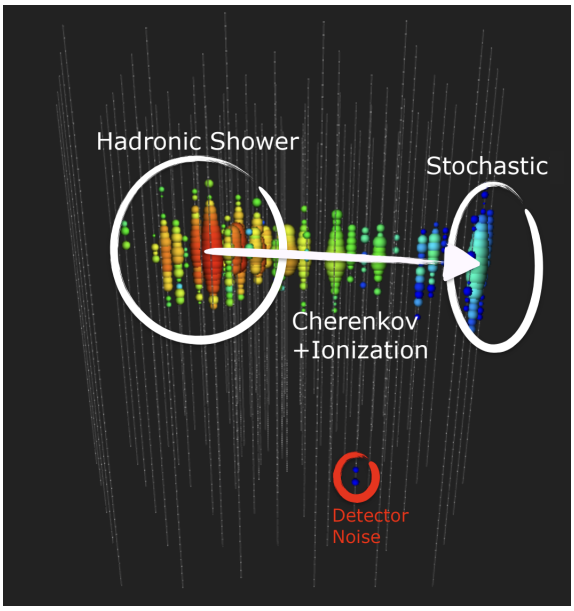

Figure 4.6: This figure shows the energy losses in an event. The initial burst is the result of a hadronic shower. The particle (in this case, a muon) travels through the detector, depositing energy via Cherenkov radiation and ionization. Toward the end of the track, there are some larger deposits of light, which may be due to stochastic losses. There is also a small amount of detector noise at the bottom of this event. A high energy track such as this one is easier to separate from background, which means there is very little detector noise. Figure from [107].

4.2.3 South Pole Ice

One of the main reasons the South Pole was selected as the site for IceCube is the optical clarity of the ice. The gradual compression of snow over thousands of years has led to optically clear, realtively bubble-free ice 1.4 km below the surface. The region of ice from the surface to 1.4 km has more air bubbles and leads to higher rates of scattering. Determining the direction of a Cherenkov cone would be incredibly difficult if too many of the photons were scattered before reaching the DOMs, which is why the IceCube detector begins at 1,450 meters below the surface of the glacier. Figure 4.7 shows the absorption and scattering of the ice by depth.

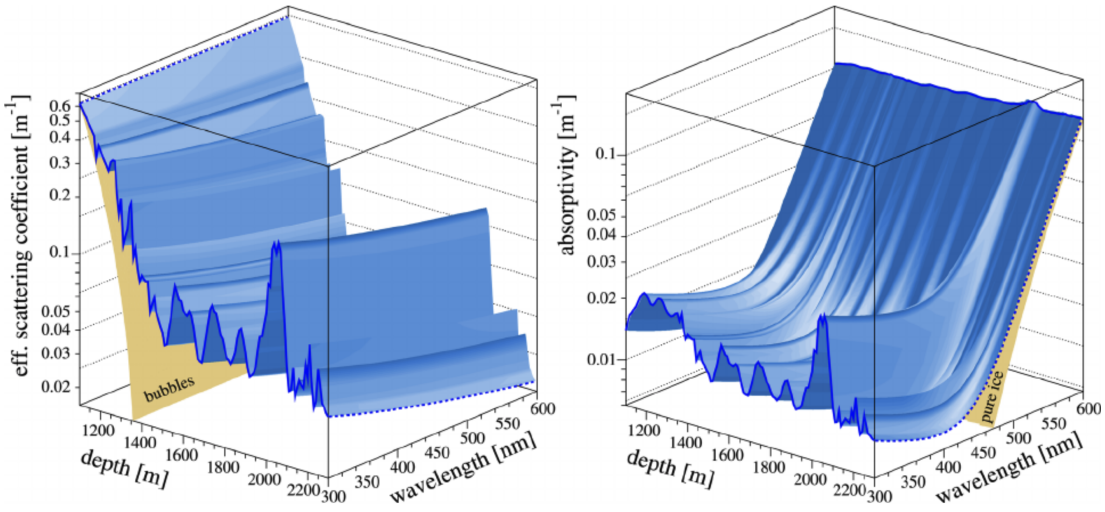

Figure 4.7: The scattering (left) and absorption (right) coefficients of ice from 1100-2300 meters. This includes nearly the entire detector volume for IceCube, as well as some of the region dominated by bubbles. Figure from [110].

Careful measurements of the ice were made during the hot-water drilling in AMANDA and IceCube. A dust logger (see Figure 4.8) was lowered into the hole, which had been drilled with hot water, and recorded measurements of the bubbles,

dust, and volcanish ash at 10-ms intervals [106] [111]. A 404-nm source emitted light sideways out of the borehole and the amount of scattered photons that returned to the dust logger was recorded. The most prominent dust feature is located between 2.0-2.1 km below the surface. This is known within IceCube as the "dust layer" and is carefully considered in simulation. Figure 4.9 shows the scattering across the entire depth of ice.

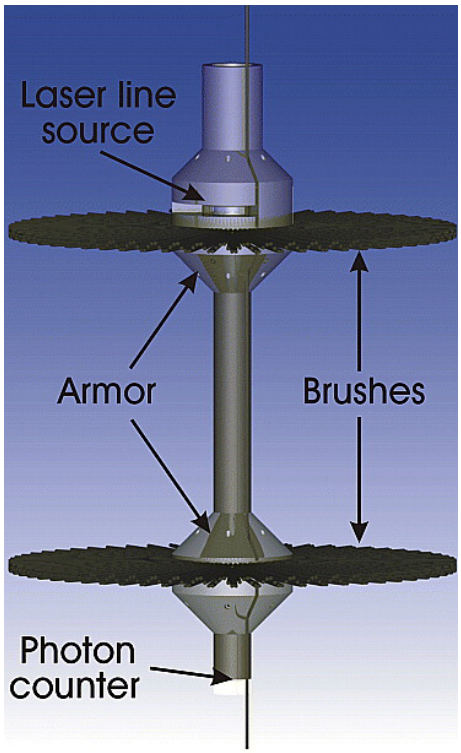

Figure 4.8: The dust logger used to map the bubbles, dust, and volcanic ash in an IceCube borehole. Figure from [111].

Each DOM in IceCube also contains LEDs that can be turned on and off to measure scattering in situ [106]. Details of the DOM are in the following section.

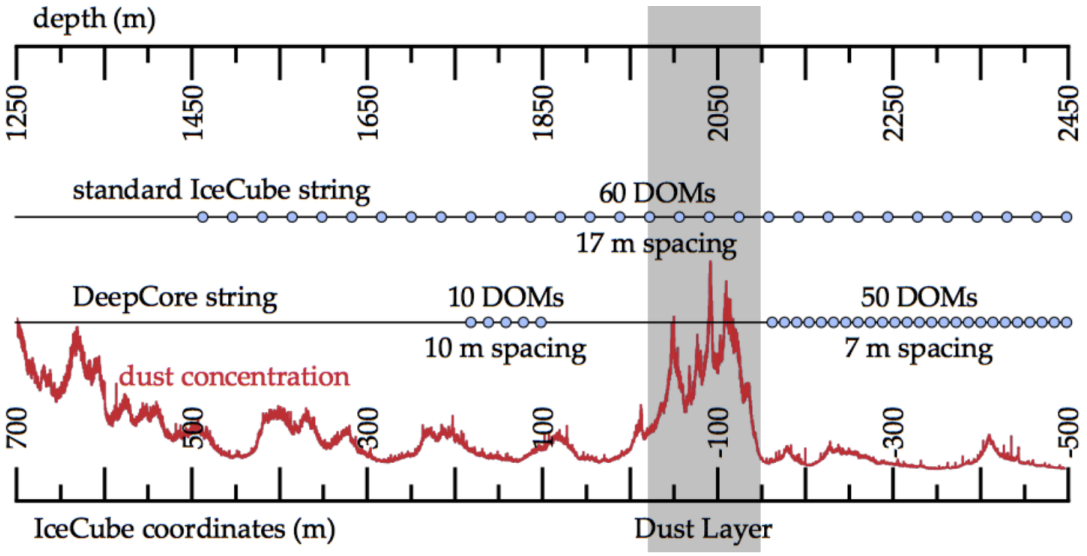

Figure 4.9: The dust concentration by depth, including the Dust Layer at 2.0-2.1 km, and the location of IceCube DOMs. Figure from [107].

4.3 Digital Optical Modules

The digital optical module (DOM) is the core piece of hardware for the IceCube detector (see Figure 4.10). Each of the 5,160 DOMs in the Antarctic ice contains (among many other components) a 10" diameter Hamamatsu R7081-02 photomultiplier tube (PMT), digitizing boards (or "main boards"), and a 20 MHz oscillator to serve as a local clock [112] [113]. These three components allow the DOM to perform the fundamental task of measuring Cherenkov photons and relaying the relevant information - the number of photoelectrons and timing - for energy and direction reconstruction back to the ICL.

4.3.1 Hardware

The Hamamatsu PMTs were selected because of their low dark noise, and the good time and charge resolution for single photons [113]. These R7081-02 PMTs were custom-made for IceCube using a low radioactivity glass, which reduced the dark count rate to 300 Hz (down from a standard 500 Hz) from -40 C to -20 C, which is the region of interest for in-ice equipment [113]. In a typical PMT, a photon hits the photocathode to produce an electron, which accelerates toward a series of dynodes, producing a cascade of electrons. By the time the electrons reach the anode, there are many orders of magnitude more electrons, which is how a single photon can turn into a large enough signal to measure.

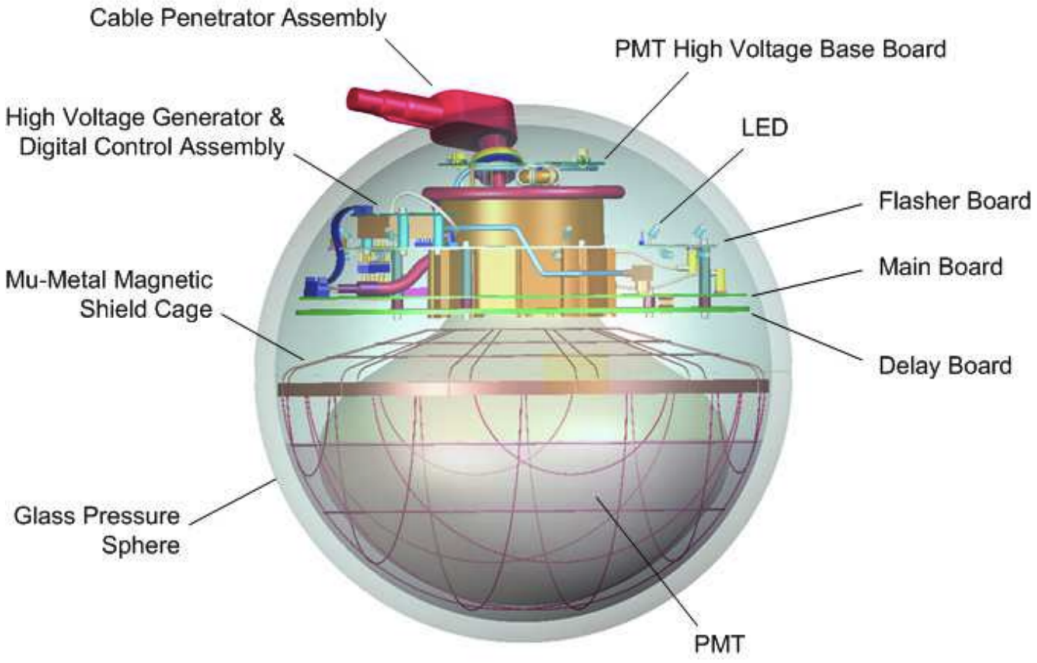

Figure 4.10: This figure shows a schematic of the digital optical module (DOM) with the major components highlighted. Figure from [112].

The Hamamatsu PMT has 10 linear focused dynode stages, reaching a gain of

10^7 electrons at the anode, and giving a voltage drop that is roughly 8 mV for each photoelectron (PE) collected from the photocathode. These PMTs have a quantum efficiency of 25% at 390 nm, which means there is a 25% chance a Cherenkov photon hitting a PMT inside the DOM will produce a readable signal [113]. The PMTs require high voltage, around 1300 V, to achieve a maximum collection efficiency and still produce 10^7 gain. An unintentional scintillation effect in the glass envelope of the DOM's pressure sphere produces background light that rises with decreasing temperature, but the efficiency of this DOM is still excellent in the range required by IceCube. In fact, for a high-energy neutrino track, the short measurement time for each DOM would mean only 1% of muons would have problematic noise, making the effect on reconstruction and background rejection quite small [113].

The DOM was designed to be robust and withstand indefinite deployment in the ice. These DOMS operate reliably in cold, high-pressure conditions due to the combination of high-quality commercial parts and well-designed original components. The PMTs are half-spherical with the bulbs facing downward (see Figure 4.10) surrounded by a mu-metal grid to reduce the effects of Earth's magnetic field. Each PMT is secured to the pressure vessel with optical silicone gel. The gel was tested to have minimum light reflection and high durability at -45 C [98]. Only 87 of 5,160 DOMs failed during deployment, freeze-in, and post-commissioning, which is a pretty impressive success rate [95].

The main board digitizes the analog PMT signal in the DOM. Digitizing the signal before sending it to the ICL minimizes the loss of information due to the analog signal degrading over a long cable [112]. This ensures high-quality signals

and a reduced computational load at the surface. The main board controls all the devices in the DOM, and also communicates with neighboring DOMs.

The local clock provides time stamps for internal DOM operations and allows for precise timing of the photon arrival. The local clock drift is less than 2 ns per second compared to the master clock at the surface [112].

All the components of the DOM are housed in a 35.6 cm diameter glass pressure sphere, which is strong enough to withstand the high pressures of hole-ice. The ice is melted as part of the drilling process, and after the DOMs are deployed the water is allowed to freeze, causing very high pressures (650 atm during freeze-in and 300 atm after freeze-in [90] [114]) several kilometers below the surface.

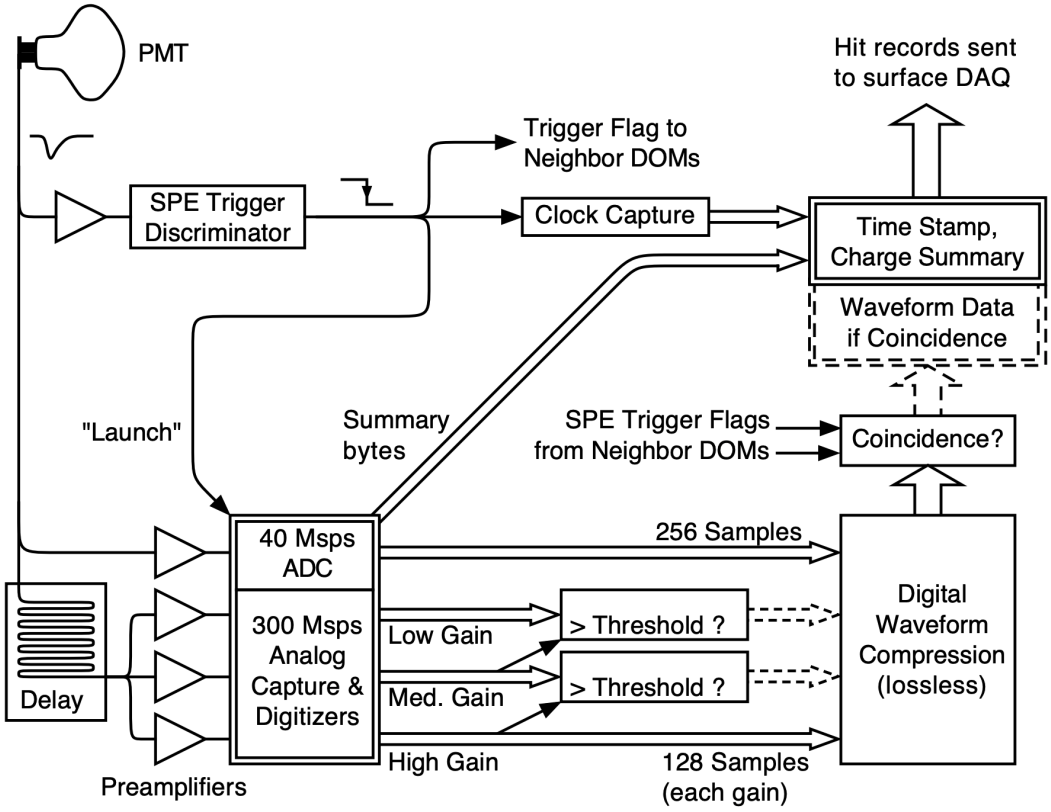

Figure 4.11: This figure shows a block diagram of the DOM main board. This is responsible for waveform digitization. Figure from [95].

4.3.2 Waveform Digitization

Waveform digitization takes place on the DOM main board, which is coupled to the anode of the PMT via a transformer. Figure 4.11 shows a block diagram of the main board. After an analog signal comes from the PMT (upper left in Figure 4.11), the discriminator on the DOM will trigger if the voltage corresponds to at least 0.25 photoelectrons. Once this digitization process begins, the neighboring DOMs are alerted to determine the local coincidence. If there is a Hard Local Coincidence (HLC), meaning one of the four neighboring DOMs (two above and two below) on the same string also records a discriminator trigger within 1 μs, then all the digitized information will be sent to the ICL. If the HCL condition is not met, then the information is instead tagged as a Soft Local Coincidence (SLC) and far less information is stored. While the decision of HLC vs. SLC is being made, the digitized waveforms are stored in DOM memory.

The actual digitization happens in the fast analog-to-digital converter (FADC) and Analog to Digital Waveform Digitizer (ATWD), which are both controlled by a Field Programmable Gate Array (FPGA). The FADC bins the information at 40×10^6 samples per second for the 6.4 microseconds following the discriminator trigger [95]. The ATWD uses much finer binning at 322 bins with 3.3 nanoseconds per bin (compared to 25 ns for the FADC) [115]. The FADC has low time resolution, but samples for a much longer time overall. This is helpful for lower amplitude signals with longer photon traveling times. The ATWD provides more detail because of the finer binning, and this information is preferred over the FADC if both are

available.

There are two ATWDs, each with four gain channels with 128 sampling capacitors [95]. As the signal is digitized, the ATWD can experience up to 29 μs of dead time. The secondary ATWD is able to record new pulses while the first ATWD is in use. If both ATWDs are in use, then the DOM is unable to record additional pulses. This reduces the dead time to roughly 22 μs based on the average noise rate [116]. Each of the two ATWDs uses three of the four gain channels to optimize the waveform fit (the fourth channel is used for calibration). The PMT waveform is amplified to three different gains: $\times 16$, $\times 2$, and $\times 0.25$ [98]. The unsaturated channel with the highest gain is recorded.

If the result is a soft local coincidence, then only three FADC samples corresponding to the highest amplitude portion of the waveform are sent to the ICL. All waveforms are sent to the ICL for hard local coincidences. The waveforms are then analyzed by a Non-Negative Least Squares algorithm called Wavedeform. The goal is to determine the number of photoelectrons detected by the PMT, as well as their time of arrival. The number of photoelectrons is fit by beginning with a single photoelectron (SPE) (Figure 4.12 shows a typical SPE waveform). SPE waveforms are typically dominated by a Gaussian peak with a width of 3.2 nanoseconds [113]. Wavedeform performs the least squares minimization on a single pulse to find the best-fit time. A second pulse is added and the fit is performed again. This continues until the goodness-of-fit improvement from adding an additional pulse is neglible.

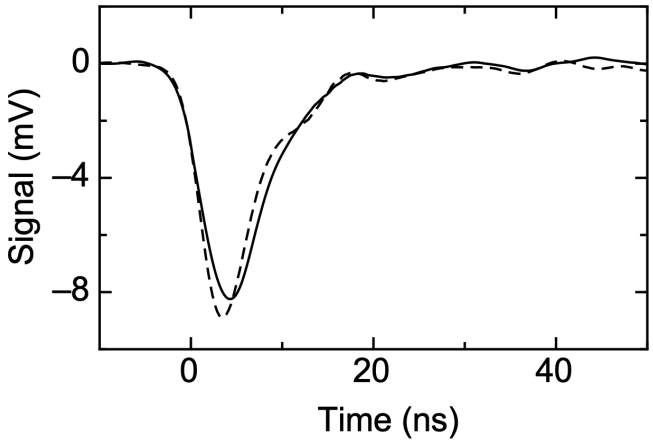

Figure 4.12: Average of 10,000 single photoelectron (SPE) waveforms from one PMT used in a typical IceCube DOM. Other PMTs show consistent results, indicating this waveform is a valid estimate for SPEs measured by a typical DOM in the detector. The solid line shows the transformer used in the deployed DOMs (dashed line indicates testing on an older version of the transformer). Figure from [113].

Triggering the DAQ leads to a window of at least 10 μs while the HLC and SLC information is stored. 10 μs is a *very* long time in terms of background noise. Large amounts of noise can interfere with accurate particle reconstructions. The pulse series produced by Wavedeform goes through a cleaning step to remove noise. A simple method using the $r - t$ causality condition is used [90]. A pulse must occur within 150 m and 1 μs of another pulse. Only HLC pulses satisfying this $r - t$ condition with other HLC pulses are kept. If a pulse fails the condition, it is considered in another two iterations where pulses are added to see if the condition is then met.

4.3.3 Calibration

Every DOM includes a flasher board, which contains 12 LEDs that produce bright UV optical pulses that are observable by other DOMs [117]. These flashers are used to calibrate DOMs by simulating Cherenkov photons, and are also used to study the optical properties of the ice. The 12 LEDs, six of which are pointed horizontally while the other six are tilted slightly upward, can be flashed independently [114].

Additionally, a low-light LED pulser - controlled by the DOM CPU program called DOMcal - is used for calibration [17]. DOMcal is run annually for in-ice PMTs (monthly for IceTop PMTs). The goal is to use the minimum voltage to trigger the discriminator and precisely test the features of the DOM's main board. The 128 sampling capacitors in each of the ATWD's four channels are used to map the input-output voltage, and the gains of the three amplifiers are tested as well [117]. This calibration is then used for the next year of data event processing.

The 20 MHz clock in every DOM must be calibrated to the other DOMs and the ICL clock. The clock in the ICL, called "IceCube Time" (ICT) is the master clock for the in-ice DOM clocks. A Reciprocal Active Pulsing (RAPcal) procedure is used to calibrate timing among clocks [117]. The RAPcal procedure is to send a pulse from the ICL to the DOM, then have the DOM wait for some fixed delay δ, and then return the pulse, along with the digitized waveform of the original pulse, back to the ICL. The timestamps of the pulse waveforms received on the DOM and returned are used to calibrate the master and local clocks. RAPcal signals are distributed to all DOMs in the array every 5 seconds. This may sound like a

calibration burden that would dominate the communications lines, but the exchange of RAPcal signals takes less than 1.5 ms for the entire array [117]. This means the communications bandwidth used is relatively small considering the timing precision that is gained. The measured DOM-to-DOM timing accuracy is 1.2 ns [95].

4.4 Data Acquisition

The purpose of the data acquisition system (DAQ) is to store HLC and SLC readouts from individual DOMs and prepare the event data for initial processing. The DAQ also prepares the data to transmit to the north via satellite.

4.4.1 Trigger

The DOMs are constantly transmitting waveform data to the ICL. This information - either for an HLC or SLC state - goes to a DOMHub computer, which is responsible for a string in IceCube. A DOMHub supplies power to the string as well as communication. The DAQ monitors all the DOMHubs, waiting for coinditions to be satisfied that indicate a physics event. The most common trigger type is a Simple Multiplicity Trigger (SMT), which looks for coincidences between DOMs reporting HLC launches. The SMT-8 trigger, which is the standard trigger used in astronomy analyses in IceCube, occurs when eight HLC launches (a discriminator trigger on the DOM's main board is called a "launch") are received during a 5 μs window. The event includes data from 4 μs before and 6 μs after the time when at least one trigger condition was met [90]. If, after 6 μs, no trigger condition is satisfied, then

that event data is finalized. This final event data bundle is called a "frame" and is the fundamental unit used in the processing and filtering system [90].

4.4.2 Processing & Filtering

An SMT-8 trigger occurs roughly at a rate of 2.0-2.4 kHz (the rate varies depending on the time of year), but only ∼10 mHz is expected to be from neutrino interactions (see Figure 4.13) [116]. The rest of the SMT-8 triggers are due to muons from cosmic-ray showers (see Chapter 2). A data rate of over 2,000 triggers per second is too high to send to the north via satellite. Therefore, the online processing and filtering (PnF) system performs pulse extraction, calibrations, and reconstructions while everything is still at the South Pole. The full waveform data is stored on disks in the ICL for every trigger, and that disk archive is physically carried north once per year.

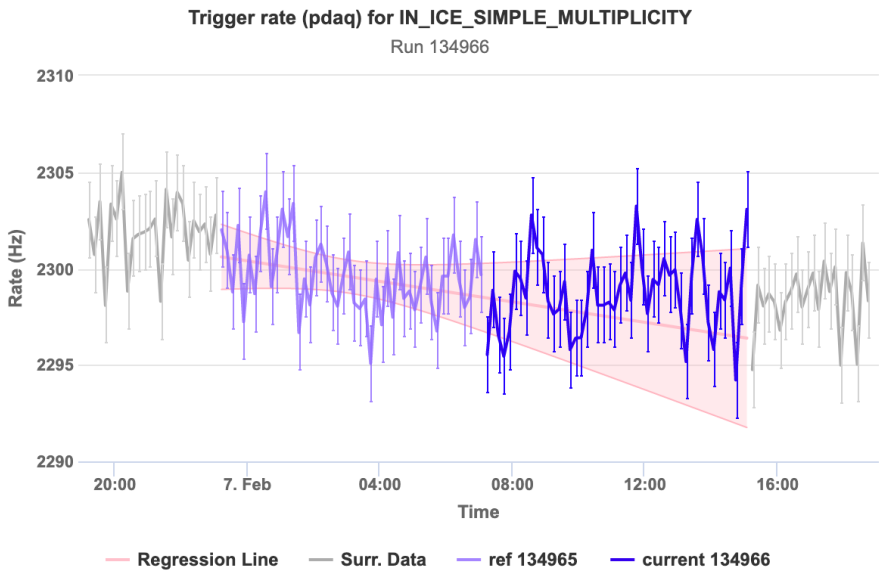

Figure 4.13: This figure is taken from live.icecube.wisc.edu, the web interface for IceCube monitoring. For this randomly chosen run, the SMT-8 triggers are around 2.3 kHz. The rates range from 2.0-2.4 kHz over a given year due to seasonal variation.

The IceCube PnF system runs basic physics reconstructions on the event frames produced by the DAQ. Simple and fast algorithms are favored in this step to keep computational needs low. The waveforms from the ATWD and FADC are converted into a series of PE pulses (see the discussion on Wavedeform in 4.3.2). Reconstructions performed on the pulse series provide an estimate of the particle direction, particle energy, total collected charge on the DOM, and quality of reconstruction.

Filters are applied to the pulse series reconstructions in an effort to select interesting physics events. Each filter has a signal hypothesis and the subset of events is selected to pass based on specific criteria. One of the more commonly used filters is the Muon Filter (5.1.1), which targets high-energy downgoing muons, as well as upgoing muons that are well-reconstructed. This filter alone reduces the

event rate from ∼2 kHz to ∼30 Hz.

Many other filters are in place, including the GFU filter. The GFU filter is described in 5.2.1, and directly produces part of the dataset used in this analysis. Figure 4.14 gives an overview of the main filters in IceCube.

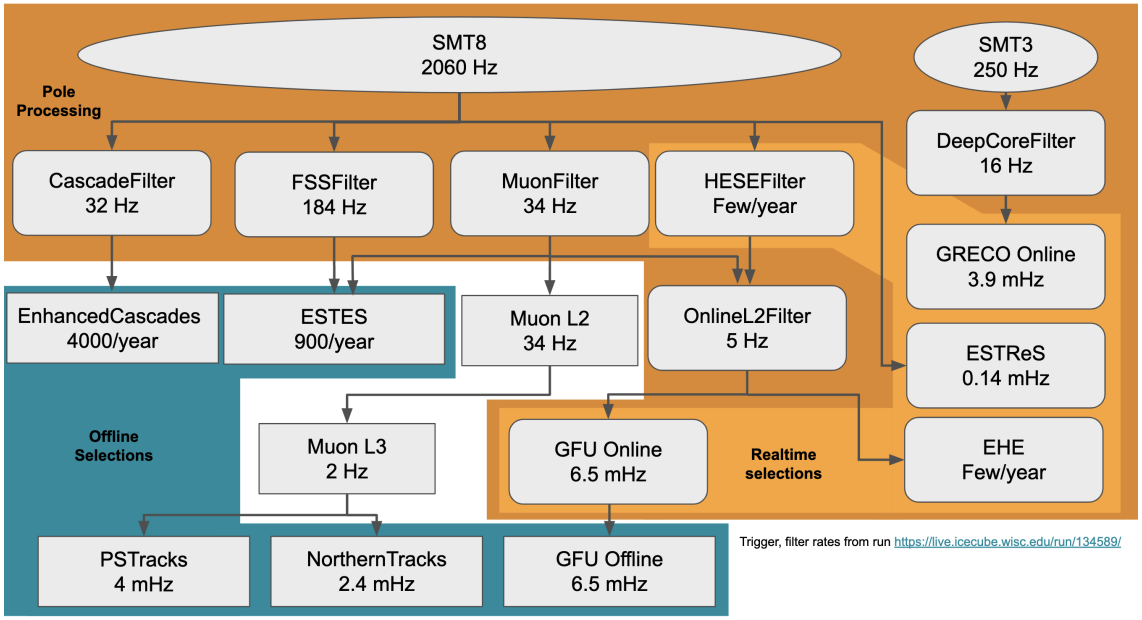

Figure 4.14: This figure shows the trigger rates of the most common filters in IceCube. The SMT-8 trigger rate (typically 2.0-2.4 kHz) is shown at the top and is reduced depending on the filter selected. Most high-energy astronomy analyses, including this one, use the MuonFilter as one of the cuts. The GFU Online and GFU Offline filters are discussed in Chapter 5. Figure from [118].

After data is sent north, the specific cuts and more rigorous reconstructions are performed for each dataset within IceCube. The procedure for the Gamma-Ray Follow-Up (GFU) sample is described in detail in Chapter 5.

4.4.3 Monitoring

IceCube's hardware is maintained by a core team of experts, and is monitored in shifts by members of the general collaboration. Detector operation information

is stored in a databased called IceCube Live, which has a web interface for easy searching and monitoring. Individual run statistics are available, including filter pass-rates, DOM launch rates, and other paramaters related to individual DOMs. A map of the detector makes it simple to see if certain DOMs had problems during a run, or if the DOMs have recurring issues. Roughly 100 DOMs are permanently removed from HLC pulse processing because of a problematic HCL connection (though 20 of those are available for SLC pulse processing because that communication line is intact) [17].

IceCube is stable and has an excellent uptime (see Figure 4.15). A typical "run" is eight uninterrupted hours of data-taking, with roughly 130 files per run. Once filtered, this data is sent north via satellite (usually within one day). All stable runs are included on the "good run list," which is maintained by the detector operations team. Runs can be excluded if there is a power outage or DOMHub crash, and calibration runs are not included in the good run list. Issues such as a power outage are managed by the two IceCube Winter Overs, who reside at the South Pole for a full year.

Figure 4.15: The detector uptime from the beginning of construction to the present day. The uptime stabilized after construction was completed in early 2011. Figure from live.icecube.wisc.ed, the web interface for IceCube monitoring.

Some of the GRBs in this sample were detected during detector downtime. For these cases, a test statistic (6.8) of zero is assigned to the time window to be conservative. There is no two-week period of detector downtime, which means every GRB will have at least one time window with data. Therefore, no GRBs are excluded due to problems with the good run list.

Chapter 5: Gamma-Ray Follow-Up (GFU) Dataset

The dataset used in this analysis is called the "Gamma-Ray Follow-Up" (GFU) sample within IceCube. There are two branches of this dataset: "GFU Online" and "GFU Offline." GFU Online is a 6.5 mHz sample of neutrino candidate events that is processed entirely at Pole and transmitted north via satellite within roughly one minute of triggering the detector. GFU Offline takes the online events and performs additional reconstructions using Level 1 data. "Level 1" refers to data that has gone through Wavedeform (see section 4.3.2) and additional filtering. The reconstructions applied in the north to create the GFU Offline sample are described in 5.2.2. GFU Offline, which runs from May 13, 2011 through October 13, 2018, is used in this analysis and described in this chapter. The GFU dataset [119] was created by Thomas Kintscher, with contributions from Elisa Bernardini and Konstancja Satalecka.

5.1 Event Reconstruction

5.1.1 Muon Filter

The Muon Filter is the first filtering level for IceCube, where the goal is to reduce the event rate enough to transmit via satellite. The input to this filter is the SMT-8 trigger, which looks for eight DOMs reporting HLC launches within a 5 μs window (see 4.4.1). These HLCs can be anywhere in the detector, which means most of these triggers are random noise arriving close in time. There are roughly 2,000-2,400 of these triggers every second, dominated by downward going cosmic-ray shower muons, which is far too high a rate for sending data via satellite to the north.

5.1.1.1 LineFit

To cut down on the event rate, a first guess fit algorithm called "LineFit" is used to reconstruct all SMT-8 triggers as a starting point for the full reconstruction. This method approximates the reconstruction as a least-squares fit of pulses to an infinite muon track [120]. The geometry of the Cherenkov cone is ignored, and the picture is simplified to light traveling with a velocity $\vec{v}$ along a 1-dimentional path through the detector. For PMTs at positions $\vec{r_i}$, which are hit at time t_i, the least-squares fit yields the following:

$$\vec{r} = \langle \vec{r} \rangle + \vec{v} \cdot \langle t_i \rangle \tag{5.1}$$

where $\vec{r}$ is the vertex through which the muon passes and the brackets indicate an average over DOMs. The velocity of the muon is then given by:

$$\vec{v} = \frac{\langle \vec{r} \cdot t_i \rangle - \langle \vec{r}_i \rangle \cdot t_i}{\langle t_i^2 \rangle - \langle t_i \rangle^2} \tag{5.2}$$

The vertex position, $\vec{r}$, and the direction of the muon velocity vector, $\vec{v}$, are helpful seed parameters for the next step of level 1 filtering.

The procedure described so far (and in [120]) is the original LineFit method. Improvements to LineFit are now widely used within IceCube [121]. This reconstruction, known as "ImprovedLineFit" reduces the impact of highly scattered light by applying a Huber penalty [122] to outlier pulses. ImprovedLineFit still disregards the Cherenkov geometry to keep the fits fast and simple, but an additional timing component is included to reduce the weight of pulses that travel for a relatively long time [121]. If light has been significantly scattered from the original trajectory, then it would be better to reduce the weight of those pulses within the fit. The optimal value to begin applying the penalty was found to be 156 meters, which means events that are more than 156 meters from the muon fit track trajectory at the time of the PMT hit are penalized [121].

Another way to identify outliers was to simply remove events that were too late and far from nearby DOMs. For a given hit, h_i, the neighboring hits within 156 meters are checked for time stamps. If any neighboring hits, h_j, were more than 778 ns before the original hit, then the pulse in question is considered scattered. If, within a reasonable distance of 156 m, a DOM is still recording hits in this region

after 778 ns, then it is unlikely to be a direct Cherenkov photon (i.e., not scattered) and should be removed from the fit.

These improvements - applying a Huber penalty and removing likely outliers based on clustering - nearly double the accuracy of the seed values, $\vec{r}$ and $\vec{v}$, passed to the SPE fit.

5.1.1.2 SPE Fit

The single photoelectron (SPE) likelihood performs a track reconstruction using the charge and timing information from only the first hit from each DOM, because the first photon is less likely to be scattered [120]. The measured photon is compared to the expected light production, which includes scattering and absorption models in the ice. A maximum likelihood method is used to estimate the track parameters. For an observed PMT hit position $\vec{r}_i$ and time t_i, and a muon passing through a vertex $\vec{r}$ at time t with velocity $\vec{v}$, the probability of observing the hit from the muon is given by the probability distribution function:

$$Probability = P\left(\vec{r}_i, t_i | \vec{r}, t, \vec{v}\right) \tag{5.3}$$

and the likelihood for several hits, $\{\vec{r}_i, t_i\}$, is given by:

$$L\left(\{\vec{r}_i, t_i\} | \vec{r}, t, \vec{v}\right) = \Pi_i P\left(\vec{r}_i, t_i | \vec{r}, t, \vec{v}\right) \tag{5.4}$$

Minimizing the negative log likelihood (LLH) with respect to $\vec{r}$, t, and $\vec{v}$ gives the most likely muon trajectory. The velocity of the muon is assumed to be close to

the speed of light (i.e., $|\vec{v}| \approx c_{vacuum}$), which simplifies this likelihood space slightly. It is important to remember that the position of the muon, $\vec{r}$, is fit in terms of the zenith and azimuth angles,[1] θ and ϕ. Therefore, equation 5.4 ([90] adapted from [120]) is in 5-dimensional parameter space.

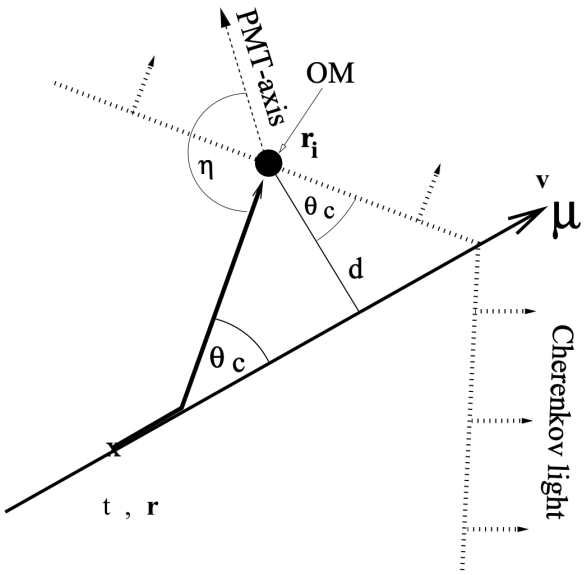

Figure 5.1: The geometry of the Cherenkov cone produced by a muon near IceCube DOMs. θ_c is the angle of Cherenkov light with respect to $\vec{v}$. Figure from [120].

Scanning the entire LLH parameter space is very computationally intensive. Instead, the numerical minimizers focus on finding a local minimum around the seed values, which are given by LineFit. The improvements to LineFit, described in the previous section, are important to ensure the minimizer is likely to find the global optimum by scanning the correct region of the likelihood. An effort is also made to include properties of the ice in this fit. Detailed PDFs constructed from spline fits of measured ice properties are approximated using the Pandel function [90] [123].

The Pandel function is a modified Gamma distribution that yields a PDF of

[1] Angles θ_c and η from Figure 5.1 are folded into the photospline tables discussed in 5.1.1.3.

the arrival time for photons based on the case of an isotropic, monochromatic, and point-like light source [120] [124]. For a photon from the Cherenkov cone in Figure 5.1, the time of arrival at a PMT is given by:

$$t_{geo} = t_0 + \frac{|\vec{v}| \cdot (\vec{r_i} - \vec{r}) + d \tan \theta_c}{c_{vacuum}} \tag{5.5}$$

The relative time of arrival, known as a time residual, is given by:

$$\Delta t = t_{hit} - t_{geo} \tag{5.6}$$

A limitation of the Pandel PDF is that it cannot handle negative time residuals (Δt). Negative time residuals can result due to time jitter in the detection devices [124] and early noise hits that survive the pulse cleaning processes [90]. Therefore, a convolution of the Pandel PDF with a Gaussian is done to ensure the finite time resolution of the detector is considered [124]. This gives a Pandel PDF of:

$$p_{pandel}\left(\Delta t\right) = \frac{\left(\Delta t\right)^{d_{\text{eff}}/\lambda - 1}}{\Gamma\left(d_{\text{eff}}/\lambda\right)\left(\frac{1}{\tau} + \frac{c_{medium}}{\lambda_a}\right)} e^{-\Delta t\left(\frac{1}{\tau} + \frac{c_{medium}}{\lambda_a}\right)} \tag{5.7}$$

where $c_{medium} = \frac{c_{vacuum}}{n}$ is the speed of light in ice, λ_a is the absorption length, and $\Gamma\left(\frac{d}{\lambda}\right)$ is the Gamma function [120]. The absorption length, λ_a, along with the free parameters τ and λ, are fit in simulated data and found to have the following values:

$$\begin{aligned} \tau &= 557\ ns \\ \lambda &= 33.3\ m \\ \lambda_a &= 98\ m \end{aligned} \tag{5.8}$$

The distance between the PMT and Cherenkov cone, represented by d and η, respectively, in Figure 5.1, must also be fit in the Pandel function [120]. The relative effect of scattering, depending on angle η, between the unscattered light path and the PMT axis is determined using an empirical effective impact parameter, d_{eff}. This is why d_{eff} appears in equation 5.7 instead of d shown in Figure 5.1. The best parametrization for d_{eff} is given by:

$$\begin{aligned} d_{\text{eff}} &= a_0 + a_1 \cdot d \\ a_1 &= 0.84 \\ \frac{a_0}{[m]} &= 3.1 - 3.9\cos(\eta) + 4.6\cos^2(\eta) \end{aligned} \tag{5.9}$$

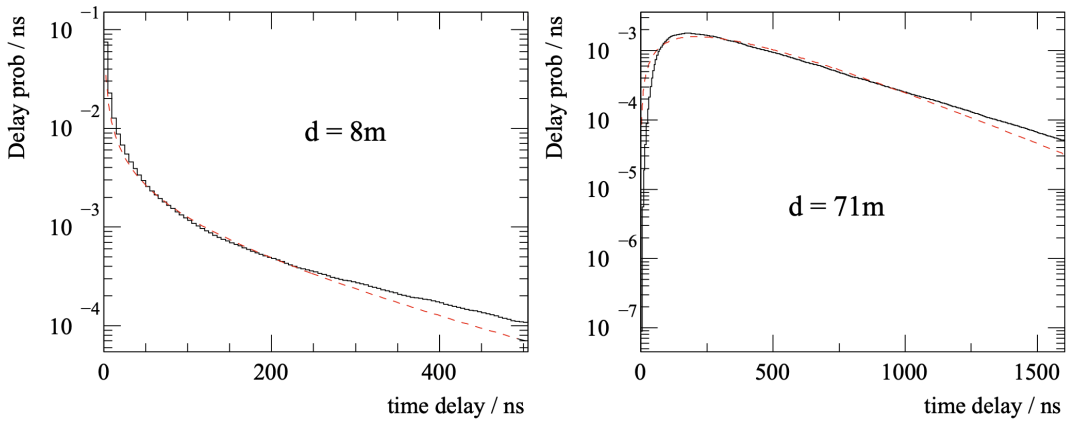

Figure 5.2: This figure shows the parametrized Pandel function (values in equations 5.8 and 5.9). Left: A relatively small distance, d, highlights a pole at $t = 0$ resulting from the Pandel function. Right: A larger distance, d does not have a pole at $t = 0$. Figure from [120].

Figure 5.2 shows the Pandel function using the values in equations 5.8 and 5.9. The Pandel function has a pole at $t = 0$ for small distances, which corresponds to a photon that is likely unscattered [120].

The SPE reconstruction finds the vertex, $\vec{r}$, and angles of incidence, θ and ϕ, that maximize the likelihood (or minimize the log of that likelihood) given in equation 5.4. The probability in equation 5.4 is given by the Pandel PDF in equation 5.7. There is, of course, some bias associated with only using the earliest photon when the Pandel PDF was constructed based on any random photon from the Cherenkov cone. This bias is addressed by using a multiple photoelectron (MPE) fit (see 5.1.1.3). The value in using the SPE first is to improve the angular resolution of the tracks compared to LineFit. The SPE fit is performed twice, and the result that yields the best likelihood is saved and passed as a seed for the MPE fit.

5.1.1.3 MPE Fit

The previous section described the reconstruction based on fitting pulses from the first photon to arrive at each DOM. The Pandel PDF fits can be improved by allowing more than the first pulse to contribute to the reconstruction. The total charge, n_{PE}, is included in the PDF:

$$P_{MPE}(\Delta t) = n_{PE} \cdot p_{SPE}(\Delta t) \cdot \left[\int_{\Delta t}^{\infty} p_{SPE}(t')dt'\right]^{n_{PE}-1} \tag{5.10}$$

The integral in this modified PDF is computationally intensive, and could only be implemented as part of the Muon Filter starting in the second year of full-detector data, which is known as IC86, 2012, because the computing resources at the South Pole were expanded [119]. Several helpful variables for cutting out background can be derived from the MPE fit, including a scaled log-likelihood, the number of DOMs that register a direct hit, and the reconstructed track length [119].

The scaled log-likelihood is the maximum likelihood value divided by the number of degrees of freedom:

$$S_{LogL}(x) = \frac{-\log_{10}(\max L)}{N_{DOM} - x} \tag{5.11}$$

where N_{DOM} is the number of hit DOMs, and x is the number of parameters determined by the fit. The fit often finds $x = 5$, because there are two angles and three coordinates. Due to an energy-dependent bias for the estimated errors in the track fits (see Figure 5.8), a cut is made at $S_{LogL}(3.5) \leq 8$ to reduce the bias

[119]. Table 5.1 shows that this cut does a good job reducing the rate of atmospheric muon background hits.

The number of direct DOM hits, or N_{DOM} is another great tool for determining the quality of a track reconstruction. Reconstructing a track requires understanding the journey of the photon from the Cherenkov cone to the DOM. As discussed in section 5.1.1.2, the longer the photon takes to arrive, the more uncertainty there is in the original location due to likely scattering. Therefore, the most reliable information comes from photons that travel directly to the DOM without scattering. These photons are called "direct hits" and tend to arrive in a very small time residual: $t_{res} \in [-15\ ns, 75\ ns]$ of the expected time for Cherenkov emission [119]. Only the first photon is counted for a direct hit per DOM, which means the variable N_{dir} is counting the number of DOMs that receive a direct hit. The length of the track determined by the direct hits is known as the "direct length." The direct length is another helpful variable for cutting out background events.

The log likelihood in 5.11 compares the number of hits to the expected number from simulation. The simulation propagates an infinite track through the detector for a given starting position and direction. The energy loss (assuming a minimum ionizing muon) is recorded along the track. This process is repeated for every possible starting position and direction. The resulting massive amount of information is stored in a table and splined using the photospline package [125] [126]. These photospline tables are used to calculate charge expectations in the "splineMPE" reconstruction used at final level.

5.1.1.4 Muon Filter Cut

The Muon Filter decision is based on the results of the SPE fit. The Muon Filter divides the sky into roughly upgoing and downgoing regions. The first region, mostly upgoing, is defined by a zenith angle of $\theta \geq 78.5°$. In this region, the background events are downgoing muons that have been misreconstructed as upgoing. For every atmospheric neutrino, there are 10^6 atmospheric muons entering the detector. Cutting on the parameters that characterize the reconstruction quality of the event is the main method of removing this background [119]. For events in the downgoing region, zenith angle $\theta < 78.5°$, the high-energy muon tracks from cosmic ray air showers are the primary background. These muons have an energy spectrum of $E^{-3.7}$, which is much steeper than the expected E^{-2} signal spectrum. The primary method of removing background in this region is to simply cut on energy-related variables.

All events in the upgoing region (zenith angle $\theta_{SPE} \geq 78.5°$) are selected that fulfill:

$$\frac{-\log_{10}(\max(L_{SPE}))}{N_{DOM} - 3} \leq 8.7 \tag{5.12}$$

where $\max(L_{SPE})$ is the maximum value of the likelihood function of the SPE track fit (equation 5.4), and N_{DOM} is the number of triggered DOMs that passed the filter for the given event [119]. The total passing rate of the Muon Filter is roughly 30-40 Hz.

5.1.2 Online Level 2 Filter

5.1.2.1 Angular Uncertainty

An important aspect of reconstructing event directions is understanding the uncertainty in those reconstructions. IceCube generally uses three angular uncertainty estimators: Cramer-Rao, Parabaloid, and Bootstrap. The Parabaloid and Bootstrap methods are too computationally intensive to perform on all events in the Online Level 2 processing, and are only performed if the reconstructions will finish quickly (see 5.2.2). Cramer-Rao, on the other hand, is relatively fast and gives a lower bound on the true resolution.

The Cramer-Rao lower bound relation [127] [128] places a limit on angular uncertainty based on the per-DOM PDFs near the fit minimum from the Pandel-based MPE PDFs. The per-DOM arrival time probabilities (for hit DOMs only) are summed in a Fisher information matrix [17]. The Cramer-Rao inequality places a lower bound on the covariance of pairs of track parameters:

$$\mathrm{cov}(\mu_m, \mu_k) \geq I(\vec{\mu})^{-1} \tag{5.13}$$

where the Fisher information matrix is given by:

$$I_{mk}(\vec{\mu}) = -\left\langle \sum_i \frac{\partial^2}{\partial \mu_k \partial \mu_m} \ln\, p(\Delta t_i | \vec{\mu}) \right\rangle \tag{5.14}$$

Here, $\vec{\mu}$ represents the x, y, and z coordinates of the vertex, as well as the reconstructed

direction angles θ and ϕ. All possible values of Δt_i are averaged (indicated by the angle brackets) and weighted by the MPE PDF values, $p(\Delta t_i|\vec{\mu})$ [90]. The Cramer-Rao variances determine the angular uncertainty of a track reconstruction. The variances are given by $\sigma_{\theta,CR} = \sqrt{(I^{-1})_{\theta\theta}}$ for zenith and $\sigma_{\phi,CR} = \sqrt{(I^{-1})_{\phi\phi}}$ for azimuth. The final error circle for each event comes from the combination of these variances:

$$\sigma_{CR} = \sqrt{\frac{\sigma^2_{\theta,CR} + \sigma^2_{\phi,CR} \sin^2 \theta_{MPE}}{2}} \tag{5.15}$$

The decision to sum over hit DOMs (rather than summing over all DOMs) produces a per-event angular error estimate that is comparable to the paraboloid method [90]. The paraboloid reconstruction is still preferred when possible, which is why the additional offline reconstructions are done on the final events (see 5.2.2 for details of the paraboloid method).

5.1.2.2 Split Fits

Two overlapping down-going tracks are sometimes fit as an up-going track. It is easy to imagine a scenario where two background muons arrive close in time (perhaps a corner clipper or another poorly reconstructed track) and the reconstruction algorithms treat these two events as a single upgoing track. The split fits defend against this by dividing the pulses into two parts, either by their average time or at the center of gravity. For a true single track, splitting the pulses either of these ways will still yield a similar reconstructed direction. For two separate tracks, the

reconstructions will be drastically different when split.

A geometrical splitting of pulses relies on the center of gravity (COG) of all the hits. The pulses are divided based on their position with respect to the center of gravity, which is given by:

$$\vec{x}_{COG} = \frac{\sum_{i=1}^{N_{DOM}} q_i \times \vec{x}_i}{\sum_{i=1}^{N_{DOM}} q_i} \tag{5.16}$$

where $\vec{x}_i$ refers to the positions of individual hit DOMs, and q_i is the charge for those DOMs [119]. Each individual hit position is projected onto the track generated by the MPE fit. The COG position is also projected onto the track, and it serves as the divider between sets of pulses. A time-based splitting simply divides the hits into early and late groups. The mean of all hit times, t_{mean}, is the dividing point and splits the pulses into two sets as well.

The four subsets - the two from the COG position on the track and the two from either side of the t_{mean} - are fit again using LineFit. The result from LineFit is used as a seed for the double-iteration of the SPE maximum-likelihood fit. The zenith angle, θ_i, is used to define the cut variable (Table 5.1) for the split fit:

$$\Delta_{\frac{\text{Split}}{\text{SPE}}} = \max_{i \in \text{split fits}} (\cos\theta_i - \cos\theta_{\text{SPE}}) \tag{5.17}$$

5.1.2.3 Bayesian LLH Ratio

The purpose of this filter is to reduce the background rate using relatively quick processing at the Pole, so a reasonable amount of data can be sent north via

satellite. The probability of an event being a true upgoing, neutrino-induced muon - rather than a mis-reconstructed air-shower muon - after the Online Level 2 Filter is roughly one in a thousand [119]. The event rate is still around 2 Hz and needs another significant cut. One way to do this (without adding another reconstruction) is cutting on a likelihood ratio to the SPE fit using a Bayesian approach [129] to the event reconstruction [119].

Bayes' Theorem describes the probability of an event A occuring given that B is true:

$$P(A|B) = \frac{P(B|A)P(A)}{P(B)} \tag{5.18}$$

This can be adapted to the case of the muon track by considering a track hypothesis (i.e., a downgoing, atmospheric muon), μ, and the data recorded for an event in the detector. Then, equation 5.18 becomes:

$$P(\mu|\text{data}) = \frac{L_{\text{SPE}}(\text{data}|\mu)P(\mu)}{P(\text{data})} \tag{5.19}$$

Here, the probability of the data given the track μ is the SPE likelihood function. $P(\mu)$ is the probability of a muon passing through the IceCube detector, which is known as the prior function. $P(\text{data})$ can be dropped because it is a normalization factor that is constant for the observed event. The prior function, $P(\mu)$, is given by:

$$P(\mu) = 2.50 \times 10^{-7} \cos\theta^{1.68} \exp\left(-\frac{0.78}{\cos\theta}\right) \tag{5.20}$$

Incorporating this prior information, $P(\mu)$, into the reconstruction accounts for the strong prior that the event is likely to be down-going. The rate of expected downgoing atmospheric muons is zenith-dependent, and is many orders of magnitude larger than the rate of upgoing neutrino-induced muons [129]. Including this function in a likelihood ratio provides another way to cut down on background down-going muons that are mis-reconstructed as up-going (particularly for events with zenith angles close to the horizon).

The SPE likelihood fit and the Bayesian-fit LLH are combined to make the following cut variable, which is included in Table 5.1:

$$\Delta_{\frac{\text{SPE}}{\text{Bayesian}}} = \log_{10} L_{\text{SPE}} - \log_{10} \left(L_{\text{SPE}}(\text{data}|\mu) P(\mu) \right) \tag{5.21}$$

5.1.2.4 Energy Estimator

The energy of the muon is estimated based on the light deposited along the track in the detector. For HESE events, described in 3.1.1, the muon track is almost entirely contained in the detector volume, which means a very good estimate for the energy of the muon and the neutrino can be achieved. Most events, however, are not fully contained within IceCube. For these events, the exact energy of the initial muon is not known (any reference to a "true energy" refers to simulation) and various energy estimators are used to estimate the muon energy. The muon energy is used as a lower bound for the neutrino energy. A precise neutrino energy extrapolation is only possible if the muon interaction point is known.

This lower bound neutrino energy is more precise for the southern hemisphere, because the potential path length for an interacting muon is shorter through the glacial ice than through the Earth's volume. Therefore, the true neutrino energy is going to be closer to the muon energy because the muon will not have traveled as far through a medium before entering the detector. The muon's deposited energy can be used as a cut for upgoing and downgoing tracks, because the downgoing muons will deposit more energy.

Two energy estimators are used in the GFU event sample. The first is called "MuEX" and is a single template scaling of expected light output of a simulated event to match observed data [115]. Here, a template refers to one of the photospline tables described in 5.1.1.3. The single template approach assumes the muon is minimum ionizing, which means $\frac{dE}{dx}$ is roughly constant. The energy deposited in the detector is then determined by comparing the number of photons observed by the DOMs to the expected photons from a template muon with some reference energy. Following the derivation in [115], the number of detected photons by a single DOM can be defined as a Poisson distribution of muon energy E:

$$\lambda = \Lambda E + \rho \tag{5.22}$$

where Λ is the expected photon yield per unit energy and ρ is the number of noise photons. The Poissonian likelihood of observing k photons is given by:

$$L = \frac{\lambda^k}{k!} \exp(-\lambda) \tag{5.23}$$

Taking the natural log of both sides, and plugging 5.22 into 5.23, the likelihood of detecting k photons in a single DOM is then:

$$\ln(L) = k\ln(E\Lambda + \rho) - (E\Lambda + \rho) - \ln(k!) \tag{5.24}$$

This can be extended to include all DOMs and maximized with respect to E:

$$\begin{aligned} 0 &= \sum (k_j \Lambda_j / (E\Lambda_j + \rho_j) - \Lambda_j) \\ \sum \Lambda_j &= \sum k_j \Lambda_j / (E\Lambda_j + \rho_j) \end{aligned} \tag{5.25}$$

Equation 5.25 can be maximized with respect to the energy, E, to determine the muon energy. This is done using gradient-descent numerical minimization algorithms [115].

MuEX is a relatively simple energy reconstruction. An attempt to improve this estimator is called "Truncated Energy," which aims to address the stochastic losses that contribute light to a track. MuEX assumes the muon is minimum ionizing and therefore deposits roughly constant energy. Stochastic losses contribute additional bursts of light that can bias the single-template scaling. Truncated energy removes the highest energy losses, assuming they are the result of stochastic losses, and averages the remaining energy losses along the track as if they were minimum ionizing [130]. The result is a more accurate energy reconstruction compared to MuEX.

Truncated Energy is configured to use photospline tables (see 5.1.1.3) based on the South Pole ice model with scattering from Mie et al. [106] rather than attempt to fit the energy [131]. The mean energy loss rate of a muon, given by $\left\langle \frac{dE}{dx} \right\rangle$, is roughly proportional to its energy above 1 TeV (see 4.2.2). Large stochastic losses in the detector can saturate the DOMs and lead to a poor energy reconstruction. Truncating portions of the track with the highest loss rates leads to a more robust measurement of the energy loss rate [115]. Removing the bins with the largest energy losses cuts outliers from the average and variance in the $\left\langle \frac{dE}{dx} \right\rangle$ calculation. Therefore, the muon energy is reduced and a better data-MC agreement is reached.

The MuEX energy is used to make cuts on the dataset at different selection points. For example, it is required that an Online Level 2 event have a successful MuEX reconstruction to be accepted by the GFU Filter. However, the energy for each event in the final sample is the value determined by the Truncated Energy.

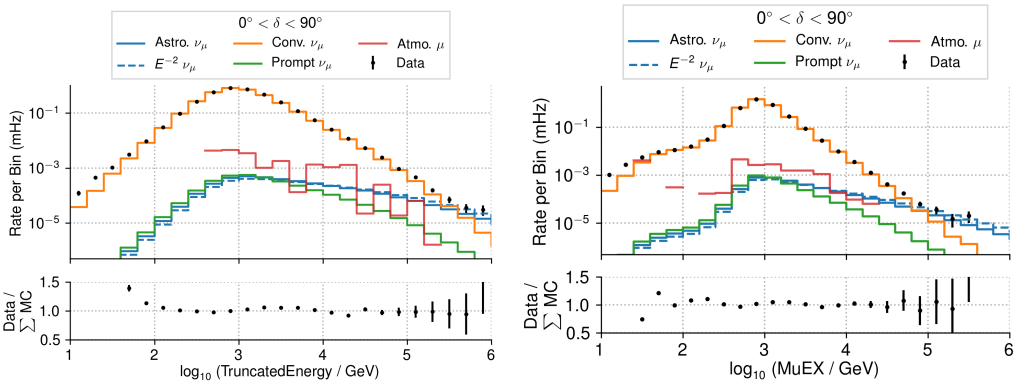

Figure 5.3: These plots show the truncated energy reconstruction (left) versus MuEX (right) in the northern hemisphere data. Figure from [131].

5.2 Event Selection

5.2.1 GFU Filter

The final step of online processing at the South Pole is the GFU Filter. This takes the 2 Hz Online Level 2 events and only keeps them if they have a successfully converged SplineMPE fit, have a Cramer Rao uncertainty estimate for a SplineMPE track, and have a successful MuEX reconstruction [131]. The detailed cuts given in Table 5.1 drop the rate down to roughly 6.5 mHz. The cuts are tuned to be sensitive to a neutrino signal with a spectrum of E^{-2} because of First Order Fermi Acceleration, which is described in detail in section 3.1.2.

Cut Level	Selection criterion	Atms. μ (mHz)	Data (mHz)	Atms. ν_μ (mHz)	Astro. $\times 10^{-3}$ (mHz)
0	$\cos\theta_{\mathrm{MPE}} \leq 0$	1010.5	1523.81	7.166	6.23
1	SLogL(3.5) ≤ 8	282.49	504.44	5.826	5.62
2	$N_{\mathrm{Dir}} \geq 9$	8.839	22.01	3.076	4.06
3	(($\cos\theta_{\mathrm{MPE}} > -0.2$) AND ($L_{\mathrm{Dir}} \geq 300$ m) OR ($\cos\theta_{\mathrm{MPE}} \leq -0.2$) AND ($L_{\mathrm{Dir}} \geq 200$ m))	1.124	4.30	2.313	3.69
4	$\Delta_{\mathrm{Split/MPE}}$ <0.5	0.100	2.15	1.899	3.26
5	(($\cos\theta_{\mathrm{MPE}} \leq -0.07$) OR (($\cos\theta_{\mathrm{MPE}} > -0.07$) AND ($\Delta_{\mathrm{SPE/Bayesian}} \geq 35$)))	0.080	2.08	1.880	3.25
6	(($\cos\theta_{\mathrm{MPE}} \leq -0.04$) OR (($\cos\theta_{\mathrm{MPE}} > -0.04$) AND ($\Delta_{\mathrm{SPE/Bayesian}} \geq 40$)))	0.075	2.06	1.875	3.24

Table 5.1: The GFU event selection cuts corresponding to the passing event rate for IC86, 2012. An event is selected if it passes all 0-6 cut levels. Figure from [119].

Both the upgoing and downgoing selections for the GFU filter use Boosted Decision Trees (BDTs) to classify events as signal and background. The final BDT cuts were chosen to optimize point source sensitivity. The public software package *scikit-learn* [132] was used for BDT training, and the IceCube software package

pyBDT [133] was used for classification.

The final event rates as a function of the true neutrino energy and zenith, determined by running the filters on simulated data, are shown in Figures 5.4 and 5.5, respectively.

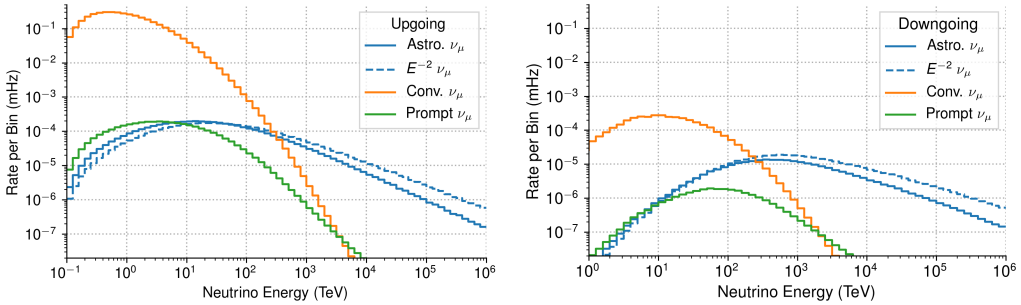

Figure 5.4: These plots show event rate versus true neutrino energy. The upgoing (northern) selection is shown on the left and the downgoing (southern) is on the right. The atmospheric muons are not shown on this plot, but they dominate below ∼1 PeV in the southern sky. The blue solid line refers to the best fit astrophysical neutrino spectrum (described in 3.1.1), which is approximately $E^{-2.28}$. Figure from [131].

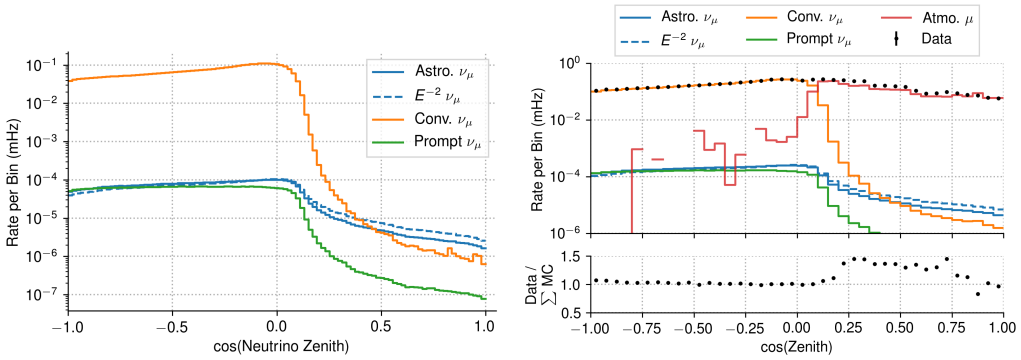

Figure 5.5: This plot shows the true neutrino zenith (left) and reconstructed zenith (right) versus event rate in the final GFU sample. Figure from [131].

5.2.2 Offline Processing

The entire processing chain up to this point is completed at the Pole and sent north for immediate use in real-time analyses. Additional processing, discussed in

this section, is completed offline in the north and used for archival studies.

There are three angular estimators used regularly in IceCube: Cramer-Rao, Paraboloid, and Bootstrap. Cramer-Rao is the fastest, which is why it is favored by the online analysis. However, it is also the least accurate of the three. Once the events passing the GFU Filter are sent north, the Paraboloid and Bootstrapping methods are applied to the events.

The Paraboloid estimator is derived directly from the reconstruction likelihood space [134]. This method takes the minimum from the track fit and scans the nearby likelihood space by varying the fit parameters. The resulting points in that likelihood space are fit with a parabola [119]. This method requires fitting the likelihood function repeatedly, which is why it is too slow for online reconstruction. It is particularly slow for events with high numbers of DOM fits.

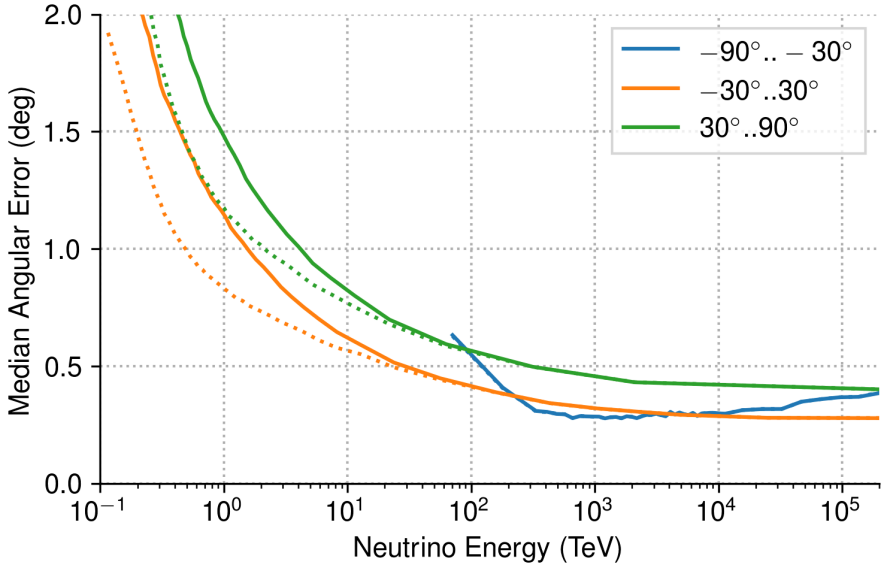

Figure 5.6: This plot shows the median angular resolution by energy bin of the neutrino (solid lines) and muon (dotted lines) as a function of true neutrino energy. The caption refers to the declination range being tested. Figure from [131].

The Bootstrap estimator does not directly evaluate a likelihood. Instead, the process is to randomly remove hits and refit the track direction. This process is repeated to define the uncertainty in track direction. If a single hit from far away is removed and the direction changes significantly, then the angular uncertainty will be relatively large. If all the hits align, then removing one will have little impact and the angular uncertainty will be small. This is a helpful angular estimator because it will always return a value. Paraboloid, on the other hand, can fail to return a result.

All three angular estimators are used in this event selection. The runtime for each estimator is related to the number of photons in each event. The number of DOMs hit and the reconstructed energy determine which estimator is used for each event. If the reconstructed energy from MuEX (5.1.2.4) is below 4 TeV, then Paraboloid is used. For a MuEX value above 4 TeV, Bootstrapping is used if fewer than 300 DOMs are hit and Cramer-Rao is used for more than 300 DOMs [131].

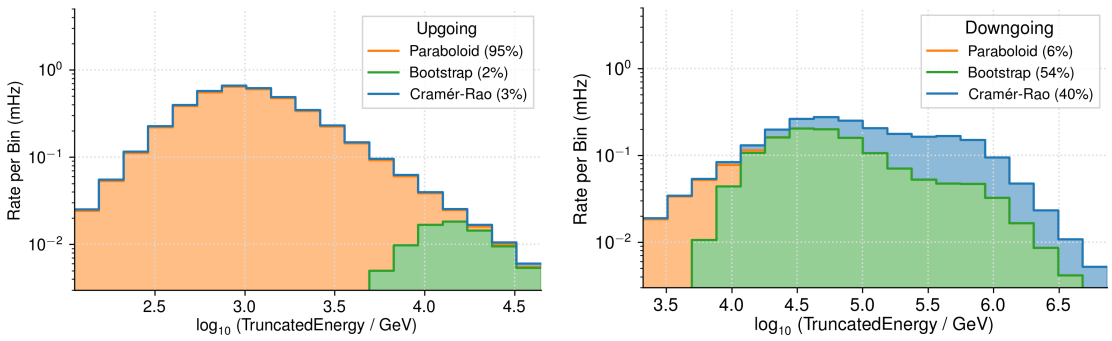

Figure 5.7: This plot shows the rate of Cramer-Rao, Paraboloid, and Bootstrap estimators used in the northern (left) and southern (right) sky. Figure from [131].

The resulting angular uncertainty is shown in Figure 5.6. Each event has a correction applied called a "pull." A pull correction is used because the Monte

Carlo simulation's angular uncertainty is unrealistically small. Figure 5.8 shows this tendency, which is particularly dramatic at higher energies, in simulation by plotting the true direction divided by the reconstructed direction. The solution in this dataset is to divide each energy bin by some factor to pull the ratio of $\frac{\Psi_{true}}{\Psi_{reco}}$ to a flat line (also shown in Figure 5.8).

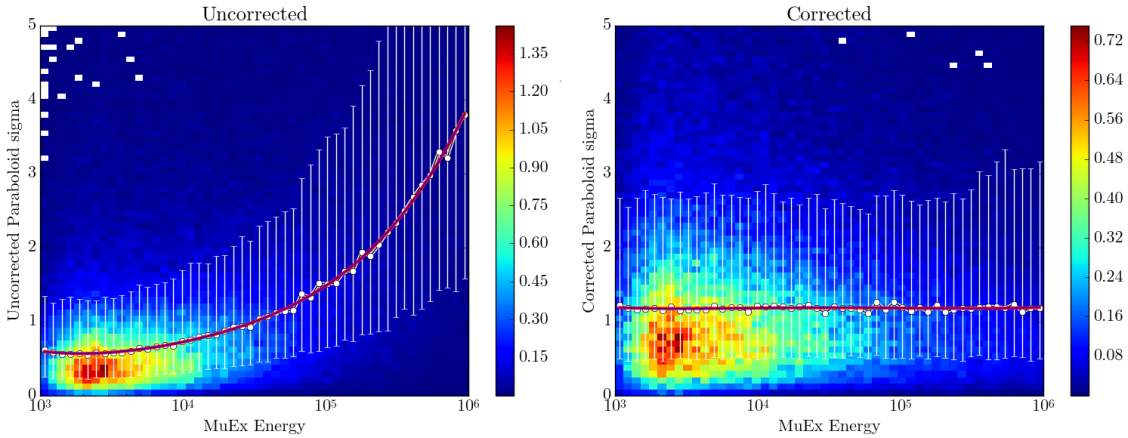

Figure 5.8: Left: Uncorrected ratio of true direction to reconstructed direction errors. The high energy values increase dramatically due to the unrealisitically small reconstructed angular uncertainty in simulated data. Right: The corrected ratio pulled down to a value of 1.1774σ. Figure from [135].

The values in each bin are corrected to a value of 1.1774 [131] [135]. This decision comes from difficulties mapping the two-dimensional direction (e.g., δ and ϕ) onto the one-dimensional sigma. This is clearly illustrated in Figure 5.9, which shows the reconstructed values will correctly fall within 68% containment for each angle, leading to a grid. However, the single sigma value can only be used to make a circle, which loses information in the corners of the grid created by two reconstructed angles. The result of a pull correction to a value of 1σ will only lead to 39% containment. A compromise of 1.1774σ is used to achieve 50% containment,

which is the median pull correction.

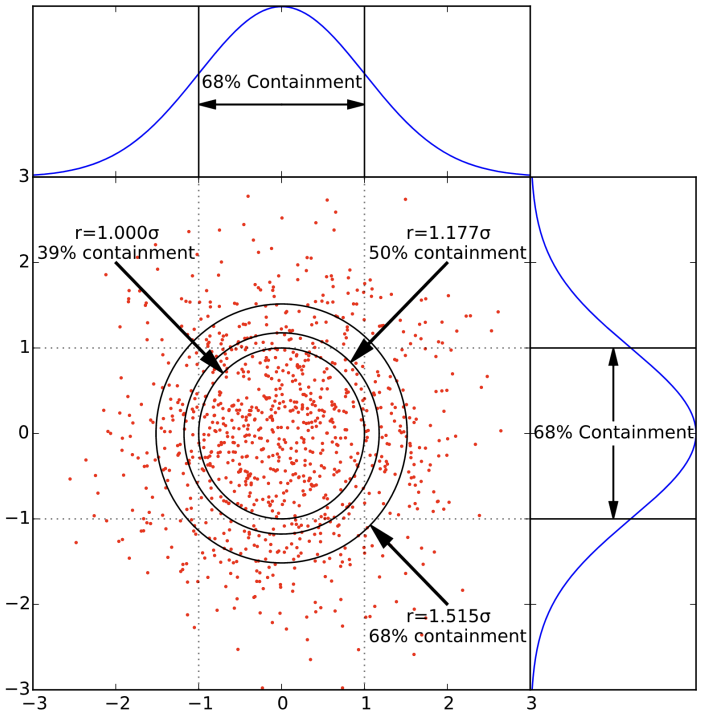

Figure 5.9: This figure shows how information is lost attempting to map the two-dimensional reconstructed direction uncertainty onto a one-dimensional value of sigma. A value of 1.1774σ must be used to achieve 50% containment, which is known as the median pull correction. Figure from [135].

5.2.3 Neutrino Effective Area

The effective area of an event selection is used to compare datasets to one another. Effective area (m^2) represents the size target the detector becomes to a particle of a given energy and declination. This quantity is independent of signal spectrum and flux. The goal is to show how sensitive the dataset is to a particle of a certain energy coming from a particular direction. This is very useful if an analyzer is interested in signal neutrinos in a specific energy range, because all the datasets within IceCube are optimized for different energy ranges. Comparing the

effective areas can be a good way to decide what dataset is best for a given study. The effective area for the GFU selection is shown in Figure 5.10.

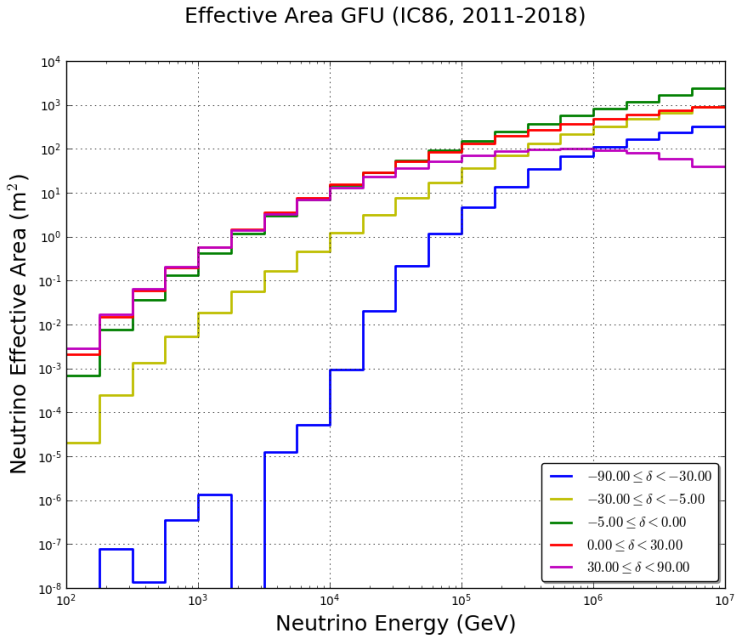

Figure 5.10: The neutrino effective area of the 2011-2018 GFU Offline sample by declination. Effective area generally increases as a function of energy. At high declinations, the effective area peaks and drops due to Earth absorption.

5.3 Simulation

Reliable simulation of IceCube data is essential to any physics analysis. An analyzer uses simulated data to develop the steps of an analysis and determine the sensitivity and discovery potential of the analysis. If the simulation data is completely different from true detector data, then all the tests and decisions made for the analysis are useless. The goal of simulated data is to accurately model the common backgrounds in the northern and southern sky. In the northern sky, the most common background is from atmospheric neutrinos interactions that produce

muons. In the southern sky, the muons from cosmic ray air showers enter the detector directly as a source of background (this does not happen for the northern sky because the Earth acts as a shield). These sources of background are simulated in Monte Carlo datasets.

Common background events are muon bundles and corner clippers. Muon bundles refer to muons arriving from the same air shower with very small spatial separation [120]. Corner clippers are muons that pass just outside the detector. They send some photons into the detector, mimicking an upgoing muon, but the reconstruction is poor and only provides a small amount of light near the edge of the detector.

5.3.1 Cosmic Ray Simulation

A software package called CORSIKA (**CO**smic **R**ay **SI**mulations for **KA**scade) [136] is used to simulate cosmic ray air showers. CORSIKA is a detailed Monte Carlo program that has been developed into a tool for many scientific collaborations. The simulated air showers are induced by a range of cosmic ray primaries, including protons, light nuclei up to iron, and photons [136]. The compositions and energies of these cosmic ray primaries are generated randomly from the Polygonato model [137]. The output of CORSIKA is coordinates and momenta of resulting shower particles, which includes a correctly weighted energy spectrum.

CORSIKA provides the simulated background of cosmic-ray muons that dominates the lower level IceCube data, particularly in the downgoing region. Coincident air-

shower events, which includes several muons from distinct air showers that appear as one event, are also simulated. The muons are tracked from the air shower in the atmoshpere down to the IceCube detector, approximately 1.4 kilometers below the ice. The muons are propagated through IceCube's detector volume as if they were produced in charged current interactions (see 4.2). Only muons are simulated all the way to the detector because other particles will not survive the thick layer of ice.

5.3.2 Neutrino Simulation

A Monte Carlo generator called ANIS (**A**ll **N**eutrino **I**nteraction **S**imulation) is the software foundation for IceCube's neutrino-generator ("NuGen"), which simulates the neutrino events [138]. The simulation includes both atmospheric neutrino backgrounds and astrophysical signals. The neutrinos are prepared based on the desired spectrum, propagated through the Earth, and then interactions are simulated near the detector volume. This simulation software requires elaborate models for neutrino-nucleon interaction cross-sections [139] and propagation through the Earth. The Preliminary Reference Earth Model [140] provides the density profile for Earth in ANIS [138] (see Figure 5.11).

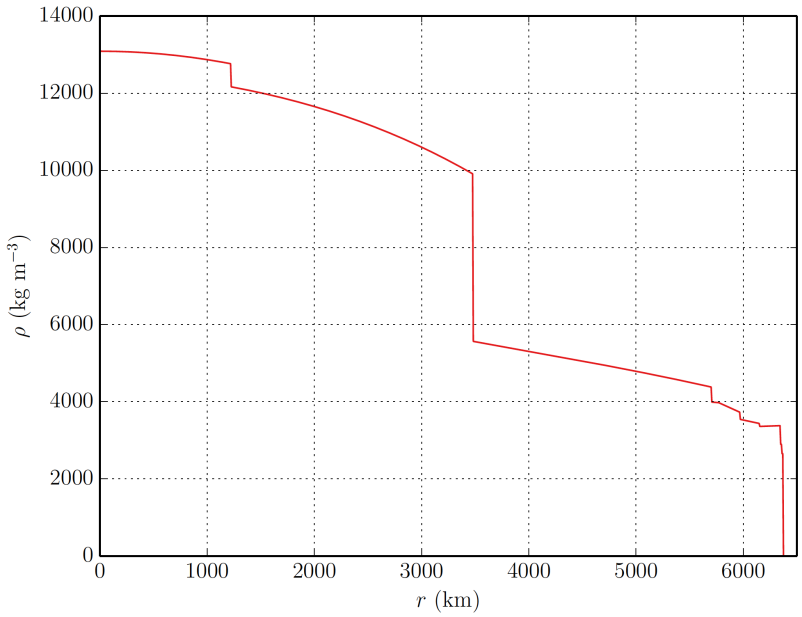

Figure 5.11: The density profile of Earth from the Preliminary Reference Earth Model is shown here. This is used to understand how neutrinos would propagate through the Earth. Figure from [17], plotting the values from Table 1 in [140].

There are several steps to producing an accurate neutrino simulation. The first is to simulate a spectrum of neutrinos with enough statistics at high energies, which can be computationally expensive for analyses focused on TeV-energy ranges. The atmospheric neutrinos have an energy spectrum of $E^{-3.7}$, which means one would have to simulate billions of neutrinos to start seeing high statistics in the TeV-range. Rather than spend a lifetime simulating neutrinos with the proper spectrum, a generic primary spectrum is generated: $\frac{dN}{dE_\mu} \approx E_\nu^{-\gamma}$ with $\gamma = 1$ or $\gamma = 2$ [119]. This generic spectrum can be re-weighted to apply the correct probability of being detected.

The next step is to model the neutrino-nucleon cross section, which is taken from the parton distribution function calculated in [103], and calculate the probability

the neutrino will interact before reaching (or inside) the detector. Neutrinos are propagated in small steps through the Earth and all interactions (absorption, resonant scattering, neutral current interactions, etc.) are included. Of course, the simulated neutrino could interact far away and produce a muon that does not reach the detector. This is computationally expensive considering the low probability of yielding an event that deposits enough energy in the detector volume to trigger an event. The solution is to force neutrinos to interact at a random vertex near the simulated detector, even though this unrealistically improves the efficiency of low-energy neutrinos, and weight the probability of interaction by the trigger-level effective area. This is a complicated way of saying the neutrinos interact near the detector, but each neutrino sees a different size target depending on its energy. Once the neutrino has propagated to the interaction vertex and its energy is calculated, the neutrino interacts according to the Standard Model. At these energies, the neutrino mostly interacts by deep inelastic scattering via the charged or neutral current, depending on the cross-section and interaction energy.

All these simulation steps in NuGen include randomization parameters that contribute to per-weight events known as $OneWeight$. The dataset size, volume of interaction, generic spectrum, and more all contribute to $OneWeight$. The units of $OneWeight$ are $GeV\ cm^2\ sr$, and it is given by:

$$\text{OneWeight} = \left(\frac{P_{\text{int}}}{E^{-\gamma}}\right) \cdot Area \cdot \Omega \int_{E_{\min}}^{E_{\max}} E'^{-\gamma} dE' \tag{5.26}$$

Here, P_{int} is the total interaction probability weight and $E^{-\gamma}$ is the neutrino

generation energy spectrum shape. *Area* is the area over which neutrino events are generated, Ω is the solid angle, and γ is the spectral index from $E_{\min}$ to $E_{\max}$. Since $OneWeight$ incorporates the generic spectrum that produced neutrinos (e.g., E^{-1}), the actual weight on each neutrino event must include the physical spectrum (e.g., $E^{-3.7}$). Therefore, the weight for each event is given by:

$$w_i = \frac{\text{OneWeight}}{N_{events}} \times \frac{d\Phi_\nu(E_\nu)}{dE_\nu} \tag{5.27}$$

Using $OneWeight$ requires three pieces: $OneWeight$, known as "ow" in standardized dataset files, which has units of $GeV \cdot cm^2 \cdot sr$; the flux model, Φ, which is in $GeV^{-1} \cdot cm^{-2} \cdot sr^{-1} \cdot s^{-1}$, is the desired neutrino spectrum; and the total of amount of time, t, measured in seconds. This leads to:

$$w_{event} = ow \cdot \Phi \cdot t \tag{5.28}$$

The sum of the weights then gives the number of expected events:

$$N_{expected} = \sum_{i}^{events} w_i \tag{5.29}$$

5.3.3 Detector Simulation

Once the neutrino interaction is simulated, the next step is to propagate the resulting particles through the ice and identify where light is produced (see Figure 5.12). This light can come from Cherenkov emission of the muon or from stochastic

losses. Once those photons are created in the simulation, they are propagated outward until they are detected by a DOM, absorbed, or move too far from the detector. This portion of the simulation is conducted by a Monte Carlo software package called PROPOSAL (**Pr**opagator with **O**ptimal **P**recision and **O**ptimized **S**peed for **A**ll **L**eptons)[2] [141]. PROPOSAL calculates the continuous energy loss of the muon, as well as the stochastic losses (bremsstrahlung, pair production, etc.).

The photons produced must be propagated with consideration for scattering and absorption in the ice. The Photon Propagation Code (PPC) [142] and CLSim [143] are used to simulate these photons. The result is a set of times each DOM is hit by simulated photons and includes effects from ice models, photon wavelength, and PMT quantum efficiency. Noise associated with the DOM glass scintillation is simulated with Vuvuzela [116]. The response of the PMTs is simulated in PMTResponseSimulator [144], which considers the entire waveform digitization process within the DOM, including the trigger system.

[2] That acronym is, perhaps, a stretch.

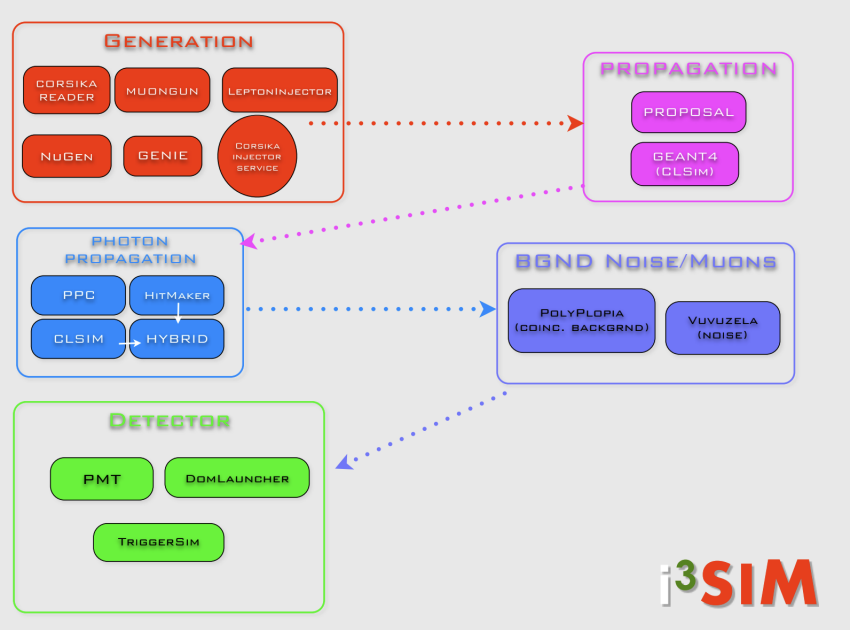

Figure 5.12: The simulation chain in IceCube. Figure from [107].

Simulated data is reconstructed and filtered following the same steps described in 5.1 and 5.2, including online processing at Pole and the offline processing in the north.

5.4 Seasonal Variation

There is some natural variation in the IceCube data based on atmospheric temperature (see Figure 5.13). When the air temperature increases, the atmospheric density decreases and the decay probability increases, which means the rate of high-energy muons increases [9]. Because this analysis uses pre-computed all-sky scans (see 7.5) instead of scrambled data strictly around the time of the GRB, the seasonal variation was a source of concern for the analysis. To check the impact of seasonal variation, the sensitivity and 3σ discovery potential were calculated using the median

expected background rate from Figure 5.13 compared to the maximum background.

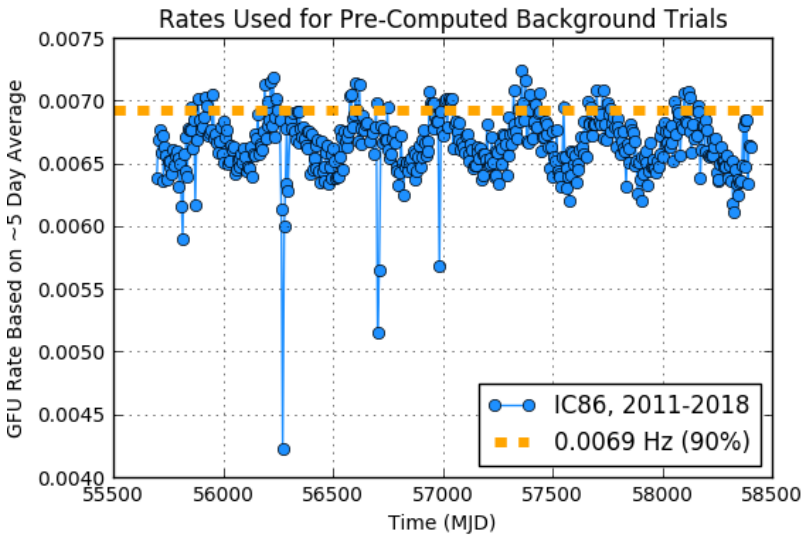

Figure 5.13: The seasonal variation of the 2011-2018 GFU Offline sample. Runs are grouped into five days and the average rate among those runs is used. The orange line indicates the 90% rate of this dataset.

The ratio of the median background rate to the maximum background rate is shown in Figure 5.14. There is very little change in the sensitivity and 3σ discovery potential due to the higher background rate. There are small impacts in the longest time windows, but there is never more than a 10% change. This is especially clear in Figure 5.15, which shows how many bins in the declination vs. time window grid had any change in sensitivity. A vast majority of bins had no change in sensitivity, and no bins changed more than 10%. The final decision in this analysis was to use the 90% background rate to have a slightly conservative estimate of expected background events. The 90% background rate refers to the orange line in Figure 5.13, which is 90% of the maximum 5-day rate from the entire dataset.

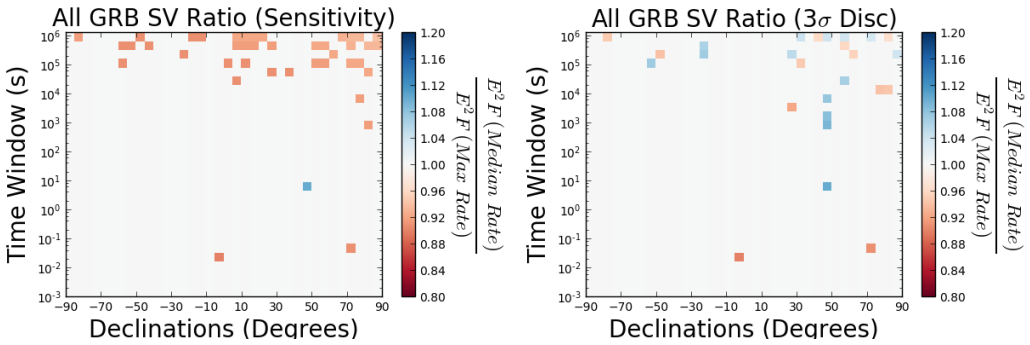

Figure 5.14: The change in sensitivity due to different expected background rates. The median and maximum rates refer to values taken from Figure 5.13. These figures confirm the effects of seasonal variation are quite small and mostly limited to long time windows and extreme declinations.

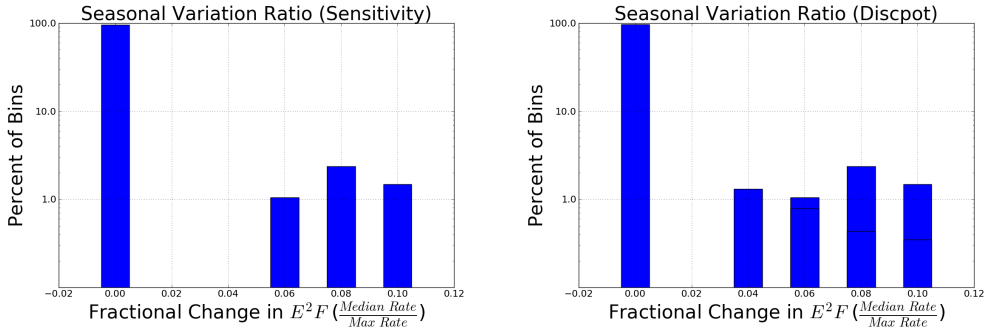

Figure 5.15: These figures highlights how few bins change from Figure 5.14. Only a small fraction of bins change, and the ones that do mostly change by a few percent. No bins change more than 10%.

Chapter 6: Unbinned Likelihood Method and Frequentist Approach

The unbinned likelihood method and frequentist approach used in this analysis[1] determines the significance of neutrinos coincident with GRBs. Although rare, due to the sheer number of atmospheric neutrinos, an accidentally coincident neutrino-GRB detection is possible. The probability of each neutrino event being signal versus accidental coincidence is calculated based on its reconstructed energy, arrival time, and reconstructed direction relative to the GRB.

It is possible to perform this analysis using a binned likelihood approach. In this case, the number of events within some angular bin around the GRB's position (determined by the detector's angular resolution) would be considered [146]. The number of events measured would be compared to the number of expected background events from Poisson statistics. This method is computationally efficient, but the bin limitation risks losing signal events that are just beyond the bin edge. An unbinned likelihood, on the other hand, considers the contribution from all neutrinos. In practice, only events within roughly 10 degrees are calculated in the likelihood, because any events beyond that will have a negligible impact on the test statistic (see 6.8).

[1] and previous GRB analyses from recent years [17] [90] [145]

The goal of this entire chapter is to set up a method to assign a probability that the data is consistent with typical background. The information from all the individual neutrinos gets combined into a test statistic, which represents the GRB as a whole. Using frequentist statistics, this test statistic can be converted into a p-value, a probability that this data is consistent with background. If we find the data is very *inconsistent* with background, then we have found evidence of astrophysical neutrinos correlated with a GRB. Finally, the outcome of a Binomial test reveals if the collection of GRB p-values is consistent with background-only neutrinos, or if, instead, there is evidence that sub-populations of GRBs are producing detectable fluxes of neutrinos.

6.1 Likelihood Method

The likelihood is used to understand the background neutrinos and to apply reasonable models for the signal neutrinos. The data is assumed to have both background and signal events, which are modeled using three signal and three background probability density functions (PDFs): space, energy, and time [146]. Each neutrino candidate near a given GRB will get scored based on the six PDFs, and those event scores get combined into a likelihood, and ultimately a test statistic.

6.1.1 HEALPix

HEALPix (**H**ierarchical **E**qual **A**rea iso**L**atitude **Pix**elization of a sphere) is a mathematical framework to make skymaps by dividing a spherical surface into

pixels that cover equal surface area [147] [148] [149] [150]. "Healpy" is a software package that generates the "HEALPix" maps described throughout this thesis. In this analysis, we divide the sky into HEALPix maps with $N_{side} = 128$, meaning each pixel represents approximately half a degree in the sky. The number of pixels, N_{pix}, in a HEALPix map is calculated with the following (from [150]):

$$N_{pix} = 12N_{side}^2 \tag{6.1}$$

which results in pixels of the same area:

$$\Omega_{pix} = \frac{\pi}{3N_{side}^2} \tag{6.2}$$

A plot of a few common pixelizations is shown in Figure 6.1. The unbinned likelihood is evaluated at the center of each pixel. Each pixel, representing a GRB position, will have a test statistic, and that test statistic is the result of contributions from the individual neutrinos across the sky.

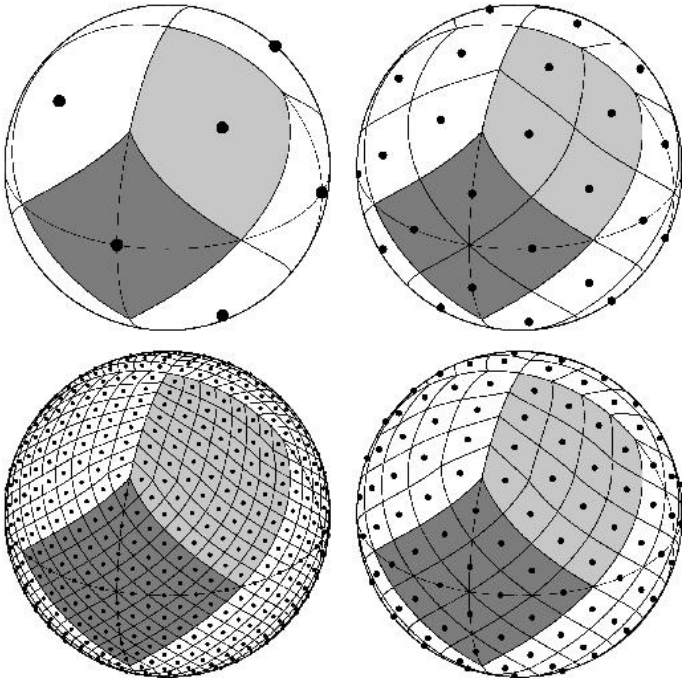

Figure 6.1: An example of a sphere divided into 12, 48, 192, and 768 pixels. There are 196,608 pixels in the maps used for this analysis (N_{side}=128). Figure from [147].

6.2 Probability Density Functions (PDFs)

Probability density functions (PDFs) describe an expected distribution of values of a continuous random variable. A PDF is defined to have its integral equal to 1, and therefore provides a relative likelihood. It is important to understand that a PDF plot, such as Figure 6.4, may have a distribution of values that appears to lead to a total probability greater than 1. The variable is continuous, and integrating that continuous function leads to a value of 1. A spline is fit to the PDFs to provide an instantaneous value at every point.

PDFs are generated for the energy, space, and time of background (atmospheric muons and neutrinos) and signal (astrophysical neutrinos). These six PDFs are used to determine the probability of an event being of astrophysical origin. Because the

PDFs offer relative likelihoods (rather than absolute likelihoods), the ratio of signal to background is used (see 6.8). The signal and background PDFs are combined for each event:

$$S(x) = S_{space}(\vec{x}) \times S_{time}(t) \times S_{energy}(E, \delta) \tag{6.3}$$

$$B(x) = B_{space}(\vec{x}) \times B_{time}(t) \times B_{energy}(E, \delta)$$

where δ indicates the declination-dependence of the energy PDF. The background PDFs show distributions in energy, time, and space for typical atmospheric neutrinos. When the background is well-understood, there is a good separation between signal and background events. This leads to an understanding of what to expect from background-only fluctuations without any signal (i.e. the Null Hypothesis) [151]. The signal PDFs are predicted distributions in energy, time, and space based on Monte Carlo simulation. The signal PDFs also include several assumptions, such as the energy spectrum from a source. In this analysis, an E^{-2} energy spectrum is assumed for neutrinos produced in a GRB.

The background energy PDF is constructed from data, which is intended to represent the atmospheric neutrino spectrum. This is not a perfect representation for several reasons. First, there is significant contribution from cosmic-ray muons, particularly in the southern sky. Second, the PDF is constructed from reconstructed muon energy, which is a lower bound on the true neutrino energy. The reconstructed muon energy is used, because the neutrino (and therefore its energy) is not measured

directly. Finally, the events included in data must pass a series of cuts, which means the fluxes are scaled by the effective area of the detector at the final processing level. The background energy spectrum is softer than that of signal, with many low-energy events predicted and a steep drop at higher energies. A spline fit to the data is used as the actual background energy PDF. These splines are done per-declination using the same $sin(\delta)$ bins in the space PDFs in Figure 6.4. These splines are shown for a few declinations in Figure 6.2. There are very clear differences between the northern and southern sky (see 5.2), which is why the declination-dependent PDF is most appropriate.

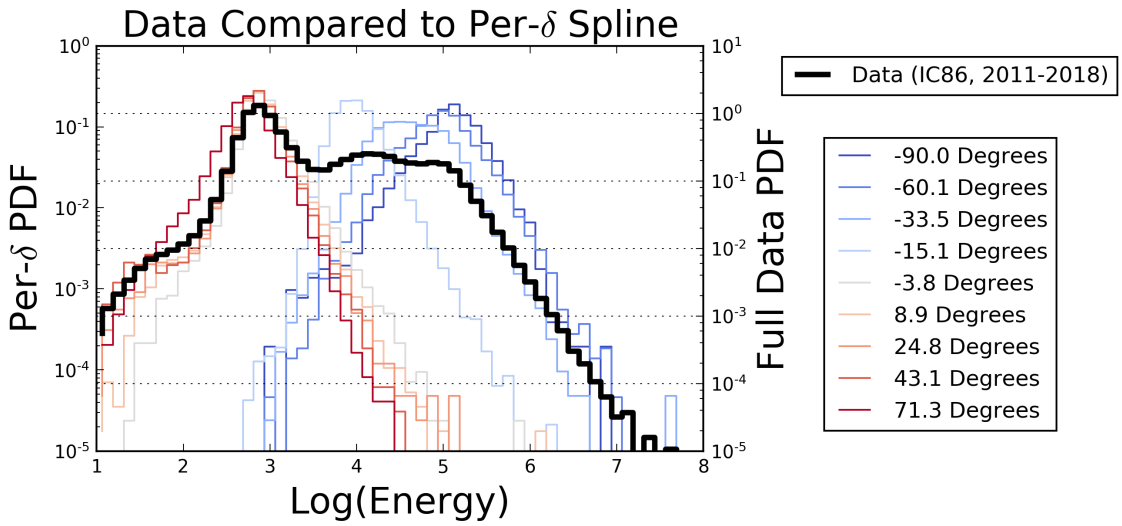

Figure 6.2: The reconstructed energy from data is used to make the background energy PDF in this analysis. A spline is fit to the data for the actual PDF values at different declinations. The solid black line shows the full data binned by energy, and the color-coded lines show the spline fits (the actual PDFs) at a few representative declinations.

The signal energy PDF is the assumed spectrum of astrophysical neutrinos. In GRB analyses, this is assumed to be E^{-2} (see 3.1.2). The PDF is parametrized from the reconstructed (or "proxy") energy distribution of events from a simulated E^{-2}

spectrum. Figure 6.3 shows the ratio of the signal energy PDF to the background energy PDF at a few representative declinations.

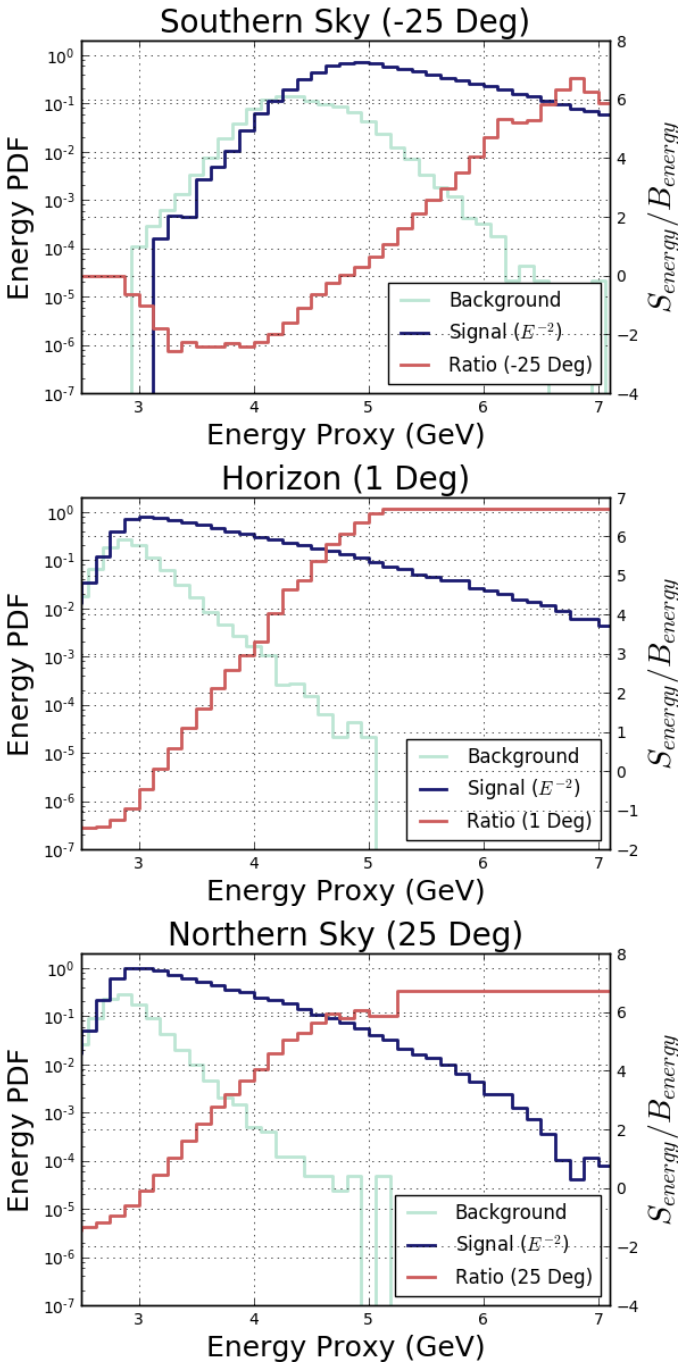

Figure 6.3: These three plots show how the ratio of the signal energy PDF to the background energy PDF varies with declination.

The time PDF is relatively straightforward. The background time PDF is

assumed to follow a uniform distribution across the analysis time window, because background events can be independently produced at any time. The signal PDF is a uniform box, meaning the PDF value is constant when the events falls within the time window and 0 when they fall outside the time window. Previous GRB analyses [17] [90] [145] in IceCube have tried to soften the boundary by using a Gaussian tail for a falling PDF value at both ends of the time window. Those analyses were limited to the prompt phase of the GRB and used the Gaussian tails to extend beyond the T_{100} with a reduced weight in case there were neutrinos near the boundary edge. For this analysis, a box time profile is sufficient because several time windows are included that extend far beyond the typical time of a GRB's gamma-ray emission. This ensures signal neutrinos will not be missed if they are close to (but not coincident with) the time of the GRB. The specific time windows, and the accompanying compuational complications, are discussed in detail in 7.4.

The background space PDF is created from data and expressed in Equation (6.4). To first order, IceCube is assumed to have azimuthal symmetry, which means the background is uniform within a declination band. There is some azimuthal anisotropy present in IceCube, but the effects get smoothed out as the detector rotates over long time windows. A spline fit to a histogram of $\sin(\delta)$ is enough information for a background space PDF, and the specific source location does not matter beyond the declination band [151]. This is shown in Figure 6.4, where the northern and southern sky have been split to emphasize the difference.

The background space PDF is given by:

$$B\left(\delta_i, \phi_i, \sigma_i\right) = \frac{1}{2\pi} P\left(\delta_i\right) \tag{6.4}$$

where δ_i is the declination of the event being considered. Note that although the right ascension, ϕ_i, and the angular error, σ_i, of the event do not contribute to the background spatial likelihood, this information will be highly relevant to the signal spatial PDF.

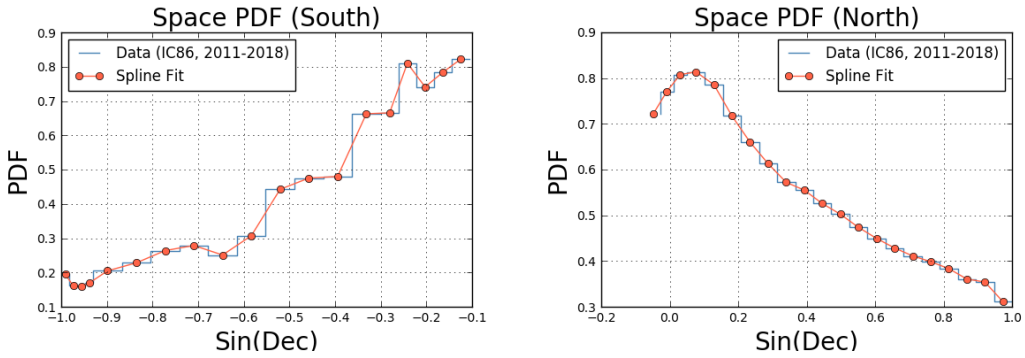

Figure 6.4: The real data is used to make the background space PDF in this analysis. A spline is fit to the data for the actual PDF values. The southern sky (left) ranges from $-90° < \delta < -5°$ and the northern sky (right) covers $-5° < \delta < 90°$.

The probability of detecting neutrinos at particular energies varies dramatically across the sky. Figure 6.5 demonstrates the difference between the northern and southern sky in terms of energy and declination. The northern sky is shielded by the Earth, which becomes opaque to high-energy neutrinos because their interaction cross-section increases with energy. The highest energy neutrinos are only observable from the southern sky where there is no such shielding.

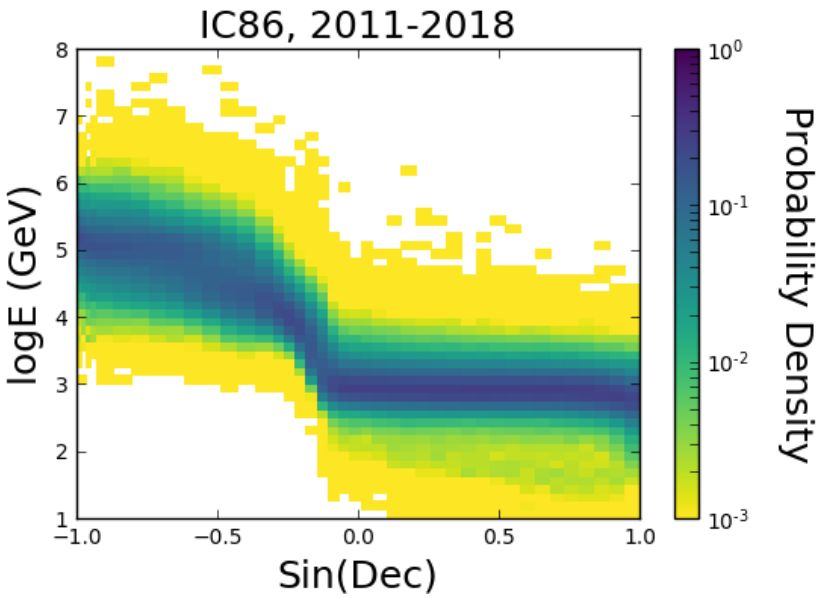

Figure 6.5: This figure shows a 2D histogram of the data by energy and declination. The northern sky ($\sin(\delta)$ greater than 0.087) shows a higher probability of seeing neutrinos up to tens of TeV, while the southern sky expects energies up to the PeV range.

The signal space PDF is a 2D Gaussian, meaning the probability of an event being spatially correlated with a GRB drops off with Gaussian probability [146].

$$S\left(\vec{x}_i, \sigma_i | \vec{x}_{src}\right) = \frac{1}{2\pi\sigma_i^2} e^{-\frac{|\vec{x}_i - \vec{x}_{src}|^2}{2\sigma_i^2}} \tag{6.5}$$

where $\vec{x}_i$ is the reconstructed direction of the neutrino in right ascension and declination, σ_i is the uncertainty on that reconstructed neutrino direction, and $\vec{x}_{src}$ is the position of the GRB [146]. In this analysis, the GRB position uncertainty is often quite large. In that case, many positions on the sky have test statistics calculated and a penalty is applied after the test statistic calculation. This is described in more detail in 7.5.

6.3 Log Likelihood

The PDFs described in the previous section get combined following Equation 6.3. Equation 6.3 includes x_i to represent all the event characteristics (space, energy, and time) for each candidate neutrino (indicated by i). The individual event probability densities are multiplied together to get the overall likelihood of the data:

$$L(n_s|n_b, x_i) = P_N \prod_{i=1}^{N} [p_s S(x_i) + p_b B(x_i)] \tag{6.6}$$

The probabilities are then $p_s = \frac{n_s}{n_s+n_b}$ and $p_b = \frac{n_b}{n_s+n_b}$, and n_s and n_b are the number of expected signal and background counts, respectively. Given these expected signal and background counts, P_N is the Poisson probability of the total observed event count:

$$P_N = \frac{(n_s + n_b)^N e^{-(n_s+n_b)}}{N!} \tag{6.7}$$

If we write this out fully, it is clear we can remove the $(n_s + n_b)^N$ term from outside and the $\frac{1}{n_s+n_b}$ from inside the product:

$$L = \frac{\cancel{(n_s + n_b)^N} e^{-(n_s+n_b)}}{N!} \prod_{i=1}^{N} \left[\frac{n_s}{\cancel{n_s + n_b}} S(x_i) + \frac{n_b}{\cancel{n_s + n_b}} B(x_i) \right]$$

The next step is to take the log of the likelihood, which is where we get the shorthand "log likelihood" (or "LLH"). Note that a log of a product will become a

sum.

$$\ln(L) = \ln\left(\frac{e^{-(n_s+n_b)}}{N!}\prod_{i=1}^{N}\left[n_s S(x_i) + n_b B(x_i)\right]\right)$$
$$= -n_s - n_b - \ln(N!) + \sum_{i=1}^{N}\ln\left[n_s S(x_i) + n_b B(x_i)\right]$$

The test statistic is the ratio of the likelihood with the best-fit $\hat{n}_s$ and the likelihood with $n_s = 0$.

$$TS = \ln\left[\frac{L(\hat{n}_s)}{L(n_s = 0)}\right]$$
$$= \ln(L(\hat{n}_s)) - \ln(L(n_s = 0))$$
$$= -\hat{n}_s - \cancel{n_b} - \cancel{\ln(N!)} + \sum_{i=1}^{N}\ln\left[\hat{n}_s S(x_i) + n_b B(x_i)\right]$$
$$- \left(-\cancel{n_b} - \cancel{\ln(N!)} + \sum_{i=1}^{N}\ln\left[n_b B(x_i)\right]\right)$$
$$= -\hat{n}_s + \sum_{i=1}^{N}\ln\left[\frac{\hat{n}_s S(x_i) + n_b B(x_i)}{n_b B(x_i)}\right]$$
$$= -\hat{n}_s + \sum_{i=1}^{N}\ln\left[\frac{\hat{n}_s S(x_i)}{\langle n_b\rangle B(x_i)} + 1\right]$$

Finally, the log likelihood ratio is maximized with respect to n_s to find the test statistic. The PDFs and likelihood can be combined into a single test statistic to determine if an event is more likely created in Earth's atmosphere (background)

or beyond (signal). Here, $\hat{n}_s$ indicates the fit value of n_s that maximizes the LLH.

6.4 The Test Statistic and Frequentist Method

The previous section outlined the steps to obtain the test statistic:

$$TS = \ln\left[\frac{L(\hat{n}_s)}{L(n_s = 0)}\right] = -\hat{n}_s + \sum_{i=1}^{N} \ln\left[\frac{\hat{n}_s S(x_i)}{\langle n_b \rangle B(x_i)} + 1\right] \tag{6.8}$$

This log likelihood ratio combines information about expected signal and background data, producing a number that indicates if the observed events at a location on the sky is more signal-like or more background-like. Unfortunately, it is not so simple to declare if a point on the sky is signal-like. The analysis described in this thesis uses a frequentist approach to the calculation of signficance. The basic idea is to determine baseline background behavior using scrambled data (see 7.5 for a description of scrambles) and see how far the real (unscrambled) data strays from that baseline. If the real data is very similar to the baseline, then it is considered consistent with background. If the data is very different, then it is said to be inconsistent with background. The background is sometimes referred to as the "null hypothesis" because there is no injected signal. Instead of claiming a result is signal-like to some extent, the goal is to reject the null hypothesis as strongly as possible.

The first step is understanding the background, meaning a dataset with no signal[2] in it. The baseline behavior of the data must be understood for each GRB

[2]This analysis assumes that the diffuse neutrino flux measured by IceCube is present in the dataset, and is testing whether it is correlated with GRBs (signal-like) or not (background-like).

in order for the test statistic to have any meaning. The frequentist approach is to calculate the test statistic for the same GRB using different realizations of background-only data. If this is repeated many times (at least 10^4 scrambles) then the random fluctuations in background data will lead to different test statistics. This group of many test statistics is called a test statistic distribution. Figure 6.6 shows an example test statistic distribution for a well-localized GRB (position uncertainty $<1^\circ$) at a few different time windows. For very short time windows, most test statistics are zero, but the longer time windows begin to have a very clear tail of non-zero test statistics.

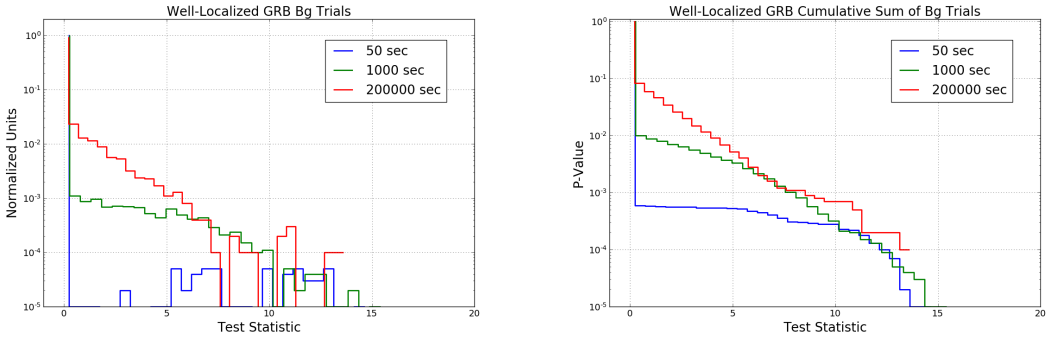

Figure 6.6: This plot shows the shape of test statistic distributions (left) and their cumulative sums (right) for a well-localized GRB near the horizon at three different time windows. Short time windows have almost all test statistics equal to zero, while longer time windows have more nonzero test statistics.

It is clear from Figure 6.6 that $TS = 5$ means something very different for the three time windows. Now that there are many test statistics clarifying the expectation of the background, it is much easier to make a statement about the significance of a measured test statistic. The p-value can be read off the cumulative sum (the plot on the right in Figure 6.6). The p-value is the fraction of test statistics above the threshold value (i.e., the measured TS value). If the measured test statistic

is, for example, the tenth highest test statistic out of 10^4 trials, then the p-value would be: $P = \frac{10}{10^4} = 10^{-3}$. A p-value of 10^{-3} is close to a 3σ result, which would certainly be considered interesting in the context of a neutrino-GRB analysis. In this case, σ refers to a standard deviation of a standard normal distribution. The p-value can be determined for any test statistic by comparing it to the rest of the test statistic distribution (or reading it off the y-axis of a cumulative sum).

When constructing an analysis, it is important to set expectations for the unblinded results, including sensitivity and discovery potential. The idea behind these terms is to set thresholds in advance that identify a potentially interesting result. A sensitivity is defined as the amount of signal present such that 90% of test statistics are greater than the median of the background-only test statistic distribution. In other words, this is the median 90% upper limit one would set if there were no signal observed in real data. This does not mean the unblinded data must be measured many times. The sensitivity threshold is found by injecting simulated signal into scrambled data, and increasing the amount of injected signal, until a distribution is created with 90% of trials above the median background test statistic. This threshold represents an amount of signal that would make the unblinded data *just different enough* from the expected background that there are hints of signal present in the data. For a GRB analysis, a sensitivity can be difficult to define because most background-only test statistics are zero. A stronger threshold is required to truly identify signs of signal present in the data.

A discovery potential is a much stronger threshold, and typically refers to an amount of signal present such that 50% of the test statistics are greater than the

5σ test statistic of the background-only test statistic distribution (in other words, 99.99998% of test statistics). In the realm of particle physics, where one may be looking for evidence of a new particle, the burden of proof is far higher because the existence and detection of the particle must be demonstrated. The diffuse neutrino flux, on the other hand, has already been demonstrated beyond 5σ. A true discovery is still expected at the 5σ threshold, but if any portion of this analysis (a single GRB p-value or a binomial p-value) passed the 3σ threshold (99.865% of trials) then it would still be a noteworthy result.

The injected signal refers to an amount of neutrino flux generated by the GRB (see 5.3.2). This is also discussed as time-integrated flux as well. Figure 6.7 shows the passing fraction versus injected flux, which determines the sensitivity of an example GRB in a given time window.

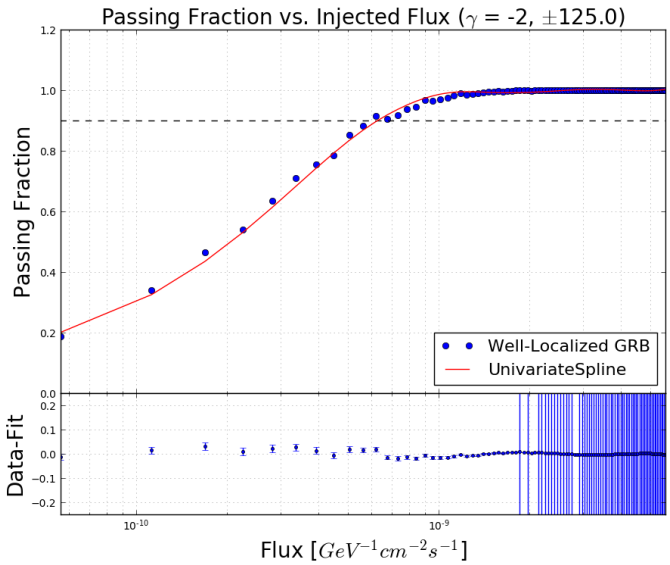

Figure 6.7: This curve shows the flux injected to determine the sensitivity for an example well-localized GRB. The y-axis shows the fraction of test statistics greater than the median of the background-only test statistic distribution. The background test statistic distribution has 10^5 trials and the injected signal distributions have 300 trials per point. In this example, the analysis is sensitive to a flux of 6.7×10^{-10} GeV^{-1}cm^{-2}s^{-1}.

Figure 6.7 shows the result of the method to determine the sensitivity for a single time window for a GRB. This can be repeated for every time window to demonstrate how the sensitivity and discovery potential change with time window. The flux from the x-axis of the passing fraction plot is often re-written as E^2F, which has units of GeV $\cdot$ cm^{-2}:

$$E_0^2 F = E_0^2 \int \Phi dt \tag{6.9}$$

where Φ is the flux injected as signal, t is the time of signal injection, which is assumed to be the entire time window, and E_0 is 1 TeV. F is known as the time-integrated flux.

It is important to note that the 3σ discovery potential can be very close to the sensitivity for shorter time windows because of the pile-up at test statistics equal to zero. The typical GRB test statistic distribution has a median background TS of 0 and relatively few nonzero TS values in the tail. When considering a 3σ discovery potential, the 3σ threshold TS value may be quite close to zero. This may lead to a situation where it requires more injected signal to get 90% of trials greater than zero compared to only 50% of trials above a TS slightly greater than zero. Therefore, it is often easier to show a modified 3σ discovery potential where 90% of trials are above the background-only 3σ value. Figure 6.8 shows this for an example GRB roughly 10° north of the horizon.

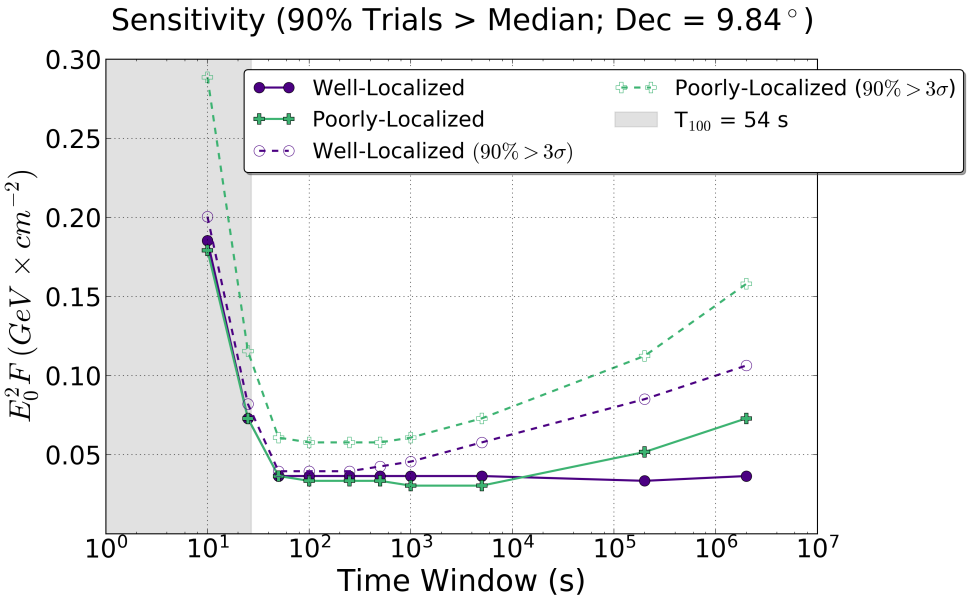

Figure 6.8: This plot shows the neutrino time-integrated flux sensitivity and modified 3σ discovery potential for an example GRB that is poorly-localized (GRB 180423A) compared to a simulated well-localized GRB centered at the same declination (9.84°). The solid lines show the sensitivity and the dashed lines show the 90% above the background-only 3σ. This GRB had a T_{100} of 54 seconds, making it a northern sky long GRB.

It is important to study how this sensitivity changes with time window and

declination. Figure 6.9 shows this behavior for a few example time windows. The behavior is clear with respect to declination: the northern sky is an order of magnitude more sensitive than the southern sky, with the most sensitive region within 10° of the horizon. The difference between time windows is more significant for the 3σ discovery potential, while the sensitivities remain quite similar, even for drastically different time windows.

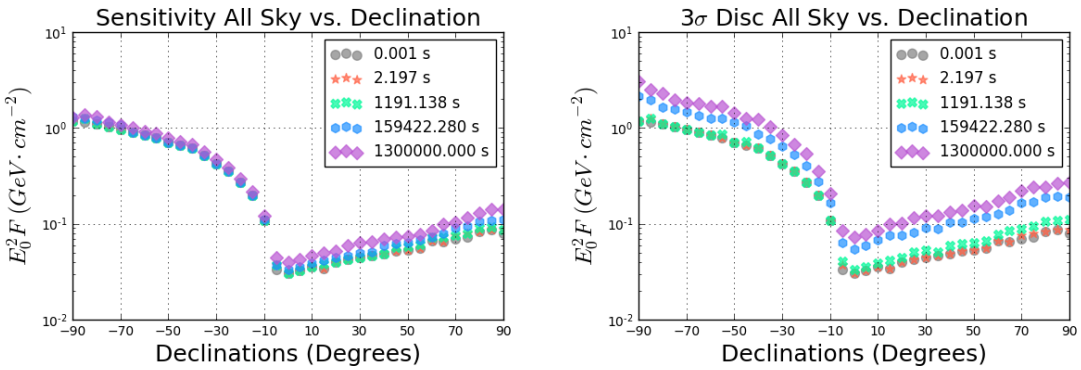

Figure 6.9: The different colors represent a range of time windows, from a fraction of a second out to two weeks. For sensitivity, this has very little impact on the time-integrated flux. For discovery potential, the impact is more significant, but is still less pronounced than the impact of declination. The southern sky is an order of magnitude less sensitive than the northern sky.

6.4.1 Stacked Test Statistic

The test statistic described in this chapter considers events on the sky within a specific time window, contributing to a test statistic for a single GRB. Another common approach is to consider the events within specified time windows of *many* GRBs, all of which contribute to a test statistic for a collection of GRBs. This is known as a "stacked" test statistic.

Equation 6.8 is still valid, and now i runs over all events on-time with any of

the GRBs. The stacked test statistic is not used in the pre-unblinding portion of this analysis. The purpose of the stacked test statistic is to set limits on the collection of GRBs post-unblinding if no significant results are found from individual GRBs or the Binomial test (described in the next chapter).

Chapter 7: Eight-Year Analysis Details

7.1 Overview

The goal of this analysis is to study 2,091 GRBs over the time period from May 2011 - October 2018 individually and as an ensemble. This is accomplished by searching for coincident neutrino emission from each GRB at 10 time windows, determining the most significant of those time windows using the frequentist methods described in section 6.4, and running a Binomial test on the collection of p-values to understand if the entire set is significant. This chapter outlines the details required to run these tests, including the complicated procedure of evaluating each GRB using HEALPix maps and pre-generated all-sky scans.

In particular, section 7.5 explains how the test statistic distribution is created for each GRB, including those with complicated probability maps. In addition to the log likelihood and test statistic procedure explained in section 6.1, a penalty is applied to each test statistic based on its proximity to the GRB position.

Figure 7.1 gives an overview of the analysis steps. Each step in this diagram is explained in detail in this chapter.

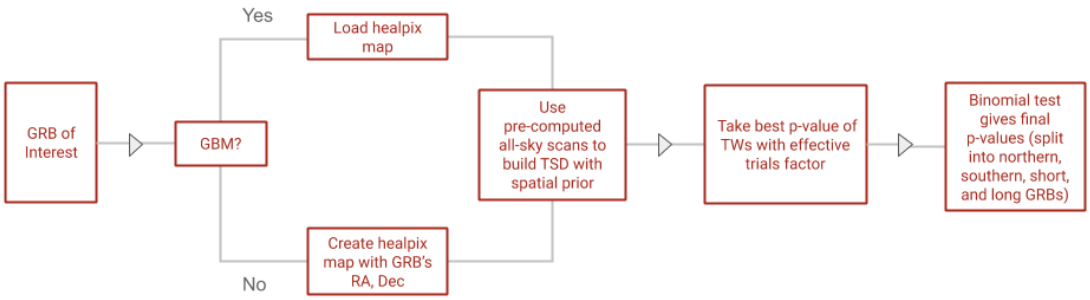

Figure 7.1: This flow chart outlines the steps in this analysis. Each GRB is considered individually. If the burst's position was *only* detected by the Fermi-GBM satellite, then the HEALPix map provided by the Fermi Collaboration is loaded and used as a probability map for the GRB. If the burst's position is not determined by GBM (or is determined by GBM and also a satellite with better localization), then a HEALPix map is generated using the source position uncertainty provided by GRBweb (with a minimum of 1°). The pre-computed all-sky scans are used to build a test statistic distribution for each time window (TW) and the most significant p-value is selected to represent the GRB. A Binomial test is performed on these final p-values to determine the significance of the collection of p-values.

7.2 GRB Catalog

GRBs were selected for this analysis if they fell within the dates of the neutrino dataset described in chapter 5, and if they had a measured start and stop time in GRBweb (see section 2.3.2). 2,125 GRBs met these criteria; however, 34 of those GRBs were localized solely by Fermi-GBM but did not have a HEALPix map (6.1.1). These 34 GRBs were not included in this analysis and have been noted for study in the near future when the Fermi team can re-run their analysis. This led to a final

Sub-Population	Number of GRBs	Percent of Catalog
Northern Long	960	46%
Northern Short	183	9%
Southern Long	814	39%
Southern Short	134	6%

Table 7.1: The number of GRBs in each sub-population out of a total of 2,091. Short GRBs have a $T_{90} \leq 2$ seconds, while long GRBs have $T_{90} > 2$ seconds. The southern sky has a declination of $\delta < -5^{\circ}$ and the northern sky has $\delta \geq 5^{\circ}$. GRB information from GRB Web [62].

catalog of 2,091 GRBs.

These 2,091 GRBs are split into four-subpopulations. The first split is by short and long GRBs, because they are commonly thought to have different progenitors (see section 2.2). The second split is by the northern and southern sky at a declination of $\delta = -5^{\circ}$. This was done because of the dramatic difference in sensitivity of our analysis between the northern and southern sky. Figure 7.2 shows the clear declination-dependence of the sensitivity for a well-localized GRB, which motivates the split into northern and southern sky sub-populations. Another reason to split the GRBs by hemisphere is the expected neutrino energy. The southern sky has no shielding from Earth, which means higher energy neutrinos will reach the detector that would otherwise interact in rock and never send photons into the ice.

All GRBs are searched with the same time windows, regardless of the T_{100} duration. The T_{100} is defined by the earliest reported start time and the latest reported stop time from any satellite for the given GRB, even if those values are from different satellites. The final p-values are divided into four sub-populations for a binomial test, which means the result of this analysis is four binomial p-values. The breakdown of GRBs by sub-population is given in Table 7.1.

7.3 Sensitivity

Section 6.4 describes the method to determine the sensitivity of a GRB from frequentist statistics. Figure 6.8 shows an individual GRB's sensitivity over ten time windows. The following plots show the sensitivity for a broader range of GRBs. Figure 7.2 considers many different declinations and time windows for a well-localized GRB and shows the splined sensitivity. The sensitivity is roughly flat along time windows and shows an order of magnitude difference in sensitivity between northern and southern sky.

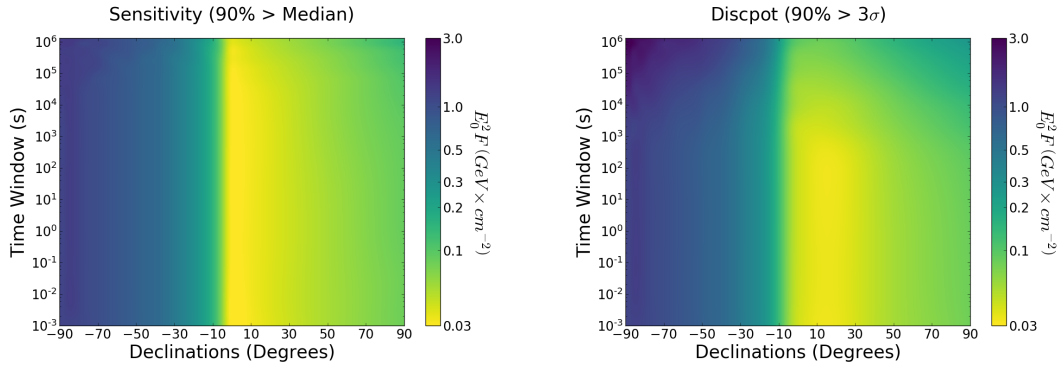

Figure 7.2: This figure shows the sensitivity (left) and 3σ discovery potential (right) of a well-localized GRB (position uncertainty $< 1°$) and the strong declination-dependence of that sensitivity. As section 6.4 explains, the sensitivity is defined as the amount of time-integrated neutrino flux required for 90% of trials to have a test statistic above the median background-only TS value. The 3σ discovery potential is the same, with the requirement that 50% of trials be above the 3σ test statistic of the background-only distribution. This plot indicates this analysis is consistently sensitive along a given declination until the very longest time windows. The analysis is less sensitive at the very longest time windows and the most extreme northern and southern declinations.

The relatively constant sensitivity along a given declination is the result of the low background rate in this dataset. 6-7 events are expected on the entire sky every 1,000 seconds, which means the $1°$ circle around a well-localized GRB has an

expected background of zero events until very long time windows. Figure 7.3 shows the number of events in the dataset in a 1° circle at a given declination and time window, as well as the number of events in a 1° declination band for a given time window. Even with an entire declination band, there are very few events until the very longest time windows.

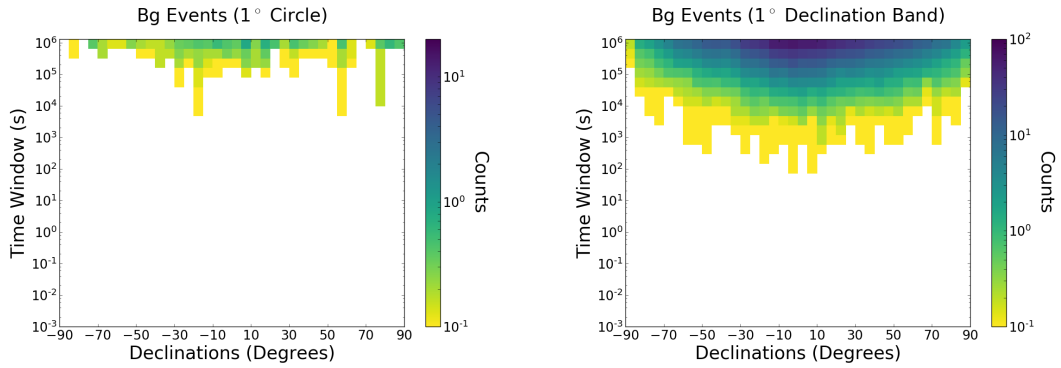

Figure 7.3: This figure demonstrates the low expected background for well-localized GRBs by considering the number of events in a 1° circle (left) and a 1° band (right) around each declination for a given time window. The counts in each bin are averaged over many times in the dataset to wash out effects from seasonal variation.

Figures 7.4 and 7.5 show the differential sensitivity for example declinations in the northern sky, southern sky, and near the horizon. The differential sensitivity is found by injecting signal within specific energy bins. The horizon is the most sensitive region in all time windows. The northern sky is more sensitive than the southern sky for events below 1 PeV. Above 1 PeV, the southern sky is dramatically more sensitive than the northern sky, but still loses out to the horizon.

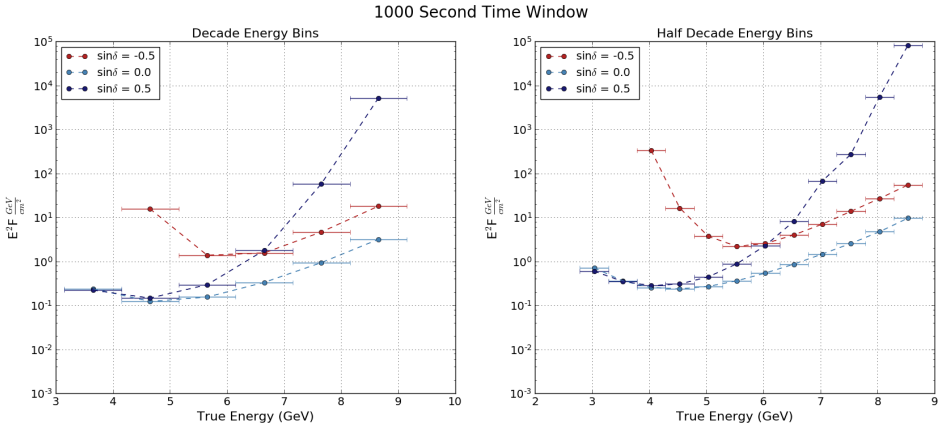

Figure 7.4: Left: Differential sensitivity over decade energy bins for an example GRB in the northern sky, southern sky, and horizon for a 1000 second time window. Right: Differential sensitivity for half-decade bins in the same regions and time window.

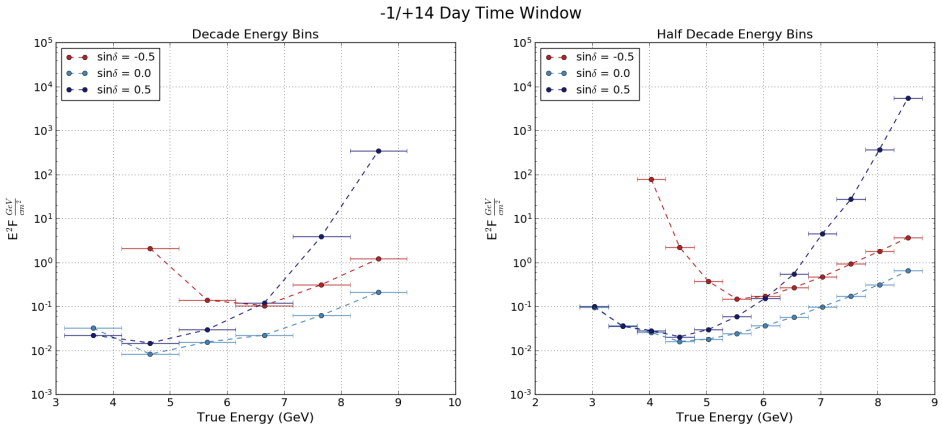

Figure 7.5: Left: Differential sensitivity over decade energy bins for an example GRB in the northern sky, southern sky, and horizon for a -1/+14 day time window. Right: Differential sensitivity for half-decade bins in the same regions and time window.

7.4 Extended time windows

Every GRB has ten identical time windows tested, based on the center of the GRB's T_{100}. The first nine time windows are symmetric, ranging from ±5 seconds to ±1 day. The final time window is asymmetric, searching from -1 day to +14

days. The time windows were chosen to finely sample the most common T_{100} times, while also stretching out to -1 day/+14 days. All ten time windows are tested, including ones shorter than the T_{100} of the GRB, which will make this analysis translate smoothly into a realtime follow-up for GRBs with the IceCube detector. A cartoon of these time windows is shown in Figure 7.6.

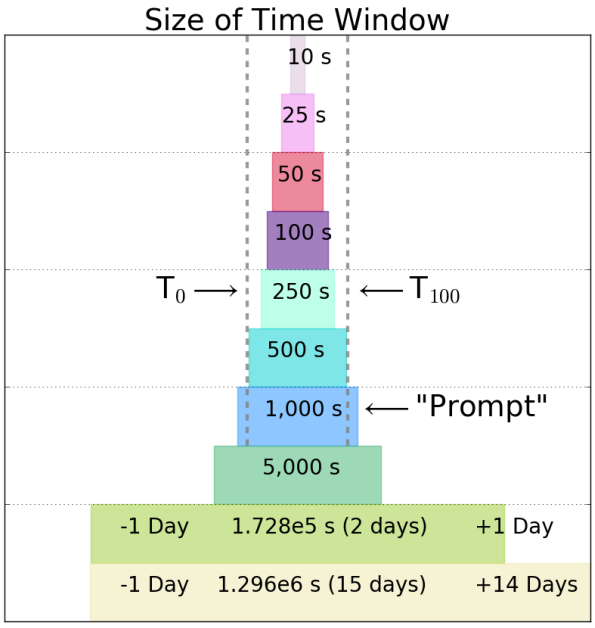

Figure 7.6: Cartoon illustration of time windows used in this analysis. Grey dashed lines indicate the T_0 and T_{100} of a hypothetical GRB.

All of the 2,091 GRBs in this search have a T_{100} of less than 1,000 seconds. Figure 7.2, and the plots in section 6.4, show the sensitivity is quite flat in this region, even for poorly localized GRBs. Figure 7.3 illustrates the low expected background, especially in shorter time windows. The shortest time window chosen for this analysis is 10 seconds, which is sufficient to study the shorter time windows as well due to the low background.

These time windows were chosen to minimize the amount of background being let in by choosing the shortest pre-defined time window to represent the T_{100}. Figure 7.7 shows the short and long GRB distributions in terms of the T_{100}. The black and red dots above show options of time windows considered to illustrate how the final (red) time windows were chosen. The evenly spaced time windows were initially considered; however, the clustered time windows sample the most common T_{100} values more finely and let in less background (see Figure 7.8).

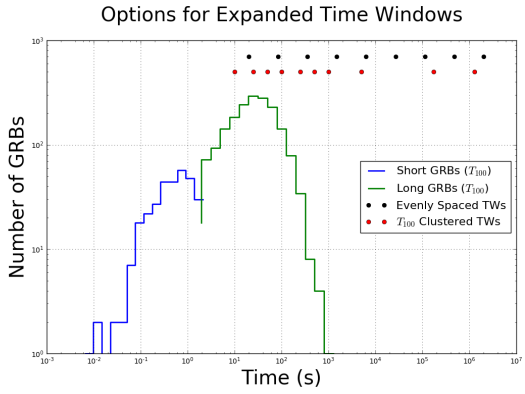

Figure 7.7: The GRB distributions and the chosen time windows for this analysis (red) compared to evenly spaced time windows (black).

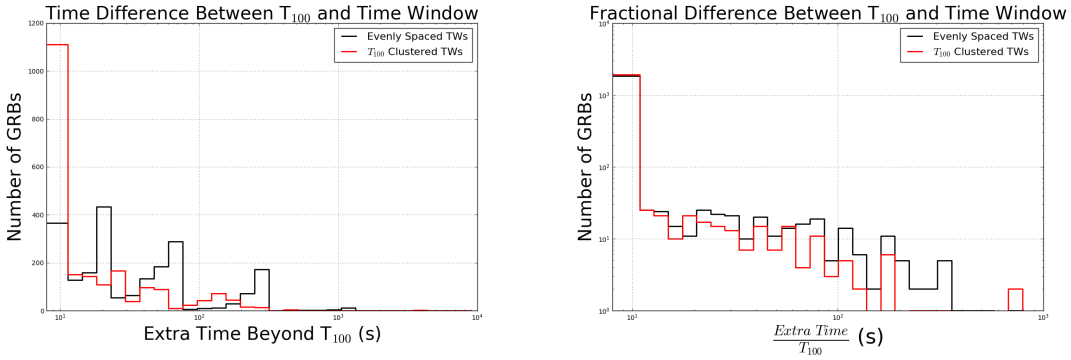

Figure 7.8: Left: the difference between the T_{100} and prompt time window (shortest pre-defined time window that fully includes the t_{100}). Right: the fractional difference between the T_{100} and prompt time window.

Both Figures 7.7 and 7.8 show the clustered time windows do a better job

of reducing extra background resulting from the pre-defined time window method. Although both sets of time windows seem to ignore the short GRBs, the background is effectively zero at these times, and the 10 second time window is sufficient to study these short GRBs. While the discovery potential may improve for a neutrino landing in an extremely short time window, the goal of this analysis is not to *miss* any possible neutrino-GRB correlation. Including another time window would simply add to the computational requirements and trials factor with minimial gain.

The final three time windows were selected to search for precursor and afterglow neutrinos. 5,000 seconds, two days, and fifteen days were chosen as these longer time windows. The purpose of the longer time windows is to catch a possible excess of neutrinos while the background rate from data is still relatively low. For a well-localized GRB, the sensitivity remains quite flat out to several weeks (see Figure 7.2). A poorly-localized GBM burst may become overwhelmed with background after a few days. All the time windows are extended symmetrically around the center of the GRB's T_{100} up to +/-1 day. The longest time window (15 days) is asymmetric, scanning -1/+14 days. The choice to emphasize the afterglow on the longest timescale is due to the potential for higher energy neutrinos. Some models predict GeV-TeV neutrinos in the precursor stage and $>$ PeV neutrinos in both the prompt and afterglow phase [152]. Unfortunately, GeV-TeV neutrinos are difficult to separate from background, and a one-day timescale is long enough to begin seeing coincidence from random chance at those energies. PeV neutrinos are far more likely to be astrophysical and can be distinguished from background, even over longer timescales.

7.5 Pre-Generated All-Sky Scans

This analysis requires that an unblinded test statistic, along with a test statistic distribution from scrambled data, is calculated for each time window shown in Figure 7.6. This allows for the calculation of a p-value for each time window as well[1]. However, producing that much scrambled data would take hours to days for each GRB, especially for the longer time windows and poorly localized GRBs. Instead of making new trials every time, this analysis takes advantage of all-sky scans that are generated in advance to build the test statistic distributions. This method is only possible because the ten time windows are fixed; if the time windows varied depending on the duration of the GRB T_{100}, then it would be impossible to use pre-computed all-sky scans[2]. Pre-generated all-sky scans speed up the analysis to approximately 20 minutes per GRB, compared to hours or days of generating trials without the scans.

An all-sky scan begins with the full neutrino candidate dataset randomly scrambled by time (with new right ascensions calculated). A random selection of that scrambled data is then chosen based on the time window. For example, the shortest time window selects 10 seconds of that scrambled data. For most of the all-sky scans, there will be no events on the sky in a random 10 seconds. An example all-sky scan for 5,000 seconds of data is shown in Figure 7.9, because this is enough time to have several neutrinos appear on the sky. The HEALPix skymap shows the

[1] Narrowing down from ten p-values to one p-value requires a trials correction, which is explained in section 7.6.

[2] Or we would need enough all-sky scans to cover every possible T_{100} time.

test statistic calculated at each pixel on the sky based on the on-time neutrinos.

These all-sky scans were generated before unblinding this analysis. One all-sky scan yields one test statistic for the background test statistic distribution. 10^4-10^6 trials were generated for each time window. The +/-1 day and -1/+14 day time windows take 2-3 minutes to combine 10^4 all-sky scans with a GRB map. The 50-5,000 second time windows are somewhat faster and have 10^5 scans for their test statistic distributions in roughly 1 minute. The shortest time windows require less than one minute to combine scans and the GRB map, which allows 10^6 scans. This pre-generated all-sky scan method is fast enough to produce background test statistic distributions (with 10^4-10^6 trials) for all ten time windows in roughly four minutes. Calculating the unblinded test statistic requires scanning over every pixel near on-time events, which is a computationally intensive procedure and lasts another 12-15 minutes per GRB.

Figure 7.9 also shows an example GRB probability map from the Fermi-GBM data. This map shows the source position uncertainty from the GBM data.

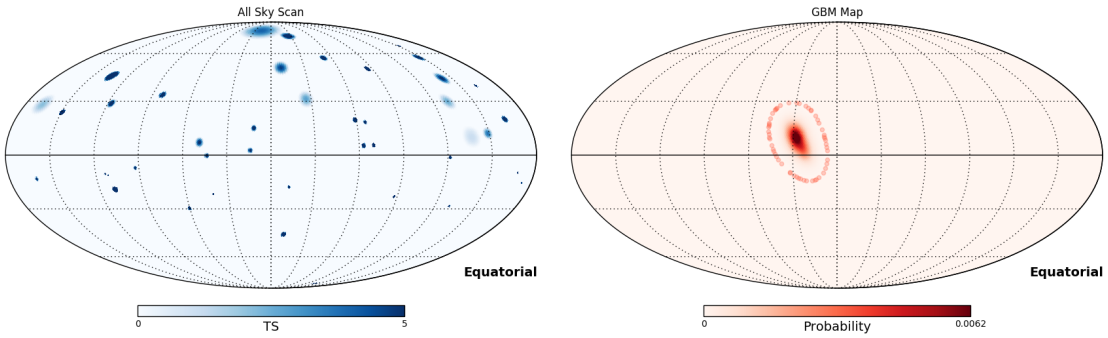

Figure 7.9: Left: An example of 5,000 seconds of IceCube data with a test statistic calculated at every pixel on the sky. Right: An example GBM map with a probability at every pixel on the sky.

The skymaps from Figure 7.9 are combined by applying a penalty to the test statistics based on the proximity of a given neutrino data pixel to the higher probability pixels in the GRB map:

$$TS_{prior} = TS_{original} - TS_{penalty} \tag{7.1}$$

In this equation, $TS_{original}$ refers to the neutrino data from the all-sky scan (left plot in Figure 7.9). $TS_{penalty}$ is the penalty term we wish to apply based on the GRB healpix map (right plot in Figure 7.9). TS_{prior} refers to the final test statistic after the GRB's spatial prior has been applied to the neutrino data (Figure 7.10). The healpix map is provided in terms of p-values rather than test statistics, which means the value of $TS_{penalty}$ is actually $2 \ln P$. Because the probabilities are less than 1, the log of the p-value at the most significant spot will be the largest, but still negative, possible value. The penalty is established so the most significant GRB pixels maintain their original test statistic ($TS_{original}$), and the pixels far from the most likely position of the GRB receieve a large penalty. The penalty is therefore calculated using the following:

$$TS_{prior} = TS_{original} - [-2 \ln(P)] \tag{7.2}$$

$$TS_{prior} = TS_{original} + 2 \times [\ln(P_{GBM}) - \ln(P_{GBM,max})]$$

In this method, the test statistic is not allowed to be negative. After applying the

penalty, the final step to determine a test statistic for this one all-sky scan is to take the maximum test statistic remaining on the sky.

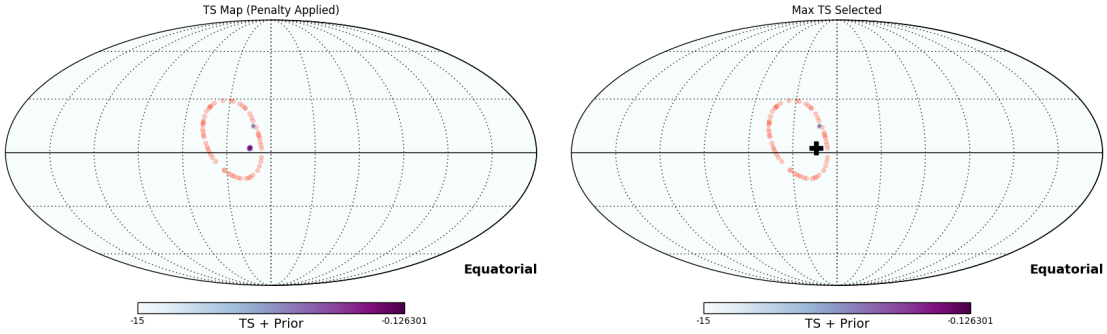

Figure 7.10: Left: The outline of the GRB probability map is shown over the neutrino data, which has the penalty from Equation 7.2 applied. Right: The maximum test statistic for this all-sky scan and GRB is indicated by the plus sign.

Figures 7.9 and 7.10 show the steps to calculate a single test statistic for a GRB in one time window. This process would be repeated 10^4-10^6 times (depending on which time window) to build the entire test statistic distribution. This is done for all ten time windows every time a GRB is analyzed. A few example test statistic distributions are shown in Figure 7.11

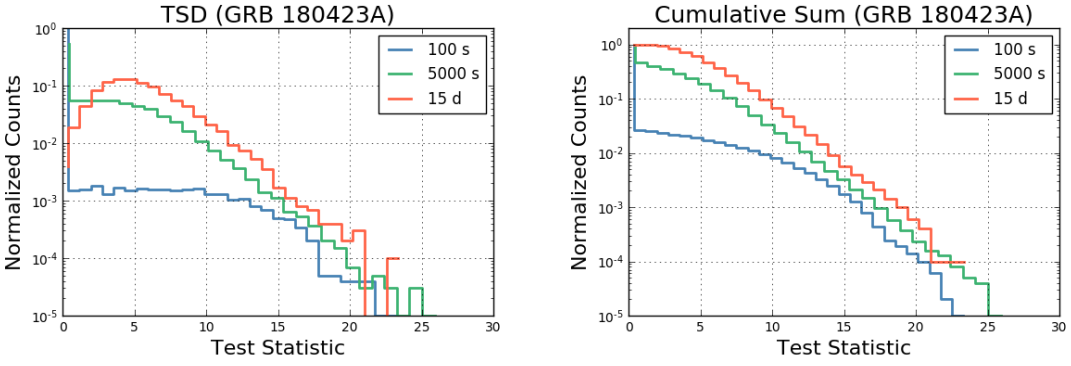

Figure 7.11: Left: The test statistic distribution of GRB 180423A, which has its localization from the Fermi-GBM data. This is the GRB shown in Figure 7.9. Right: The cumulative sum for the same GRB and time windows.

After assembling a test statistic distribution, the unblinded test statistic is

compared to the overall distribution. This is explained in more detail in section 6.4 and illustrated in Figure 7.12.

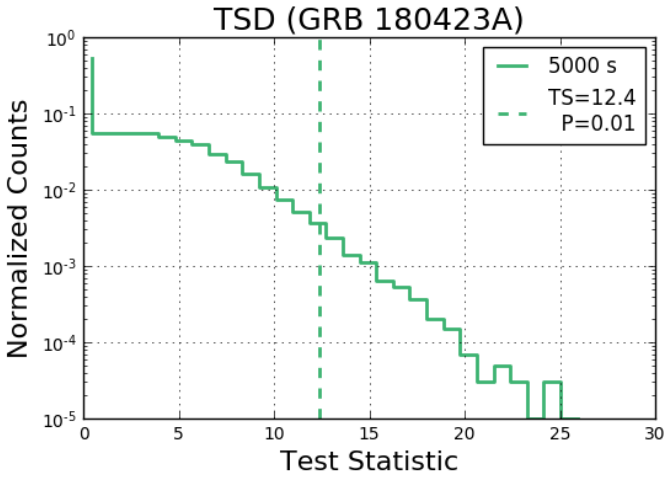

Figure 7.12: The test statistic distribution for the 5,000 second time window of GRB 180423A is shown here. This is a GBM burst, which explains the large test statistic values for a relatively short time window. An example unblinded test statistic is marked with a vertical dashed line. The p-value is found by dividing the number of test statistics larger than the unblinded test statistic by the total in the distribution. For an example test statistic of 12.4, the p-value is 1%.

Previous IceCube GRB analyses have used the T_{100} for the prompt time window of the GRB, plus a small Gaussian tail to soften the time window edge. Using fixed time windows requires an approximation of the prompt time window because the pre-computed scans will only have specific time values. The shortest time window that contains the entire T_{100} is therefore used to esimate the prompt time window. The dashed grey lines in Figure 7.6 show the duration of an example GRB, which has a T_{100} somewhere between 500 and 1,000 seconds. In this example, the 1,000 second time window is considered prompt because it completely contains the T_{100}. The prompt window is only used for setting limits and is not part of determining the most significant p-value for a given GRB.

7.6 Effective Trials Factor

Any time a search is repeated, there is a chance to find a significant result simply by the large number of attempts. For example, having four coins land with heads is quite unlikely if you only flip the coins one time. If you repeat this experiment one million times, then you will certainly have all four coins land heads at some point. One would have to consider the number of coin flips to decide if having all four coins landing heads was statistically significant.

In the case of this analysis, searching ten time windows increases the chances of randomly finding a significant result from pure background. If these were ten independent time windows, then we could simply multiply the most significant p-value by ten and be done. However, these time windows overlap with each other, which means they are not independent. This allows us to determine an effective trials factor that is smaller than ten. The goal is to compare background test statistics against background test statistic distributions, select the most significant of the ten p-values, and understand how this set of p-values compares to a uniform distribution.

To determine the effective trials factor, a separate set of all-sky scans is generated with 10^4 scans in each time window. These scans are carefully controlled to ensure the scrambled data is the same in each time window. This means the data in the 10 second time window is exactly contained in the 25 second time window, and so on. These 10^4 scans are then used to create background test statistic distributions for each time window.

A background-only test statistic distribution is often used to determine the significance of an unblinded test statistic. However, in this situation, the test statistic distributions are used to compare background against background. Each of the 10^4 test statistics is compared to the other 9,999 in the test statistic distribution[3] to calculate 10^4 p-values for each time window. The most significant p-value of 10 time windows is selected for each of the 10^4 trials. This set of background-against-background p-values is then plotted in a cumulative sum (Figure 7.13). This is done for every GRB and the bins of this cumulative sum serve as a look-up table to correct the initial p-value.

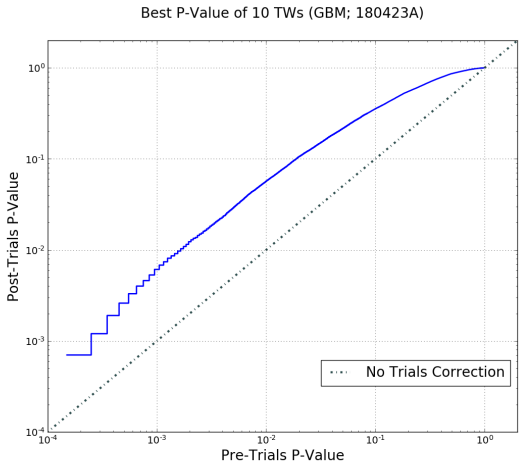

Figure 7.13: Background-only test statistics are compared to background-only test statistic distributions in each time window. The most significant p-value of these ten is selected in 10^4 trials. These p-values are plotted in a cumulative sum to indicate the trials correction needed for this particular GRB. For example, if this GRB initially yielded a most significant p-value of 1×10^{-2} then the result would be closer to 6×10^{-2} after the effective trials correction.

In early versions of this analysis, only one trials correction was used for each GBM burst and one correction was used for all non-GBM bursts. This caused quite a

[3]It would be ideal to have one set of 10^4 scans for the TSD and another for each of the 10,000 test statistics, but this requires a prohibitive amount of CPU time.

few problems with the p-values, which were discovered during Binomial test checks. When several effective trials corrections are plotted as cumulative sums, it is quite clear that each GRB is different enough to require its own correction (see Figure 7.14). The solution was to perform an effective trials correction for every individual GRB. Using the additional 10^4 scans, this takes 1-2 minutes per GRB.

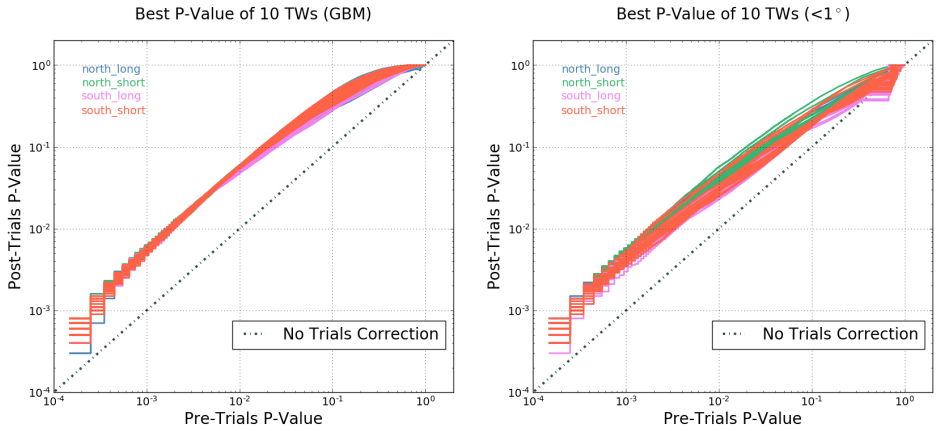

Figure 7.14: The procedure from Figure 7.13 was repeated for 100 GRBs in each sub-population. The spread in effective trials factors is shown for GBM bursts (left) and well-localized bursts (right).

This effective trials correction works nicely to correct the distribution of p-values for each sub-population, as shown in Figure 7.15. This plot shows the individual p-values as a scatter plot in ascending order. These are background-only p-values, which is why they are expected to follow the dashed line, indicating a uniform p-value distribution. If the unblinded p-values were inconsistent with background (meaning more signal-like) then the p-values would be expected to deviated from this uniform distribution.

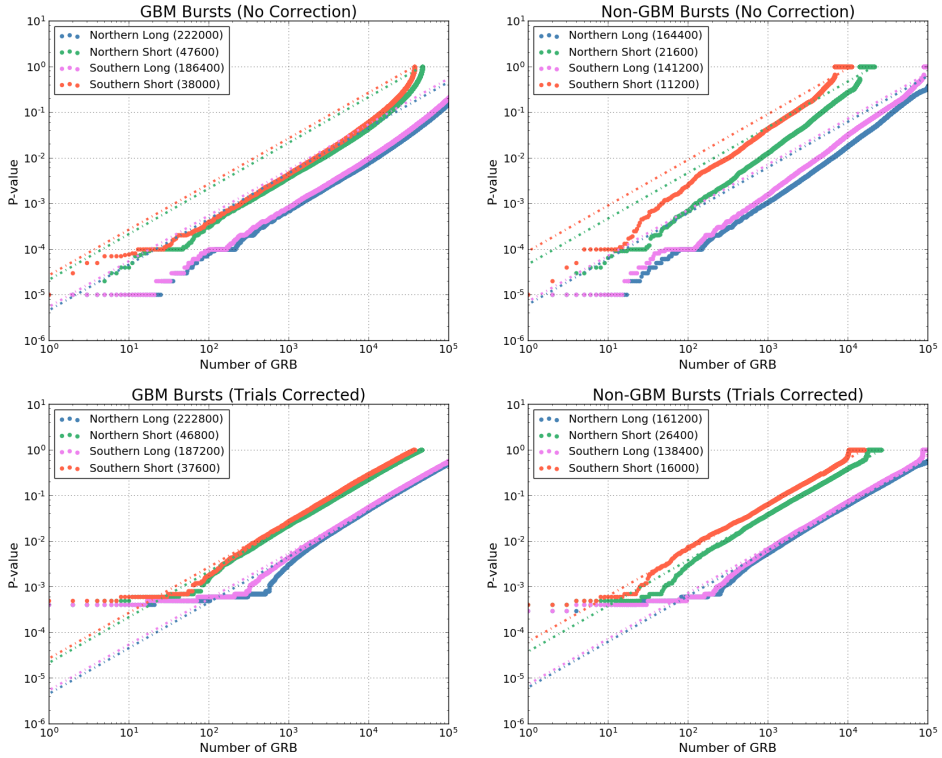

Figure 7.15: The effective trials correction is applied to each individual GRB, with the sub-populations highlighted. These are scatter plots, meaning each dot is a single GRB p-value and the p-values are plotted in order from most significant on the left to least significant on the right. The top row shows the p-values without a trials correction straying far from a uniform p-value distribution. The bottom row includes the correction and is much closer to a uniform distribution.

7.7 Binomial Test

It is always challenging to make a statement about a catalog search when there is no obvious detection of signal. Early IceCube searches for neutrinos coincident with GRBs were found to be consistent with a background-only hypothesis, including in extended time windows [84] [85] [86]. More recent searches attempted to amplify a small signal by stacking all the GRBs together [90] [145] [34]. This approach is

ideal if all GRBs are contributing a small amount. Another option is to take the best p-value from the sample and use it to represent the entire population (with a trials correction for the number of sources in the catalog) [17]. This approach is valid, but it may miss a "warm" population, meaning a small number of GRBs that are contributing signal, but not necessarily all GRBs. A binomial test is a nice compromise, because it allows a search for this warm population as long as the p-values are well-behaved and uniformly distributed between 0 and 1.

A Binomial test is performed on each of the sub-populations: northern sky long GRBs, northern sky short GRBs, southern sky long GRBs, and southern sky short GRBs. The Binomial p-value is calculated with Equation 7.3:

$$P(k) = \sum_{m=k}^{N} \frac{N!}{(N-m)!m!} p_k^m \left(1 - p_k\right)^{N-m} \tag{7.3}$$

P(k) is the binomial probability, which is updated for each GRB (the GRBs are considered in order of increasing p-value). The binomial test evaluates how likely it is to have "k" GRBs with a certain p-value or more significant. This is the threshold p-value, because only the number of p-values below this threshold is relevant, rather than the actual p-values themselves. For example, a trial that yields k=10 means the most interesting binomial p-value occurred when considering the lowest 10 p-values. This would be a hint of a "warm" population and those 10 GRBs may warrant additional study. Of course, k alone is not the whole story. The resulting binomial p-value is of interest and indicates the significance of the sample as a whole.

Figure 7.16 shows an example Binomial test performed on scrambled data in each sub-population. The black dots are the p-values representing a single GRB, and these p-values have the effective trials correction (for choosing the best of 10 time windows) applied. The blue dots show the Binomial test for a given threshold p-value. The lowest (and therefore most significant) Binomial p-value is selected to represent the sample.

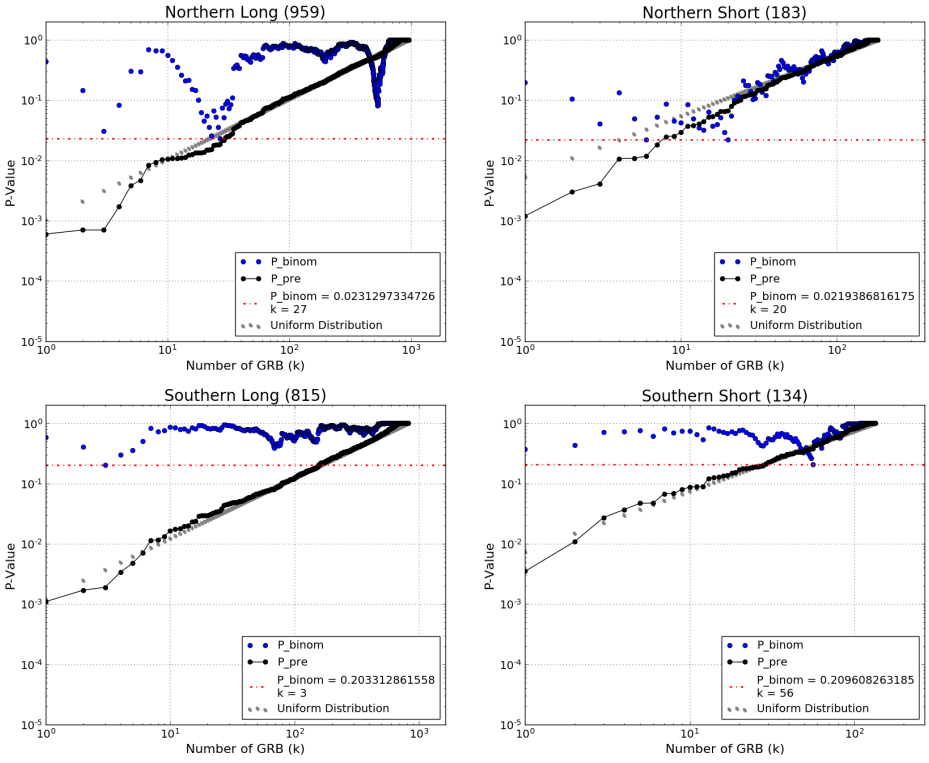

Figure 7.16: An example binomial test performed on the four sub-populations. The GRB p-values are shown in ascending order in black. The grey dotted line is shown to guide the eye to see the GRB p-values are following a uniform distribution, which is expected for scrambled background data. The Binomial p-values are shown in blue, and the most significant result is highlighted with a red horizontal line.

There is no trials correction for the number of GRBs applied to the p-values

in the Binomial test. The method for handling the number of GRBs studied is very similar to the effective trials correction described in the previous section for selecting the most significant of ten time windows. The Binomial test is repeated on many sets of scrambled data, and the resulting Binomial p-values are plotted in a cumulative sum (see Figure 7.17). The cumulative sum is used as a look-up table for the initially calculated Binomial p-value. The corrected Binomial p-value for each sub-population is the final output of this Binomial test.

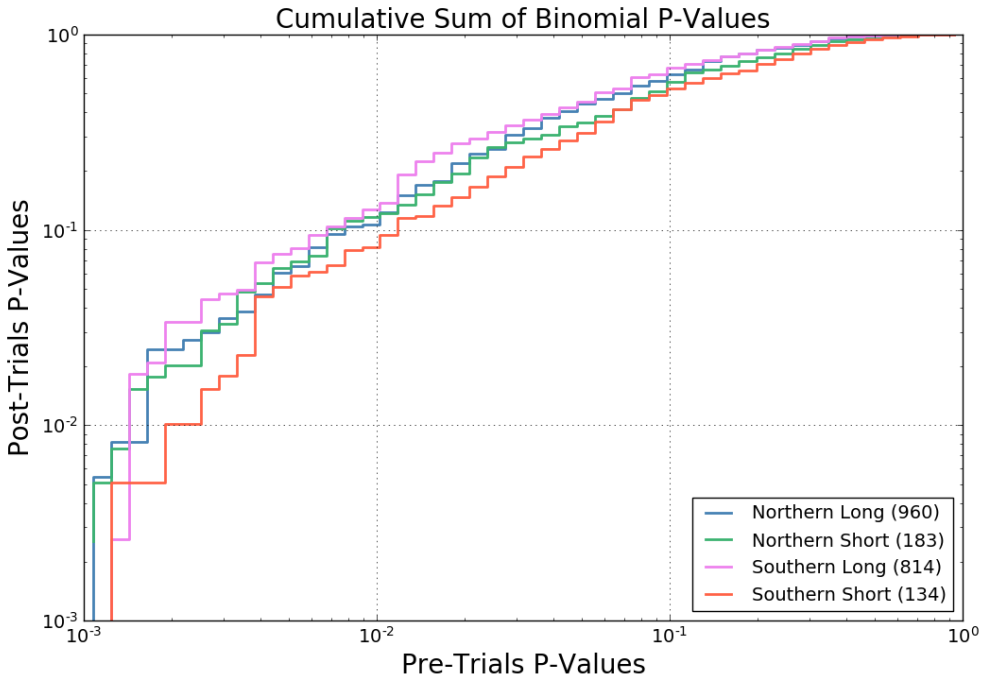

Figure 7.17: The Binomial test is run many times on scrambled data to determine the trials correction for the final p-value in each sub-population. The p-values in the Binomial test are corrected for searching ten time windows, but there is no correction for population size. These cumulative sums serve as a look-up table to determine the final Binomial p-value.

Chapter 8: Results

The results of the analysis described in Chapter 7 are presented here. 2,091 GRBs were analyzed individually and in four sub-populations split by northern and southern sky as well as duration. The most significant GRB is a northern sky long GRB from 2014, with the most significant time window being +/-1 day (see Table 8.1).

The four sub-populations are studied with a Binomial test, which is intended to reveal possible "warm" populations. A warm population might mean a handful of GRBs with a fairly significant p-value rather than a single outstanding GRB with $> 5\sigma$. The Binomial test did not indicate the presence of a handful of significant GRBs.

The results of this search - the individual GRBs and confirmed by the Binomial test - are consistent with background. Therefore, limits are set using the GRBs to constrain neutrino emission. The stacked test statistic (section 6.4.1) is used to determine a test statistic for a group of GRBs, and then signal is injected to determine a 90% confidence limit. The limits are consistent with those set in [34], and go further by setting limits on the sub-populations as well.

8.1 Binomial Test Results for Sub-Populations

The results of the Binomial test (described in 7.7) do not indicate a significant subset of GRBs. The post-trials Binomial p-value never falls below 1%, which is the generous threshold used in IceCube to indicate a need for further study. In general, a threshold of 3σ is required to declare evidence of a given phenomenon, and 5σ is necessary to claim a discovery. The results of the Binomial test are presented in Figure 8.1.

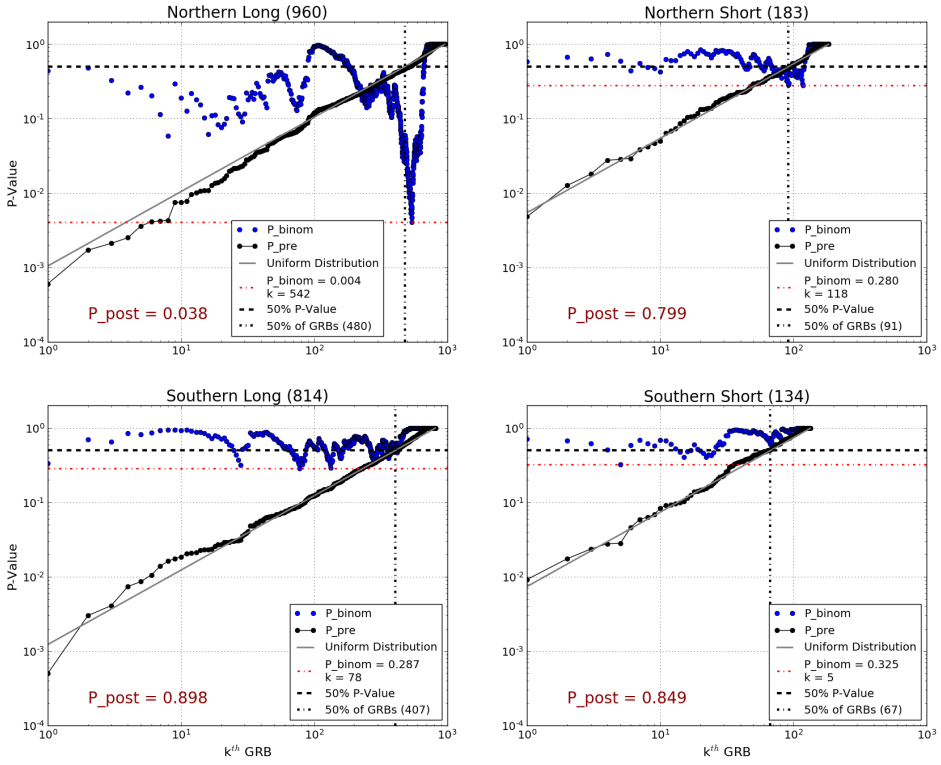

Figure 8.1: The unblinded results of the Binomial test for all four sub-populations. The black dots show the unblinded p-values for each sub-population, and the blue dots show the Binomial p-value for the k^{th} GRB p-value. The post-trials Binomial p-value, written in red in each plot, gives the final result for each sub-population. None of the post-trials Binomial p-values indicates a significant subset of GRBs.

The northern long sub-population may seem suspicious due to the post-trials p-value of 3.8%; however, this result is still consistent with background. The large value of k suggests this is not a set of uniform p-values, which is a prerequisite for the Binomial test. If the p-values are not uniform, then it is possible to see features such as the extremely low binomial p-value in the 400-600 GRB range. Closer inspection of this range (Figure 8.2) reveals a few hundred GRBs with slightly-below-uniform p-values. If this region is discounted, and a "best" Binomial p-value is selected from the first 150 GRBs, then the post-trials p-value becomes 44.5%, which is consistent with background.

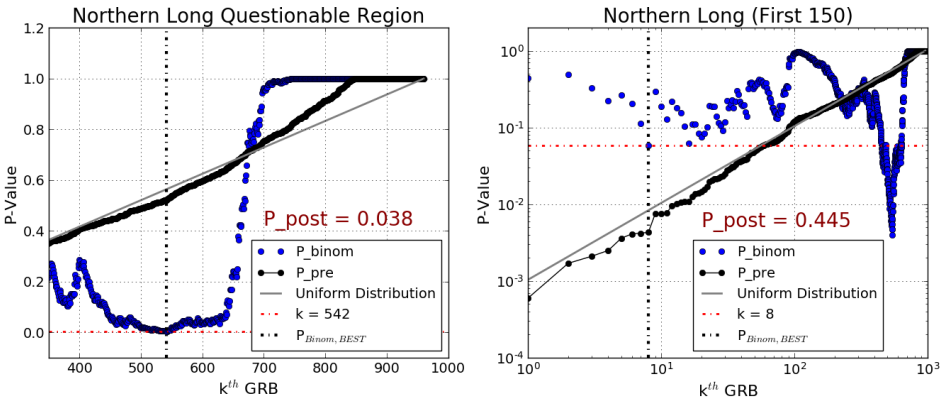

Figure 8.2: Left: A zoomed in view of the low p-values leading to a large value of k in the northern long GRB sub-population. Right: The post-trials Binomial p-value if limited to $k < 150$.

The GRBs in this suspicious region tend to select the two longest time windows as the most significant more frequently than the total northern long population (see Figure 8.3). This suggests that the two longest time windows (+/-1 day and -1/+14 days) are not handled perfectly, resulting in slightly lower p-values in the northern sky. No changes were made to the pre-trials p-values after this was discovered. A

correction would make the result less significant, which is unnecessary given the result already qualifies as a "non-detection."

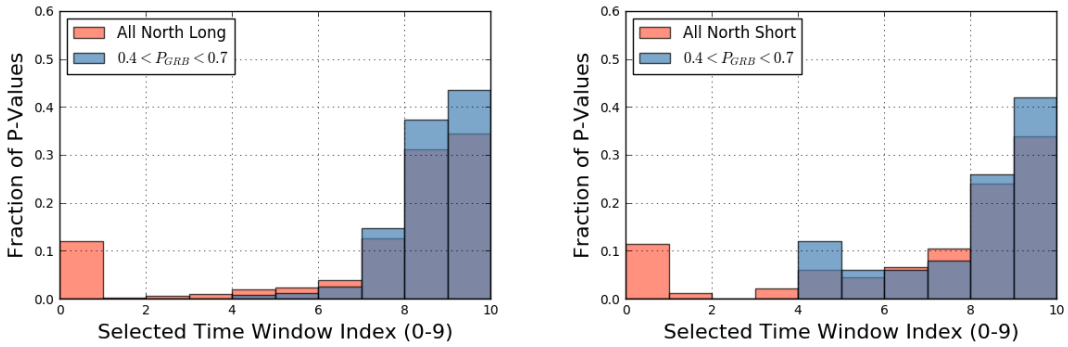

Figure 8.3: The time window index indicating the most significant time window selected. A time window index of 0 refers to the 10 second time window and 9 refers to the -1/+14 day time window. If all time windows have a p-value of 1, then time window 0 is selected. Left: All northern long p-values (red) compared to the region with low p-values (blue). The three longest time windows have larger shares of p-values in the questionable region (highlighted in Figure 8.2). Right: The same comparison for the northern short GRBs. This set of p-values is better behaved in the Binomial test and has a smaller excess in the longest three time windows.

8.1.1 Correlations

There was initial concern that the same neutrino could contribute to the test statistic of more than one GRB. If this were the case, then the Binomial p-values would not truly be uncorrelated and the results would be invalid. The most significant GRBs were checked for correlations. The GRBs with a p-value less than 0.01 (or 0.04 for the southern short population to include the top $k = 5$) were examined. The time window selected as the most significant was checked for each of these "most significant" GRBs. Out of 32,405 events contributing to the most significant time window of the top 23 GRBs, no events were repeated.

Figure 8.4 shows the potential overlap of poorly-localized GRBs. In particular,

GRBs measured by the Fermi-GBM instrument had the potential to cover large portions of the sky. This could lead to more neutrinos contributing to the test statistic, increasing the chances of a single neutrino contributing to multiple GRBs. The purpose of this figure was to raise awareness of the possibility of correlations, but also to ease concerns that this would be a big problem. The plot clearly shows most GRBs do not overlap with each other.

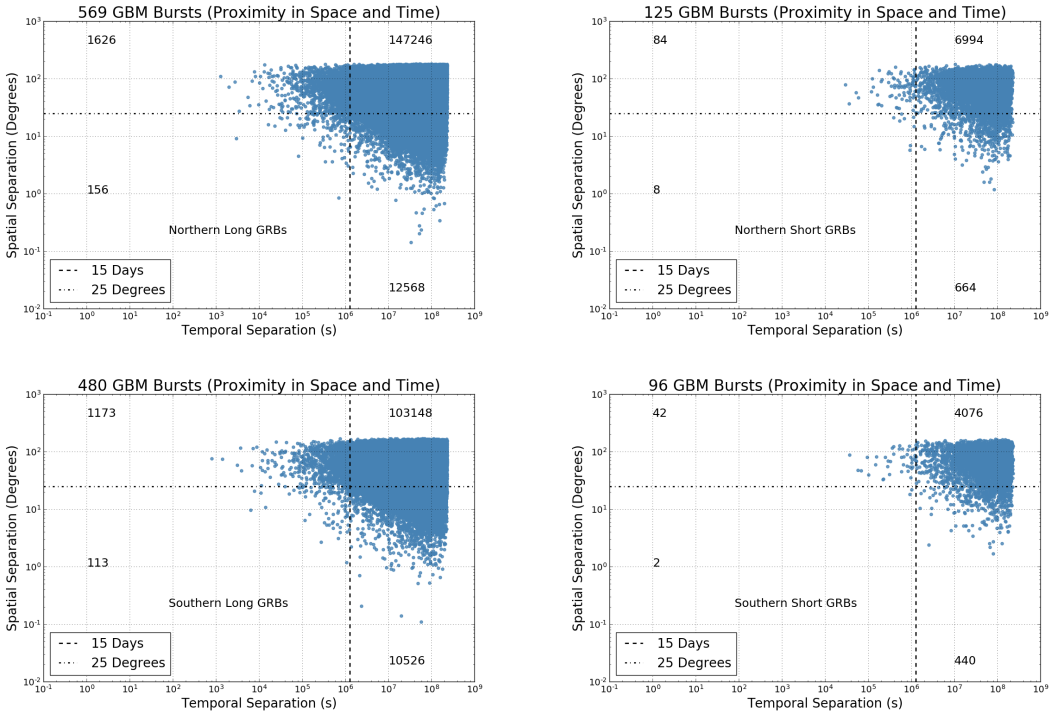

Figure 8.4: This plot illustrates the potential for one neutrino to contribute to the test statistics of multiple GRBs. Each dot represents the temporal and spatial separation between two GRBs. Note that each GRB is compared to every other GRB in the sub-population. A small number of GRBs fall within 15 days and 25 degrees of another GRB, but even this does not guarantee there will be overlap of events.

8.2 Detailed Study of Significant GRBs

The most significant GRBs are listed for each sub-population in this section. A handful of those GRBs are illustrated in plots showing upper limits, signal-to-background ratios, event times, and event energies. The plots for all the most significant GRBs are provided in Appendix A.

8.2.1 Northern Long GRBs

The most significant long GRBs from the northern hemisphere are shown in Table 8.1. They are sorted by p-value, which has been corrected for searching 10 time windows (see section 7.6), but not for the 960 GRBs in this sub-population. GRBs with a p-value less than 0.01 are considered in this "most significant" category.

GRB	RA(°)	Dec(°)	σ(°)	z	T_{start}(MJD)	$T_{100}(s)$	TW	TS	P
140607A	86.4	18.9	1.5e-02	—	56815.718	109.90	2 d	12.8	6.0e-04
141121A	122.7	22.2	6.5e-05	1.47	56982.150	1419.90	15 d	11.8	1.7e-03
161125A	59.4	28.1	4.7e+00	—	57717.930	69.63	25 s	18.8	2.1e-03
120911A	358.0	63.1	2.1e-04	—	56181.298	22.02	250 s	10.6	2.5e-03
120504A	329.9	46.8	8.8e+00	—	56051.468	41.98	1000 s	19.4	3.6e-03
170131A	341.4	64.0	2.3e-02	—	57784.969	23.04	5000 s	10.6	4.1e-03
120711B	331.7	60.0	2.3e-04	—	56119.133	60.00	2 d	11.8	4.2e-03
180721A	347.7	4.9	2.8e-04	—	58320.463	47.60	2 d	11.7	4.3e-03
140114A	188.5	28.0	1.8e-04	3.0	56671.498	139.70	2 d	11.0	7.5e-03
160201A	312.7	69.3	3.1e+00	—	57419.883	40.51	1000 s	13.4	7.5e-03
120217A	122.4	36.8	5.0e+00	—	55974.808	5.89	25 s	15.7	7.7e-03
180623B	199.4	-4.3	2.5e+00	—	58292.849	17.73	50 s	11.5	9.6e-03

Table 8.1: The most significant long GRBs from the northern hemisphere. The "TW" column indicates the best time window leading to the p-value in the final column. The σ column refers to the GRB's positional uncertainty, which may be many degrees in the case of a Fermi-GBM localization. The p-value has an effective trials correction for searching 10 time windows, but is not corrected for the size of the sub-population (960).

A closer look at the most significant GRB from this sub-population shows a relatively high-energy neutrino landing on top of the GRB (Figure 8.5). The neutrino in question has a reconstructed energy of roughly 10.5 TeV. The declination is 19.41° and right ascension is 86.42°. The event's spatial coincidence contributes significantly to the ratio of signal to background, which is shown for this GRB in Figure 8.6. The neutrino arrives roughly 7 hours after the GRB, which is only seen by the longest two time windows. This is the most significant p-value out of all

2,091 GRBs.

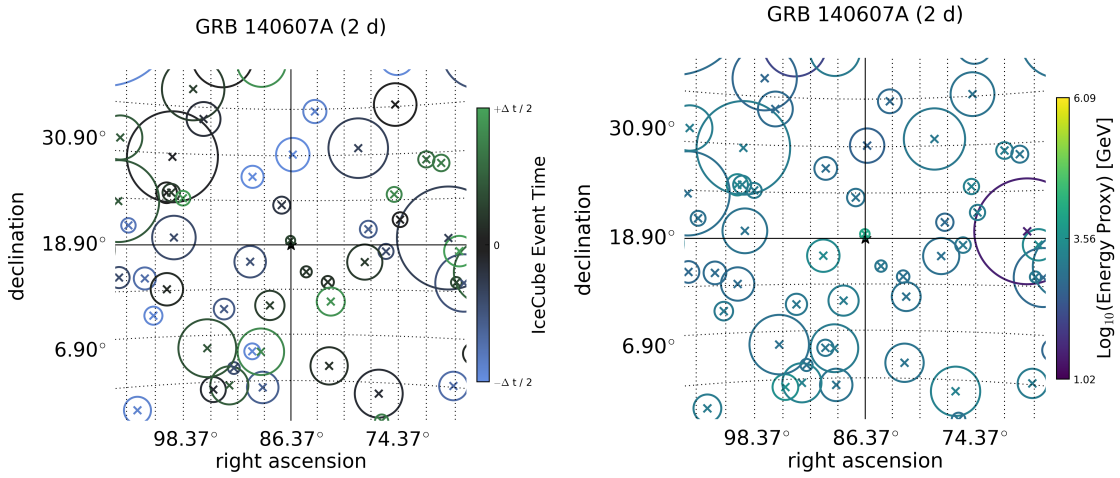

Figure 8.5: The relative times (left) and reconstructed energies (right) for the events arriving within +/-1 day of GRB 140607A. The GRB's reported position is identified with a star at the center of the grid. The neutrino candidates are identified with an "x" at the reconstructed positions, and the size of the circle indicates the angular uncertainty of the event. All events have a minimum of 0.2° uncertainty. The high-energy event that sits directly on top of the GRB location is a 10.5 TeV event that arrives roughly 7 hours after the GRB.

A two-day time window has roughly 1,000 events in the GFU sample, many of which are low-energy and do not contribute to the test statistic. To emphasize the most important contributing events to the signal-to-background ratio, a threshold is set based on the number of fit events in the test statistic. This fit number of events, n_s, provides a threshold of $\frac{S}{B} \geq 3 \times n_s$. Therefore, only events with a signal-to-background value greater than this threshold are plotted in Figure 8.6.

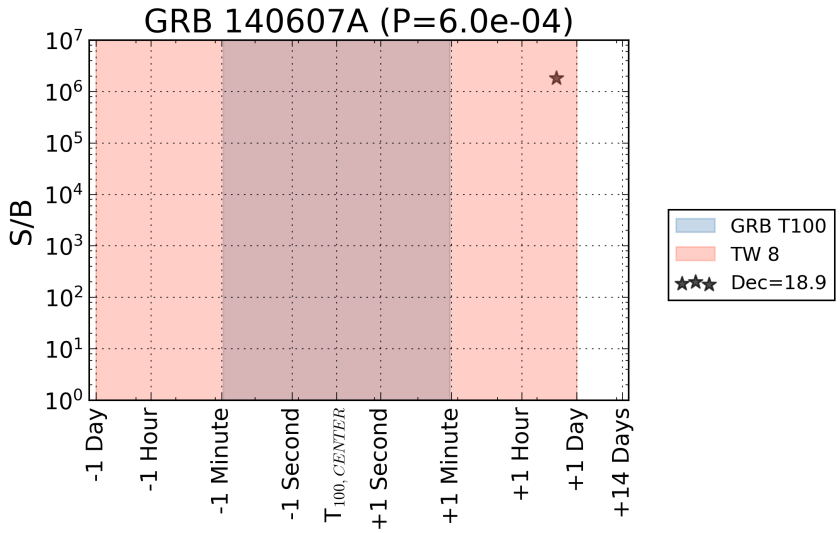

Figure 8.6: The signal-to-background ratio for GRB 140607A. The blue indicates the duration of the GRB, beginning with the trigger time on the left. The pink region indicates the most significant time window selected by the analysis. While there are many on-time events, there is only one event with a high enough S/B to be plotted here ($\frac{S}{B} \geq 3 \times n_s$). The event arrives roughly 7 hours after the GRB and has a reconstructed energy of 10.5 TeV.

The 90% upper limit for this GRB is shown in Figure 8.7. The upper limit is found for each time window based on the unblinded test statistics. Signal is injected until 90% of trials are above the unblinded test statistic. If the unblinded test statistic happens to be an under-fluctuation, then the median of the background test statistic distribution is used (making the upper limit equivalent to the sensitivity). The upper limits are plotted for all ten time windows.

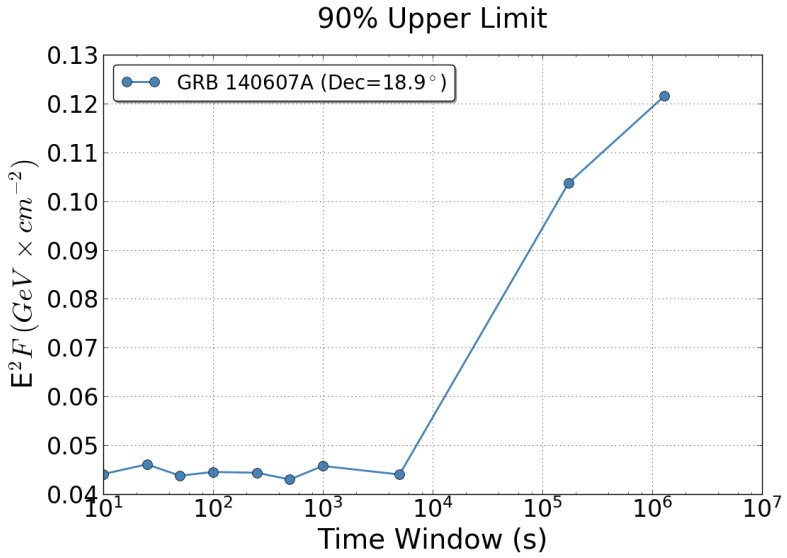

Figure 8.7: The 90% upper limit for GRB 140607A in all ten time windows. The two day time window was found to be the most significant.

8.2.2 Northern Short GRBs

The most significant short GRB from the northern hemisphere is shown in Table 8.2. The p-value has been corrected for searching 10 time windows (see section 7.6), but not for the 183 GRBs in this sub-population. GRBs with a p-value less than 0.01 are considered in this "most significant" category.

GRB	RA(°)	Dec(°)	σ(°)	z	T_{start}(MJD)	$T_{100}(s)$	TW	TS	P
140807A	200.2	26.5	4.4e+00	—	56876.500	0.51	100 s	15.7	4.8e-03

Table 8.2: The most significant short GRBs from the northern hemisphere. The "TW" column indicates the best time window leading to the p-value in the final column. The σ column refers to the GRB's positional uncertainty, which may be many degrees in the case of a Fermi-GBM localization. The p-value has an effective trials correction for searching 10 time windows, but is not corrected for the size of the sub-population (183).

Only one GRB meets the criteria for additional study from the northern sky

short GRB sub-population. The event times and energies are shown in 8.8 and the signal-to-background plot is shown in 8.9.

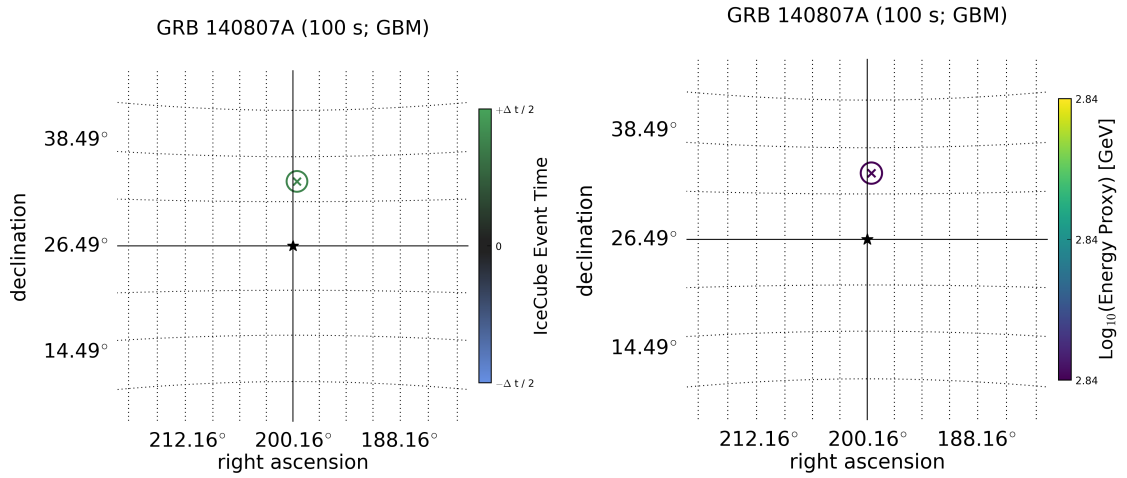

Figure 8.8: The relative times and reconstructed energies for the events arriving within 100 seconds of GRB 140807A. The GRB's reported position is identified with a star at the center of the grid. The single on-time neutrino candidate is identified with an "x" at the reconstructed position, and the size of the circle indicates the angular uncertainty of the event. GRB 140807A is a GBM burst, which is why an event roughy 10 degrees from the reported position can result to a high test statistic. In this case, the event is quite low energy, but arrives within 100 seconds of the GRB, leading to a more significant p-value.

The same relatively low-energy event shows up in the signal-to-background ratio plot. The event arrives within 1 minute of the GRB, which is why the p-value is more significant.

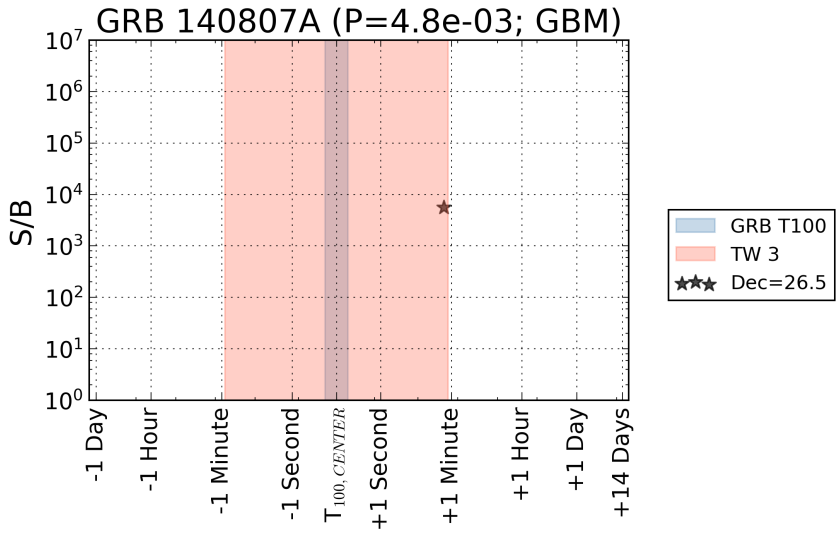

Figure 8.9: The signal-to-background ratio for GRB 140807A. The blue indicates the duration of the GRB, beginning with the trigger time on the left. The pink region indicates the most significant time window selected by the analysis. There is one nearby on-time event contributing to the S/B to be plotted here ($\frac{S}{B} \geq 3 \times n_s$). The event has a reconstructed energy of 0.69 TeV, but arrives within 100 seconds of the GRB, leading to a more significant p-value.

The upper limit for GRB 140807A is shown for all 10 time windows in Figure 8.10.

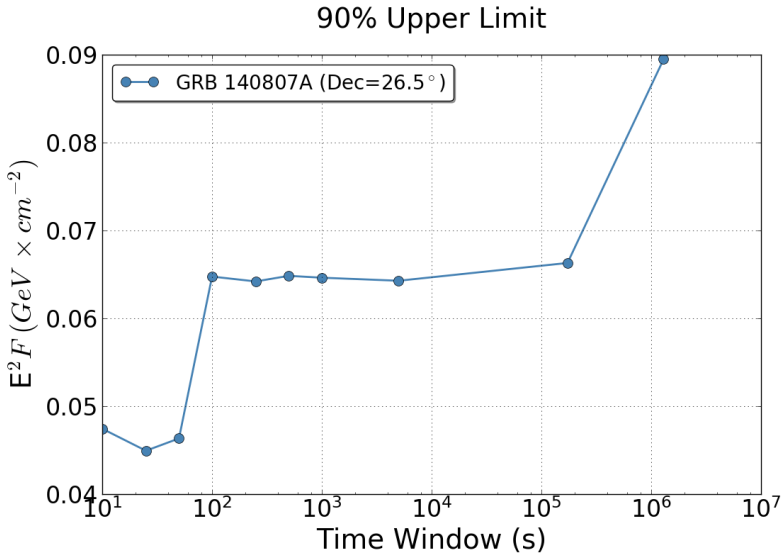

Figure 8.10: The 90% upper limit for GRB 140807A in all ten time windows. The 100 second time window was found to be the most significant.

8.2.3 Southern Long GRBs

The five most significant long GRBs from the southern hemisphere are shown in Table 8.3. They are sorted by p-value, which has been corrected for searching 10 time windows (see section 7.6), but not for the 814 GRBs in this sub-population. GRBs with a p-value less than 0.01 are considered in this "most significant" category.

GRB	RA(°)	Dec(°)	σ(°)	z	T_{start}(MJD)	$T_{100}(s)$	TW	TS	P
150202A	39.2	-33.1	2.2e-04	—	57055.965	25.70	2 d	18.6	5.0e-04
150118B	240.2	-35.8	5.0e-01	—	57040.409	48.65	2 d	12.9	3.0e-03
170923C	228.3	-10.8	9.1e+00	—	58019.566	27.65	1000 s	19.7	4.1e-03
150626A	111.3	-37.8	2.3e-04	—	57199.092	144.00	15 d	11.2	7.4e-03
180906A	104.8	-67.0	3.6e+00	—	58367.597	52.03	25 s	9.7	8.6e-03

Table 8.3: The most significant long GRBs from the southern hemisphere. The "TW" column indicates the best time window leading to the p-value in the final column. The σ column refers to the GRB's positional uncertainty, which may be many degrees in the case of a Fermi-GBM localization. The p-value has an effective trials correction for searching 10 time windows, but is not corrected for the size of the sub-population (814).

GRB 150202A was chosen to represent this group of GRBs (the other four have plots in Appendix A). This GRB has three precursor events with reconstructed energies above 30 TeV. The earliest of these precursors has a reconstructed energy of 105 TeV. The event times and energies are shown in 8.11 and the signal-to-background plot is shown in 8.12.

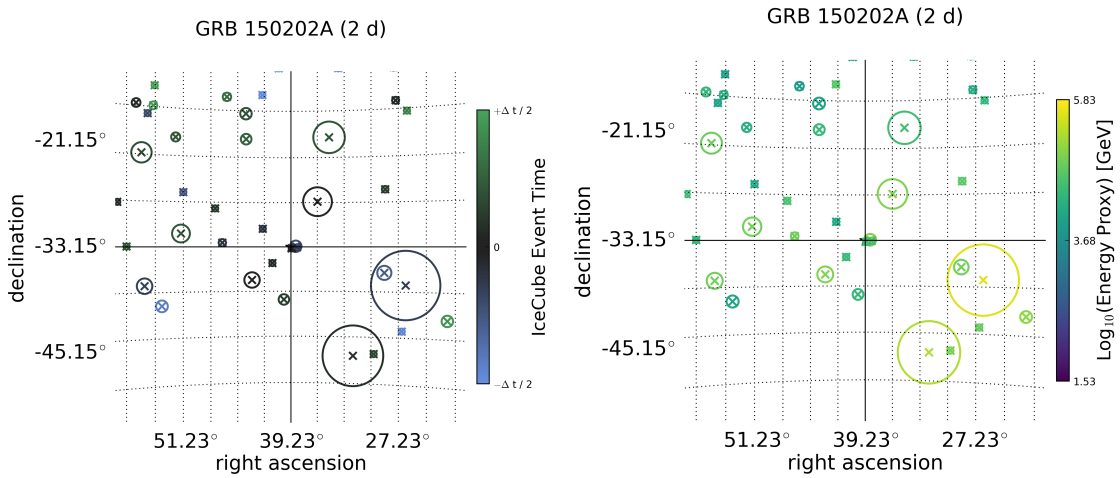

Figure 8.11: The relative times and reconstructed energies for the events arriving within +/-1 day of GRB 150202A. The GRB's reported position is identified with a star at the center of the grid. The neutrino candidates are identified with an "x" at the reconstructed positions, and the size of the circle indicates the angular uncertainty of the event. All events have a minimum of 0.2° uncertainty. GRB 150202A is a well-localized burst, which is why several events landing very close to the reported GRB position increases the TS. This is one of the most significant p-values in the entire collection of 2,091 GRBs.

Only three of the events in this time window contribute substantially to the test statistic. The threshold of $\frac{S}{B} > 3n_s$ eliminates all but three events. These three precursor events are shown in Figure 8.12.

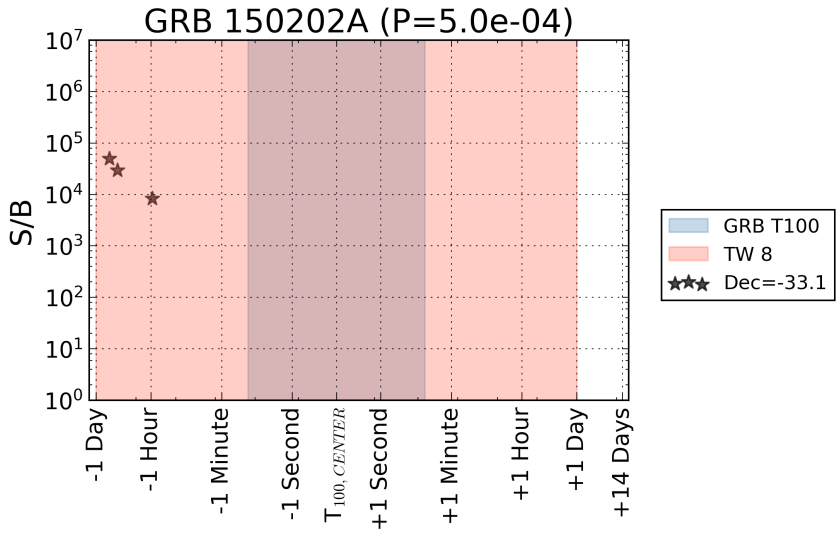

Figure 8.12: The signal-to-background ratio for GRB 150202A. The blue indicates the duration of the GRB, beginning with the trigger time on the left. The pink region indicates the most significant time window selected by the analysis. While there are many on-time events, only three pass the $\frac{S}{B} \geq 3n_s$ threshold. The events arrive roughly 1, 7, and 11 hours before the GRB. The earliest event has a reconstructed energy of roughly 105 TeV, and the other two are roughly 30 TeV. In the northern hemisphere, an event would need roughly 200 TeV to have an equal chance of being signal or background. At -33.1°, the energy needs to be closer to 1 PeV to be considered signal-like.

The upper limit for GRB 150202A is shown for all 10 time windows in Figure 8.13.

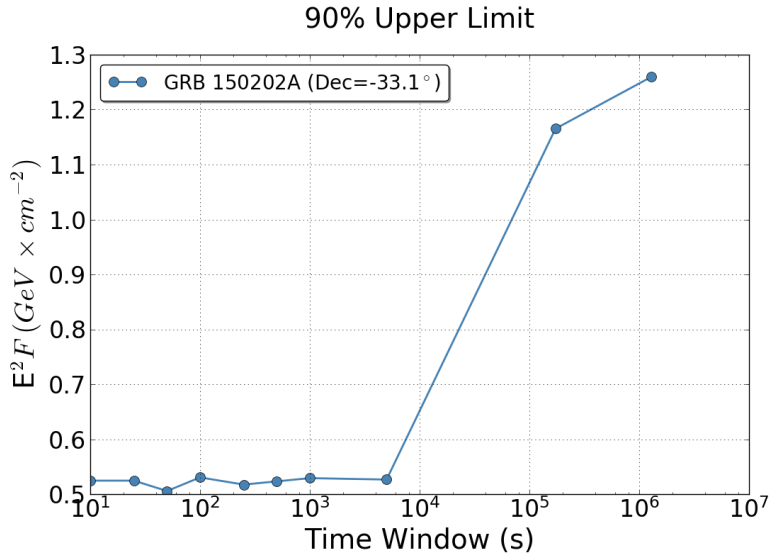

Figure 8.13: The 90% upper limit for GRB 150202A in all ten time windows. The two day time window was found to be the most significant.

8.2.4 Southern Short GRBs

The five most significant short GRBs from the southern hemisphere are shown in Table 8.4. They are sorted by p-value, which has been corrected for searching 10 time windows (see section 7.6), but not for the 134 GRBs in this sub-population. GRBs with a p-value less than 0.04 are considered in this "most significant" category. This deviates from the other three sub-populations, because the Binomial test resulted in **k=5** GRBs. Therefore, the top five GRBs are considered in this section.

GRB	RA(°)	Dec(°)	σ(°)	z	T_{start}(MJD)	$T_{100}(s)$	TW	TS	P
140511A	329.8	-30.1	8.5e+00	—	56788.095	1.41	2 d	20.3	9.2e-03
130919B	297.4	-11.7	5.2e+00	—	56554.173	0.96	5000 s	16.2	1.8e-02
160411A	349.4	-40.2	2.8e-04	—	57489.062	1.26	2 d	8.1	2.4e-02
120212B	303.4	-48.1	1.0e+01	—	55969.353	0.86	500 s	17.8	2.8e-02
141102B	223.2	-17.4	9.2e+00	—	56963.112	0.02	15 d	18.6	2.8e-02

Table 8.4: The most significant short GRBs from the southern hemisphere. The "TW" column indicates the best time window leading to the p-value in the final column. The σ column refers to the GRB's positional uncertainty, which may be many degrees in the case of a Fermi-GBM localization. The p-value has an effective trials correction for searching 10 time windows, but is not corrected for the size of the sub-population (134).

GRB 140511A was chosen to represent this group of GRBs (the other four have plots in Appendix A). This is a GBM burst, and includes neutrinos arriving before and after the burst contributing to the test statistic. The event times and energies are shown in 8.14 and the signal-to-background plot is shown in 8.15.

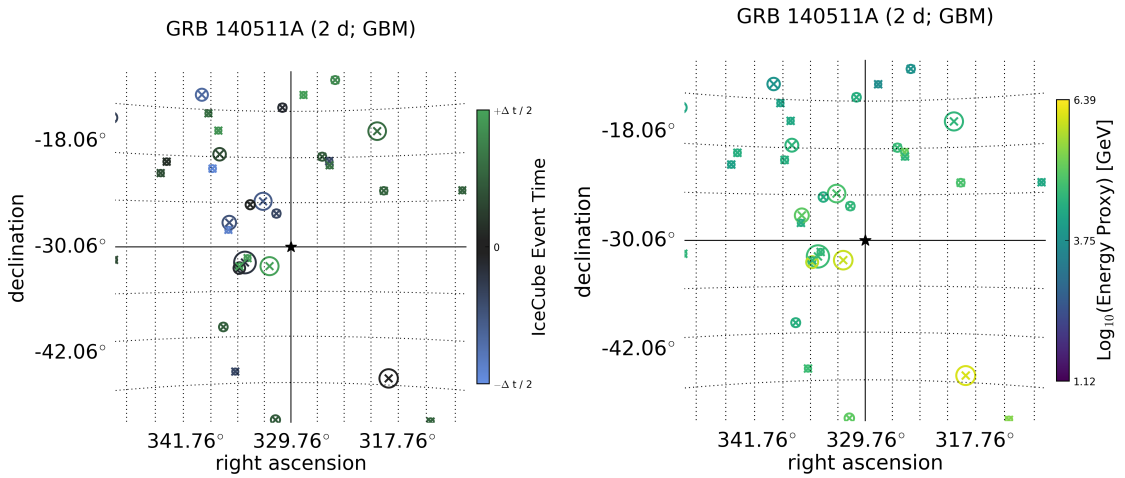

Figure 8.14: The relative times and reconstructed energies for the events arriving within +/-1 day of GRB 140511A. The GRB's reported position is identified with a star at the center of the grid. The neutrino candidates are identified with an "x" at the reconstructed positions, and the size of the circle indicates the angular uncertainty of the event. All events have a minimum of 0.2° uncertainty. GRB 140511A is a GBM burst. The many coincident events are shown in these two plots. The relative event times are in the plot on the left, and the reconstructed energies are shown on the right.

The threshold of $\frac{S}{B} > 3n_s$ leaves three events contributing to the test statistic: two precursors and one afterglow. These are shown in Figure 8.15.

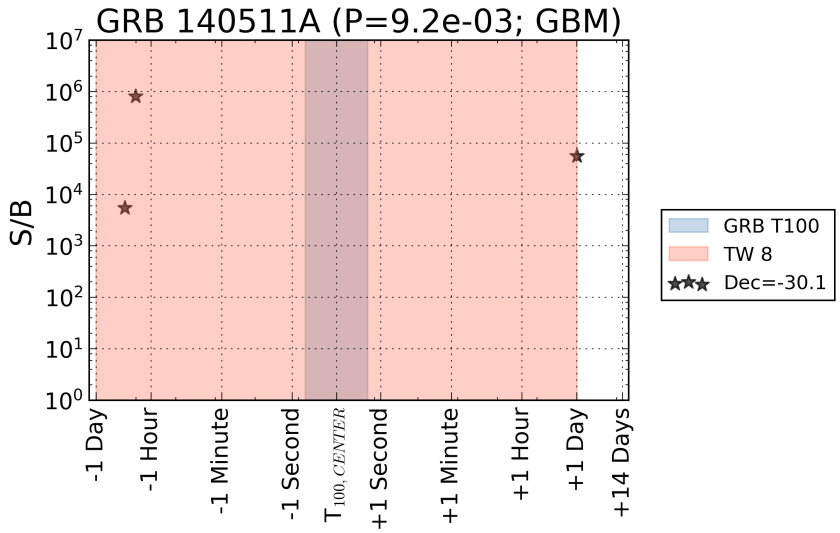

Figure 8.15: The signal-to-background ratio for GRB 140511A. The blue indicates the duration of the GRB, beginning with the trigger time on the left. The pink region indicates the most significant time window selected by the analysis. While there are many on-time events, only three pass the $\frac{S}{B} \geq 3n_s$ threshold. Two precursors and one afterglow event survive this cut.

The upper limit for GRB 150202A is shown for all 10 time windows in Figure 8.16.

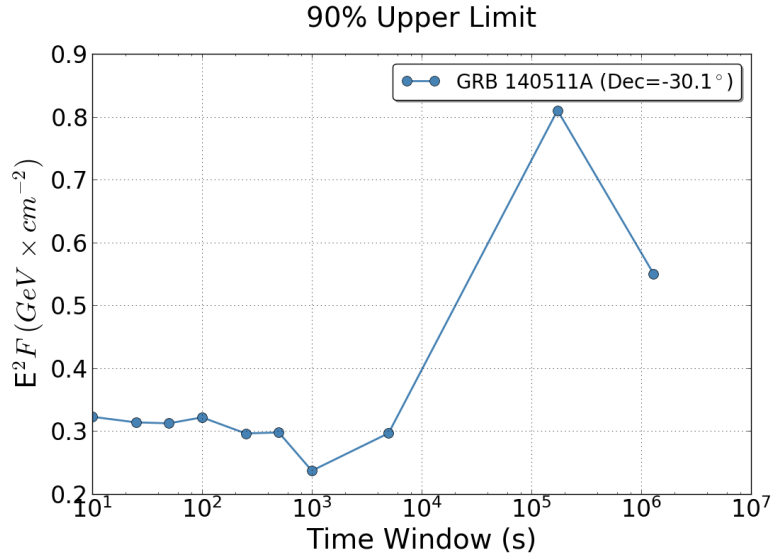

Figure 8.16: The 90% upper limit for GRB 140511A in all ten time windows. The two day time window was found to be the most significant.

8.3 Stacked Limits

Because the result of this analysis is consistent with a background-only hypothesis, the logical next step is to set a limit on the possible neutrino production from GRBs. If GRBs are, in fact, producing neutrinos, then the results of this analysis can be used to constrain the energy and time of production of those neutrinos. If GRBs were producing many high-energy neutrinos on-time (and in the same direction) with the GRBs, then the results of this analysis would look very different. Individual upper limits were shown in the previous section for a few select GRBs, but a more powerful approach to setting limits is to take advantage of the stacked test statistic.

A stacked test statistic (described in 6.4.1) is the result of combining the signal-to-background values from events over many GRBs. Signal is injected until 90% of the stacked test statistics are greater than the unblinded stacked test statistic. This approach leads to limits on contributions to the diffuse flux, GRB population assumptions, and a generic double broken power emission spectrum.

A quick sanity check is to confirm the number of events in the stacked time is consistent with the number of events expected from background. The stacked time results from stitching the most significant time windows together for all GRBs in the sub-popultion. Table 8.5 shows the number of events in each sub-population compared to the total expected from data. This result emphasizes that the overall number of neutrinos is consistent with background.

Sub-Population	$\sum T_{100}$ (Hours)	Events Expected	Events Measured	Poisson Probability
Northern Long	23.3	534.05	549	25.06%
Northern Short	5.4	128.54	123	66.75%
Southern Long	21.1	488.03	494	38.22%
Southern Short	4.1	96.57	97	45.55%

Table 8.5: This table presents the number of measured events (all-sky) during the stacked test statistic T_{100} time compared to the expected number from typical background. The time comes from stitching together the most significant time windows of all the GRBs. The measured events are consistent with expected numbers of events from background.

8.3.1 Generic Double Broken Power Law Limits

The constraints on a generic double broken power law (described in 3.2.1) are shown in Figures 8.17-8.19. The models from Waxman-Bahcall and Ahlers et. al. are plotted against the 90% limits of all the GRBs, all short/long, all north/south, and the four sub-populations. It is not surprising that these models are ruled out by most sub-populations; both the Waxman-Bahcall and Ahlers et. al. models assume GRBs alone are responsible for the UHECR flux and therefore predict fairly large neutrino emission. The limits from all GRBs, all northern GRBs, all long GRBs, and the northern long GRBs rule out both models at greater than 90% confidence. The southern sky and short GRBs, taken on their own, do not rule out the Waxman-Bahcall model at 90% confidence.

The time-integrated flux in each stacked test statistic is assumed to be equal

for each GRB at Earth. This time-integrated flux is then scaled to the quasi-diffuse flux, assuming a density of 667 GRBs per year. The constraint on the double broken power law is a function of the first break energy, ε_b, and the flux normalization, Φ_0.

The limits on the generic double broken power law spectrum were only calculated for the prompt. The shortest time window that completely included the t_{100} was assigned as the prompt. Although the southern sky and short GRBs do not constrain the double broken power law at 90%, these limits do continue to cast doubt on the hypothesis that GRBs are significant produces of UHECRs. At the very least, only a fraction of GRBs are contributing to the highest energy cosmic rays.

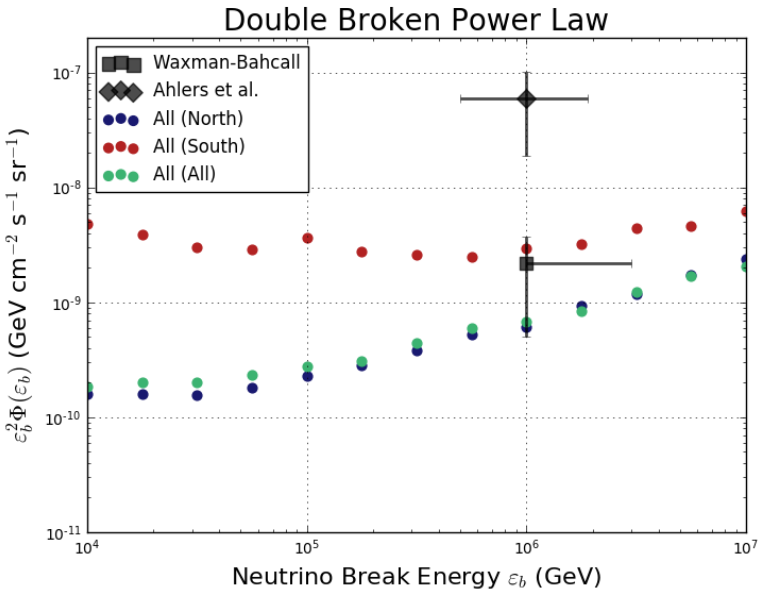

Figure 8.17: The double broken power law constraints set by the northern sky GRBs (blue) and southern sky GRBs (red). The limit for all 2,091 GRBs is shown in green as a reference.

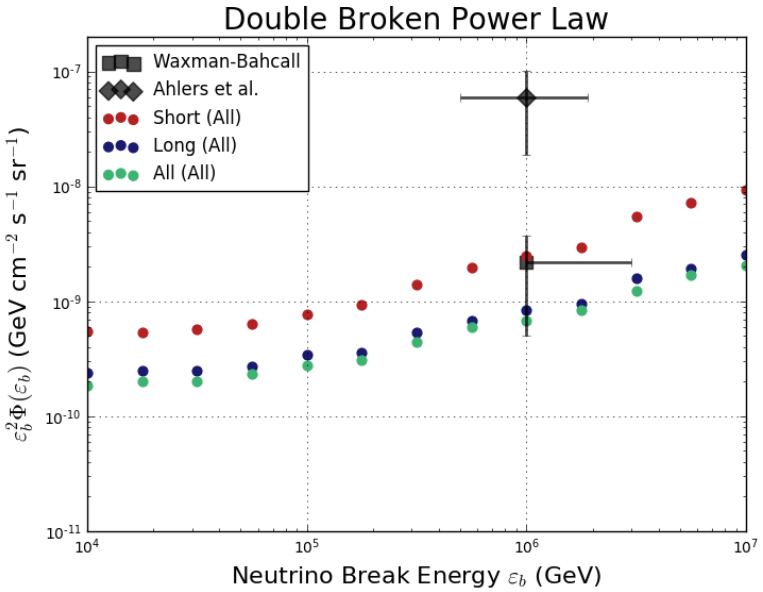

Figure 8.18: The double broken power law constraints set by the long GRBs (blue) and short GRBs (red). The limit for all 2,091 GRBs is shown in green as a reference.

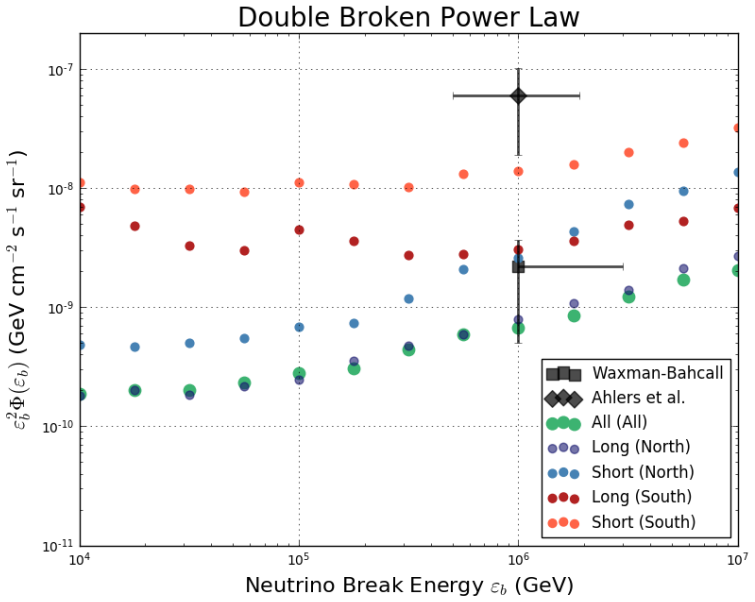

Figure 8.19: The double broken power law constraints set by the four sub-populations. The limit for all 2,091 GRBs is shown in green as a reference. The northern long GRBs are nearly indistinguishable from the limits set by all 2,091 GRBs.

8.3.2 Quasi-Diffuse Flux and Density Limits

The stacked test statistic (6.4.1) is very powerful on its own. Simply injecting signal until 90% of stacked test statistic trials are greater than the unblinded value can provide an interesting limit on GRB contributions to the quasi-diffuse flux. This injected flux can be converted to a diffuse flux (see 3.2.2 for details), which is compared to the measured diffuse flux in IceCube. This conversion assumes each GRB is contributing equal time-integrated flux at Earth, and that GRBs have a population density of 667 GRBs per year.

The stacked limit on the quasi-diffuse flux is shown in Figures 8.20-8.22. Each time window has a limit on the flux (indicated by the filled circles) and a prompt limit on the flux (dashed line). The prompt limits are comparable to the limits set in 3.7 (the dashed lines in Figure 3.8). The limits in the previous search are stronger by roughly a factor of 2. Although this analysis includes more GRBs (which should lead to a stronger stacked limit), the generic time windows coupled with the handling of Fermi-GBM errors includes larger backgrounds, which is likely the cause of the looser constraint.

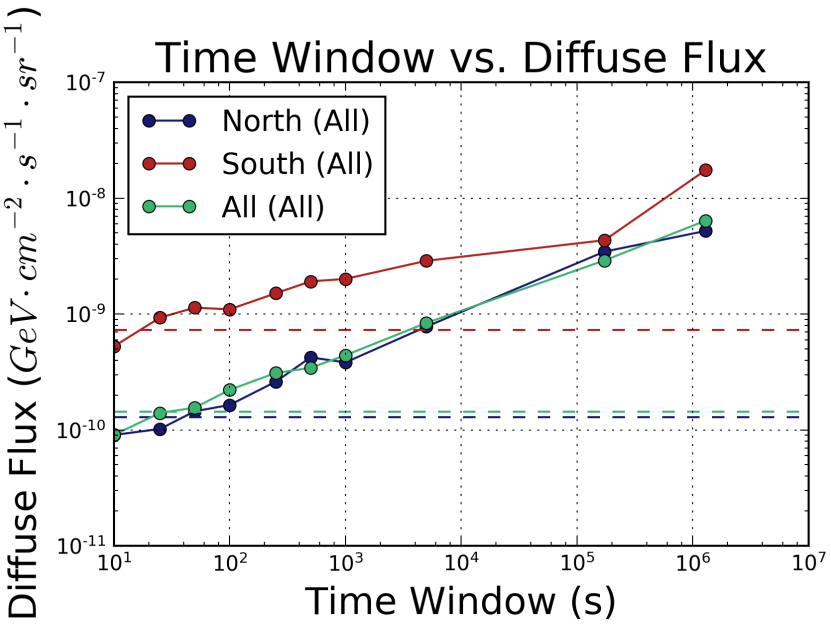

Figure 8.20: The stacked limit on the quasi-diffuse flux for all northern GRBs (blue) and all southern GRBs (red). The limits for all 2,091 GRBs are shown in green for reference. Each dot indicates the 90% confidence limit for the given time window, and the dashed lines show the limit for the prompt.

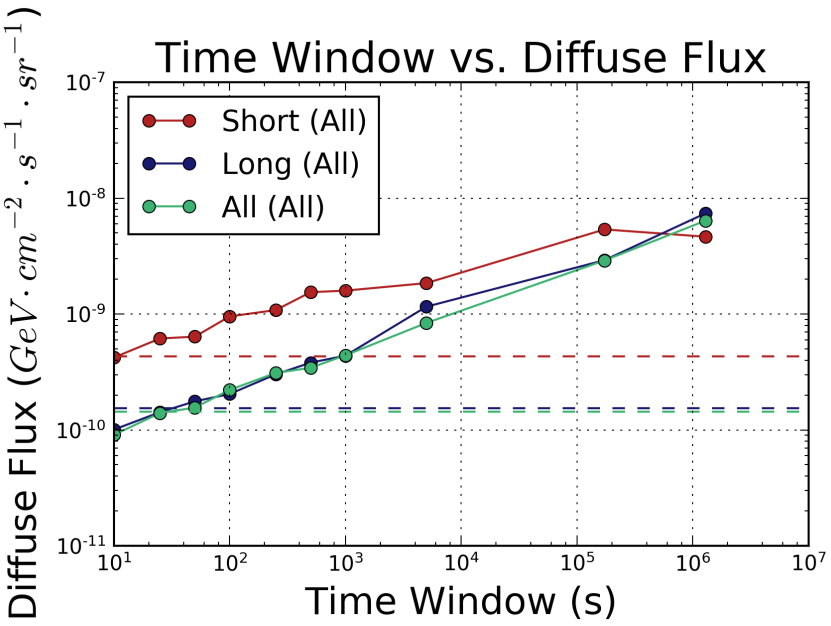

Figure 8.21: The stacked limit on the quasi-diffuse flux for all long GRBs (blue) and all short GRBs (red). The limits for all 2,091 GRBs are shown in green for reference. Each dot indicates the 90% confidence limit for the given time window, and the dashed lines show the limit for the prompt.

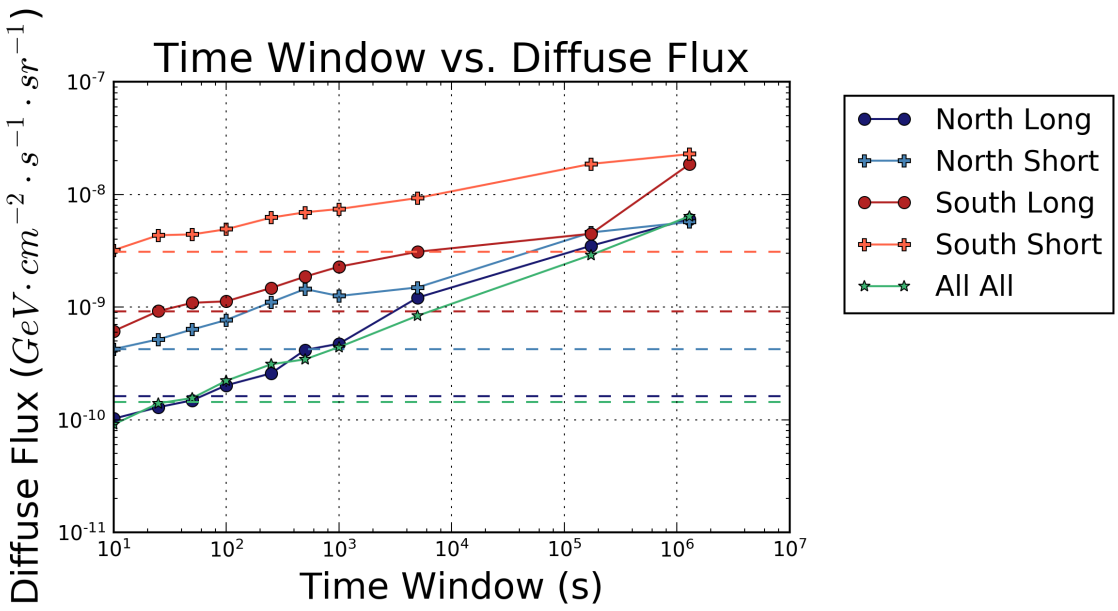

Figure 8.22: The stacked limit on the quasi-diffuse flux for all four sub-populations. The limits for all 2,091 GRBs are shown in green for reference. Each dot indicates the 90% confidence limit for the given time window, and the dashed lines show the limit for the prompt.

The final comment from the stacked test statistics applies to the assumption of 667 GRBs per year. Equation 3.25 shows the conversion from a time-integrated flux to the quasi-diffuse flux. This diffuse flux is then compared to the measured value and a percentage of diffuse flux from GRBs is determined. If, instead, the percentage of diffuse flux generated by GRBs was assumed, then the limit could be placed on density. The top plot in Figure 8.23 shows the first step to limit this density. The typical approach would assume 667 GRBs and increase the flux until 90% of trials were above the threshold value. In this method, the flux is fixed and the density changes. For a given fraction of diffuse flux, the density that leads to 90% of trials above the threshold is the result.

The bottom plot in Figure 8.23 shows this density limit for all the time windows

and the prompt. The limits are calculated for 1%, 10%, and 100% of the diffuse flux. While this result does not necessarily rule out 667 GRBs per year as the accurate source density, it does raise the question of the validity of the assumption. A higher density would mean more sources producing fewer neutrinos. A lower density would suggest each GRB has a higher neutrino luminosity. It is possible that GRBs are far more dense, but not producing as many neutrinos as expected.

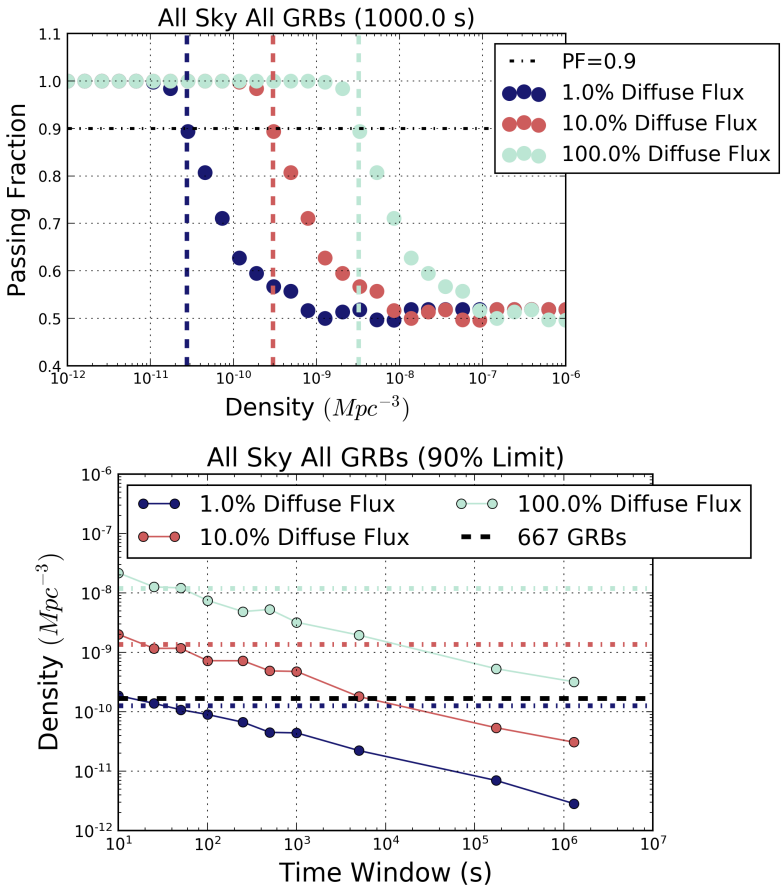

Figure 8.23: Top: The passing fraction plot to determine the source density that yields 90% of trials above a threshold value. The three curves are for a flux equivalent to 1%, 10%, and 100% of the measured diffuse flux. Bottom: The density limits by time window and the prompt. The historic 667 GRBs per year value is shown as a black dashed line for reference. The red, light blue, and dark blue dashed lines indicate limits on the prompt, while the dots of the same colors refer to limits on each time window. The densities are found by assuming a number of GRBs per year (e.g., 667) and converting to the source density per Mpc^3 that produces that number of GRBs in a year with FIRESONG.

8.3.3 FIRESONG Standard Candle Quasi-Diffuse Flux Limits

FIRESONG is a simulation software package that simulates sources (and their fluxes) for a given local density and stellar evolution model [91]. Section 3.2.3 details the stellar evolution model chosen for this analysis. The GRBs were assumed to be standard candles, which differs from the approach used in the double broken power law and stacked quasi-diffuse limits where fluxes at Earth are assumed to be equal. It is perhaps better to assume the GRBs follow a power-law neutrino luminosity (to match the gamma-ray spectrum) rather than being standard candles. However, the lack of correlation measured between GRBs and neutrinos suggests there is no obvious choice for neutrino luminosity and standard candles are an equally valid assumption.

One point of comparison between the stellar evolution model described in [93] and data is the distribution of redshifts. Using the sources generated by FIRESONG, a distribution is compared to the redshifts of the GRBs in this catalog (see Figure 8.24). Out of 2,091 total GRBs, only 206 of those had a measured redshift. It is quite difficult to measure a redshift for a transient source because of the short duration. Furthermore, the redshift is determined by optical follow-up, which introduces sources of observer bias. An astronomer may not be able to measure the redshift unless it happens to be a longer and brighter GRB, making it easier to observe the optical follow-up. It is also possible that small redshift sources will be favored, because an astronomer may not even attempt to measure the redshift of a distant and faint GRB. The combination of only being able to measure certain

GRB redshifts, and only choosing to attempt low redshift GRBs, could explain the discrepancy in Figure 8.24. Of course, it is always possible that this model is an incomplete explanation for GRBs and the two redshift populations could improve with a better model.

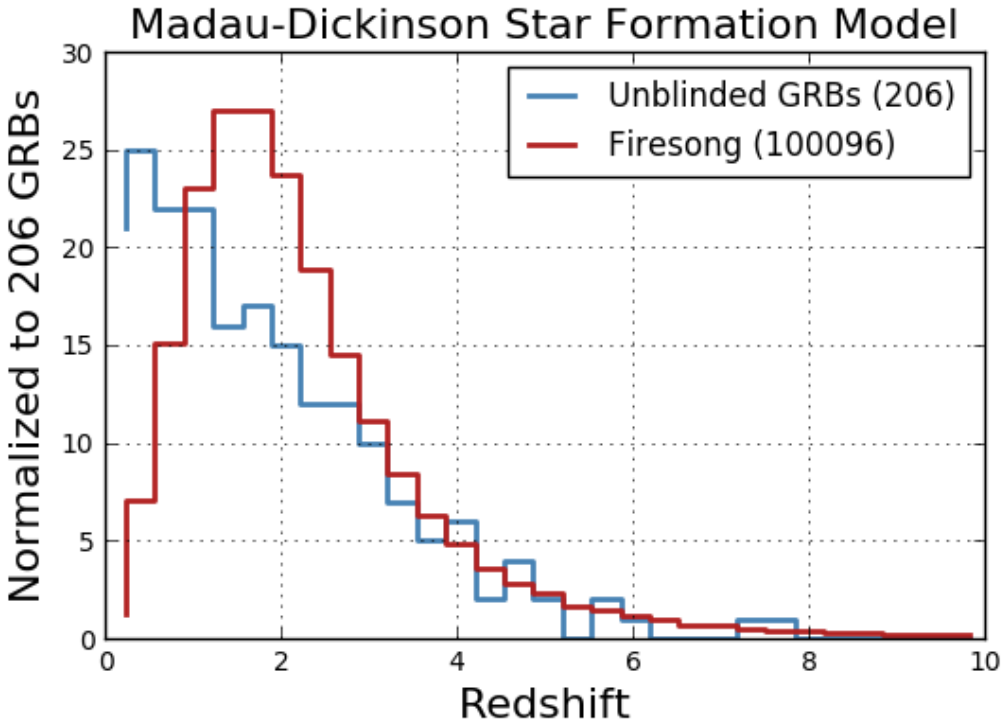

Figure 8.24: This plot shows many simulated FIRESONG GRBs normalized to 206 to match the catalog. The GRB catalog for this analysis contains 2,091 GRBs, but only 206 of those have a measured redshift. The difference between the two distributions may be caused by difficulty measuring distant GRB redshifts and an observer selection bias to only attempt measurement for low redshift GRBs.

FIRESONG generates a list of simulated sources, ranging from tens to thousands per year, for a given density and GRB luminosity (see 3.2.3 for more detail). The standard candle neutrino luminosity is constant per GRB. For each density and luminosity, 300 stacked test statistics are calculated. This stacked test statistic is found by randomly drawing 2,091 FIRESONG fluxes and assigning them to a GRB

declination. The flux is converted into an expected number of neutrinos injected, and signal-to-background values are calculated based on the expected background of the declinaton. The luminosity is converted to a total GRB energy in neutrinos by:

$$E_\nu = L_\nu \times \frac{timescale}{3.15 \times 10^7 \ s/yr} \tag{8.1}$$

This conversion is a result of FIRESONG producing luminosities over a year. It is necessary to convert using the time of the GRB as well. The "timescale" here is considered the source time in FIRESONG. However, this is also used as the observer time when injecting flux to the GRB. It is natural to assume one should use $timescale \times (1+z)$ to capture the full neutrino emission time on Earth. In fact, FIRESONG simulates neutrino production for a given timescale (e.g., 1000 seconds) in the source frame. The redshifted time for this would be much longer on Earth than the source time. However, the neutrino-GRB search is conducted in uniform time windows, independent of the GRB's redshift. This means the actual analysis applies a penalty on GRBs far away by measuring the same time window for all GRBs. It is important to accurately reflect this in the simulation.

The result of testing several densities and total energies is a grid where each point has 300 trials of an injected flux. The fraction of test statistics greater than the unblinded test statistic is saved for that grid point. A 2D spline is used to smooth this grid, and 500×500 bins are used for both the density and total energy. The result for the 1000 second time window is show in Figure 8.25. The other time

windows are shown in Appendix A.

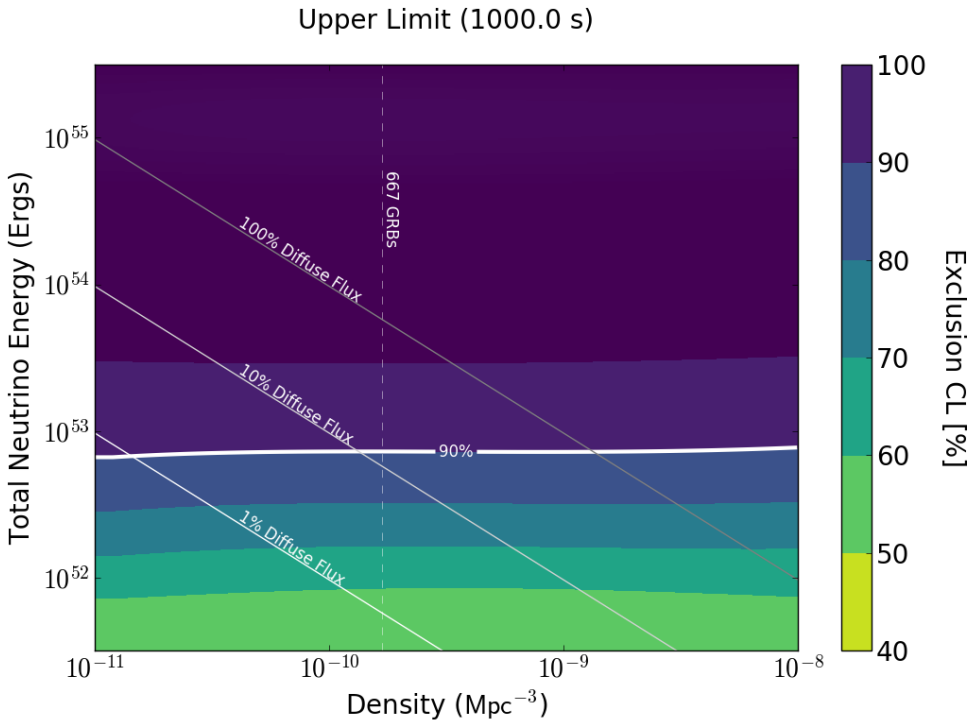

Figure 8.25: The 90% limit on the total neutrino energy from the 1000 second time window based on FIRESONG's standard candle simulation. The 90% exclusion confidence limit is roughly flat across densities because 2,091 GRBs are always drawn from the set of simulated sources. The FIRESONG source density that reproduces the historic choice of 667 GRBs per year is indicated with a vertical dashed line. The limits on the diffuse flux are indicated with the diagonal lines. If GRBs are standard candles with a density of 667 GRBs/Mpc^3, then this plot clearly shows that GRBs are ruled out at 90% confidence from producing more than 11% of the diffuse neutrino flux.

Figure 8.25 is a bit strange because the limits are roughly flat across all densities studied. This happens because the same number of sources (2,091) is considered regardless of simulated source density. If GRBs were producing neutrinos as standard candles, and 2,091 of those GRBs were observed, then energies and luminosities above the white line would have shown up in this analysis 90% of the time. The historic choice for a density of GRBs in IceCube stacked analyses is

667 per year, which refers to the number of detectable GRBs per year by operating satellites. The density required to produce 667 GRBs in the Madau-Dickinson stellar evolution model is indicated by a vertical dashed line for reference.

This same approach was carried out for all 10 time windows. The results are shown in red in Figure 8.26. The FIRESONG limit on the diffuse flux is shown as a percentage of the diffuse flux normalization, which is 0.9×10^{-8} $\frac{GeV}{cm^2 \cdot s \cdot sr}$. This flux normalization is based on a spectral index fit of 2.13, which differs from the assumption of $\gamma = 2.0$ in this analysis.

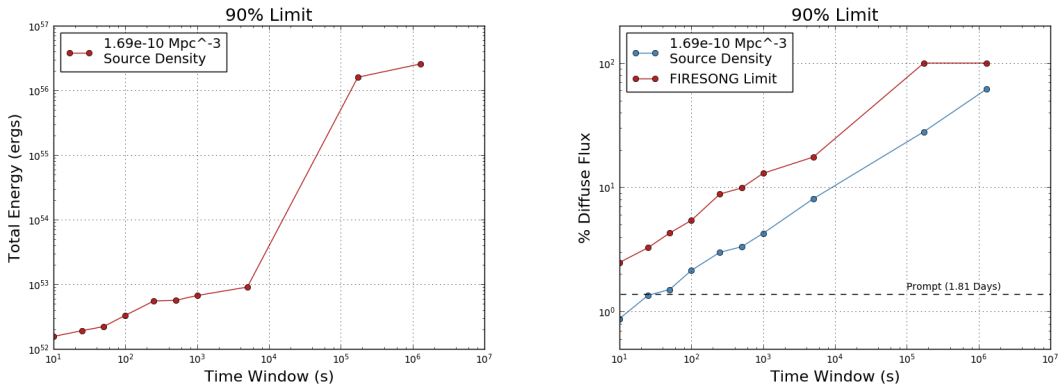

Figure 8.26: Left: The limits on standard candle source energy from FIRESONG for each time window in terms of total energy. The longest time windows are unable to constrain this value significantly. Right: The limits on standard candle neutrino emission in terms of diffuse flux percentage. The blue line shows the limits from the stacked analysis (8.3.2) for all 2,091 GRBs by time window and prompt (dashed line). The stacked analysis also includes the density assumption of 667 GRBs per year, which translates to 1.69×10^{-10} Mpc^{-3} in the Madau-Dickinson stellar evolution model (3.2.3). The FIRESONG limits (red) are capped at 100% for the longest time windows, because they are unable to constrain the standard candle hypothesis for GRB contribution to the diffuse flux.

8.4 Systematic Uncertainties

The results of this GRB search were consistent with background, leading to the upper limits presented earlier in this chapter. Determining those limits requires injecting simulated neutrino events, which brings in systematic uncertainties in ice models, DOM response, and other features of detection. The impact of these systematic uncertainties has been widely studied and quantified in previous analyses that use similar event selections, making them applicable to the limits presented in this chapter. A conservative estimate of total systematic uncertainty of 15% is applied to every limit in this chapter.

The main focus for these systematic uncertainties is in Mote Carlo simulation. The uncertainties in background are considered negligible, because the data itself is used to characterize the analysis. The simulation uncertainty is estimated by varying model parameters, processing that simulation to final event level, and calculating a new sensitivity. The change in sensitivity is summarized in Tables 8.7 and 8.6. The uncertainty for the northern sky is based on the 2015 northern sky track sample described in [90], as well as an updated 2021 northern tracks event selection [153] [154]. The southern sky uncertainty is based on the 2017 southern sky track sample described in [17].

Description	Effect relative to baseline (%) ICMART	Standard	Photospheric	E^{-2}
DOM efficiency −10%	+2.1	+1.4	+1.8	+4.0
Absorption & Scattering +10%	+1.7	+1.2	+2.1	+1.7
Other errors	+8	+8	+8	+8
Total	+8.5	+8.2	+8.50	+9.1

Table 8.6: A summary of systematic uncertainties determined for the 2015 northern sky track sample described in [90]. A conservative estimate of 15% uncertainty is applied to the upper limits in this section. The relevant column for this analysis is E^{-2}, as the other columns refer to model-specific studies.

8.4.1 Absorption and Scattering in Ice

The South Pole ice model is a potential source of uncertainty. The photon propagation simulation includes many assumptions about ice properties, which can be parametrized by light absorption and scattering coefficients (Figure 4.7). The uncertainty of absorption and scattering cofficients for the northern sky study ranged from ±10%, while the southern sky estimated a change of -7.1%/+10%. An increased absorption coefficient would lower the total light available for DOMs to record. This would lead to lower energy estimates, which would impact event selection cuts related to the energy proxy.

8.4.2 DOM Efficiency

The PMT contained in the DOM was studied before deployment by IceCube. Those studies indicated that the PMT detection efficiency was 7.7%, with an additional 2% uncertainty in the measurement of each position on the PMT face [113]. Reduced

DOM efficiency would lead to poorer direction and energy reconstructions. The efficiency of the DOM is therefore estimated at ±10% for both the northern and southern hemispheres.

Systematic	Change w.r.t. Baseline Limit			
	E^{-2}	IS Fireball	Photo. Fireball	ICMART
Anisotropic Ice Model	-1.0%	+0.8%	+1.2%	+1.5%
Absorption +10%	+6.4%	+4.4%	+4.7%	+2.6%
Scattering +10%	+9.9%	+7.5%	+9.4%	+6.1%
Absorption/Scattering -7.1%	-7.9%	-7.7%	-8.2%	-8.4%
DOM Efficiency -10%	+6.8%	+4.9%	+5.3%	+2.1%
DOM Efficiency +10%	-4.8%	-4.0%	-4.4%	-4.6%
Neutrino Cross Section	±5%	±5%	±5%	±5%
ALLM91 Nuclear Cross Section [136]	-0.4%	-2.0%	-1.7%	-1.2%
BB81 Nuclear Cross Section [137]	+1.7%	+1.8%	+0.5%	-0.4%
Total	+14.6%	+11.3%	+12.8%	+8.7%

Table 8.7: A summary of systematic uncertainties determined for the 2017 southern sky track sample described in [17]. A conservative estimate of 15% uncertainty is applied to the upper limits in this section. The relevant column for this analysis is E^{-2}, as the other columns refer to model-specific studies.

8.4.3 Summary

Ice models and DOM efficiency are the primary sources of uncertainty. Additional errors, such as interaction cross section, muon energy loss during propagation, and rock density near the detector are estimated to contribute up to 8%. The results of varying potential sources of uncertainty are summarized in Tables 8.7 and 8.6.

The total systematic uncertainty for E^{-2} in the southern sky was found to be 14.6% [17]. This is rounded to 15% as a conservative estimate of error. The total systematic uncertainty for the northern sky from [90] was found to be 9.1% for E^{-2}. The 2021 northern tracks sample estimates this uncertainty is at most 15% [153]

[154]. Out of an abundance of caution, the 15% error is applied to the northern sky as well.

Chapter 9: Outlook

This thesis presented an all-sky search for muon neutrinos correlated with 2,091 GRBs. The individual GRBs were studied at ten time windows, ranging from ten seconds to 15 days. P-values were calculated for each of the time windows, and the most signifcant p-value was selected for a Binomial test. The Binomial test was performed on four sub-populations of GRBs, split by northern and southern sky as well as by short (<2 s) and long (>2 s) GRBs.

Previous GRB searches focused on the prompt gamma-ray emission time and performed stacked analyses to determine if all GRBs were contributing small neutrino fluences. These searches were found to be consistent with background and GRBs were demoted to sources producing only a few percent of observed neutrinos. The tight constraints on the prompt emission from stacking searches, which assume all GRBs contribute a small neutrino fluence, led to the current study performing the Binomial test in search of a smaller "warm" popultion of GRBs within the larger group. The Binomial test in this analysis was also found to be consistent with background.

The 23 most significant GRBs in this search were studied in greater detail and, while hints of possible precursors or afterglow neutrinos taunt the analyzer,

the results are consistent with statistical flucuations from background. The most significant pre-trials p-value for the northern long sub-population is 6×10^{-4} for GRB 140607A. This translates to a post-trials p-value of 0.44 for a correction of 960 GRBs in the sub-population and a post-trials p-value of 0.71 if corrected for the entire 2,091 GRB sample. The most significant GRB of the entire group was the southern long GRB 150202A with 5×10^{-4} for the pre-trials p-value. This is a post-trials p-value of 0.33 for the 814 southern long sub-population correction, and 0.65 for an overall post-trials p-value correction. These top GRBs are completely consistent with background.

And yet, this is not quite a death knell for GRBs as major neutrino emitters. The tight constraints from stacked limits in this (and previous) studies assume all GRBs produce equal neutrino fluence on Earth, which has no physical motivation. GRBs vary by orders of magnitude in terms of photon fluence and energy, making a "one size fits all" assumption incomplete. The benefit of the standard candle approach is to demonstrate that different assumptions allow GRBs to produce up to $\sim$10% of the diffuse neutrino flux rather than $\sim$1%. Additional study of neutrino production models from GRBs is warranted.

In particular, it is worth studying the impact of source density and brightness on neutrino emission. There may be populations of GRBs that are not detected because they 1) are not emitting gamma rays due to choked jets [155] [156] or 2) have lower source energies and therefore are not bright enough in gamma rays. If GRBs are more dense than the typical assumption of 667 per year, then each individual source may emit fewer neutrinos and be more difficult to detect. If a subset of GRBs

are gamma-ray-dark, but still producing neutrinos, then these could be searched using afterglow signatures that are comparable to those of gamma-ray-bright GRBs without the gamma-ray precursor.

A focus of future IceCube studies should be the real-time follow-up of all detected GRBs. This analysis was designed to study any GRBs efficiently, requiring only 20 minutes to scan the prompt, +/-1 day, and -1/+14 days. Incorporating this (or a similar) analysis into IceCube's real-time framework will provide valuable insight to the GRB community. New models of choked jet and low luminosity GRBs are constantly being developed, and the results from IceCube can be very helpful for shaping those models. A Binomial test or stacked analysis could be done at the end of every season to study the population results and provide an IceCube limit.

The study presented in this thesis supports the mounting evidence that GRBs observed by satellites are not major contributors to the diffuse neutrino flux or the highest energy cosmic rays. If GRBs are standard candle neutrino emitters, then they account for a maximum of 11% of the diffuse flux up to 1,000 second timescales. This may indicate a need for additional subclasses of gamma-ray bursts [157] or further study of choked jets GRBs, which may have the conditions for hadron acceleration and neutrino production without the high-energy gamma rays. Although no longer the favored candidate for UHECR acceleration, GRBs are still worth analyzing for neutrino counterparts and may surprise us all in the world of real-time analyses.

Appendix A: Additional Plots

The results for the most significant GRBs are shown below. The three plots are the same for each GRB: the event times, energies, and S/B for the on-time events in the most significant time window. The most significant GRB of each group is discussed in greater detail in 8.2.

A.1 Most Significant Individual GRBs

A.1.1 Northern Sky Long GRBs

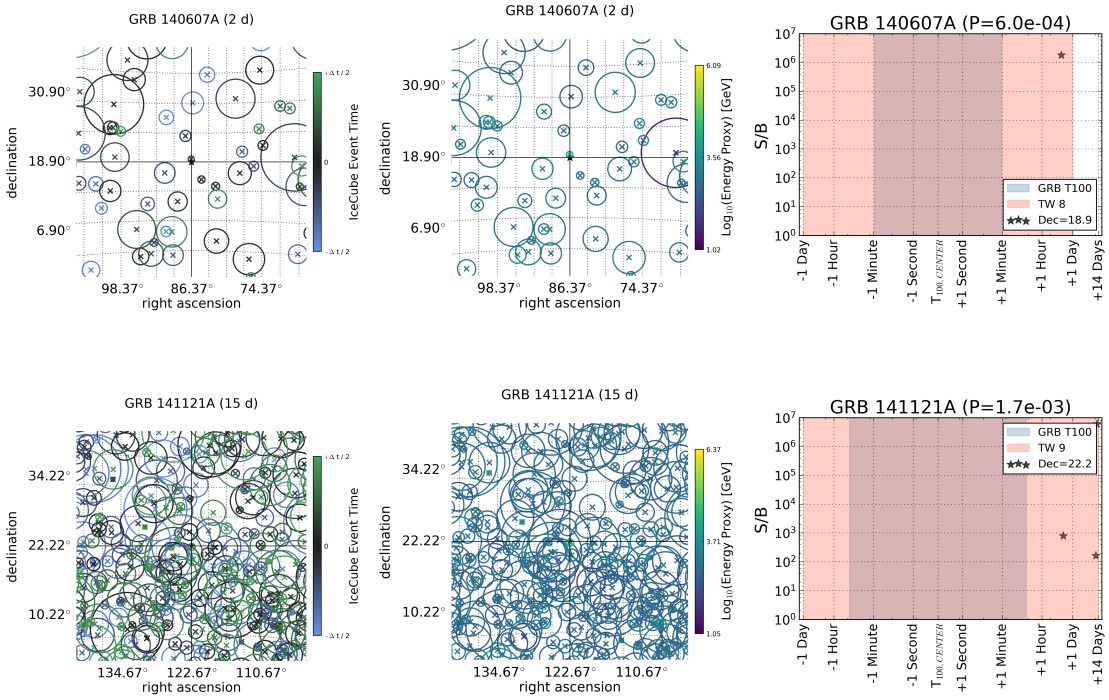

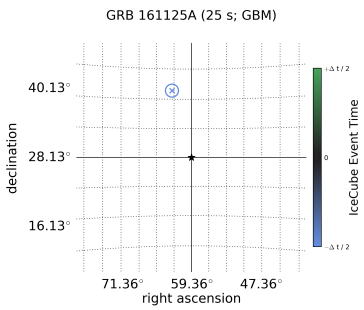
GRB 161125A (25 s; GBM)
declination
right ascension
IceCube Event Time

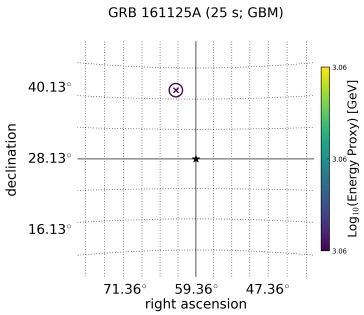
GRB 161125A (25 s; GBM)
declination
right ascension
Log10(Energy Proxy) [GeV]

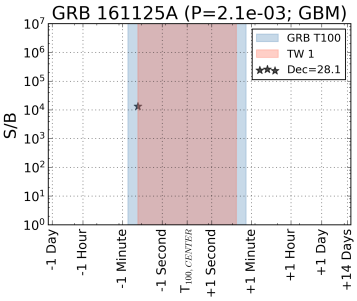
GRB 161125A (P=2.1e-03; GBM)
GRB T100
TW 1
Dec=28.1
S/B

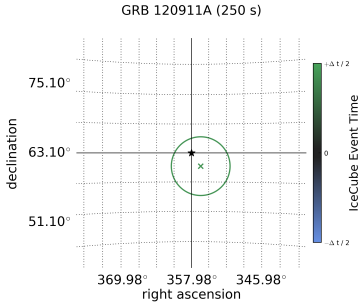
GRB 120911A (250 s)
declination
right ascension
IceCube Event Time

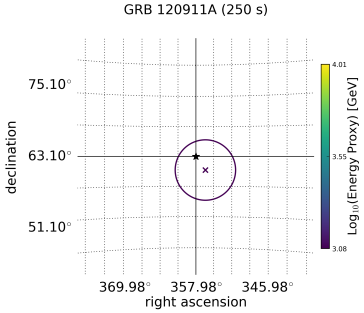
GRB 120911A (250 s)
declination
right ascension
Log10(Energy Proxy) [GeV]

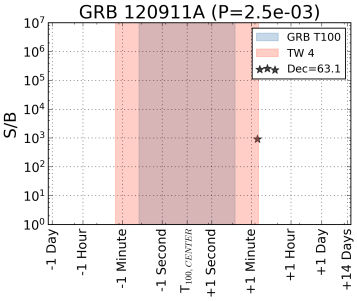
GRB 120911A (P=2.5e-03)
GRB T100
TW 4
Dec=63.1
S/B

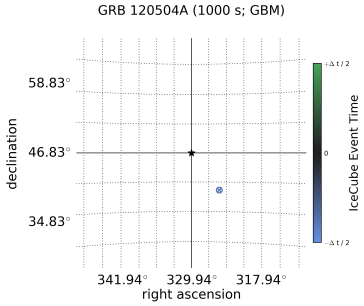
GRB 120504A (1000 s; GBM)
declination
right ascension
IceCube Event Time

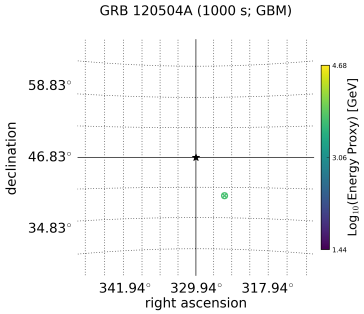
GRB 120504A (1000 s; GBM)
declination
right ascension
Log10(Energy Proxy) [GeV]

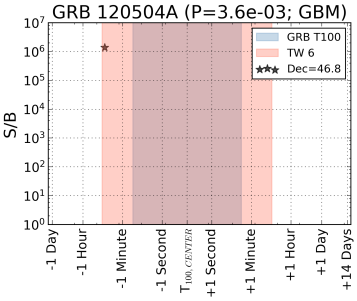
GRB 120504A (P=3.6e-03; GBM)
GRB T100
TW 6
Dec=46.8
S/B

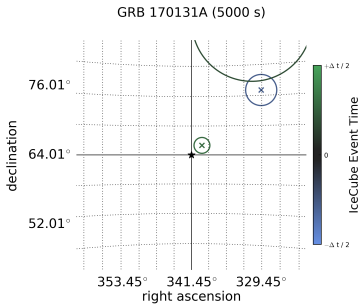
GRB 170131A (5000 s)
declination
right ascension
IceCube Event Time

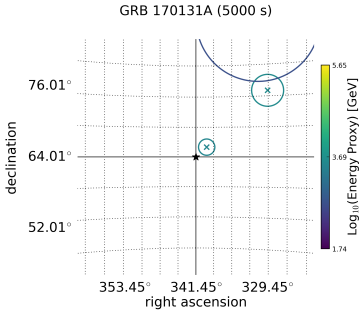
GRB 170131A (5000 s)
declination
right ascension
Log10(Energy Proxy) [GeV]

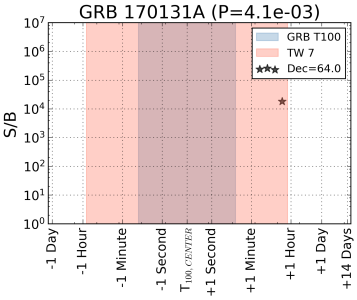
GRB 170131A (P=4.1e-03)
GRB T100
TW 7
Dec=64.0
S/B

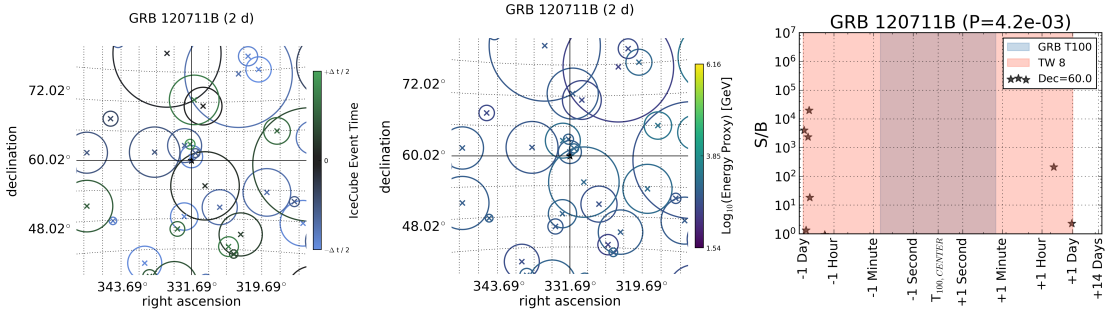
GRB 120711B (2 d)
declination
right ascension
IceCube Event Time
GRB 120711B (2 d)
declination
right ascension
Log10(Energy Proxy) [GeV]
GRB 120711B (P=4.2e-03)
S/B
GRB T100
TW 8
Dec=60.0
-1 Day
-1 Hour
-1 Minute
-1 Second
T100, CENTER
+1 Second
+1 Minute
+1 Hour
+1 Day
+14 Days

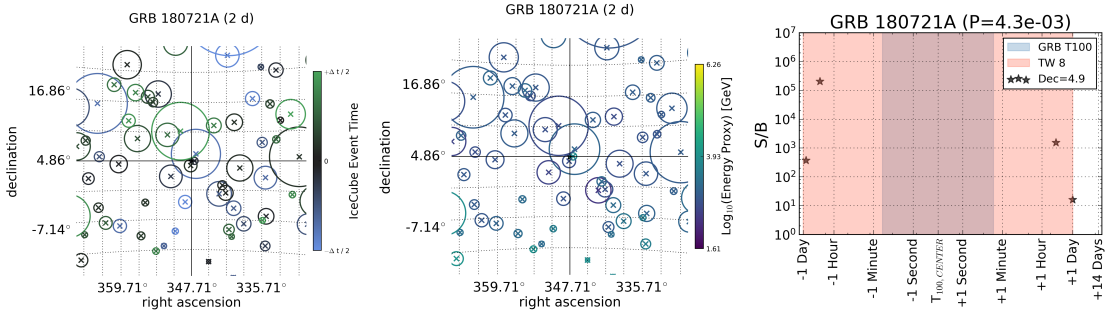
GRB 180721A (2 d)
declination
right ascension
IceCube Event Time
GRB 180721A (2 d)
declination
right ascension
Log10(Energy Proxy) [GeV]
GRB 180721A (P=4.3e-03)
S/B
GRB T100
TW 8
Dec=4.9
-1 Day
-1 Hour
-1 Minute
-1 Second
T100, CENTER
+1 Second
+1 Minute
+1 Hour
+1 Day
+14 Days

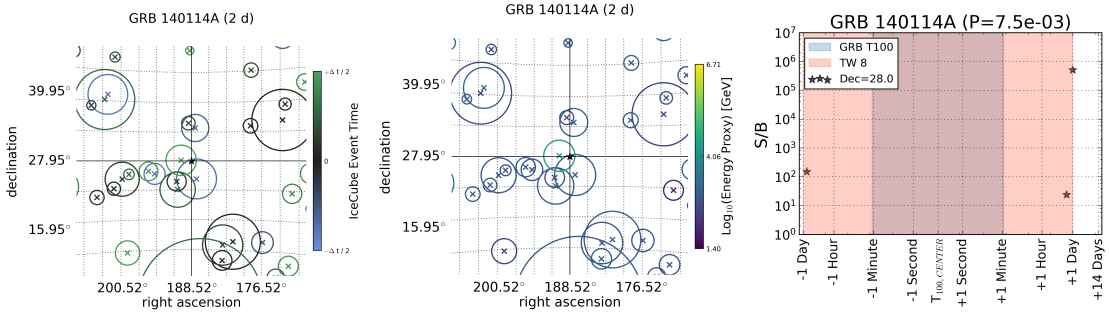
GRB 140114A (2 d)
declination
right ascension
IceCube Event Time
GRB 140114A (2 d)
declination
right ascension
Log10(Energy Proxy) [GeV]
GRB 140114A (P=7.5e-03)
S/B
GRB T100
TW 8
Dec=28.0
-1 Day
-1 Hour
-1 Minute
-1 Second
T100, CENTER
+1 Second
+1 Minute
+1 Hour
+1 Day
+14 Days

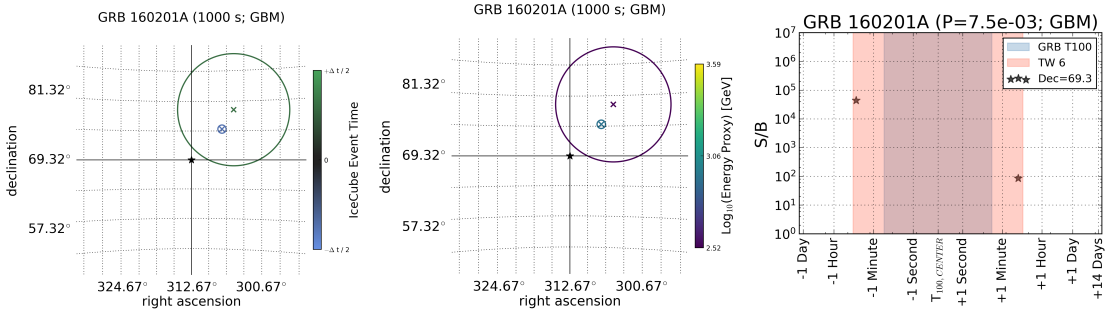
GRB 160201A (1000 s; GBM)
declination
right ascension
IceCube Event Time
GRB 160201A (1000 s; GBM)
declination
right ascension
Log10(Energy Proxy) [GeV]
GRB 160201A (P=7.5e-03; GBM)
S/B
GRB T100
TW 6
Dec=69.3
-1 Day
-1 Hour
-1 Minute
-1 Second
T100, CENTER
+1 Second
+1 Minute
+1 Hour
+1 Day
+14 Days

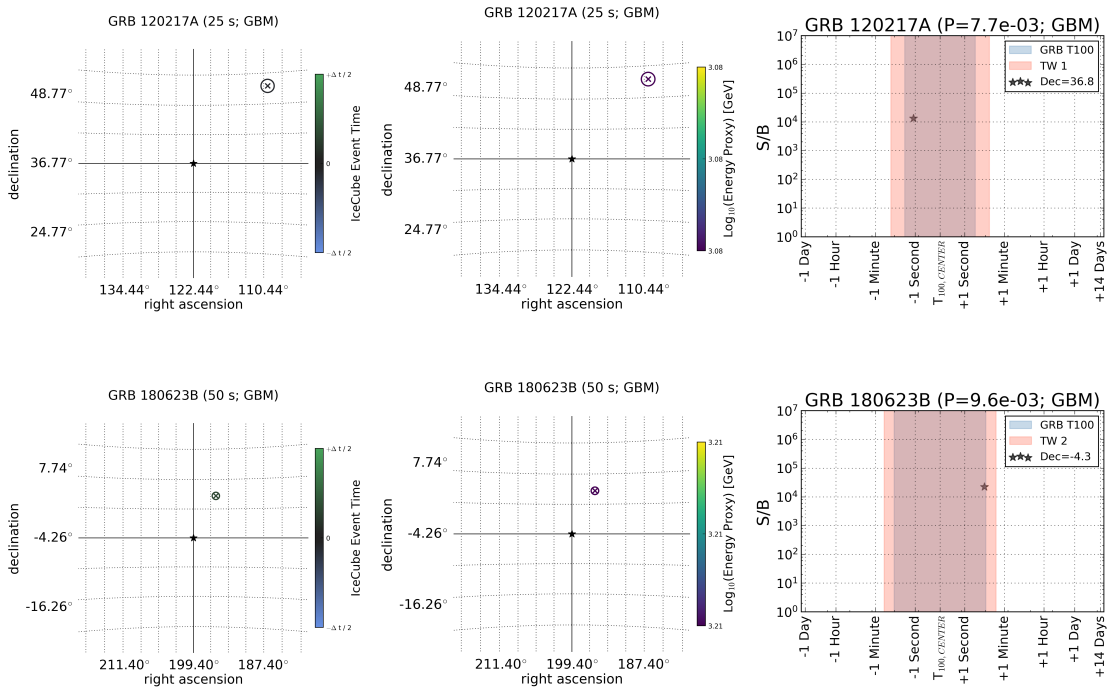

A.1.2 Northern Sky Short GRBs

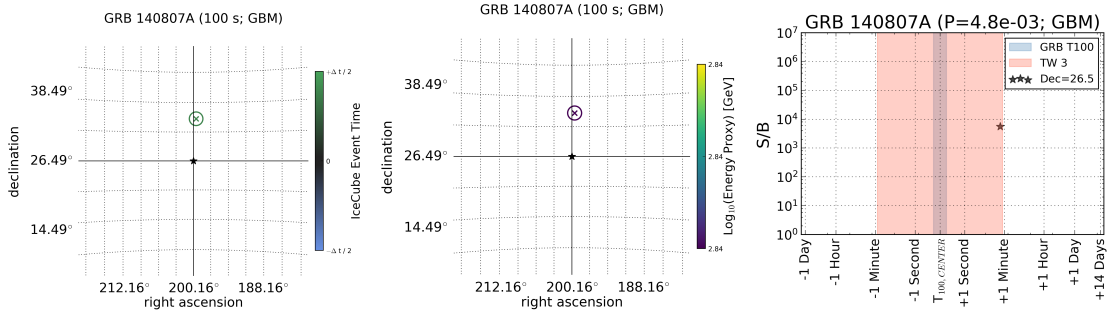

A.1.3 Southern Sky Long GRBs

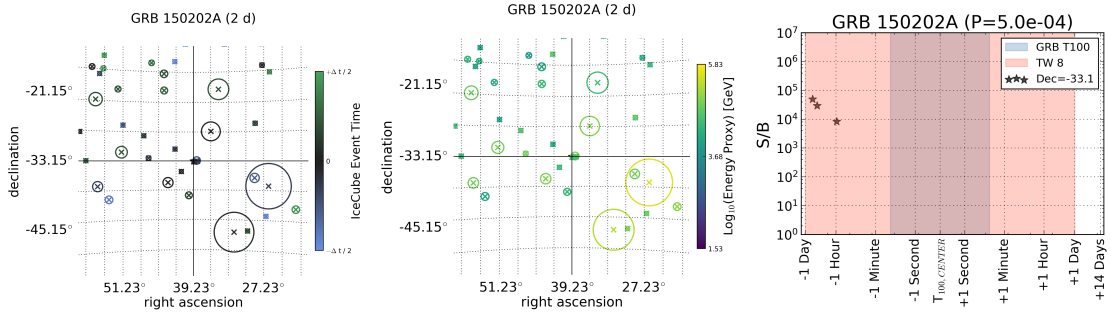

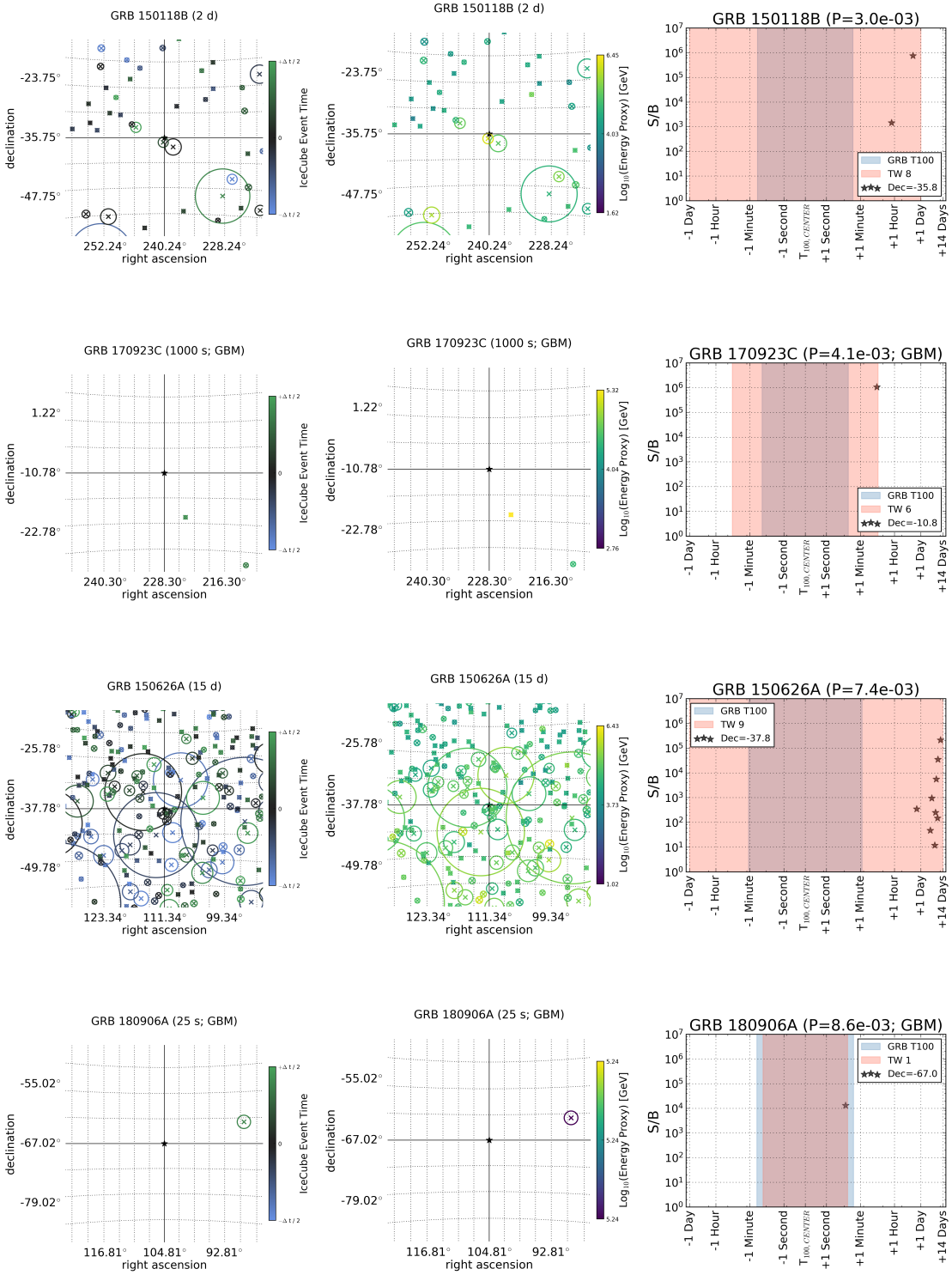
GRB 150118B (2 d)
declination
-23.75°
-35.75°
-47.75°
252.24°
240.24°
228.24°
right ascension
IceCube Event Time
GRB 150118B (2 d)
declination
-23.75°
-35.75°
-47.75°
252.24°
240.24°
228.24°
right ascension
Log10(Energy Proxy) [GeV]
6.45
4.03
1.62
GRB 150118B (P=3.0e-03)
S/B
GRB T100
TW 8
Dec=-35.8
-1 Day
-1 Hour
-1 Minute
-1 Second
T100, CENTER
+1 Second
+1 Minute
+1 Hour
+1 Day
+14 Days
GRB 170923C (1000 s; GBM)
declination
1.22°
-10.78°
-22.78°
240.30°
228.30°
216.30°
right ascension
IceCube Event Time
GRB 170923C (1000 s; GBM)
declination
1.22°
-10.78°
-22.78°
240.30°
228.30°
216.30°
right ascension
Log10(Energy Proxy) [GeV]
5.32
4.04
2.76
GRB 170923C (P=4.1e-03; GBM)
S/B
GRB T100
TW 6
Dec=-10.8
-1 Day
-1 Hour
-1 Minute
-1 Second
T100, CENTER
+1 Second
+1 Minute
+1 Hour
+1 Day
+14 Days
GRB 150626A (15 d)
declination
-25.78°
-37.78°
-49.78°
123.34°
111.34°
99.34°
right ascension
IceCube Event Time
GRB 150626A (15 d)
declination
-25.78°
-37.78°
-49.78°
123.34°
111.34°
99.34°
right ascension
Log10(Energy Proxy) [GeV]
6.43
3.72
1.02
GRB 150626A (P=7.4e-03)
S/B
GRB T100
TW 9
Dec=-37.8
-1 Day
-1 Hour
-1 Minute
-1 Second
T100, CENTER
+1 Second
+1 Minute
+1 Hour
+1 Day
+14 Days
GRB 180906A (25 s; GBM)
declination
-55.02°
-67.02°
-79.02°
116.81°
104.81°
92.81°
right ascension
IceCube Event Time
GRB 180906A (25 s; GBM)
declination
-55.02°
-67.02°
-79.02°
116.81°
104.81°
92.81°
right ascension
Log10(Energy Proxy) [GeV]
5.24
5.24
5.24
GRB 180906A (P=8.6e-03; GBM)
S/B
GRB T100
TW 1
Dec=-67.0
-1 Day
-1 Hour
-1 Minute
-1 Second
T100, CENTER
+1 Second
+1 Minute
+1 Hour
+1 Day
+14 Days

A.1.4 Southern Sky Short GRBs

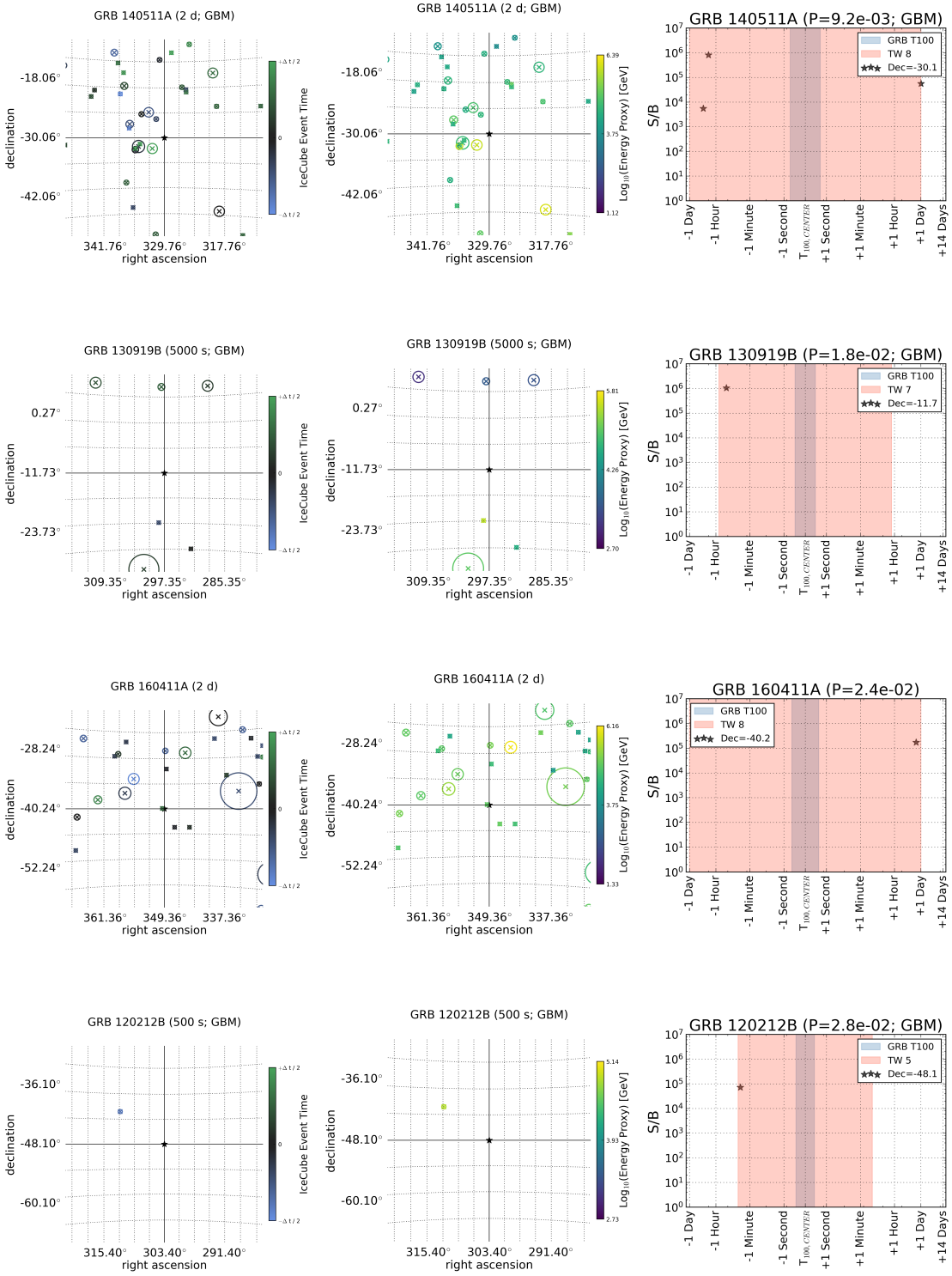

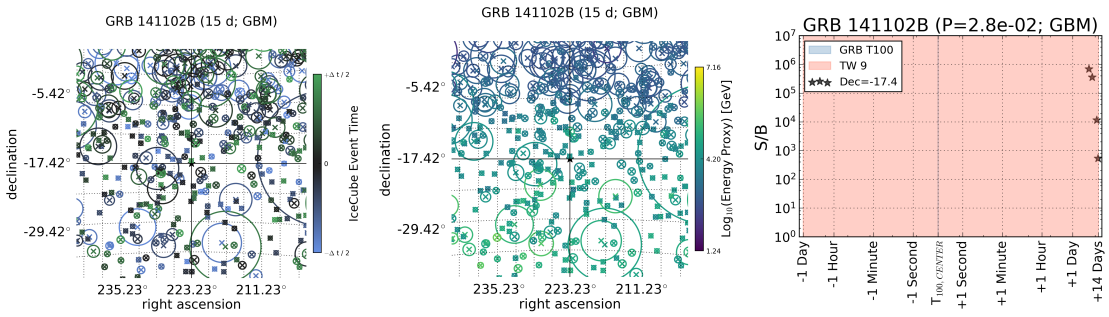

A.2 Firesong Limits

The 90% limit on the total neutrino energy for the ten time windows based on FIRESONG's standard candle simulation. The 90% exclusion confidence limit is roughly flat across declinations because 2,091 GRBs are always drawn from the set of simulated sources. The historic choice of 667 GRBs/Mpc^3 per year is indicated with a vertical dashed line. The limits on the diffuse flux are indicated with the diagonal lines. This is discussed in detail for the 1000 second time window in 8.3.3.

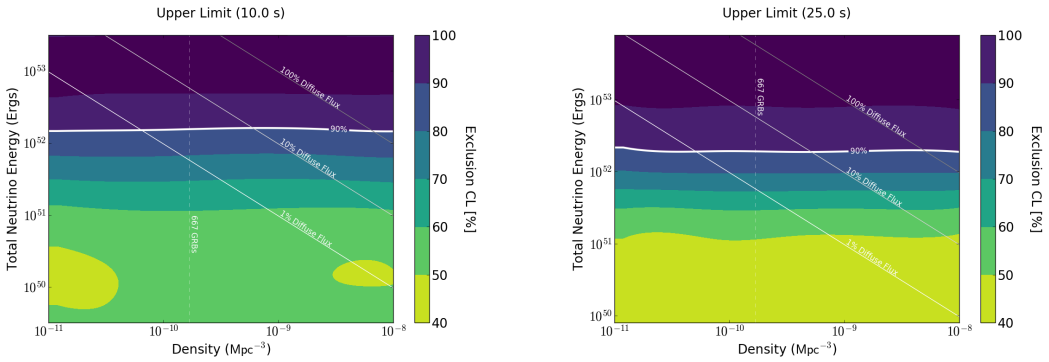

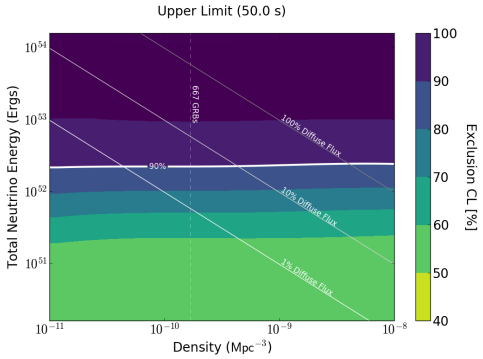
Upper Limit (50.0 s)
667 GRBs
100% Diffuse Flux
10% Diffuse Flux
1% Diffuse Flux
90%
Total Neutrino Energy (Ergs)
Density (Mpc^{-3})
Exclusion CL [%]

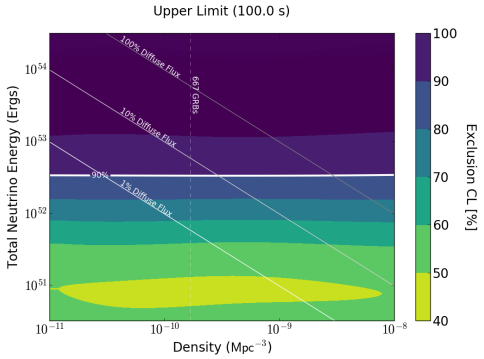
Upper Limit (100.0 s)
667 GRBs
100% Diffuse Flux
10% Diffuse Flux
1% Diffuse Flux
90%
Total Neutrino Energy (Ergs)
Density (Mpc^{-3})
Exclusion CL [%]

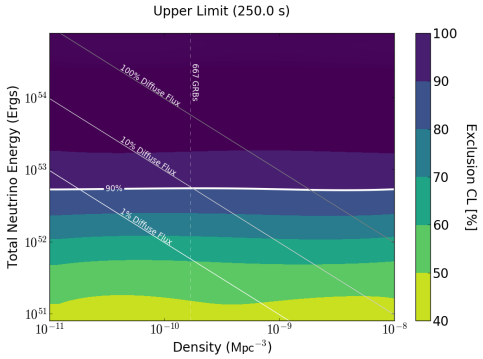
Upper Limit (250.0 s)
667 GRBs
100% Diffuse Flux
10% Diffuse Flux
1% Diffuse Flux
90%
Total Neutrino Energy (Ergs)
Density (Mpc^{-3})
Exclusion CL [%]

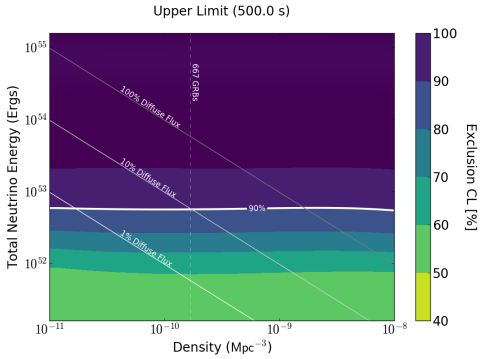
Upper Limit (500.0 s)
667 GRBs
100% Diffuse Flux
10% Diffuse Flux
1% Diffuse Flux
90%
Total Neutrino Energy (Ergs)
Density (Mpc^{-3})
Exclusion CL [%]

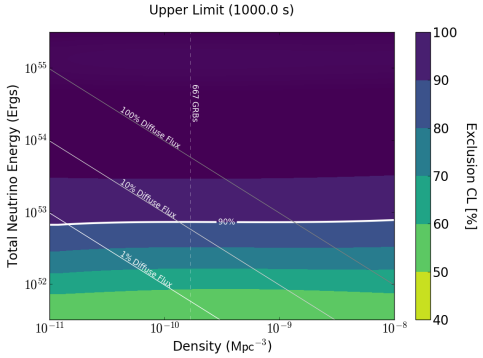
Upper Limit (1000.0 s)
667 GRBs
100% Diffuse Flux
10% Diffuse Flux
1% Diffuse Flux
90%
Total Neutrino Energy (Ergs)
Density (Mpc^{-3})
Exclusion CL [%]

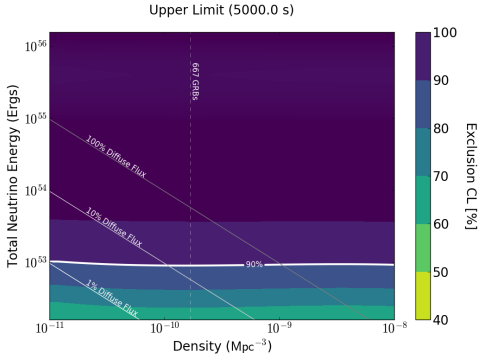
Upper Limit (5000.0 s)
667 GRBs
100% Diffuse Flux
10% Diffuse Flux
1% Diffuse Flux
90%
Total Neutrino Energy (Ergs)
Density (Mpc^{-3})
Exclusion CL [%]

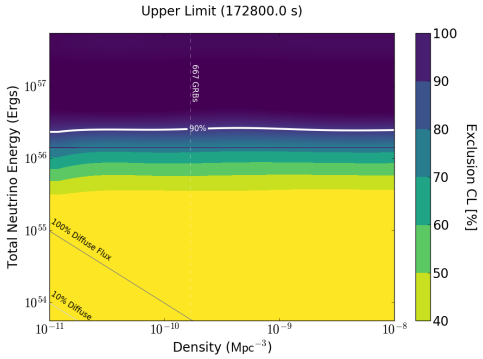
Upper Limit (172800.0 s)
667 GRBs
90%
100% Diffuse Flux
10% Diffuse
Total Neutrino Energy (Ergs)
Density (Mpc^{-3})
Exclusion CL [%]

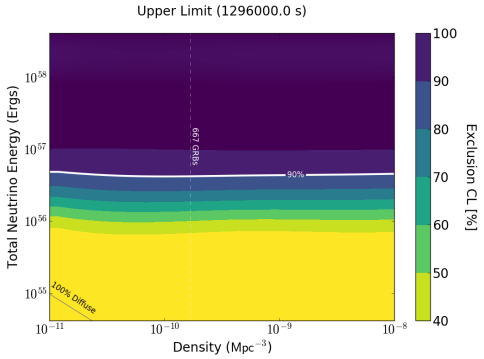
Upper Limit (1296000.0 s)
667 GRBs
90%
100% Diffuse
Total Neutrino Energy (Ergs)
Density (Mpc^{-3})
Exclusion CL [%]

Bibliography

[1] Chodos, Alan. *This Month in Physics History*. 2010. URL: https://www.aps.org/publications/apsnews/201004/physicshistory.cfm.

[2] The Pierre Auger Collaboration. "Combined fit of spectrum and composition data as measured by the Pierre Auger Observatory". In: (2016). DOI: 10.1088/1475-7516/2017/04/038. eprint: arXiv:1612.07155.

[3] R.U. Abbasi, M. Abe, and T. Abu-Zayyad et al. "Study of Ultra-High Energy Cosmic Ray composition using Telescope Array's Middle Drum detector and surface array in hybrid mode". In: *Astroparticle Physics* 64 (2015), pp. 49–62. URL: https://doi.org/10.1016/j.astropartphys.2014.11.004..

[4] R. U. Abbasi, T. Abu-Zayyad, and et al. Al-Seady. "Indications of Proton-Dominated Cosmic-Ray Composition above 1.6 EeV". In: *Phys. Rev. Lett.* 104 (16 2010), p. 161101. DOI: 10.1103/PhysRevLett.104.161101. URL: https://link.aps.org/doi/10.1103/PhysRevLett.104.161101.

[5] Hans Peter Dembinski et al. "Data-driven model of the cosmic-ray flux and mass composition from 10 GeV to 10Î1 GeV". In: *PoS* ICRC2017 (2017). URL: https://arxiv.org/pdf/1711.11432.pdf.

[6] Luke O'C. Drury. "Origin(s) of Cosmic Rays". In: *PoS* CRISM 2014 (2014). eprint: https://arxiv.org/pdf/1412.1376.pdf.

[7] Emma de Oña Wilhelmi et al. "SNR G39.2-0.3, an hadronic cosmic rays accelerator". In: *Monthly Notices of the Royal Astronomical Society* 497.3 (2020), 3581–3590. ISSN: 1365-2966. DOI: 10.1093/mnras/staa2045. URL: http://dx.doi.org/10.1093/mnras/staa2045.

[8] ENRICO Fermi. "On the Origin of the Cosmic Radiation". In: *Phys. Rev.* 75 (8 1949), pp. 1169–1174. DOI: 10.1103/PhysRev.75.1169. URL: https://link.aps.org/doi/10.1103/PhysRev.75.1169.

[9] Thomas K. Gaisser, Ralph Engel, and Elisa Resconi. *Cosmic rays and particle physics*. Cambridge University Press, 2016.

[10] Matthew G. Baring. "Diffusive shock acceleration: The Fermi mechanism". In: *32nd Rencontres de Moriond: High-Energy Phenomena in Astrophysics*. 1997, pp. 97–106. arXiv: astro-ph/9711177.

[11] Ackermann, M. et al. "Detection of the Characteristic Pion-Decay Signature in Supernova Remnants". In: *Science* 338 (6121 2013), pp. 807–811.

[12] Felix Aharonian, Ruizhi Yang, and Emma de Oña Wilhelmi. *Massive Stars as Major Factories of Galactic Cosmic Rays*. 2019. arXiv: 1804.02331 [astro-ph.HE].

[13] Matthiae, Giorgio. "The cosmic ray energy spectrum as measured using the Pierre Auger Observatory". In: *New Journal of Physics* 12.7 (2010), p. 075009. DOI: 10.1088/1367-2630/12/7/075009.

[14] A. M. Hillas. "The Origin of Ultrahigh-Energy Cosmic Rays". In: *Ann. Rev. Astron. Astrophys.* 22 (1984), pp. 425–444. DOI: 10.1146/annurev.aa.22.090184.002233.

[15] LUIS ANCHORDOQUI et al. "ULTRAHIGH ENERGY COSMIC RAYS: THE STATE OF THE ART BEFORE THE AUGER OBSERVATORY". In: *International Journal of Modern Physics A* 18.13 (May 2003), pp. 2229–2366. DOI: 10.1142/s0217751x03013879. URL: https://doi.org/10.1142/s0217751x03013879.

[16] Tsvi Piran. "Magnetic Fields in Gamma-Ray Bursts: A Short Overview". In: *AIP Conference Proceedings* 784 (1 2005), pp. 2229–2366. DOI: https://doi.org/10.1063/1.2077181. URL: https://aip.scitation.org/doi/pdf/10.1063/1.2077181.

[17] Maunu, Ryan Edward. "A search for muon neutrinos in coincidence with gamma-ray bursts in the southern hemisphere sky using the IceCube neutrino observatory". PhD thesis. University of Maryland, 2016.

[18] Greisen, Kenneth. "End to the Cosmic-Ray Spectrum?" In: *Phys. Rev. Lett.* 16 (17 1966), pp. 748–750. DOI: 10.1103/PhysRevLett.16.748. URL: https://link.aps.org/doi/10.1103/PhysRevLett.16.748.

[19] Zatsepin, G. T. and Kuzmin, V. A. "Upper limit of the spectrum of cosmic rays". In: *JETP Lett.* 4 (1966), pp. 78–80.

[20] P Sommers and S Westerhoff. "Cosmic ray astronomy". In: *New Journal of Physics* 11 (2009), p. 055004.

[21] Thomas K. Gaisser, Francis Halzen, and Todor Stanev. "Particle astrophysics with high energy neutrinos". In: *Physics Reports* 258.3 (1995), 173–236. ISSN: 0370-1573. DOI: 10.1016/0370-1573(95)00003-y. URL: http://dx.doi.org/10.1016/0370-1573(95)00003-Y.

[22] Physics Open Lab. *Cosmic Ray Muons & Muon Lifetime*. 2016. URL: http://physicsopenlab.org/2016/01/10/cosmic-muons-decay/.

[23] Lorenzo Amati. "The Ep,i–Eiso correlation in gamma-ray bursts: updated observational status, re-analysis and main implications". In: *Monthly Notices of the Royal Astronomical Society* 372 (1 2006), pp. 233–245. DOI: https://doi.org/10.1111/j.1365-2966.2006.10840.x. URL: https://academic.oup.com/mnras/article/372/1/233/976830.

[24] T. Sakamoto et al. “THE SECOND SWIFT BURST ALERT TELESCOPE GAMMA-RAY BURST CATALOG”. In: *The Astrophysical Journal* 195 (2011). URL: https://iopscience.iop.org/article/10.1088/0067-0049/195/1/2.

[25] LIGO Scientific Collaboration et al. “Gravitational Waves and Gamma-rays from a Binary Neutron Star Merger: GW170817 and GRB 170817A”. In: (2017). DOI: 10.3847/2041-8213/aa920c. eprint: arXiv:1710.05834.

[26] B. P. Abbott, R. Abbot, and et al. Abbott T.D. “GW170817: Observation of Gravitational Waves from a Binary Neutron Star Inspiral”. In: *Physical Review Letters* 119.16 (2017). ISSN: 1079-7114. DOI: 10.1103/physrevlett.119.161101. URL: http://dx.doi.org/10.1103/PhysRevLett.119.161101.

[27] Jens Hjorth and Joshua S. Bloom. “The Gamma-Ray Burst - Supernova Connection”. In: (2011). eprint: arXiv:1104.2274.

[28] William S. et al. Paciesas. “The Fourth BATSE Gamma-Ray Burst Catalog (Revised)”. In: *The Astrophysical Journal Supplement Series* 122.2 (1999), 465–495. ISSN: 1538-4365. DOI: 10.1086/313224. URL: http://dx.doi.org/10.1086/313224.

[29] Klebesadel, R. W., Strong, I. B., and Olson, R. A. “Observations of Gamma-Ray Bursts of Cosmic Origin”. In: *Astrophysical Journal* 182 (1973), p. L85.

[30] Bonnell, J. *A Brief History of the Discovery of Cosmic Gamma-Ray Bursts*. 1995. URL: https://apod.nasa.gov/htmltest/jbonnell/www/grbhist.html.

[31] Cline, T. L. et al. “Energy Spectra of Cosmic Gamma-Ray Bursts”. In: *Astrophysical Journal* 185 (1973), p. L1.

[32] Hurley, K. “Receding from our grasp”. In: *Nature* 357 (1992), pp. 112–113.

[33] D. Guetta et al. “Neutrinos from individual gamma-ray bursts in the BATSE catalog”. In: *Astroparticle Physics* 20.4 (2004), 429–455. ISSN: 0927-6505. DOI: 10.1016/s0927-6505(03)00211-1. URL: http://dx.doi.org/10.1016/S0927-6505(03)00211-1.

[34] The IceCube Collaboration. “Extending the search for muon neutrinos coincident with gamma-ray bursts in IceCube data”. In: *Astrophysical Journal* (2017). DOI: 10.3847/1538-4357/aa7569. eprint: arXiv:1702.06868.

[35] Bing Zhang and Pawan Kumar. “Model-Dependent High-Energy Neutrino Flux from Gamma-Ray Bursts”. In: *Physical Review Letters* 110.12 (2013). ISSN: 1079-7114. DOI: 10.1103/physrevlett.110.121101. URL: http://dx.doi.org/10.1103/PhysRevLett.110.121101.

[36] Soebur Razzaque, Peter Mészáros, and Eli Waxman. “Neutrino tomography of gamma ray bursts and massive stellar collapses”. In: *Physical Review D* 68.8 (2003). ISSN: 1089-4918. DOI: 10.1103/physrevd.68.083001. URL: http://dx.doi.org/10.1103/PhysRevD.68.083001.

[37] Peter Mészáros and Eli Waxman. "TeV Neutrinos from Successful and Choked Gamma-Ray Bursts". In: *Physical Review Letters* 87.17 (2001). ISSN: 1079-7114. DOI: 10.1103/physrevlett.87.171102. URL: http://dx.doi.org/10.1103/PhysRevLett.87.171102.

[38] D. Guetta et al. "Neutrinos from individual gamma-ray bursts in the BATSE catalog". In: *Astroparticle Physics* 20.4 (2004), 429–455. ISSN: 0927-6505. DOI: 10.1016/s0927-6505(03)00211-1. URL: http://dx.doi.org/10.1016/S0927-6505(03)00211-1.

[39] *The Neil Gehrels Swift Observatory*. URL: https://swift.gsfc.nasa.gov/.

[40] Scott D. Barthelmy et al. "The Burst Alert Telescope (BAT) on the SWIFT Midex Mission". In: *Space Science Reviews* 120.3-4 (2005), 143–164. ISSN: 1572-9672. DOI: 10.1007/s11214-005-5096-3. URL: http://dx.doi.org/10.1007/s11214-005-5096-3.

[41] David N. Burrows et al. "The Swift X-Ray Telescope". In: *Space Science Reviews* 120.3-4 (2005), 165–195. ISSN: 1572-9672. DOI: 10.1007/s11214-005-5097-2. URL: http://dx.doi.org/10.1007/s11214-005-5097-2.

[42] Peter W. A. Roming et al. "The Swift Ultra-Violet/Optical Telescope". In: *Space Science Reviews* 120.3-4 (2005), 95–142. ISSN: 1572-9672. DOI: 10.1007/s11214-005-5095-4. URL: http://dx.doi.org/10.1007/s11214-005-5095-4.

[43] Myers, J.D., ed. *About the Swift Gamma-Ray Burst Mission*. 2012. URL: https://swift.gsfc.nasa.gov/about_swift/#science.

[44] *Swift's Burst Alert Telescope (BAT)*. URL: https://swift.gsfc.nasa.gov/about_swift/bat_desc.html.

[45] Ryba, Jeanne, ed. *Swift Mission: Spacecraft & Instruments*. 2010. URL: https://www.nasa.gov/mission_pages/swift/spacecraft/index.html.

[46] Dunbar, Brian, ed. *Fermi Gamma-ray Space Telescope*. 2017. URL: https://www.nasa.gov/content/goddard/fermi-spacecraft-and-instruments.

[47] Wild, Flint, ed. *What is the Fermi Gamma-ray Space Telescope?* 2017. URL: https://www.nasa.gov/audience/forstudents/5-8/features/nasa-knows/what-is-the-fermi-telescope-58.html.

[48] C. Winkler et al. "The INTEGRAL mission". In: *Astronomy & Astrophysics* 411 (2003). DOI: https://doi.org/10.1051/0004-6361:20031288.

[49] R. L. Aptekar et al. "Konus-W gamma-ray burst experiment for the GGS Wind spacecraft". In: *Space Science Reviews* 71 (1995). DOI: https://doi.org/10.1007/BF00751332.

[50] M. Matsuoka et al. "The MAXI Mission on the ISS: Science and Instruments for Monitoring All-Sky X-Ray Images". In: *Publications of the Astronomical Society of Japan* 61 (5 2009), pp. 999–1010. DOI: https://doi.org/10.1093/pasj/61.5.999.

[51] M. Tavani et al. "The AGILE mission". In: *Astronomy & Astrophysics* 502 (2009), pp. 995–1013. DOI: https://doi.org/10.1051/0004-6361/200810527.

[52] M. Feroci et al. "SuperAGILE: The hard X-ray imager for the AGILE space mission". In: *Astronomy & Astrophysics* 581 (3 2007). DOI: https://doi.org/10.1016/j.nima.2007.07.147.

[53] K. Yamaoka et al. "Design and In-Orbit Performance of the Suzaku Wide-Band All-Sky Monitor". In: *Publications of the Astronomical Society of Japan* 61 (sp1 2009), S35–S53. DOI: https://doi.org/10.1093/pasj/61.sp1.S35.

[54] T. Takahashi et al. "Hard X-Ray Detector (HXD) on Board Suzaku". In: *Publications of the Astronomical Society of Japan* 59 (sp1 2007), S35–S51. DOI: https://doi.org/10.1093/pasj/59.sp1.S35.

[55] K. Hurley et al. "The Third Interplanetary Network". In: *AIP Conference Proceedings* 1279 (2010). DOI: https://doi.org/10.1063/1.3509301.

[56] *GCN: The Gamma-ray Coordinates Network (TAN: Transient Astronomy Network)*. 2018. URL: https://gcn.gsfc.nasa.gov/.

[57] Erik Blaufuss et al. *The Next Generation of IceCube Realtime Neutrino Alerts*. 2019. arXiv: 1908.04884 [astro-ph.HE].

[58] The IceCube Collaboration. *Follow-up of astrophysical transients in real time with the IceCube Neutrino Observatory*. 2020. arXiv: 2012.04577 [astro-ph.HE].

[59] Kevin Meagher, Alex Pizzuto, and Justin Vandenbroucke. *IceCube as a Multi-messenger Follow-up Observatory for Astrophysical Transients*. 2019. arXiv: 1909.05834 [astro-ph.HE].

[60] A. von Kienlin et al. "The Fourth Fermi-GBM Gamma-Ray Burst Catalog: A Decade of Data". In: *The Astrophysical Journal* 893.1 (2020), p. 46. ISSN: 1538-4357. DOI: 10.3847/1538-4357/ab7a18. URL: http://dx.doi.org/10.3847/1538-4357/ab7a18.

[61] Amy Lien et al. "THE THIRDSWIFTBURST ALERT TELESCOPE GAMMA-RAY BURST CATALOG". In: *The Astrophysical Journal* 829.1 (2016), p. 7. ISSN: 1538-4357. DOI: 10.3847/0004-637x/829/1/7. URL: http://dx.doi.org/10.3847/0004-637X/829/1/7.

[62] P. Coppin. *GRBweb*. URL: https://icecube.wisc.edu/~grbweb_public/index.html.

[63] A. Goldstein et al. "Evaluation of Automated Fermi GBM Localizations of Gamma-Ray Bursts". In: *The Astrophysical Journal* 895.1 (2020), p. 40. ISSN: 1538-4357. DOI: 10.3847/1538-4357/ab8bdb. URL: http://dx.doi.org/10.3847/1538-4357/ab8bdb.

[64] P. Coppin. *Private Communication*. 2019.

[65] *HEASARC: NASA's Archive of Data on Energetic Phenomena*. URL: https://heasarc.gsfc.nasa.gov/FTP/fermi/data/gbm/bursts/2018/bn180423033/current/glg_skymap_all_bn180423033_v00.png.

[66] *HEASARC: NASA's Archive of Data on Energetic Phenomena*. URL: https://heasarc.gsfc.nasa.gov/FTP/fermi/data/gbm/bursts/2018/bn180423033/quicklook/README.

[67] A. von Kienlin et al. "The Fourth Fermi-GBM Gamma-Ray Burst Catalog: A Decade of Data". In: *The Astrophysical Journal* 893.1 (2020), p. 46. URL: https://iopscience.iop.org/article/10.3847/1538-4357/ab7a18.

[68] Hoffman, K. "High energy neutrino telescopes". In: *New Journal of Physics* 11 (2009). URL: http://iopscience.iop.org/article/10.1088/1367-2630/11/5/055006/meta.

[69] Sullivan, G. W. and The IceCube Collaboration. "Results from the IceCube Experiment". In: *Nuclear Physics B - Proceedings Supplements* 235-236 (2013), pp. 346–351. DOI: 10.1016/j.nuclphysbps.2013.04.031. URL: https://doi.org/10.1016/j.nuclphysbps.2013.04.031.

[70] IceCube Collaboration. "Evidence for High-Energy Extraterrestrial Neutrinos at the IceCube Detector". In: *Science* 342.6161 (2013). ISSN: 0036-8075. DOI: 10.1126/science.1242856. URL: https://science.sciencemag.org/content/342/6161/1242856.

[71] IceCube Collaboration M. G. Aarsten et al. "Evidence for High-Energy Extraterrestrial Neutrinos at the IceCube Detector". In: *Science* 342.6161 (2013), 1242856–1242856. ISSN: 1095-9203. DOI: 10.1126/science.1242856. URL: http://dx.doi.org/10.1126/science.1242856.

[72] IceCube Collaboration M. G. Aarsten et al. "Observation of High-Energy Astrophysical Neutrinos in Three Years of IceCube Data". In: *Physical Review Letters* 113.10 (2014). ISSN: 1079-7114. DOI: 10.1103/physrevlett.113.101101. URL: http://dx.doi.org/10.1103/PhysRevLett.113.101101.

[73] IceCube Collaboration R. Abbasi et al. "The IceCube high-energy starting event sample: Description and flux characterization with 7.5 years of data". In: *Publication Forthcoming* (2020).

[74] C. Haack C. Wiebusch on behalf of the IceCube Collaboration. "A measurement of the diffuse astrophysical muon neutrino flux using eight years of IceCube data." In: *PoS* ICRC2017 (2017). DOI: https://doi.org/10.22323/1.301.1005.

[75] IceCube Collaboration J. Stettner. "Measurement of the Diffuse Astrophysical Muon-Neutrino Spectrum with Ten Years of IceCube Data." In: *PoS* ICRC2019 (2019). URL: https://arxiv.org/pdf/1908.09551.pdf.

[76] "Neutrino emission from the direction of the blazar TXS 0506+056 prior to the IceCube-170922A alert". In: *Science* (2018), eaat2890. DOI: 10.1126/science.aat2890. URL: https://doi.org/10.1126/science.aat2890.

[77] The IceCube Collaboration, Fermi-LAT, et al. "Multimessenger observations of a flaring blazar coincident with high-energy neutrino IceCube-170922A". In: *Science* (2018), eaat1378. DOI: 10.1126/science.aat1378. URL: https://doi.org/10.1126/science.aat1378.

[78] IceCube Collaboration Aartsen et al. "Time-Integrated Neutrino Source Searches with 10 Years of IceCube Data". In: *Physical Review Letters* 124.5 (2019). ISSN: 1079-7114. DOI: 10.1103/physrevlett.124.051103.

[79] Robert Stein et al. "A tidal disruption event coincident with a high-energy neutrino". In: *Nature Astronomy* (2021). ISSN: 2397-3366. DOI: 10.1038/s41550-020-01295-8. URL: http://dx.doi.org/10.1038/s41550-020-01295-8.

[80] Fang, Ke and Murase, Kohta. "Linking high-energy cosmic particles by black-hole jets embedded in large-scale structures". In: *Nature Physics* 14 (2018), pp. 396–398.

[81] Eli Waxman and John Bahcall. "High Energy Neutrinos from Cosmological Gamma-Ray Burst Fireballs". In: *Phys. Rev. Lett.* 78 (12 1997), pp. 2292–2295. DOI: 10.1103/PhysRevLett.78.2292. URL: https://link.aps.org/doi/10.1103/PhysRevLett.78.2292.

[82] Andrea Palladino. *Production mechanisms of high energy neutrinos and multi-messenger connections*. 2016. URL: https://agenda.infn.it/event/19259/contributions/98104/attachments/68928/85422/Palladino-nuday2019.pdf.

[83] P. Mészáros. "Astrophysical Sources of High-Energy Neutrinos in the IceCube Era". In: *Annual Review of Nuclear and Particle Science* 67.1 (2017), pp. 45–67. DOI: 10.1146/annurev-nucl-101916-123304. eprint: https://doi.org/10.1146/annurev-nucl-101916-123304. URL: https://doi.org/10.1146/annurev-nucl-101916-123304.

[84] Abbasi, R. et al. "An absence of neutrinos associated with cosmic-ray acceleration in gamma-ray bursts". In: *Nature* 484.7394 (2012), pp. 351–354. DOI: 10.1038/nature11068. URL: https://doi.org/10.1038/nature11068.

[85] Casey, James. "SEARCH FOR HIGH ENERGY GRB NEUTRINOS IN ICECUBE". PhD thesis. Georgia Institute of Technology, 2015.

[86] R. Abbasi et al. "Limits on Neutrino Emission from Gamma-Ray Bursts with the 40 String IceCube Detector". In: *Physical Review Letters* 106.14 (2011). ISSN: 1079-7114. DOI: 10.1103/physrevlett.106.141101. URL: http://dx.doi.org/10.1103/PhysRevLett.106.141101.

[87] M. G. Aartsen et al. "SEARCH FOR PROMPT NEUTRINO EMISSION FROM GAMMA-RAY BURSTS WITH ICECUBE". In: *The Astrophysical Journal* 805.1 (2015), p. L5. ISSN: 2041-8213. DOI: 10.1088/2041-8205/805/1/l5. URL: http://dx.doi.org/10.1088/2041-8205/805/1/L5.

[88] M. G. Aartsen et al. "AN ALL-SKY SEARCH FOR THREE FLAVORS OF NEUTRINOS FROM GAMMA-RAY BURSTS WITH THE ICECUBE NEUTRINO OBSERVATORY". In: *The Astrophysical Journal* 824.2 (2016), p. 115. ISSN: 1538-4357. DOI: 10.3847/0004-637x/824/2/115. URL: http://dx.doi.org/10.3847/0004-637X/824/2/115.

[89] M. Ahlers, M.C. Gonzalez-Garcia, and F. Halzen. "GRBs on probation: Testing the UHE CR paradigm with IceCube". In: *Astroparticle Physics* 35.2 (2011), 87–94. ISSN: 0927-6505. DOI: 10.1016/j.astropartphys.2011.05.008. URL: http://dx.doi.org/10.1016/j.astropartphys.2011.05.008.

[90] Richman, Michael David. "A Search For Muon Neutrinos Coincident With Gamma-Ray Bursts Using IceCube". PhD thesis. University of Maryland, 2015.

[91] Ignacio Taboada, Chun Fai Tung, and Joshua Wood. *Constrains on the extragalactic origin of IceCube's neutrinos using HAWC*. 2018. arXiv: 1801.09545 [astro-ph.HE]. URL: https://arxiv.org/abs/1801.09545.

[92] *The IceCube Neutrino Observatory*. 2015. arXiv: 1510.05223 [astro-ph.HE]. URL: https://arxiv.org/abs/1510.05223.

[93] Piero Madau and Mark Dickinson. "Cosmic Star-Formation History". In: *Annual Review of Astronomy and Astrophysics* 52.1 (2014), 415–486. ISSN: 1545-4282. DOI: 10.1146/annurev-astro-081811-125615. URL: http://dx.doi.org/10.1146/annurev-astro-081811-125615.

[94] W. Pauli. *Pauli Neutrino Letter*. 1930. URL: https://microboone-docdb.fnal.gov/cgi-bin/ShowDocument?docid=953.

[95] The IceCube Collaboration Aartsen M.G. et al. "The IceCube Neutrino Observatory: instrumentation and online systems". In: *Journal of Instrumentation* 12.03 (2017), P03012–P03012. ISSN: 1748-0221. DOI: 10.1088/1748-0221/12/03/p03012. URL: http://dx.doi.org/10.1088/1748-0221/12/03/P03012.

[96] The IceCube Collaboration. *IceCube Quick Facts*. URL: https://icecube.wisc.edu/science/icecube/detector.

[97] R. Abbasi et al. "IceTop: The surface component of IceCube". In: *Nuclear Instruments and Methods in Physics Research Section A: Accelerators, Spectrometers, Detectors and Associated Equipment* 700 (2013), 188–220. ISSN: 0168-9002. DOI: 10.1016/j.nima.2012.10.067. URL: http://dx.doi.org/10.1016/j.nima.2012.10.067.

[98] Cheung, Yee Lam Elim. "Measurement of Atmospheric Neutrino Oscillation Parameters Using Three Years of IceCube-DeepCore Dat". PhD thesis. University of Maryland, 2018.

[99] Juliana Stachurska. "IceCube High Energy Starting Events at 7.5 Years - New Measurements of Flux and Flavor". In: *EPJ Web of Conferences* 207 (2019). Ed. by C.Editor Spiering, p. 02005. ISSN: 2100-014X. DOI: 10.1051/epjconf/201920702005. URL: http://dx.doi.org/10.1051/epjconf/201920702005.

[100] Gen2 Collaboration. *IceCube-Gen2: The Window to the Extreme Universe*. 2020. arXiv: 2008.04323 [astro-ph.HE].

[101] Sheldon L. Glashow. "Resonant Scattering of Antineutrinos". In: *Phys. Rev.* 118 (1 1960), pp. 316–317. DOI: 10.1103/PhysRev.118.316. URL: https://link.aps.org/doi/10.1103/PhysRev.118.316.

[102] The IceCube Collaboration. "Detection of a particle shower at the Glashow resonance with IceCube". In: 591 (2020), pp. 220–224. URL: https://www.nature.com/articles/s41586-021-03256-1.

[103] Amanda Cooper-Sarkar, Philipp Mertsch, and Subir Sarkar. "The high energy neutrino cross-section in the Standard Model and its uncertainty". In: *Journal of High Energy Physics* 2011.8 (2011). ISSN: 1029-8479. DOI: 10.1007/jhep08(2011)042. URL: http://dx.doi.org/10.1007/JHEP08(2011)042.

[104] Raj Gandhi et al. "Ultrahigh-energy neutrino interactions". In: *Astroparticle Physics* 5.2 (1996), 81–110. ISSN: 0927-6505. DOI: 10.1016/0927-6505(96)00008-4. URL: http://dx.doi.org/10.1016/0927-6505(96)00008-4.

[105] P. A. Cherenkov. "Visible Radiation Produced by Electrons Moving in a Medium with Velocities Exceeding that of Light". In: *Phys. Rev.* 52 (4 1937), pp. 378–379. DOI: 10.1103/PhysRev.52.378. URL: https://link.aps.org/doi/10.1103/PhysRev.52.378.

[106] M.G. et al. Aartsen. "Measurement of South Pole ice transparency with the IceCube LED calibration system". In: *Nuclear Instruments and Methods in Physics Research Section A: Accelerators, Spectrometers, Detectors and Associated Equipment* 711 (2013), 73–89. ISSN: 0168-9002. DOI: 10.1016/j.nima.2013.01.054. URL: http://dx.doi.org/10.1016/j.nima.2013.01.054.

[107] Michael Larson. *Student Likelihood Workshop*. Tech. rep. IceCube Collaboration, Oct. 2020.

[108] D. Chirkin and W. Rhode. "Propagating leptons through matter with Muon Monte Carlo (MMC)". In: *ArXiv High Energy Physics - Phenomenology e-prints* (2004). URL: https://arxiv.org/abs/hep-ph/0407075.

[109] M. et. al. Tanabashi. "Review of Particle Physics". In: *Phys. Rev. D* 98 (3 2018), p. 030001. DOI: 10.1103/PhysRevD.98.030001. URL: https://link.aps.org/doi/10.1103/PhysRevD.98.030001.

[110] The IceCube Collaboration. "Optical properties of deep glacial ice at the South Pole". In: *Journal of Geophysical Research* 111.D13 (2006). DOI: 10.1029/2005jd006687. URL: https://doi.org/10.1029/2005jd006687.

[111] N. E. Bramall et al. "A deep high-resolution optical log of dust, ash, and stratigraphy in South Pole glacial ice". In: *Geophysical Research Letters* 32.21 (2005). DOI: 10.1029/2005gl024236. URL: https://doi.org/10.1029/2005gl024236.

[112] IceCube Collaboration A. Achterberg et al. "First year performance of the IceCube neutrino telescope". In: *Astroparticle Physics* 26.3 (2006), 155–173. ISSN: 0927-6505. DOI: 10.1016/j.astropartphys.2006.06.007.

[113] IceCube Collaboration R. Abbasi et al. "Calibration and characterization of the IceCube photomultiplier tube". In: *Nuclear Instruments and Methods in Physics Research Section A: Accelerators, Spectrometers, Detectors and Associated Equipment* 618.1-3 (2010), 139–152. ISSN: 0168-9002. DOI: 10.1016/j.nima.2010.03.102.

[114] Whitehorn, Nathan. "A Search for High-Energy Neutrino Emission from Gamma-Ray Bursts". PhD thesis. University of Wisconsin-Madison, 2012.

[115] The IceCube Collaboration Aartsen M G et al. "Energy reconstruction methods in the IceCube neutrino telescope". In: *Journal of Instrumentation* 9.03 (2014), P03009–P03009. ISSN: 1748-0221. DOI: 10.1088/1748-0221/9/03/p03009. URL: http://dx.doi.org/10.1088/1748-0221/9/03/P03009.

[116] Larson, Michael James. "A Search for Tau Neutrino Appearance with IceCube-DeepCore". PhD thesis. Niels Bohr Institute, 2018.

[117] IceCube Collaboration R. Abbasi et al. "The IceCube data acquisition system: Signal capture, digitization, and timestamping". In: *Nuclear Instruments and Methods in Physics Research Section A: Accelerators, Spectrometers, Detectors and Associated Equipment* 601.3 (2009), 294–316. ISSN: 0168-9002. DOI: 10.1016/j.nima.2009.01.001.

[118] Hans Niederhausen Michael Larson. *Nu Sources Filtering and Processing Review*. Tech. rep. IceCube Collaboration, Oct. 2020.

[119] IceCube Collaboration. In: *Journal of Instrumentation* 11.11 (2016), P11009–P11009. ISSN: 1748-0221. DOI: 10.1088/1748-0221/11/11/p11009. URL: http://dx.doi.org/10.1088/1748-0221/11/11/P11009.

[120] The AMANDA Collaboration Ahrens J. et al. "Muon track reconstruction and data selection techniques in AMANDA". In: *Nuclear Instruments and Methods in Physics Research Section A: Accelerators, Spectrometers, Detectors and Associated Equipment* 524.1-3 (2004), 169–194. ISSN: 0168-9002. DOI: 10.1016/j.nima.2004.01.065. URL: http://dx.doi.org/10.1016/j.nima.2004.01.065.

[121] The IceCube Collaboration Aartsen M.G. et al. "Improvement in fast particle track reconstruction with robust statistics". In: *Nuclear Instruments and Methods in Physics Research Section A: Accelerators, Spectrometers, Detectors and Associated Equipment* 736 (2014), 143–149. ISSN: 0168-9002. DOI: 10.1016/j.nima.2013.10.074. URL: http://dx.doi.org/10.1016/j.nima.2013.10.074.

[122] S. Boyd & L. Vandenberghe. ""Convex Optimization"". In: Cambridge University Press, 2009, pp. 190, 298–300.

[123] Pandel, Dirk. "Bestimmung vonWasser- und Detektorparametern und Rekonstruktion von Myonen bis 100 TeV mit dem Baikal-Neutrinoteleskop NT-72". PhD thesis. Humboldt-Universit at zu Berlin, 1996.

[124] G. Japaridze N. van Eijndhoven O. Fadiran. "Implementation of a Gauss convoluted Pandel PDF for track reconstruction in neutrino telescopes". In: *Astroparticle Physics* 28 (2007), pp. 456–462. ISSN: 0927-6505. DOI: 10.1016/j.astropartphys.2007.09.001. URL: https://doi.org/10.1016/j.astropartphys.2007.09.001.

[125] IceCube Collaboration. *Photospline*. 2020. URL: {https://github.com/icecube/photospline}.

[126] Paul H. C. Eilers and Brian D. Marx. "Flexible smoothing with B-splines and penalties". In: *Statistical Science* 11.2 (1996), pp. 89 –121. DOI: 10.1214/ss/1038425655. URL: https://doi.org/10.1214/ss/1038425655.

[127] H. Cramer. *"Mathematical Methods of Statistics"*. Princeton Univ. Press, 1945.

[128] C. R. Rao. "Information and accuracy attainable in the estimation of statistical parameters". In: *Bulletin of the Calcutta Mathematical Society* 37 (1945), pp. 81–91. ISSN: 0008-0659.

[129] G. C. Hill. "Bayesian event reconstruction and background rejection in neutrino detectors". In: *PoS* (2001). eprint: https://arxiv.org/pdf/astro-ph/0106081.pdf.

[130] Maintainer: Joulien Tatar. *Truncated Energy Software Documentation*. Tech. rep. IceCube Collaboration, 2020. URL: https://docs.icecube.aq/combo/trunk/projects/truncated_energy/.

[131] Thomas Kintscher Elisa Bernardini Konstancja Satalecka. *Gamma-Ray Follow-Up (GFU)*. Tech. rep. IceCube Collaboration, 2018.

[132] F. Pedregosa et al. "Scikit-learn: Machine Learning in Python". In: *Journal of Machine Learning Research* 12 (2011), pp. 2825–2830.

[133] M. Richman. *Pybdt user manual*. Tech. rep. IceCube Collaboration, 2018. URL: https://code.icecube.wisc.edu/projects/icecube/browser/IceCube/projects/pybdt/trunk/resources/docs/.

[134] Till Neunhöffer. "Estimating the angular resolution of tracks in neutrino telescopes based on a likelihood analysis". In: *Astroparticle Physics* 25.3 (2006), 220–225. ISSN: 0927-6505. DOI: 10.1016/j.astropartphys.2006.01.002. URL: http://dx.doi.org/10.1016/j.astropartphys.2006.01.002.

[135] Maintainer: Kevin Meahger. *Paraboloid Software Documentation*. Tech. rep. IceCube Collaboration, 2018. URL: https://docs.icecube.aq/combo/trunk/projects/paraboloid/index.html.

[136] D. Heck et al. *"Corsika: A Monte Carlo Code to Simulate Extensive Air Showers"*. Wissenschaftliche Berichte FZKA 6019, Forschungszentrum Karlsruhe, 1998.

[137] Jörg R. Hörandel. "On the knee in the energy spectrum of cosmic rays". In: *Astroparticle Physics* 19.2 (2003), 193–220. ISSN: 0927-6505. DOI: 10.1016/s0927-6505(02)00198-6. URL: http://dx.doi.org/10.1016/S0927-6505(02)00198-6.

[138] A. Gazizov and M. Kowalski. "ANIS: High energy neutrino generator for neutrino telescopes". In: *Computer Physics Communications* 172.3 (2005), 203–213. ISSN: 0010-4655. DOI: 10.1016/j.cpc.2005.03.113. URL: http://dx.doi.org/10.1016/j.cpc.2005.03.113.

[139] H.L. Lai et al. "Global QCD analysis of parton structure of the nucleon: CTEQ5 parton distributions". In: *The European Physical Journal C* 12.3 (2000), 375–392. ISSN: 1434-6052. DOI: 10.1007/s100529900196. URL: http://dx.doi.org/10.1007/s100529900196.

[140] Adam M. Dziewonski and Don L. Anderson. "Preliminary reference Earth model". In: *Physics of the Earth and Planetary Interiors* 25.4 (1981), pp. 297–356. ISSN: 0031-9201. DOI: https://doi.org/10.1016/0031-9201(81)90046-7. URL: https://www.sciencedirect.com/science/article/pii/0031920181900467.

[141] J.-H. Koehne et al. "PROPOSAL: A tool for propagation of charged leptons". In: *Computer Physics Communications* 184.9 (2013), pp. 2070–2090. ISSN: 0010-4655. DOI: https://doi.org/10.1016/j.cpc.2013.04.001.

[142] IceCube Collaboration. *Photon Propagation Code*. 2006. URL: {https://docs.icecube.aq/simulation/V05-01-02/projects/ppc/index.html}.

[143] IceCube Collaboration. *CLSim*. 2019. URL: {https://github.com/claudiok/clsim}.

[144] IceCube Collaboration. *PMTResponseSimulator*. 2010. URL: {https://docs.icecube.aq/combo/trunk/projects/DOMLauncher/PMTRes.html?highlight=pmtresponsesimulator}.

[145] Hellauer, Robert Eugene. "An All-Sky, Three-Flavor Search for Neutrinos from Gamma-Ray Bursts with the IceCube Neutrino Observatory". PhD thesis. University of Maryland, 2015.

[146] Jim Braun et al. "Time-dependent point source search methods in high energy neutrino astronomy". In: *Astroparticle Physics* 33.3 (2010), 175–181. ISSN: 0927-6505. DOI: 10.1016/j.astropartphys.2010.01.005. URL: http://dx.doi.org/10.1016/j.astropartphys.2010.01.005.

[147] Krzysztof M. Górski. *HEALPix*. 1997. URL: https://healpix.jpl.nasa.gov/index.shtml.

[148] HEALPix Team. *HEALPix: Data Analysis, Simulations and Visualization on the Sphere*. 1997. URL: http://healpix.sourceforge.net.

[149] Andrea Zonca et al. "healpy: equal area pixelization and spherical harmonics transforms for data on the sphere in Python". In: *Journal of Open Source Software* 4.35 (Mar. 2019), p. 1298. DOI: 10.21105/joss.01298. URL: https://doi.org/10.21105/joss.01298.

[150] K. M. Górski et al. "HEALPix: A Framework for High-Resolution Discretization and Fast Analysis of Data Distributed on the Sphere". In: *APJ* 622 (Apr. 2005), pp. 759–771. DOI: 10.1086/427976. eprint: arXiv:astro-ph/0409513.

[151] Jim Braun et al. "Methods for point source analysis in high energy neutrino telescopes". In: *Astroparticle Physics* 29.4 (2008), 299–305. ISSN: 0927-6505. DOI: 10.1016/j.astropartphys.2008.02.007. URL: http://dx.doi.org/10.1016/j.astropartphys.2008.02.007.

[152] Katsuaki Asano and Kohta Murase. "Gamma-Ray Bursts as Multienergy Neutrino Sources". In: *Advances in Astronomy* (2015). DOI: https://doi.org/10.1155/2015/568516.

[153] Theo Glauch. *Improved PS analysis: Systematic Uncertainties and Monte Carlo updates*. Tech. rep. IceCube Collaboration, Aug. 2020. URL: https://drive.google.com/file/d/1OhbAZIOBYBLqK_kMreGZtfrk602MiZlM/view.

[154] Theo Glauch et al. *Improved Northern Sky PS Analysis: Systematics III*. Tech. rep. IceCube Collaboration. URL: https://drive.google.com/file/d/1KWnbJD6RSNnikzdirnUQJjbub550WJEM/view.

[155] Nicholas Senno, Kohta Murase, and Peter Meszaros. "Choked Jets and Low-Luminosity Gamma-Ray Bursts as Hidden Neutrino Sources". In: (2015). DOI: 10.1103/PhysRevD.93.083003. eprint: arXiv:1512.08513.

[156] Michela Fasano et al. *Estimating the Neutrino Flux from Choked Gamma-Ray Bursts*. 2021. arXiv: 2101.03502 [astro-ph.HE].

[157] E. Burns et al. "Identification of a Local Sample of Gamma-Ray Bursts Consistent with a Magnetar Giant Flare Origin". In: *The Astrophysical Journal* 907.2 (2021), p. L28. ISSN: 2041-8213. DOI: 10.3847/2041-8213/abd8c8. URL: http://dx.doi.org/10.3847/2041-8213/abd8c8.